

**EDDY CURRENT NONDESTRUCTIVE EVALUATION USING
MAGNETORESISTIVE SENSING**

By

Guang Yang

A DISSERTATION

Submitted to
Michigan State University
in partial fulfillment of the requirements
for the degree of

Electrical Engineering—Doctor of Philosophy

2013

ABSTRACT

EDDY CURRENT NONDESTRUCTIVE EVALUATION USING MAGNETORESISTIVE SENSING

By

Guang Yang

Reliable inspection of hidden cracks in multilayer objects, such as the airframe structures still poses a major challenge in NDE. Conventional electromagnetic methods are limited in their abilities to detect second and third layer cracks in riveted structures. Cracks are normally found at fastener sites and the presence of steel fastener (high permeability) produces a strong signal that masks any indications from a crack. An eddy current (EC) system with sheet current source for uniform field generation and magnetoresistive (MR) sensing is studied in this dissertation.

The contributions of this research are: 1) A study of three-component measurements using MR sensors and the use of information in these components to enhance crack detection at steel fasteners. 2) Experimentally validated model-based study of Pulsed EC excitation and low frequency EC excitation systems for the inspection of buried cracks at fastener sites. 3) Rotating current excitation designed to enhance the system capability to detect cracks of all orientations at fastener sites. 4) A statistical signal processing scheme developed for automated analysis of measured data. 5) Development of a numerical model for simulating the phenomenon in time and frequency domains. Model based study is used to assist the overall system and algorithm design. Results of implementing the techniques on simulation and measurement fully validate the proposed methods.

**To my family, particularly to my mother
For their love and support**

ACKNOWLEDGEMENTS

I would like to express my sincere gratitude to my major advisor and mentor, Dr. Lalita Udpa, for her extraordinary support, guidance and encouragement during my Ph.D. study. Special thanks to her invaluable guidance and help in my writing. Dr. Lalita Udpa has advised me not only on my research, but also on my career and life. I feel fortunate to work with her and proud of being a member of NDEL research group.

I would like to express my sincere thanks to my co-advisor Dr. Satish S. Udpa for his continuous support and guidance. I would like to thank my PhD studies committee: Dr. Wei and Dr. Rothwell for their time, guidance and suggestions. I would like to express appreciation to Dr. Tamburrino for his invaluable guidance and help for my experimental research and continuous support during my PhD study.

I would like to thank my previous colleagues Dr. Zeng, Dr. Deng and Dr. Liu for their support and help. I would like to thank my present colleagues of NDEL. Special thanks goes to Gerges Dib for all his invaluable helps. Many thanks goes to Naiguang Lei. Many thanks also goes to Dr. Kim for his guidance and help in signal processing research.

I would like to express my heartfelt gratitude to my family, friends, especially my mother, for their constant support and encouragement. I would like to thank my beloved parents for their faith in me. I acknowledge their patience and understanding through various situations in my life, allowing me to reach this achievement.

TABLE OF CONTENTS

LIST OF TABLES.....	viii
LIST OF FIGURES.....	ix
CHAPTER 1. INTRODUCTION.....	1
1.1 Introduction to Nondestructive Testing.....	1
1.1.1 Radiographic Testing.....	2
1.1.2 Ultrasonic Testing.....	2
1.1.3 Electromagnetic Testing.....	3
1.2 Inspection of Multilayer Structures.....	5
1.3 Challenges and Goals.....	6
1.3.1 Problem Statement.....	6
1.3.2 Research Objectives and Methodologies.....	8
1.4 Organization of the Dissertation.....	9
CHAPTER 2. REVIEW OF ELETROMAGNETIC NDE.....	11
2.1 Introduction.....	11
2.2 Skin Depth and Development of EC Techniques.....	14
2.3 Configurations of EC Coil Probes.....	16
2.3.1 Conventional Coil Probes.....	16
2.3.2 Planar Coil Probes.....	18
2.3.3 Limitations of Coil Sensors.....	22
2.4 Magnetic Field Sensors for Hybrid EC Testing.....	23
2.5 Magneto-resistive (MR) Sensors.....	25
2.5.1 Magnetoresistance.....	25
2.5.2 Anisotropic Magneto-resistive (AMR) Sensor.....	26
2.5.3 Giant Magneto-resistive (GMR) Sensor.....	28
2.5.4 NDE Applications of MR Sensors.....	31
2.6 EC Techniques for Inspection of Riveted Structures.....	32
2.6.1 EC Magneto-Optic Imaging.....	33
2.6.2 Other EC Techniques.....	35
CHAPTER 3. EC-MR SENSOR SYSTEM – PULSE EXCITATION.....	38
3.1 Introduction.....	38
3.2 Background.....	38
3.2.1 Skin Depth in Transient Fields.....	38
3.2.2 Transient Signal Characteristics.....	40
3.2.3 Review of Transient EC NDE for Layered Structure.....	43

3.2.4	Time Domain versus Frequency Domain.....	46
3.2.5	Review of Transient Field Numerical Modeling.....	49
3.3	PEC Testing System with MR Sensor.....	50
3.3.1	Excitation Coil Configuration.....	52
3.3.2	PEC-GMR Probe Operation.....	55
3.3.3	Giant Magnetoresistive Sensor.....	56
3.3.4	Experimental Set-up.....	57
3.4	Inspection of Riveted Structures.....	58
3.4.1	A-scan Measurement of Transient Field.....	58
3.4.2	C-scan Image Measurement of Transient Field.....	61
3.5	Time-domain Modeling of PEC-GMR Testing.....	62
3.5.1	FE Modeling.....	62
3.5.2	Time-domain Modeling Schemes.....	68
3.5.3	Modeling in Frequency-domain vs. Time-domain.....	76
3.5.4	Time-domain Model Validation.....	79
3.6	MR Measurements of 3-component Transient Fields.....	81
3.6.1	Ferrous Fastener Inspection.....	82
3.6.2	Simulation Study of 3-component Measurements.....	83
3.6.3	Experimental Study of 3-component Measurements.....	86
3.7	Summary.....	88
 CHAPTER 4. ANALYSIS OF PEC-GMR INSPECTION DATA.....		89
4.1	Introduction.....	89
4.2	Review of Signal Enhancement for PEC Inspection.....	89
4.3	Multilayer Riveted Specimen.....	90
4.4	Automatic Analysis of PEC-GMR C-scan Images.....	93
4.4.1	Principal Component Analysis.....	93
4.4.2	Flaw Detection.....	95
4.5	Results of PEC-GMR Inspection.....	98
4.5.1	Detection of 2 nd and 3 rd Layer Cracks in Sample 1.....	98
4.5.2	Detection of 2 nd Layer Cracks in Sample 2.....	101
4.5.3	Flaw Detection using Tangential-component Measurements.....	104
4.6	Automatic Crack Detection using 3-component GMR Images.....	110
4.6.1	Feature Extraction.....	110
4.6.2	Crack Detection Scheme.....	112
4.7	Summary.....	124
 CHAPTER 5. EC-MR SENSOR SYSTEM – LOW FREQUENCY EXCITATION		125
5.1	Introduction.....	125
5.2	Low Frequency EC-MR Sensing.....	125
5.2.1	Experimental Set-up.....	125
5.2.2	Inspection of Cracks around Steel Fasteners-Normal Component.....	127

5.2.3	Inspection of Cracks around Steel Fasteners-Tangential Component.....	129
5.3	Model-based Study of Low Frequency 3D EC-GMR Measurements.....	131
5.3.1	FE Model of EC-GMR Imaging.....	132
5.3.2	Experimental Validation.....	135
5.3.3	Image Fusion Method.....	137
5.3.4	Model-based Study-Inspection of Non-ideal Fasteners.....	137
5.4	Summary.....	140

CHAPTER 6. EC-MR SENSOR SYSTEM – ROTATING FIELD EXCITATION

	142
6.1	Introduction.....	142
6.2	Orthogonal Current Excitation.....	142
6.2.1	Rotating Field.....	142
6.2.2	Experimental Set-up.....	143
6.3	Detection of Crack Orientation at Rivet Site.....	144
6.3.1	Parameters in a Practical Design.....	144
6.3.2	Model-based Investigation of Crack Orientation Detection.....	147
6.4	Experimental Validation.....	148
6.4.1	Experimental Detection of Crack Orientations.....	148
6.4.2	Design of Array Receiver to Crack Orientations.....	151
6.5	Summary.....	153

CHAPTER 7. PARAMETRIC STUDY OF EC-GMR DETECTION SYSTEM.....

	154
7.1	Introduction.....	154
7.2	Sensor-tilt Study.....	154
7.2.1	Sensor-tilt of GMR Sensing.....	154
7.2.2	Model-based Investigation of Sensor-tilt.....	155
7.3	Invariant Analysis.....	158
7.3.1	Transformation for Invariance to Sensor-tilt.....	158
7.3.2	Invariance Transformations of GMR signals.....	160
7.3.3	Invariance Features and Crack Detection.....	165
7.3.4	Implementation to Experimental Data.....	167
7.4	Summary.....	170

CHAPTER 8. CONCLUSIONS AND FUTURE WORK.....

8.1	Accomplishments and Conclusions.....	171
8.2	Future Work.....	173

BIBLIOGRAPHY.....	174
-------------------	-----

LIST OF TABLES

Table 3-1 PEC system summary.....	45
Table 3-2 Summary of transient field modeling and simulation.....	51
Table 3-3 Simulation error analysis of the interpolation modeling in time-domain.....	71
Table 3-4 Simulation error analysis of the impulse response based modeling.....	76
Table 3-5 Simulation signal accuracy enhancement.....	76
Table 3-6 Computation time comparison.....	78
Table 4-1 Sample 1 – aluminum fastener.....	99
Table 4-2 Sample 2 – steel fastener with 2 nd layer cracks.....	101
Table 5-1 Feature F_r quantifying the defective steel fastener.....	140

LIST OF FIGURES

Figure 1.1 NDT and NDE technology.....	1
Figure 1.2 Inspection of riveted multilayer structure: (a) Problem of ultrasonic testing and (b) Desired EC testing (For interpretation of the references to color in this and all other figures, the reader is referred to the electronic version of this dissertation.)	6
Figure 1.3 Layered structure: (a) Aircraft riveted skin structure geometry and (b) Initiation of hidden corrosion and cracks at rivet sites.....	7
Figure 2.1 Principle of the EC inspection: (a) A typical EC probe above a conducting specimen under test and (b) The measurement of coil impedance.....	13
Figure 2.2 Eddy current testing system.....	14
Figure 2.3 Demonstration of skip depth in EC testing (Comsol 3.5 simulation): (a) 100 Hz EC and (b) 1 KHz EC.....	15
Figure 2.4 Typical EC probes: (a) Pancake type coil [50] (b) Bobbin type (inner diameter) coil [2] (c) Encircling type (outer diameter) coil.....	17
Figure 2.5 Coil probes-mode of operation [49, 51]: (a) Double-function probe in absolute mode (b) Double-function probe in differential mode (c) Separate-function probe in absolute mode (d) Separate-function probe in differential mode.....	18
Figure 2.6 Planar coil configurations.....	19
Figure 2.7 Two designs of planar coil probes: (a) a basic MWM probe [56] and (b) a meander/mesh coupled probe.....	21
Figure 2.8 Hybrid probe [49, 74]: EC coil with magnetic field sensor.....	24
Figure 2.9 Magneto-resistive effect in a thin current strip.....	26
Figure 2.10 AMR device: (a) Barber-pole structure for an optimum alignment and (b) Resistance change $\Delta R/R$ vs. angle θ , and resistance R vs. applied field H	27

Figure 2.11 Illustration of the GMR effect [14]: (a) Lots of scatterings due to the alternating magnetization of the layers (b) Reduced scatterings when the magnetization of the layers is aligned by an applied field (c) Resistance variation as a function of an applied magnetic field.....	29
Figure 2.12 Microscope picture of a GMR sensor fabricated by NVE Inc.....	30
Figure 2.13 EC-MO imaging technique: (a) Faraday rotation effect in a MO sensor (b) Schematic of the MO imaging system [85] (c) MO images of riveted structures (d) Images of riveted structures using LMOI system in Europe.....	34
Figure 2.14 Self-nulling EC probe: (a) Probe schematic and (b) Inspection of ferromagnetic protruding head fasteners.....	35
Figure 2.15 EC-GMR probes for riveted structure inspection: (a) Schematic of a rotational D-shaped coil and GMR based probe [93] and (b) A sheet current and AMR sensing probe.....	36
Figure 3.1 Skin depths of conventional EC and transient EC fields (Comsol 3.5 simulation): (a) Conventional 100Hz EC result: induced eddy current and skin depth and (b) 100Hz square-wave PEC result: induced eddy current and skin depth.....	40
Figure 3.2 PEC signals: (a) A typical reference-subtracted transient response and typical features in the time domain and (b) Transient response associated with defective information at different depths (Comsol 3.5 simulation).....	42
Figure 3.3 Time domain vs. frequency domain: Transient excitations in different pulse widths and their DFT spectrum results.....	47
Figure 3.4 Square waveform as a source of pulse excitation (left) and the reconstruction of the waveform by adding Fourier series harmonics (right).....	49
Figure 3.5 Schematic of the multi-line planar probe design.....	52
Figure 3.6 Simulation results of pancake coil: (a) Tangential component (B_x) of magnetic field (T) and (b) Induced currents (A/m ²).....	52
Figure 3.7 Simulation results of multi-line coil: (a) Normal component (B_y) of magnetic field (T) (b) Induced currents (A/m ²) (c) Comparison of induced currents due to two coil configurations.....	54

Figure 3.8 Schematic of the operation of multi-line planar probe.....	55
Figure 3.9 Characteristic curve for the calibration of the GMR sensor.....	56
Figure 3.10 Schematic of the PEC-GMR inspection system.....	58
Figure 3.11 GMR measurements of the transient field B_z component along a line scan above a fastener with a subsurface crack: (a) Inspection Geometry (b) Sequence of A-scan signals within the fastener head region (c) Comparison of transient signals at the fastener head edge areas for crack indication.....	60
Figure 3.12 Three modes of PEC-GMR signals in the inspection of a riveted structure.....	61
Figure 3.13 A typical EC problem with regions, boundary sections and interface.....	64
Figure 3.14 A geometry used in the time-domain modeling: (a) Simulation geometry and three scan positions and (b) Geometry FE mesh.....	69
Figure 3.15 The excitation source signal (upper left), and the simulation results of B_z in time-domain modeling at positions P1, P2, and P3.....	69
Figure 3.16 The first peak of B_z in the simulation results at positions P1, P2, and P3.....	70
Figure 3.17 Simulation results of B_z using the time-domain interpolation modeling: (a) PEC-GMR signals at P1 (b) PEC-GMR signals at P2 (c) PEC-GMR signals at P3.....	72
Figure 3.18 The strategy for impulse response based time-domain simulation.....	73
Figure 3.19 Impulse response based simulation results vs. the reference signal for the positions P1, P2, and P3.....	75
Figure 3.20 Simulations of PEC signals using FE solver in frequency-domain: Predicted transient signal of 250 frequency steps vs. the reference signal simulated in time-domain.....	77
Figure 3.21 Simulations of PEC signals: predicted transient signal of 250 frequency steps vs. predicted transient signals with interpolation of 100 and 50 frequency steps.....	78

Figure 3.22 Model validation: Simulation signals of 250 time steps and signals of the impulse response based modeling (30 time steps) vs. experimental signals.....	79
Figure 3.23 Modeling geometry of a three layer riveted plate with a 3rd layer crack at aluminum fastener site.....	80
Figure 3.24 PEC-GMR signals at three scan positions: (a) Simulation signals and (b) Experimental signals.....	81
Figure 3.25 Numerical results illustrating the challenge of ferrous fastener inspection when measuring the normal magnetic field component (B_z): (a) Induced field at an aluminum fastener without crack (left image) and with crack (right image) (b) Induced field at a steel fastener without crack (left image) and with crack (right image) (c) C-scan image in the presence of a subsurface 8mm notch a at aluminum fastener site (left image), and at steel fastener site (right image).....	82
Figure 3.26 Simulation for steel fastener structures-Test sample: no crack vs. with 2.87mm notch.....	84
Figure 3.27 Simulation of 3-component measurements for steel fastener structures: (a)-(c) Simulation signals of B_z , B_y , B_x components respectively (d) Subtraction of the no flaw measurements from the 2.87 mm flaw measurements for each component.....	85
Figure 3.28 GMR sensing 3-component of the magnetic field.....	87
Figure 3.29 PEC-GMR measurement of a steel fastener with a 2.87 mm notch using three components: (a) Test geometry (b) C-scan images of B_z , B_y , B_x (c) Transient A-scan signals of B_z , B_y , B_x	87
Figure 4.1 Schematic of Sample 1: three layers aluminum plate with aluminum fasteners and cracks in second and third layers (a) Side view of cracks in the second layer (b) Side view of cracks in the third layer (c) Top view of Sample 1.....	90
Figure 4.2 Schematic of Sample 2: top view of a three layers aluminum plate with four rows of steel fasteners, and cracks dimensions in the second layer at each fastener site in every row.....	91
Figure 4.3 Schematic of sample 3: two layers aluminum sample with aluminum fasteners and cracks in the bottom layer.....	92

Figure 4.4 Flaw detection using the image analysis.....	96
Figure 4.5 Principle of applied PCA analysis.....	97
Figure 4.6 C-scan images of aluminum fasteners in Sample 1 using PEC-GMR measurements.....	98
Figure 4.7 Detection of cracks in the 2nd layer of Sample 1 using the PCA method (a) Detection results by PC1 vs. PC3 representations (b) Detection results by PC3 vs. PC2 representations.....	100
Figure 4.8 Detection of cracks in the 3rd layer of Sample 1 using the PCA method (a) Detection results by PC1 vs. PC3 representations (b) Detection results by PC3 vs. PC2 representations.....	100
Figure 4.9 C-scan images of steel fasteners in Sample 2 using PEC-GMR measurements.....	101
Figure 4.10 Detection of cracks around steel fasteners in Row 1 to Row 4 of Sample 2 using the 3D plots of PC1 to PC3: B_z component.....	103
Figure 4.11 Detection of cracks in the 2nd layer of Sample 2 using the PCA method (steel fasteners in Row 1 to Row 4): B_z component.....	104
Figure 4.12 PEC-GMR tangential-component measurements of steel fasteners (a) C-scan images of B_y measurements (b) C-scan images of B_x measurements.....	105
Figure 4.13 Detection of cracks around steel fasteners in Row 1 to Row 4 of Sample 2 using the 3D plots of PC1 to PC3: B_y component.....	106
Figure 4.14 Detection of cracks in the 2nd layer of Sample 2 using the PCA method (steel fasteners in Row 1 to Row 4): B_y component.....	107
Figure 4.15 Detection of cracks around steel fasteners in Row 1 to Row 4 of Sample 2 using the 3D plots of PC1 to PC3: B_x component.....	108
Figure 4.16 Detection of cracks in the 2nd layer of Sample 2 using the PCA method (steel fasteners in Row 1 to Row 4): B_x component.....	109
Figure 4.17 Orientation based feature extraction.....	111

Figure 4.18 Asymmetry quantification using moment based features (3rd & 4th orders).....	112
Figure 4.19 Overall approach for automated crack detection.....	113
Figure 4.20 Classification results of steel fasteners in Row 1 using features <i>ori</i> calculated from PC1 and PC2, <i>s</i> and <i>k</i> calculated from PC2: PEC-GMR measurements of <i>Bz</i> component.....	114
Figure 4.21 Classification results of steel fasteners in Row 2 using features <i>ori</i> calculated from PC1 and PC2, <i>s</i> and <i>k</i> calculated from PC2: PEC-GMR measurements of <i>Bz</i> component.....	115
Figure 4.22 Classification results of steel fasteners in Row 3 using features <i>ori</i> calculated from PC1 and PC2, <i>s</i> and <i>k</i> calculated from PC2: PEC-GMR measurements of <i>Bz</i> component.....	116
Figure 4.23 Classification results of steel fasteners in Row 4 using features <i>ori</i> calculated from PC1 and PC2, <i>s</i> and <i>k</i> calculated from PC2: PEC-GMR measurements of <i>Bz</i> component.....	117
Figure 4.24 Classification results of steel fasteners in Row 1 using features <i>ori</i> calculated from PC1 and PC2, <i>s</i> and <i>k</i> calculated from PC2: PEC-GMR measurements of <i>By</i> component.....	118
Figure 4.25 Classification results of steel fasteners in Row 2 using features <i>ori</i> calculated from PC1 and PC2, <i>s</i> and <i>k</i> calculated from PC2: PEC-GMR measurements of <i>By</i> component.....	119
Figure 4.26 Classification results of steel fasteners in Row 3 using features <i>ori</i> calculated from PC1 and PC2, <i>s</i> and <i>k</i> calculated from PC2: PEC-GMR measurements of <i>By</i> component.....	120
Figure 4.27 Classification results of steel fasteners in Row 4 using features <i>ori</i> calculated from PC1 and PC2, <i>s</i> and <i>k</i> calculated from PC2: PEC-GMR measurements of <i>By</i> component.....	121
Figure 4.28 Classification results of steel fasteners in (a) Row 1 (b) Row 2 (c) Row 3 (d) Row 4 using feature <i>s</i> and <i>k</i> calculated from PC1: PEC-GMR measurements of <i>Bx</i> component.....	122

Figure 5.1 Schematic of low frequency EC-GMR system: (a) Experimental Set-up and (b) Signal demodulation.....	126
Figure 5.2 C-scan images of steel fasteners in Sample 2 using low frequency EC-GMR measurements: B_z component.....	127
Figure 5.3 Inspection of steel fasteners in Sample 2 using EC-GMR detection: B_z measurements (a) Plots of conventional complex trajectories (b) Detection of hidden cracks around steel fastener sites using the PCA method (c) Polar plots with data rotation for automatic detection.....	128
Figure 5.4 C-scan images of steel fasteners in Sample 2 using low frequency EC-GMR measurements: B_y component.....	130
Figure 5.5 Inspection of steel fasteners in Sample 2 using EC-GMR detection: B_y measurements (a) Detection of hidden cracks around steel fastener sites using the PCA method (b) Polar plots with data rotation for automatic detection.....	131
Figure 5.6 Modeling study of a three layers riveted aircraft structure: (a) Test geometry and (b) Distributions of 3D induced currents.....	132
Figure 5.7 Simulation of 3-component C-scan images of three cases: (a) Quadrature part of B_z (b) Quadrature part of B_y (c) Quadrature part of B_x	134
Figure 5.8 Qualitative comparison of experimental and simulation C-scan images of B_z component for a steel fastener with 2.8 mm notch: (a)-(b) Experimental in-phase and quadrature parts (c)-(d) Simulation in-phase and quadrature parts.....	135
Figure 5.9 Qualitative comparison of experimental and simulation C-scan images of B_y component for a steel fastener with 2.8 mm notch: (a)-(b) Experimental in-phase and quadrature parts (c)-(d) Simulation in-phase and quadrature parts.....	136
Figure 5.10 Qualitative comparison of experimental and simulation C-scan images of B_x component for a steel fastener with 2.8 mm notch: (a)-(b) Experimental in-phase and quadrature parts (c)-(d) Simulation in-phase and quadrature parts.....	136
Figure 5.11 Fusion of quadrature parts of the 3-component GMR measurements.....	137
Figure 5.12 Geometries of steel fastener structures: ideal and non-ideal fasteners.....	137

Figure 5.13 Simulation geometries and results: (a) Geometries of three cases: steel fastener without defect (left), with a 2.8 mm notch (middle) and off-centered fastener without defect (right) (b)-(d) B_z , B_y and B_x components (quadrature parts) for the corresponding cases.....	138
Figure 5.14 Fused images: (a) Defect-free steel fastener (b) Steel fastener with a 2.8 mm notch (c) Off-centered steel fastener.....	139
Figure 6.1 Planar multi-line current field: (a)-(b) linear current excitation: linear current field (c) rotating current excitation: rotating current field.....	143
Figure 6.2 Experimental set-up of the rotating current field.....	144
Figure 6.3 Demonstration of crack detection using the rotating field: (a) No crack case and (b) Crack at orientation 90° (parallel to Y direction current).....	145
Figure 6.4 Probe lift-off study: (a) Model-based study of rotating field variations for the crack case (b) Model-based study of rotating field variations for the no crack case (c) Calibrated vs. ideal rotating current field for the crack case (d) Calibrated vs. ideal rotating current field for the no crack case.....	146
Figure 6.5 Detection of crack orientations: (a) Cracks geometry in all directions (b) Rotating field from cracks around aluminum fasteners (c) Rotating field from cracks around steel fasteners (steel fastener effect removed).....	147
Figure 6.6 Experimental study of rotating field: (a) Field measurement due to the top source coil (b) Field measurement due to the bottom source coil (c) Total rotating field sensitive to a crack around steel fastener site: absolute value of B_z	149
Figure 6.7 Experimental data from cracks with different orientations: (a) Geometry of crack in different orientations and (b) Rotating field measurement.....	151
Figure 6.8 GMR image measurement without probe motion: (a) B_z measurement of aluminum plate and (b) B_z measurement of a defective steel fastener.....	152
Figure 6.9 Application of GMR array receiver: B_z fast image measurement of fastener using rotating field (a) Without crack and (b) With crack at 90° orientation.....	153
Figure 7.1 Sensor-tilt variations: (a) Probe lift-off and tilt sensor and (b) GMR sensor measurements of magnetic field components.....	155

Figure 7.2 Sensor-tilt measurement: (a) Geometry and FE mesh of tested sample: three-layer riveted structure and (b) Definition of tilt degrees in two directions.....	156
Figure 7.3 Magnetic field measured under tilt GMR sensor for a crack-free fastener: (a) Real part of signals and (b) Imaginary part of signals.....	157
Figure 7.4 Diagram of ICA based transformation invariant to sensor-tilt.....	159
Figure 7.5 Transformed signals invariant to sensor-tilt in the inspection of a crack-free aluminum fastener: (a) Real part of signals and (b) Imaginary part of signals.....	160
Figure 7.6 Studied riveted geometries.....	161
Figure 7.7 Measured GMR complex signals of defect-free and defective fasteners: (a) Real parts of signals and (b) Imaginary parts of signals.....	161
Figure 7.8 Transformed GMR complex signals of defect-free and defective fasteners: (a) Real parts of signals and (b) Imaginary parts of signals.....	163
Figure 7.9 Invariance feature analysis: (a) Skewness curves of transformed GMR signals regarding different fastener states: single cracks vs. no crack (b) Two cracks on both sides.....	164
Figure 7.10 Crack detection: classification of GMR signals (the real part) using invariance features.....	166
Figure 7.11 Classification of GMR signals in Figure 7.10 using higher order invariance features.....	167
Figure 7.12 GMR signals collected under two sensor-tilt states.....	168
Figure 7.13 Results of invariance analysis: (a) Transformations of measured GMR signals and (b) Classification result using invariance features.....	169
Figure 8.1 Detection of the subsurface cracks (less than 1mm) around aluminum fasteners in Sample 3: (a) Schematic of probe in a reduced size (b-c) C-scan images of normal component (d) Automatic detection using the PCA processing.....	173

CHAPTER 1 INTRODUCTION

1.1 Introduction to Nondestructive Testing

Nondestructive testing and evaluation (NDT/NDE) is the assessment of the structural integrity of a material or component without causing any physical damage to the test object [1]. NDE techniques are well developed and widely used by industry to monitor and detect flaws or crack-like discontinuities. NDT/NDE techniques play a major role in quality control, safety maintenance, and failure prevention. The application of NDE technology has improved the reliability of operating aircraft, pipelines, bridges, nuclear power plants, etc. In order to inspect a variety of materials, a number of NDT techniques, employing different physical principles, have emerged. As show in Figure 1.1, a typical NDT method consists of an energy source that interacts with the specimen under test, and a receiving transducer that picks up the response of energy-material interaction. A measured NDT signal contains the indication of possible defect in the test object.

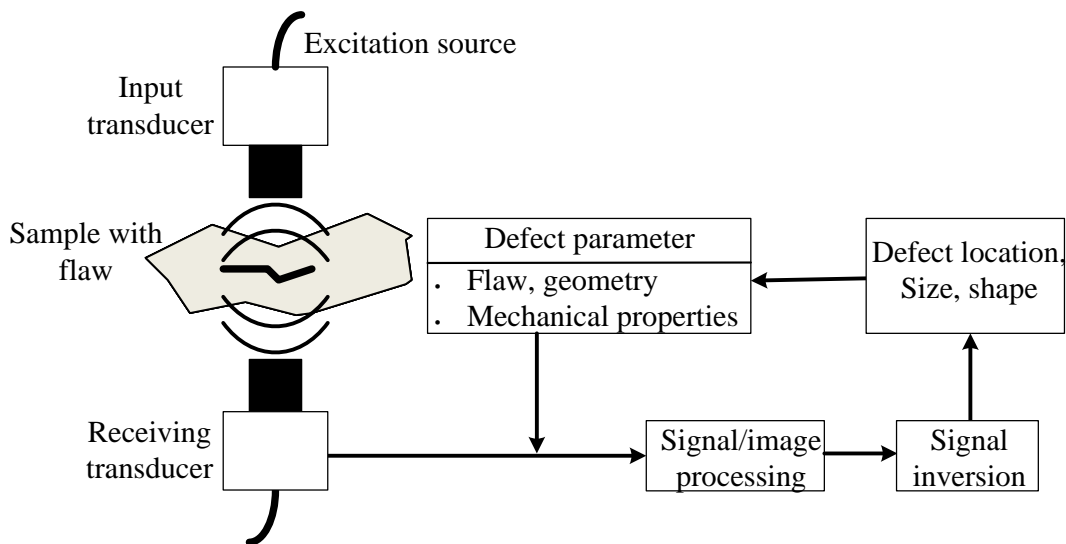


Figure 1.1 NDT and NDE technology

Each NDT/NDE method has certain advantages and limitations. Radiographic, ultrasonic, and electromagnetic methods are some of the commonly used approaches in NDE [1-4].

1.1.1 Radiographic Testing

Radiographic testing involves the use of a penetrating radiation source such as gamma rays or X-rays that travels through the object under test. The intensity of the beam energy is reduced after passing through the test specimen. The attenuation depends on material thickness and absorption coefficient. The energy distribution of the transmitted beam is imaged on a film or other imaging media. The density in a defect/crack region is generally lower than the rest of the sample, which produces intensity differences in the radiographic image [3-4].

Radiographic NDT is extensively applied to find internal defects in coating and weld inspection [4]. However, radiographic imaging is a projection of a cross-section of the test object, and it requires a two-sided access to the component under examination. The test is highly directional and a simple radiograph cannot provide depth information of the discontinuity [1, 3-4]. Moreover, radiographic NDT has limitations due to the radiation hazard involved in its use and also, the equipment is relatively expensive.

1.1.2 Ultrasonic Testing

Ultrasonic testing uses the transmission of high frequency elastic waves (0.1 and 25 MHz) into a material to detect imperfections or locate changes in material properties. Acoustic energy is transmitted, reflected and scattered within the object under test or redirected by internal interfaces or anomalies. The reflected beam is captured by the transducer that is located in contact or in close proximity to the test object, and analyzed to determine the presence and

location of flaws or discontinuities [1, 3-4]. The most common ultrasonic examination, pulse-echo testing, employs a piezoelectric transducer that is energized in a pulsed mode to direct and propagate sound energy into the specimen. The features in the received signals (echoes) are evaluated to identify discontinuities [3-4].

Ultrasonic NDT is widely used to measure material thickness and qualify the internal structure of metallic and non-metallic materials. However, ultrasonic testing needs couplant to inject energy efficiently into material and in general, cannot be used effectively in a layered structure with air gaps. Furthermore, small and thin objects and coarse-grained materials are difficult to be inspected, due to high scattering of the elastic waves in those materials. Interpretation of acquired signals demand advanced signal interpretation algorithms [3-4].

1.1.3 Electromagnetic Testing

Electromagnetic NDT techniques covering a broad range of the electromagnetic spectrum are non-contact and offer a low-cost means for high speed, large scale testing of metallic materials. Electromagnetic NDT includes magnetic flux leakage technique (static fields), eddy current (EC) method and remote field EC testing (quasi-static fields), microwave testing (high frequency fields), etc. [5]. In these techniques, the material under examination is excited electromagnetically and changes associated with electromagnetic fields are monitored and measured. Received signals contain information about material anomalies that affect electrical conductivity, magnetic permeability or dielectric permittivity. Electromagnetic methods have been used extensively in nuclear, aerospace, marine, high pressure and high temperature environments. They have been applied for flaw detection, microstructure characterization, and

evaluation of mechanical properties and residual stresses [5-8].

Electromagnetic NDT techniques differ in their detection sensitivity and capability, and signal analysis techniques for crack characterization [5]. Magnetic flux leakage testing, active or residual, is established by magnetizing a ferromagnetic material. The presence of a flaw in a material causes a discontinuity in its magnetic permeability. This distorts the distribution of the magnetic flux lines, and a part of the flux ‘leaks’ into the air in the vicinity of the flaw. During testing, the leakage field is captured by scanning the specimen’s surface with a flux-sensitive transducer. However, this method is limited to detect defects on the surface or near the surface of a ferromagnetic object. At the other end of the spectrum, microwave and Terahertz NDE methods are employed for defect detection by measuring differences in dielectric properties of non-conducting materials [6, 8-9].

Conventional EC technique is the most common electromagnetic method used for the inspection of conductive components in several industries, such as nuclear and aerospace. It is widely employed to inspect surface defects, subsurface corrosion and coating characterization of conductive materials. In particular, this NDT method offers advantages in testing layered structures [2, 6-9]. An EC testing system consists of a probe coil excited by an alternating current. The discontinuities in component properties cause changes in induced current or magnetic field. Resultant fields provide complex signals representing probe coil impedance changes, which carries information about material properties [2, 5-7]. Recently, EC testing systems using advanced magnetic sensors have been investigated [8]. A detailed review of EC techniques is presented in Chapter 2 of this dissertation.

1.2 Inspection of Multilayer Structures

The examination of multilayer structures poses a major challenge in the maintenance of aging aircraft and the aerospace industry [10-11]. Aeronautical components such as aircraft wings and riveted fuselage lap joints, undergo fatigue damage that occur around fasteners due to mechanical stresses. Undetected cracks hidden at fastener sites in layered structures can lead to catastrophic failures. Therefore, reliable NDT methods are required to detect these embedded cracks. EC methods are popularly used for detecting corrosion and subsurface fatigue cracks in riveted multilayer structures [11-12]. The penetration of low frequency electromagnetic fields through multiple layers provides the ability to detect hidden cracks in subsurface layers or small cracks under fastener heads without safety hazards. Figure 1.2 compares the penetration of electromagnetic and ultrasonic fields through the thickness of a multilayered structure.

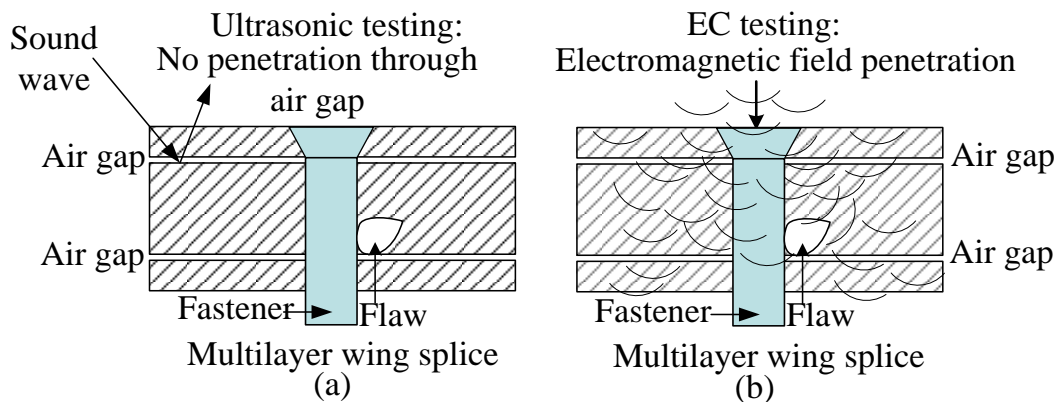


Figure 1.2 Inspection of riveted multilayer structure: (a) Problem of ultrasonic testing and (b) Desired EC testing

(For interpretation of the references to color in this and all other figures, the reader is referred to the electronic version of this dissertation.)

However, due to skin depth effect, conventional EC method suffers attenuation of EC intensity along the depth of structure under test. In addition, the fastener behaves as a strong discontinuity

through the full depth of the layered structure, masking the response or indication due to small fatigue cracks. Hence, techniques for enhancing the signal-to-noise ratio in EC measurements are required. This dissertation focuses on the development of EC NDE techniques to reliably detect small cracks at fastener sites in layered structures.

1.3 Challenges and Goals

EC techniques that offer deep penetration of induced currents have been studied for the detection of subsurface discontinuities in layered structures. These techniques include low frequency EC testing and pulsed eddy current (PEC) methods. Particularly in the aerospace industry, EC testing is currently used for detecting fastener holes in aircraft components [12-17]. Low frequency EC method offers the potential to detect cracks that are not detectable by X-ray radiography [18]. However, present EC techniques require the removal of fasteners or perform inspections limited to corrosion detection, large size subsurface slots, and near-surface cracks within a few millimeters from the surface. Additionally, these methods do not quantify the reliability of defect detection under variable factors during inspection [18]. This dissertation attempts to address these problems.

1.3.1 Problem Statement

A typical aircraft skin structure including fuselage skin or wing splice that is joined together by fasteners is shown schematically in Figure 1.3 (a). Fasteners are typically made of aluminum, titanium or steel and typical diameters are about 20 mm. This type of structure tends to produce high stress concentration around fastener holes [10-11]. Hence, fatigue flaws, stress corrosion and cracks usually initiate at rivet sites in subsurface layers, as demonstrated in Figure 1.3 (b).

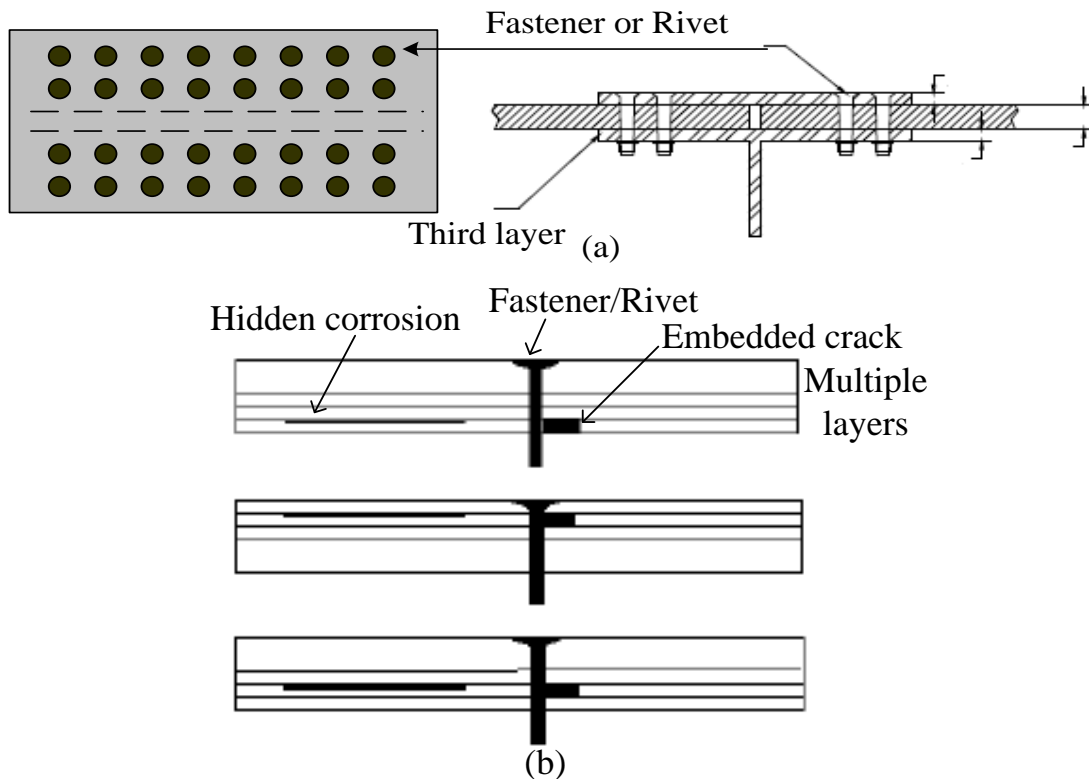


Figure 1.3 Layered structure: (a) Aircraft riveted skin structure geometry and (b) Initiation of hidden corrosion and cracks at rivet sites

EC techniques have been widely used to inspect aluminum or titanium fastener structures (non-magnetic materials). However, the examination of a ferromagnetic fastener remains a challenge [2, 7, 19-22]. Ferromagnetic materials are characterized by a large change in magnetic permeability that strongly influences the measured signals associated with the induced magnetic field. Therefore, the dominant signal from a ferrous rivet in the lap joint masks the relatively low amplitude signal from a hidden defect propagating around the fastener hole. Consequently, the presence of a ferrous fastener confounds crack detection. Currently, fastener removal is required by EC techniques during the inspection of aircraft wing structures [22]. Some of the research solutions using EC techniques for ferromagnetic fastener examination and their limitations are

reviewed in Chapter 2.

Incorporation of advances in magnetic sensors, signal and image processing, image fusion and numerical model based investigations has significantly enhanced the scope and applicability of EC techniques [23]. In particular, magnetoresistive (MR) imaging has improved EC inspection of complex structures such as riveted components. In contrast to impedance analysis of a single scan (conventional EC data analysis), flaw detection is evaluated based on asymmetry features in EC C-scan image data [24]. However, there are several potential sources of coherent noise that yield responses similar to a defect scenario. These include the asymmetric gaps between fasteners and holes, probe tilt, lift-off variation and irregular geometric factors. Such factors can interfere with defect detection [18]. Studies presented in [25-26] showed the enhanced detection of cracks beneath installed fastener heads using phase-based signal processing methods. A discussion of the benefits using phase shift or rotation to minimize the response of fastener is given in [27]. However, finding an optimum phase shift can be difficult in a noisy image. Additionally, a phase shift based flaw is affected by fastener type and lift-off variations. Model-based approaches for flaw detection and characterization, and model-assisted probability of detection (POD) have also been studied for riveted structure inspection [28-29]. However, the procedure for implementing the model-based approach is computationally intensive since these are iterative procedures involving 3D numerical models.

1.3.2 Research Objectives and Methodologies

The objective of this dissertation is to develop a reliable EC sensor system and automatic signal interpretation for detecting cracks buried around steel fastener sites in layered structures.

Additionally, the proposed system should be sensitive to cracks of all orientations emanating radially from fastener holes.

The feasibility of proposed sensor systems is investigated using modeling and experiments. The use of uniform excitation currents with 3D MR sensing is explored using laboratory specimens. Low frequency excitation current methods as well as pulsed excitation with transient response are investigated. Simulation models using efficient finite element (FE) analysis in time and frequency domains are used for conducting parametric study that could assist in system design.

1.4 Organization of the Dissertation

This chapter introduced the research problem and summarized the research objectives. This dissertation addresses several topics in EC inspection: system design and modeling, experimental validation and algorithms for data analysis. Chapter 2 presents a review of EC techniques and its application to multilayer structures. A discussion of EC testing systems developed for riveted structures is presented. Chapter 3 proposes the design of a Pulsed Eddy Current-Giant Magnetoresistor (PEC-GMR) system. A numerical model for simulating transient electromagnetic field and GMR sensing in time domain is described. The feasibility of measuring the 3-components of the magnetic field using 3D GMR sensors is investigated and proposed as a solution to find defective ferromagnetic fasteners in a layered aircraft structure. Chapter 4 introduces a signal analysis scheme for automatic detection using statistical analysis of time-domain PEC-GMR signals. Chapter 5 presents the design of low frequency EC-GMR inspection and associated data analysis in the frequency domain. Chapter 6 proposes an EC-GMR rotating current excitation design that is sensitive to orientations of radial crack around

the fastener site. Numerical modeling studies and experimental measurements using rotating field are presented. Chapter 7 describes a parametric study of the proposed EC-GMR system. An invariance analysis scheme is introduced to render the measurements insensitive to sensor tilt that could cause unwanted response received by GMR sensor. Conclusions and recommendations for future research are summarized in Chapter 8.

CHAPTER 2 REVIEW OF ELETROMAGNETIC NDE

2.1 Introduction

The operation of EC testing is based on the principles of electromagnetic induction. A harmonic field at a specific frequency (typically Hz-MHz) is produced by a time-harmonic current through a source coil, which induces eddy currents in the object under examination. The presence of a defect or discontinuity behaves as a high resistance barrier which disturbs induced current flows. The resulting perturbations of the associated magnetic field are measured [2, 5-7].

These phenomena can be described by Maxwell's equations:

$$\nabla \times \mathbf{H} = \mathbf{J} + \frac{\partial \mathbf{D}}{\partial t} \quad (\text{Ampere's Law}) \quad (2.1)$$

$$\nabla \times \mathbf{E} = -\frac{\partial \mathbf{B}}{\partial t} \quad (\text{Faraday's Law}) \quad (2.2)$$

$$\nabla \cdot \mathbf{B} = 0 \quad (\text{Gauss' Law}) \quad (2.3)$$

$$\mathbf{J} = \sigma \mathbf{E} \quad (2.4)$$

where the variables are:

\mathbf{E} : electric field intensity (volt/meter)

\mathbf{H} : magnetic field intensity (ampere/meter)

\mathbf{D} : electric flux density (coulomb/meter²)

\mathbf{B} : magnetic flux density (tesla)

\mathbf{J} : electric current density (ampere/ meter²)

σ : electric conductivity (mhos/meter)

According to Ampere's law in Eq. (2.1), a time-varying current source generates a time-varying magnetic field, as a primary field \mathbf{H} shown in Figure 2.1 (a) [5]. As dictated by Faraday's law in Eq. (2.2), a time-varying magnetic field induces an electromotive force that is proportional to the

time-rate of change of the magnetic induction flux density:

$$\varepsilon = -\frac{d\phi_B}{dt} \quad (2.5)$$

This electromotive force interacts with the test material and results in currents induced inside the specimen. The induced currents are called eddy currents. Based on Lenz's law, these eddy currents produce a secondary magnetic field that opposes the source field due to the excitation coil, as shown in Figure 2.1 (a) [5]. By sensing the changes in the total electromagnetic field, discontinuities in the conductivity or permeability of a conductive structure are detected. The net change in the magnetic flux is linked to changes of the coil impedance (z), a complex parameter with magnitude $|z|$ and phase angle ϕ as:

$$z = V / I = R + jX = |z|\phi \quad (2.6)$$

Since the inductance of a coil is associated with the flux linkage per ampere, the presence of eddy currents generate a resistive power loss. This results in a small increase in the effective resistance of the coil, which changes the coil impedance when it approaches a conducting specimen. Thereby, the net effect caused by the reduction and redistribution of eddy currents due to a defect is reflected in the variations of the probe coil's resistance and inductance. As shown in Figure 2.1 (b), the EC inspection monitors the impedance changes when the probe coil scans along the object surface. The effective inductance and resistance of the coil changes relative to the value in air [2, 5-7].

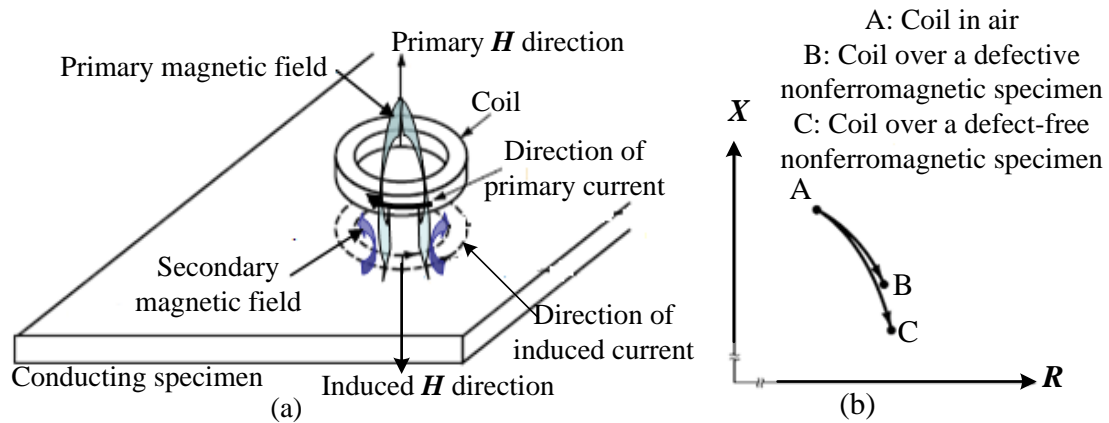


Figure 2.1 Principle of the EC inspection: (a) A typical EC probe above a conducting specimen under test and (b) The measurement of coil impedance [6]

A typical EC testing system is shown in Figure 2.2. Such a system involves excitation, signal preparation, demodulation, and analysis [2, 5-7]. A probe consisting of a coil or a set of coils is excited, and the interaction of induced electromagnetic field with the sample is measured. Traditional EC technique monitors the induced voltage of a pick-up coil (same or different from the excitation coil) or collects the variations in inductance and resistance of the same source coil. A demodulator is a phase-magnitude receiver. As the probe scans above the specimen, response signals are represented in the impedance plane after noise filtering, amplification or other signal conditioning circuitry. Discrimination, summation or comparison, and signal processing may be included at the signal interpretation stage.

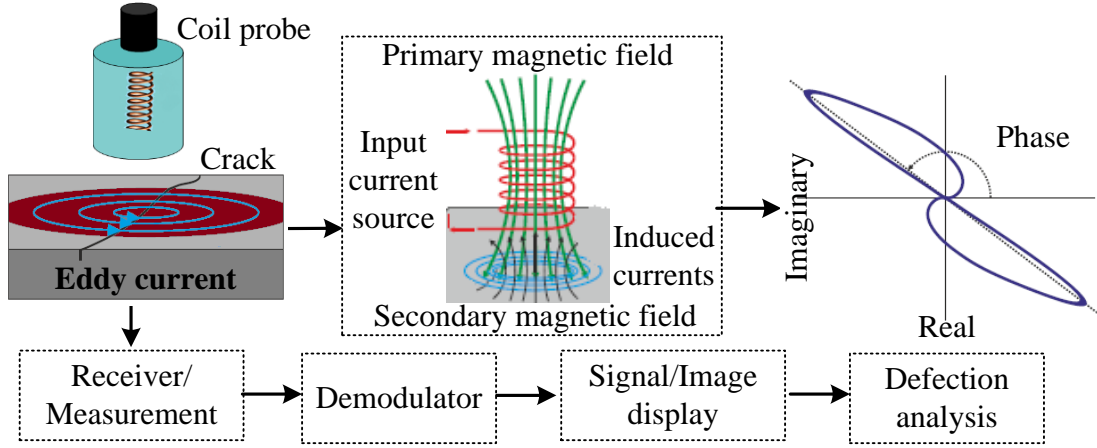


Figure 2.2 Eddy current testing system

The ability to detect a flaw depends on the orientation of the defect's largest dimension relative to the flow path of induced currents. Discontinuities are most detectable when their longest dimensions are perpendicular to induced currents [7, 30]. However, edges or boundaries in the test specimen also distort current flow paths and generate a signal similar to a flaw response, and hence must be eliminated by signal processing.

2.2 Skin Depth and Development of EC Techniques

Conventional EC techniques have a limited field penetration through the material depth as dictated by the skin effect [7]. Skin depth δ is characterized as:

$$\delta = \sqrt{\frac{1}{\pi f \sigma \mu}} \quad (2.7)$$

where σ is the conductivity of conductor under test, μ is the permeability of conductor, and f is the excitation frequency. The magnitude of induced eddy currents decreases exponentially in the conductive material. Hence, the amplitude of fields in the conductor at depths along X-axis is expressed as [7, 9, 31]:

$$J(x) = J_0 \times e^{-x/\delta} \quad (2.8)$$

The standard skin depth of penetration is defined as the depth where the eddy current density is about 37% (1/e) of its surface value. Since greater penetration depth of eddy currents is needed to inspect embedded flaws, the selection of excitation frequency is critical [5-7, 9, 31]. Detecting a deeper flaw requires lower excitation frequency. Figure 2.3 presents how the skin depth affects the distribution of eddy current densities inside a copper plate at high and low frequencies.

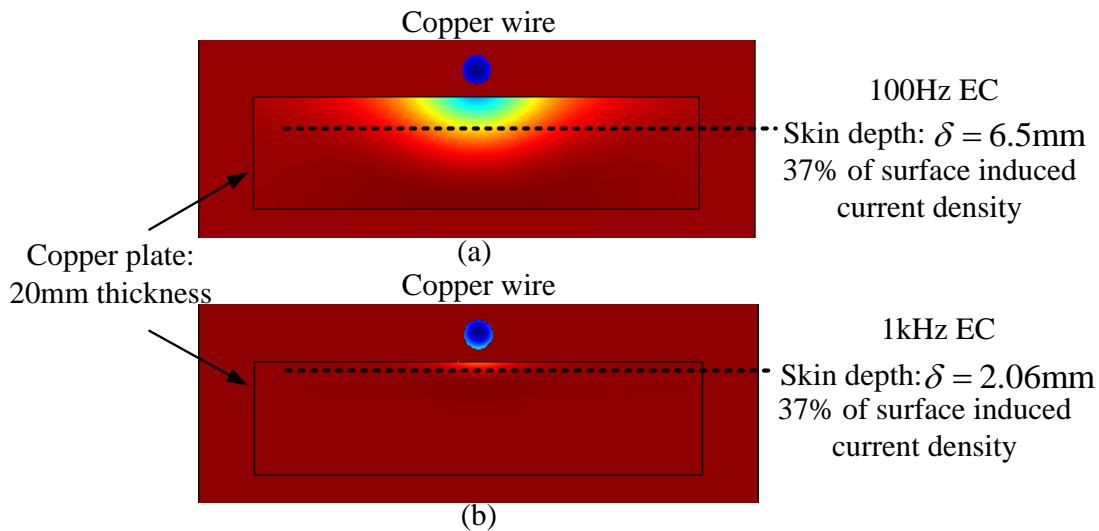


Figure 2.3 Demonstration of skip depth in EC testing (Comsol 3.5 simulation):
 (a) 100 Hz EC and (b) 1 KHz EC

The capabilities of conventional EC methods that employ single frequency excitation are limited to detecting defects at one or two skin depths. Multi-frequency EC techniques are introduced to provide additional information related to induced fields at different depths [7, 9, 32-34]. The design of a multi-frequency instrument needs to employ multiplexing strategy in the time or frequency domain [6-7]. When excitation signals at a swept-frequency mode are employed simultaneously, a frequency-division de-multiplexing method is applied to isolate individual

response signals. In references [35-37], an EC probe operated at the sinusoidal swept-frequency from a 100Hz to several MHz is used to inspect different layers. Multi-frequency EC testing is particularly useful in removing undesired signals using advanced signal processing or information mixing. Different algorithms have been utilized to selectively suppress unwanted indications due to geometry and retain defect indication [38-41].

The inclusion of a broad range of frequencies led to pulsed excitation in EC testing that applies a square, triangular, or a saw tooth waveform as a source current [7, 31, 42]. PEC techniques measure transient signals that contain a broad spectrum of frequencies and provides capabilities to detect and characterize deep corrosion and hidden defects. This technique also offers advantages in correlating depth information with time-dependent characteristics in the response signals [2, 43].

Owing to deeper field penetration, the application of PEC techniques has been extensively found in the detection of cracks hidden inside multilayered aircraft components [2, 44-48]. Studies and details of PEC technique in detecting deeply buried cracks around fastener sites are investigated in Chapters 3 and 4 of this dissertation.

2.3 Configurations of EC Coil Probes

The distribution of eddy currents primarily depends on the source coil design. The pattern of induced currents is decided by the size, orientation and shape of the source coil. Controlling the eddy currents distribution is critical for detecting discontinuities at all possible orientations [30].

2.3.1 Conventional Coil Probes

Common EC probes are designed as a flat coil, pancake coil, or encircling coil [7]. As shown in

Figure 2.4, coil configurations depend on different applications: 1) surface probes (Figure 2.4 (a)) that can be pancake shaped to scan along the surface and yield magnetic flux perpendicular to the surface; 2) Bobbin (inner diameter) probes (Figure 2.4 (b)) are wound on a bobbin to move along the inside of the tubes and produce axial magnetic flux, 3) outside diameter probes (Figure 2.4 (c)) that can be wound to encircle the specimen [2, 49-50].

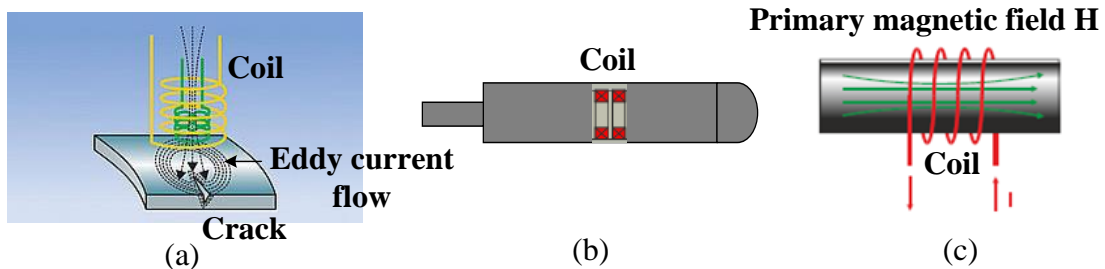


Figure 2.4 Typical EC probes: (a) Pancake type coil [50] (b) Bobbin type (inner diameter) coil [2] (c) Encircling type (outer diameter) coil [2]

Coil probes can operate in double-function mode, separate-function mode and hybrid mode, as displayed in Figure 2.5. The double-function operation includes two approaches: 1) An absolute probe which generally contains a single coil that is used as the source excitation as well as sense changes relative to induced magnetic field; 2) A differential probe which has two active coils usually wound in opposition for eddy currents generation and as well as pickup. The two coils give no signal in a flaw-free area while they produce a differential signal when the probe scans over a defect in the sample under test. The impedance change of double-function coil indicates defect existence.

Absolute probes can be overly sensitive to material variations, temperature changes, lift-off and other variations during inspection. Differential probes are relatively insensitive to slow or

gradual discontinuity or composition changes of a test structure. Additionally, a differential probe detects large flaws only when they are over the beginning and end locations of the flaw, since the output signal is canceled when it is placed over uniform parts of the defective region [2, 49-51].

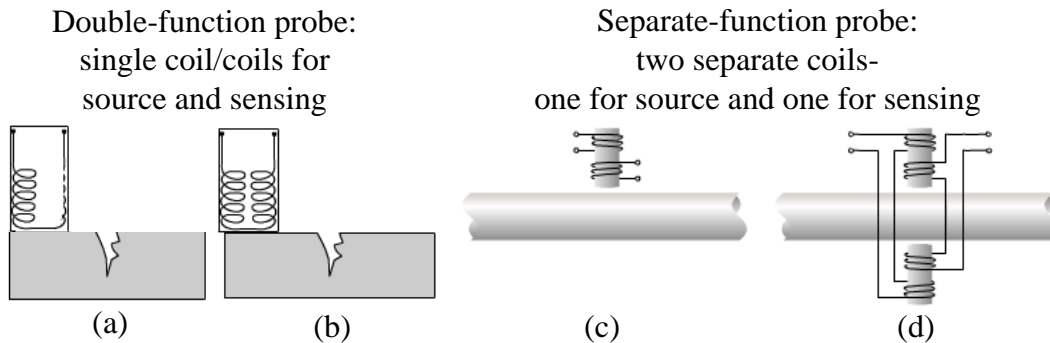


Figure 2.5 Coil probes-mode of operation [49, 51]: (a) Double-function probe in absolute mode (b) Double-function probe in differential mode (c) Separate-function probe in absolute mode (d) Separate-function probe in differential mode

Separate-function probes employ a primary coil to provide source currents and a secondary coil (pick-up coil) to sense the secondary field due to eddy currents. Separate-functions probes can also be used in an absolute or differential mode. This probe type is also called Transmit/Receive (T/R) probe. The configuration of transmit coil is specially designed for optimizing the eddy current flow pattern, and the receiving coil configuration is designed to achieve a maximum sensitivity to defect [2].

2.3.2 Planar Coil Probes

It is fundamental to EC testing that defects that distort the continuity of induced currents are detectable. Therefore, the configuration of excitation coil is critical since it decides the pattern and distribution of induced currents [7, 52]. Additionally, coil probes provide high sensitivity to defects if a flaw dimension is comparable to the size of coil transducer. Therefore, the shape,

cross-section, and size of the source coil vary for different applications [2, 52]. In the case of conventional coil probes, small diameter coil probes are preferred for higher sensitivity to small cracks. However, coil size is also crucial to obtain a signal with high signal-to-noise (SNR). With the development of microelectronics and integrated circuits, planar coil probes are being investigated in NDT areas and pursued particularly in EC probe applications [2, 52-53]. Planar coils are made of flexible windings with a certain number of turns that are fabricated on a printed circuit board (PCB).

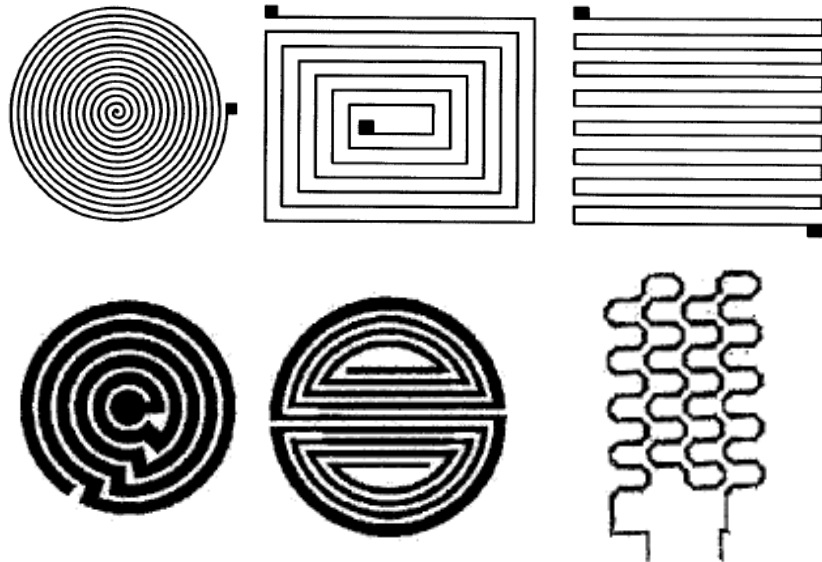


Figure 2.6 Planar coil configurations [52-53]

As shown in Figure 2.6, the patterns of the planar windings can take different forms depending on the required induced eddy current directions [52-53]. Four research groups independently studied planar coil probes designed for electromagnetic NDE.

The first study of planar coils as NDT sensors was introduced by General Electric (GE) [52-55].

In order to inspect complex engine parts, they deposited the separated driving and sensing coil

elements in a layered flexible structure as an array of EC planar probes. Their follow-on work conducted FE modeling and experimental studies for probe designs optimized for the inspection of rotating aircraft engine parts. They were able to detect Electrical Discharge Machining (EDM) notches 0.01'' long and 0.005'' deep.

A second group that has investigated the design of planar coils is JENTEK® Sensors Inc. They introduced the planar coil probe with Meandering Winding Magnetometer (MWM) and a signal processing algorithm using grid measurements (a model-based technique) [52, 56-58]. MWM coils consist of thin and conformable coils. Multiple MWMs can be integrated to form a sensor array. The coil probe has a single-drive winding (primary windings) and one or more sensing elements on a thin and conformable substrate (secondary windings). Figure 2.7 (a) shows the H field distribution introduced in a MWM probe, which is generated by the linear current I_D in the primary windings. The voltages of the secondary windings in V_{S1} and V_{S2} measure the field changes. The distance λ between windings of the planar meander coil can be optimized. In aging aircraft applications, the permanently mounted MWM array sensors were able to detect cracks of 40 μ m length and 20 μ m depth during the fatigue test of aluminum specimens [59-60].

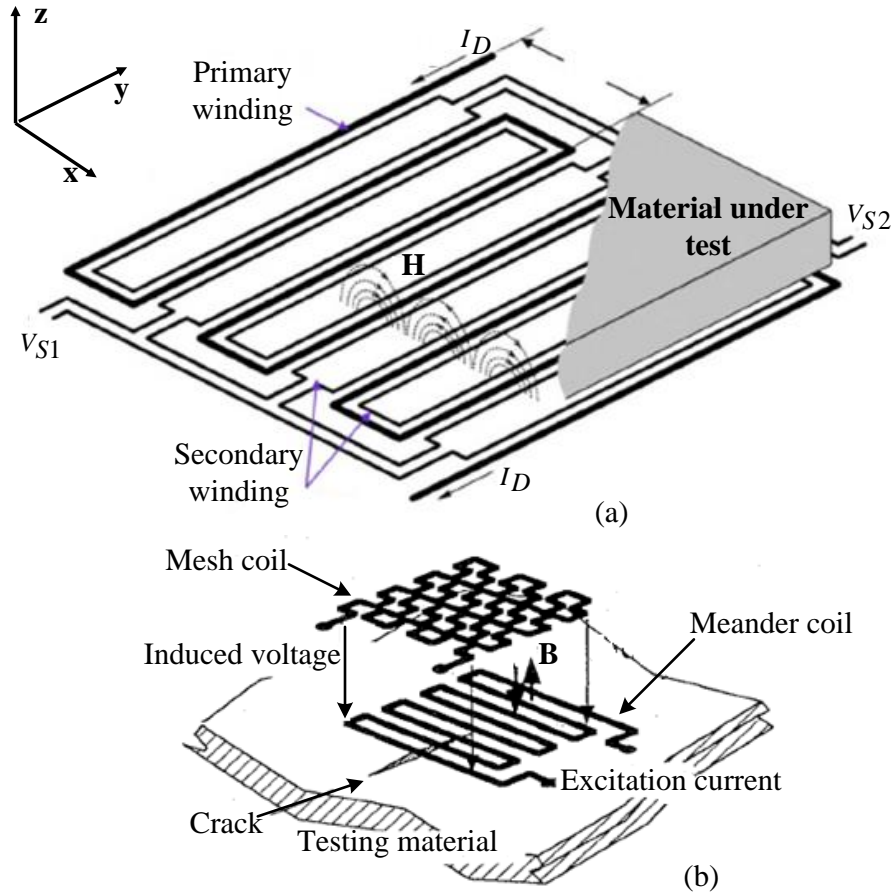


Figure 2.7 Two designs of planar coil probes: (a) a basic MWM probe [56] and (b) a meander/mesh coupled probe [61-62]

A similar design using a pair of planar coils – a planar meander as the source coil but a planar mesh as the pick-up sensor was developed by collaborative effort between Kanazwa University in Japan and the University of Toronto [52, 61-63]. Figure 2.7 (b) shows a schematic of the planar meander/mesh probe. The application of this probe was mainly for PCB inspection.

The fourth study of planar coil probes was carried out in structural health monitoring of aircraft structures [52, 64-65]. A conformable sensor film that uses planar rectangular or meandering coil configuration around the fastener shank is integrated with EC system for in situ monitoring of fatigue cracks at fastener holes in layered metallic joints. Other efforts to study planar coil probes

include the IOnic EC probe [66] that was specifically produced to detect a unique structure-friction stir welding, and a planar rectangular coil that was designed and optimized in [67].

Planar technology allows large scale production of precise and reproducible coil probes [68]. Additionally, planar coil technology enables the possibility of integrating identical array elements into an EC probe for fast inspection [8, 68-69]. Construction and characterization of EC probes with planar coils can be conducted using numerical investigations. Numerical studies are used in the design process of planar source coils for generating eddy currents in different path patterns [70-72]. PEC techniques using planar coil probes have shown considerable promise in detecting and monitoring fatigue cracks in layered structures [52].

2.3.3 Limitations of Coil Sensors

Traditional EC methods use coils as sensors (pick-up coils) to measure changes in the magnetic field. Based on the Faraday's law of induction, the voltage response of a pick-up coil is proportional to the rate of change of the induced magnetic field not the magnetic field itself.

Therefore, it results in poor SNR ratio particularly at low frequencies [2, 14, 69, 73]:

$$V_{coil\ signal} = N\pi r^2 \frac{dB}{dt} \propto N\pi r^2 f \quad (2.9)$$

where N is the number turns of coil wire, πr^2 is the area of the loops and $\frac{dB}{dt}$ is the rate of change of magnetic field that is proportional to the operating frequency f .

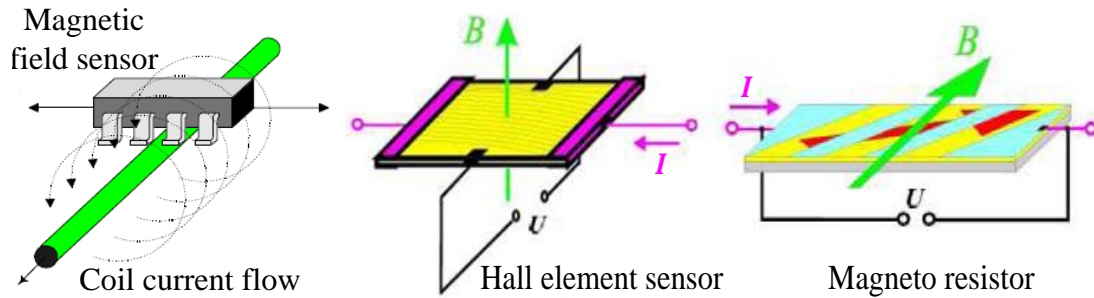


Figure 2.8 Hybrid probe [49, 74]: EC coil with magnetic field sensor

Consequently, coil sensors are fundamentally limited by the poor sensitivity at low frequencies. Unfortunately, the sensitivity at low frequency is needed in the inspection of thick components and subsurface flaws. Similar to traditional coils, planar coils also present limited sensitivity when they are used as pick-up or inductive coils for sensing low frequency magnetic field. Alternately, EC probes that are operated in hybrid mode have been developed to overcome those limitations. As shown in Figure 2.8, hybrid EC techniques employ conventional or planar coils to generate eddy currents, and utilize magnetic field sensors to directly measure field variations associated with discontinuities [2, 6, 49].

2.4 Magnetic Field Sensors for Hybrid EC Testing

The magnetic field associated with induced currents can be measured using magnetic field sensors such as magnetometers, superconducting quantum interference devices (SQUID), Hall sensors, magnetoresistive (MR) sensors, or magneto-optic sensors [51]. In contrast to pick-up coils, electromagnetic field sensors are sensitive to weak magnetic fields, obtain linear characteristics for a broadband of frequencies and produce a voltage output proportional to the magnetic field [2, 14, 69, 73]. With the help of electromagnetic sensors, hybrid EC techniques have enhanced the sensitivity and spatial resolution of detecting subsurface defects [68].

Therefore, field sensors are finding increasing applications at low frequency EC testing and electromagnetic field imaging [2, 14-15].

Hall element sensors utilize the Lorentz force that affects the trajectory of electrons in a magnetic field, and produce a proportional Hall voltage across a conductor or semiconductor that carries currents. Hall sensors are used mainly in the mT range and can be easily integrated on microelectronic circuits. However, Hall devices typically suffer limited sensitivity (much lower than MR devices), high level of noise, a relatively large offset and a limited dynamic range [2, 14, 73]. Other magnetic sensors such as fluxgates in EC testing consist of an advanced magnetometry technique. A Fluxgate sensor is a solid state device that measures the intensity and direction of a magnetic field with a sensitivity range of 10^{-10} to 10^{-4} T. However, these core saturation magnetometers require a large size for sufficient sensitivity, so lateral resolution is relatively low [75].

SQUID devices are the most sensitive magnetometers that have been applied in NDE areas. They are based on the interactions of electrical currents and magnetic fields. When the superconducting wires are cooled, SQUID sensors become superconductors below a certain temperature. Although SQUID sensors have exceptional low-frequency sensitivity and stability, testing systems using SQUID devices are of very high complexity. They require cryogenic cooling to reach the superconducting transition temperature. Therefore, the expensive cost and maintenance associated with the closed cycle refrigeration or cryogenic system significantly restrict their applications.

MR sensors based on anisotropic magnetoresistance (AMR) or giant magnetoresistance (GMR)

effects offer high sensitivity over a wide range of frequencies. The hybrid EC technique that utilizes MR sensors has been successfully introduced for higher sensitivity, particularly in low frequency electromagnetic NDE applications [14, 73-76]. Low frequency and multi-frequency EC methods using MR sensors are particularly useful in detecting hidden corrosion that typically produces a gradual thinning of structures. It is difficult to image corrosion using conventional techniques [14].

With the development of sensor fabrication and commercial packaging technology, MR sensors can be integrated with EC probes [14]. Research of planar coils used for EC probes reported the sensitivity can be improved by introducing MR sensors [57].

2.5. Magnetoresistive (MR) Sensors

2.5.1 Magnetoresistance

Magnetoresistance is a galvanomagnetic phenomenon caused by the effect when a magnetic field applied to magnetic material. With the force exerted on the material electrons, they are redirected or scattered when they try to travel along microscopic domains that form a consistent magnetic orientation, as demonstrated in Figure 2.9 (a). The amount of redirection and scattering is a function of magnetization \mathbf{M} that is decided by the direction of external magnetic field \mathbf{H}_A shown in Figure 2.9 (b) [51, 77]. Therefore, the resistance variation $\Delta R/R$ of magnetic material called magnetoresistive effect is a function of the external magnetic field \mathbf{B} [78]:

$$R=f(\mathbf{B}) \quad (2.10)$$

Ferromagnetic thin film material is commonly used in MR sensing, and as seen in Figure 2.9, the rotation direction of magnetization \mathbf{M} is determined by the film shape and the easy axis direction

that is designed during the film deposition. Hence, the application of an external magnetic field results in resistance changes associated with the rotation variation of magnetization direction [78].

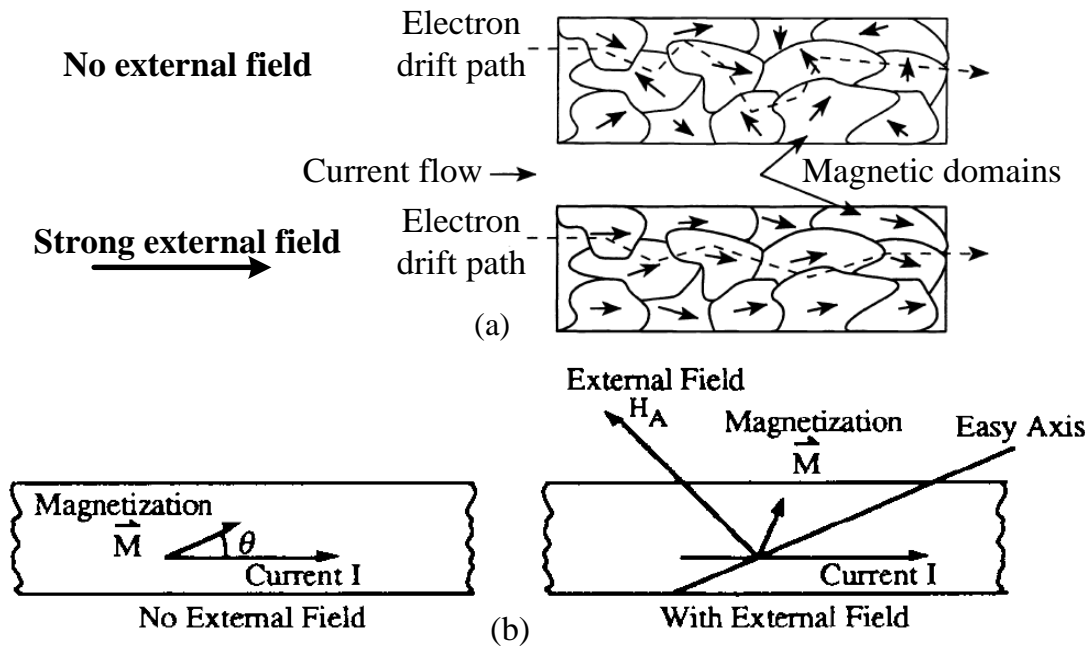


Figure 2.9 Magneto-resistive effect in a thin current strip [51, 77]

2.5.2 Anisotropic Magneto-resistive (AMR) Sensor

MR phenomenon was first studied in anisotropic magneto-resistive (AMR) materials such as iron and Permalloy (NiFe), and it was practically developed in magnetic sensing later when thin film technology was introduced [77]. Anisotropic resistance R depends on the angle θ between applied current I and magnetization M as shown in Figure 2.9 (b). This distorts electron orbits and results in different scattering. This is expressed as a function [14, 73, 78]:

$$R = R_0 + \Delta R \cos^2(\theta) \tag{2.11}$$

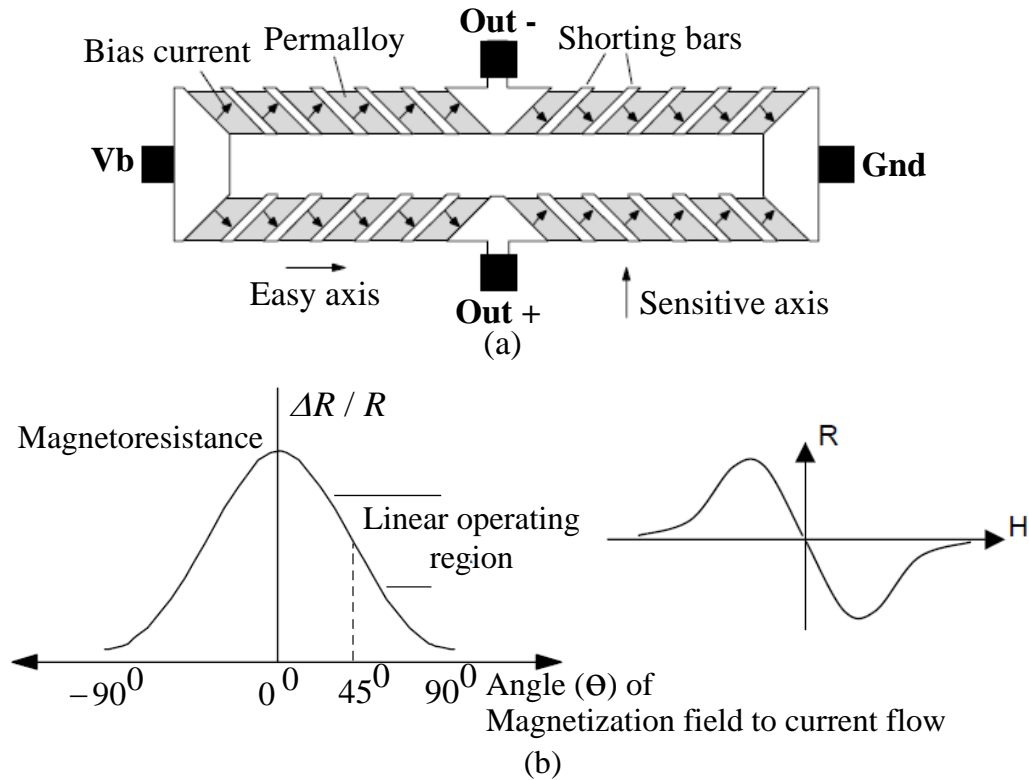


Figure 2.10 AMR device: (a) Barber-pole structure for an optimum alignment and (b) Resistance change $\Delta R/R$ vs. angle θ , and resistance R vs. applied field H [73]

The anisotropic resistance is minimum when the magnetization direction is perpendicular to the external current direction, since electrons in the film travel freely in microscopic domains. On the other hand, the maximum resistance R is produced when the two directions are perpendicular to each other, and electron orbits are blocked due to the magnetization force. According to Eq. (2.11), the maximum sensitivity and linearity is found at an angle $\theta = 45^\circ$. This 45° optimum alignment is usually designed by patterning a barber-pole configuration. As illustrated in Figure 2.10, the configuration consists of diagonal strips of highly conductive metal where the current flows in the 45° direction.

Two configurations have been used in MR material sensors: $\Delta R/R$ and dR/dH . $\Delta R/R$ or

$(R_{max}-R_{min})/R_{min}$ measures the absolute resistance change in percentage for a MR device. $dR/d\mathbf{H}$ or $(R_{max}-R_{min})/(\mathbf{H}_{sat}-0)$ measures the resistance change as the magnetic field increases from zero till the field \mathbf{H}_{sat} that achieves maximum resistance change,. The $dR/d\mathbf{H}$ configuration is preferred when the sensitivity to small magnetic field is needed [77]. In general, a ratio MR is traditionally used and it is defined as:

$$MR = \frac{R_{m a x} - R_{m i n}}{R_{m i n}} \quad (2.12)$$

Most AMR sensors commonly use Permalloy deposited onto silicon substrates in a Wheatstone bridge configuration. With an external magnetic field applied perpendicularly to the deposited film, the magnetization vector rotate and change the angle θ . Therefore, the corresponding resistance variation produces a measurable change of voltage output in the Wheatstone bridge. AMR thin film can have a resistance change MR level of 2% to 3% [73]. Available commercial AMR sensors are described in references [69, 78].

2.5.3 Giant Magnetoresistive (GMR) Sensor

Recent developments in thin-film technology have found a large resistance change in films when a magnetic field is applied to multiple thin-film layers. This giant MR effect was discovered in 1988 [73, 78-79]. GMR films have two or more ferromagnetic metal layers separated by a non-magnetic metallic spacer layer. The spacer layers need to be thin relative to the average free path of electrons and this causes free motion of electrons from one layer into the other layers instead of electron scattering [14].

As displayed in Figure 2.11, the spin due to material electrons generates small magnetic fields

when structures of magnetic and non-magnetic materials are formed in thin layers. These layers are automatically coupled in ferromagnetic mode, Figure 2.11 (a) (where the magnetic layers are aligned in the same direction) or antiferromagnetic mode, Figure 2.11 (b) (where the magnetizations are opposite).

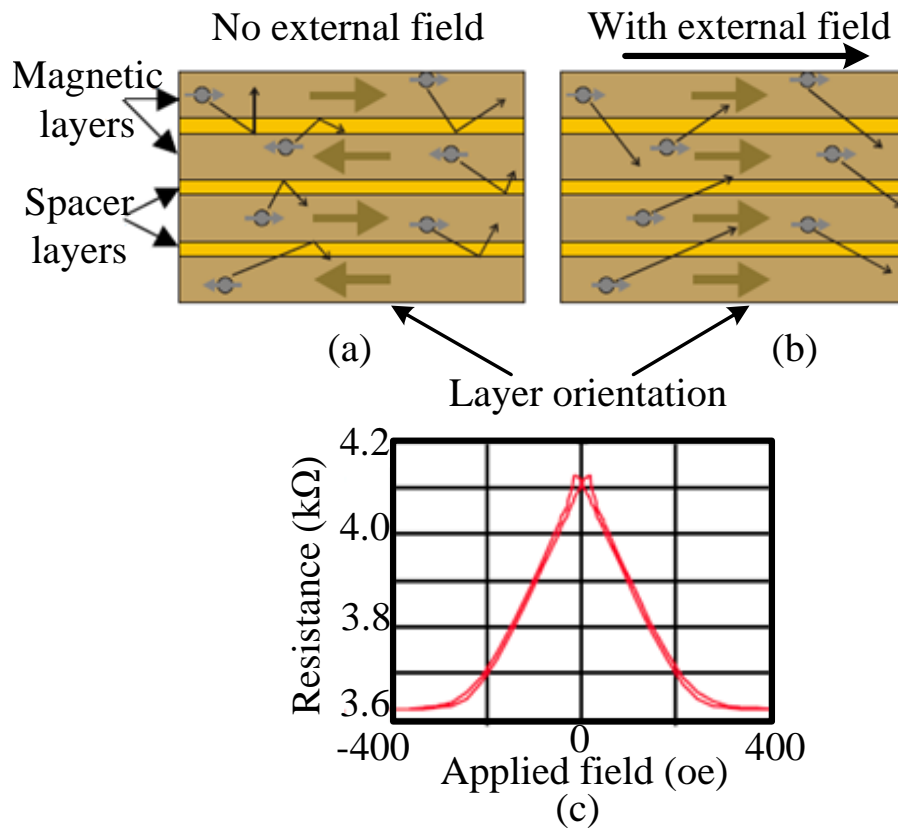


Figure 2.11 Illustration of the GMR effect [14]: (a) Lots of scatterings due to the alternating magnetization of the layers (b) Reduced scatterings when the magnetization of the layers is aligned by an applied field (c) Resistance variation as a function of an applied magnetic field

Without magnetic force, electrons are not able to move across magnetic layers without experiencing adverse interaction with the formed magnetic domains. With an external magnetic field applied to the structure, the anti-ferromagnetic coupling is overcome, and scattering of electrons is reduced at layer interfaces. Therefore, the resistance variation is produced in Figure

2.11 (c). The MR level is maximum when the magnetic layers are antiparallel and minimum when they are parallel. Typical MR levels are about 10% to 20% [14, 77, 79].

The commonly used structures in GMR sensor elements are unpinned sandwiches, antiferromagnet pinned spin valves, antiferromagnetic multilayers and magnetic tunnel junction [77-79]. GMR effects can be obtained by different arrangements of changes in the relative orientation of the magnetization in adjacent layers, and antiparallel configurations of magnetic alignment in thin ferromagnetconductor multilayers when an external magnetic field is applied.

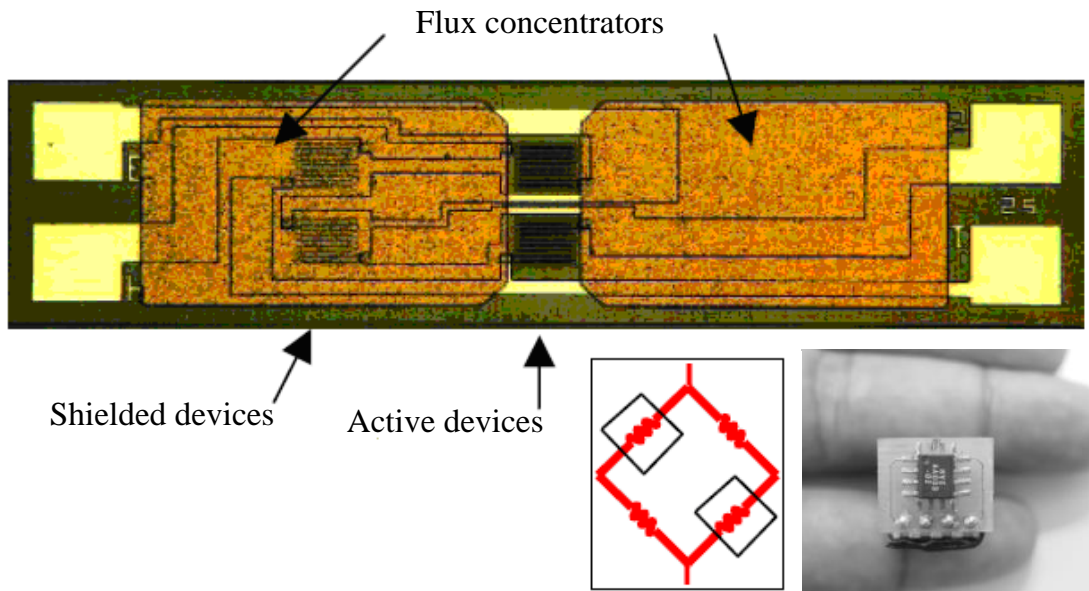


Figure 2.12 Microscope picture of a GMR sensor fabricated by NVE Inc. [14]

The challenging work in GMR research is finding materials and structures that exhibit large MR ratio at low magnetic fields. Developed structures include NiFeCo-CoFe-Cu multilayers (currently manufactured by NVE Inc. as shown in Figure 2.12), and granular films of Co-Cu and Co-Ag. They are heterogeneous alloys and exhibit GMR effects due to spin-dependent scattering in which metal particles are aligned or re-oriented and result in resistance variations with an

applied magnetic field [68, 77-79].

GMR sensors are commercially available [69, 73]. Thin-film GMR materials are deposited on silicon substrates and can be fabricated into configurations with voltage output such as resistors, resistor pairs or half bridges, and Wheatstone bridges. GMR multilayers present the sensitivity in the form of $\Delta R/R$ or dR/dH . They are similar to AMR sensors but with higher linearity in their MR response [68]. Additionally, GMR sensors have better directional characteristics than AMR sensors. MR sensors detect the vector component of a magnetic field along their sensitive axis. GMR sensors are insensitive to fields applied perpendicularly to the sensitive axis. In contrast, the sensitivity of AMR sensors is reduced by a field perpendicular to the sensitive axis due to a cross axis sensitivity. It might reverse the sensor response at high field values [75, 80-81].

Based on MR effect and magnetoresistive materials, the use of these solid-state magnetic sensors represents a significant advance in sensing low fields over traditional inductive probes. In addition, the small size and low power consumption of these sensors enable the fabrication of compact array sensors on PCB boards and on-chip sensor arrays. Thin-film sensors can be fabricated on a planar board to locally sense the magnetic field in a region as small as tens of micrometers. They could also be arranged in arrays for high resolution imaging.

2.5.4 NDE Applications of MR Sensors

The use of MR sensors in EC systems and electromagnetic imaging has grown considerably in the past few years. Their linear response makes them suitable for detecting low amplitude electromagnetic field when a low-frequency or pulsed excitation is applied [2, 8], and they have been used successfully for detected subsurface cracks under riveted structures [14, 16-17, 76]. In

particular, GMR devices have higher directionality, sensitivity, and wider bandwidth compared to other MR sensors [2, 14, 51, 75], Therefore, GMR based EC testing exhibits significant advantages in detecting complex geometry such as layered component inspection [44, 81]. The directional property of GMR sensor had been used to locate edge cracks in aluminum specimen [34, 81]. A needle type GMR imaging technique named the SV–GMR system was designed for the inspection of a bare PCB structure, and for the measurement of magnetic fluid density injected in a living body [74-75].

High resolution GMR elements fabricated in a small package of sensors arrays have been developed. An interesting application of this array probe was found in the evaluation of metal medical implants for invisible cracks [8]. A linear array of 20 GMR elements was packaged to image a hole defect in a steel plate using 1 Hz excitation. Designs of GMR array probes in identical elements were studied to detect subsurface cracks [14, 68]. High density GMR arrays are especially promising for rapid scanning of large area as well as high resolution imaging [34-35]. Another type of GMR array sensors that use two-directional elements was investigated in EC testing to detect surface cracks of unknown orientation. They measure both *X*-component and *Y*-component of the magnetic field at a same point under examination [81].

2.6 EC Techniques for Inspection of Riveted Structures

Commercial EC probes such as sliding probe fabricated with multiple coils in drive/pick-up operation, and remote field EC coil probe have been investigated for detecting aircraft skin structures employing coil sensors at low frequency excitations [82]. However, sliding probes can only detect defects in one direction and lead to false call or undetected flaws in the case of rivets

that are not aligned in a row [10].

As an improvement, imaging based EC techniques enable efficient flaw detection using richer and more comprehensive data than traditional Lissajous patterns obtained from a single EC scan [18, 83-84].

2.6.1 EC Magneto-Optic Imaging

A Magneto-optic (MO) sensor is based on Faraday rotation effect, in which the polarization plane of a linearly polarized light rotates in the presence of an applied magnetic field. When polarized light is transmitted through the specimen, the direction of polarization is rotated by the magnetic field associated with the induced currents in the specimen. A MO sensor consists of a thin film of bismuth-doped iron garnet grown on a substrate of gadolinium gallium garnet and directly produces an image. The variations due to the presence of structure like a rivet or defect generate a non-zero normal component of magnetic field. The response is imaged and viewed as the black and white images in Figure 2.13 (c) [85-86].

Shih and Fitzpatrick in the early 1990s presented a MO imaging system for detecting surface and subsurface cracks, and corrosion in aircraft skins [85-86]. As illustrated in Figure 2.13 (a-b), this technology employs an induction foil that carries an alternating current and induces eddy currents in the conductive sample under inspection. The generated magnetic flux is tangential to the specimen surface under normal conditions. Discontinuities in the specimen divert uniformly induced currents and produce a normal component of the magnetic flux density that is detected and imaged by MO sensor.

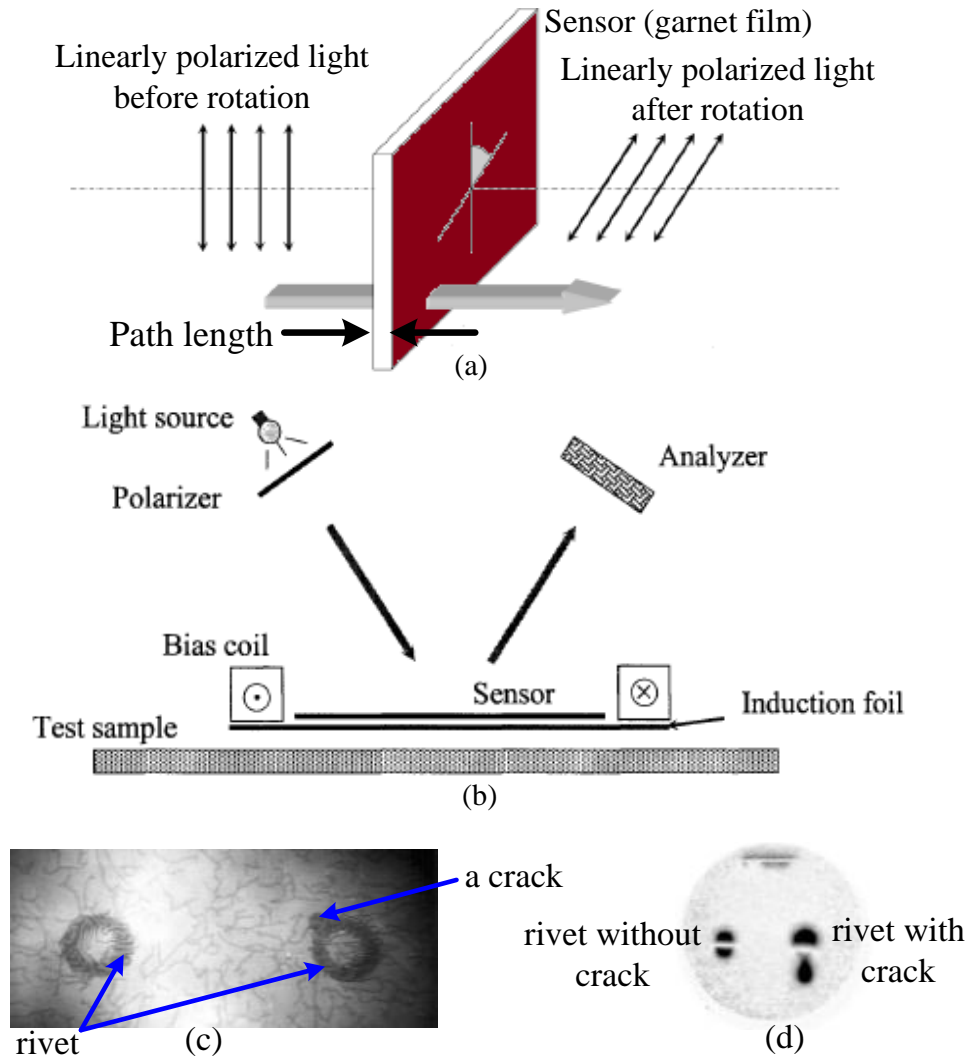


Figure 2.13 EC-MO imaging technique: (a) Faraday rotation effect in a MO sensor (b) Schematic of the MO imaging system [85] (c) MO images of riveted structures (d) Images of riveted structures using LMOI system in Europe [87]

A similar system, named the linear MO imager (LMOI) was patented in Europe [87]. It acquires an image based on the stroboscopic approach. A riveted structure results in an image with two semicircular shapes as shown in Figure 2.13 (d). Instead of using polarized light, Cheng et al [88] combined a laser into the MO imaging system. Multiple tests have shown that the MO imaging technique is fast, reliable and capable of detecting fatigue cracks and corrosions in large areas such as aircraft skins. However, current MO images of rivet holes, cracks, and corrosion lack a

quantitative measurement of fields. MO imaging systems are also costly [89-90].

2.6.2 Other EC Techniques

Wincheski et al. [91] proposed a self-nulling EC probe to detect cracks under ferromagnetic protruding head fasteners. A flux concentrator is introduced to focus the magnetic flux field and minimize the flux linkage through the pick-up coil. In this way, only a minimal magnetic field is able to reach the interior area of the probe unless any discontinuity is present in the specimen under detection. Later, he developed a rotating self-nulling probe incorporating a commercial GMR sensor to enhance low frequency capabilities [8, 92], as shown in Figure 2.14. With image processing techniques, their system improved the SNR and enhanced the detection of deeply buried flaws in conductive materials. The use of this self-nulling probe that prevents the saturation of MR sensor has imaged flaws in the 10th layer of 13 layers of 1 mm thick aluminum plates using a 185 Hz excitation frequency [14].

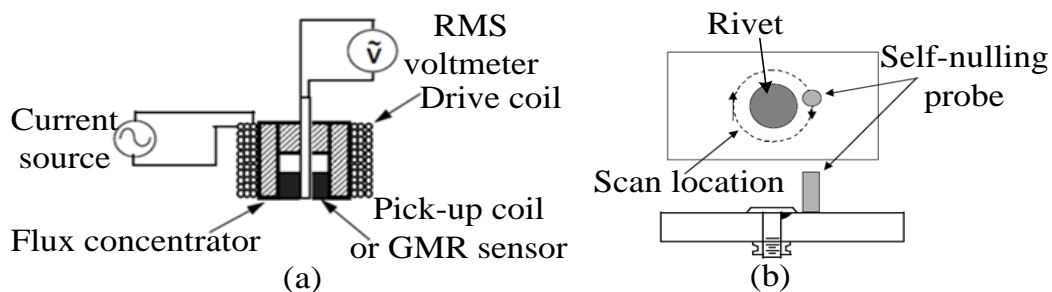


Figure 2.14 Self-nulling EC probe: (a) Probe schematic and (b) Inspection of ferromagnetic protruding head fasteners [91-92]

Similar to the GMR based self-nulling probe, a design using D-shaped excitation coils and a GMR sensor was introduced for detecting buried cracks and flaws emanating from fastener holes [93]. As displayed in Figure 2.15 (a), the D-shaped coil that is placed with its straight edge above

the fastener, rotates around the center of the fastener. The GMR sensor is attached to the excitation coil and positioned above the fastener edge with sensitivity axis tangential to the edge. Using a rotational scan, corner cracks of 2.5 mm in length were detected around a bolt hole in the 2nd layer of a 13 mm thick two-layer structure. Linear scan inspection had been also investigated using this probe. Transverse notches of 2 mm length, 1 mm height were detected around a row of holes in a two-layer specimen using linear scan probes.

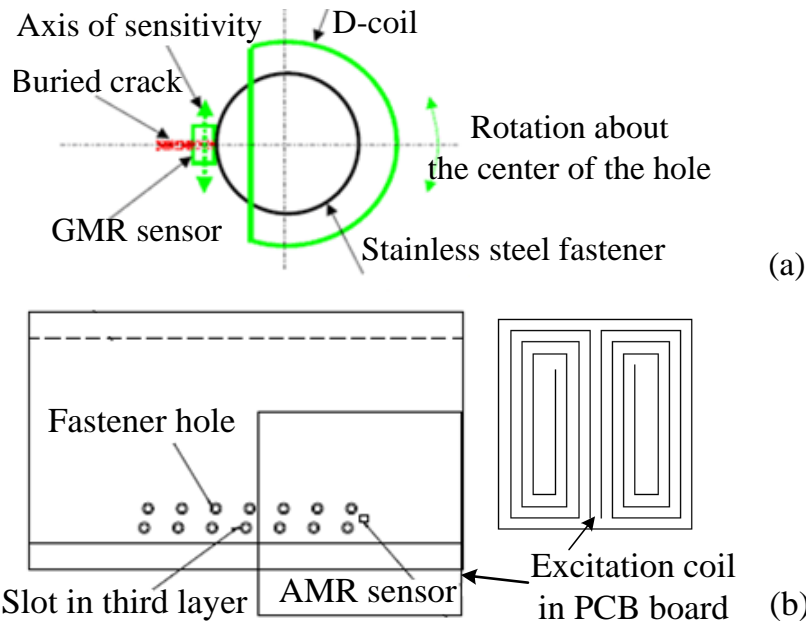


Figure 2.15 EC-GMR probes for riveted structure inspection: (a) Schematic of a rotational D-shaped coil and GMR based probe [93] and (b) A sheet current and AMR sensing probe [17]

A sheet current in a double rectangular spiral probe has been used to detect slots in the presence of stainless steel fasteners by Avrin [17]. An AMR sensor placed at the center of the coil is sensitive to the magnetic field perpendicular to the specimen surface. When the probe size is much larger than the fastener hole geometry (Figure 2.15 (b) shows the probe size of 19x19cm), it is insensitive to small lift-off variations. Subsurface slots (9.5 mm long, 6.3 mm height and

0.25 mm wide in the 3rd layer, 19 mm from the top of a three-layer 25 mm thick aluminum plate) were detected.

It has been indicated that the inspection of structures containing ferromagnetic components within thick multilayer is a challenging task. For the detection of defective ferrous fastener structure, a design proposed by Ko and Steffes [21] magnetized fasteners during inspection, to reduce the noise caused by the permeability. The use of a GMR sensor coupled with a lock-in amplifier increased the sensitivity. The EC data obtained at low frequencies was processed to detect 2nd layer defects occurring 10 mm below the surface of an aluminum sample with steel fasteners. However, the detected cracks were large (about 10 mm).

In this dissertation, the EC systems using the planar coil probe with 3-component MR sensors are studied to detect cracks hidden in non-ferromagnetic and ferromagnetic riveted structures. The configuration of source coil is designed to generate a uniform magnetic source field. Transient and low frequency EC excitations are investigated for improved sensitivity to subsurface cracks with the help of MR sensors.

CHAPTER 3 EC-MR SENSOR SYSTEM – PULSE EXCITATION

3.1 Introduction

Pulsed excitation produces transient signals with a wide range of frequency components and hence it contains more information compared to single frequency excitation. This chapter presents a study of PEC-GMR system. The detection of cracks at steel fastener sites and small cracks embedded in multilayer aircraft skin are investigated numerically and experimentally. A novel implementation of FE numerical model is developed to study the feasibility of defect detection in fasteners using transient EC techniques.

3.2 Background

Transient electromagnetic testing employs a voltage pulse or current pulse to diffuse into a conductive material. Induced transient currents are attenuated as they diffuse through the structure as the electromagnetic pulse energy is dissipated by Joule heating [94].

3.2.1 Skin Depth in Transient Fields

The analytical derivation of skin depth assumes a planar electromagnetic field propagating into a semi-infinite conductor [7]. Induced eddy currents decay exponentially with depth along the conductor in accordance with skin effect. The skin depth in conventional EC testing was presented in Chapter 2, Section 2.2. This section derives the skin depth expression due to a transient excitation.

The governing equation in terms of time-dependent magnetic field \mathbf{B} within a material is given by:

$$\nabla^2 \mathbf{B} = -\mu\varepsilon \frac{\partial^2 \mathbf{B}}{\partial t^2} + \mu\sigma \frac{\partial \mathbf{B}}{\partial t} \quad (3.1)$$

where σ is the electrical conductivity, μ is the material permeability and ε the permittivity.

For a good conductor with $\varepsilon \ll \sigma$, the first term in the right hand side of Eq. (3.1) can be neglected in the frequency range of Hz-MHz [95], reducing Eq. (3.1) to:

$$\nabla^2 \mathbf{B} = \mu\sigma \frac{\partial \mathbf{B}}{\partial t} \quad (3.2)$$

Similar to the diffusion of heat in solids, the solution of \mathbf{B} can be estimated from:

$$\frac{\partial \mathbf{B}}{\partial t} \propto \frac{\mathbf{B}}{\tau_D} \quad \text{and} \quad \nabla^2 \mathbf{B} \propto \mathbf{B} / \ell^2 \quad (3.3)$$

where τ_D is the characteristic diffusion time and ℓ is a characteristic length for the system, which is dependent on the conductor geometry.

Since the magnetic field vector can be separated in space and time domain, the general solution to diffusion equation in Eq. (3.4) is obtained by the separation of variables method in Eq. (3.5) as [95]:

$$B(t) = f(e^{-t/\tau_D}) \quad (3.4)$$

$$B(t) = F(z)e^{-k^2 t / \mu\sigma} \quad (3.5)$$

Hence, the characteristic diffusion time τ_D that is in the form of $\tau_D \propto \mu\sigma\ell^2$ can be expressed as:

$$\frac{1}{\tau_D} = \frac{k^2}{\mu\sigma} \quad (3.6)$$

As opposed to the standard skin depth of EC testing in Eq. (3.7):

$$\delta = \sqrt{\frac{1}{\pi f \sigma \mu}} = \sqrt{\frac{T}{\pi \sigma \mu}} \quad (3.7)$$

the skin depth for the transient response is obtained as:

$$\frac{1}{\delta_{\tau}} = \frac{1}{k} = \sqrt{\frac{\tau D}{\mu\sigma}} \quad (3.8)$$

Comparing Eq. (3.8) and Eq. (3.7) gives the relation:

$$\frac{\delta_{\tau}}{\delta} = \frac{1}{1/\sqrt{\pi}} = 1.77 \quad (3.9)$$

Therefore, it is found that the penetration of transient electromagnetic field within a conductor is about 1.8 times greater than the standard depth for the steady-state case. This scenario is tested by numerical simulations. Figure 3.1 compares the skin depth calculated for conventional EC field to that of transient field. It is observed that a pulsed excitation offers deeper penetration into the conductive plate.

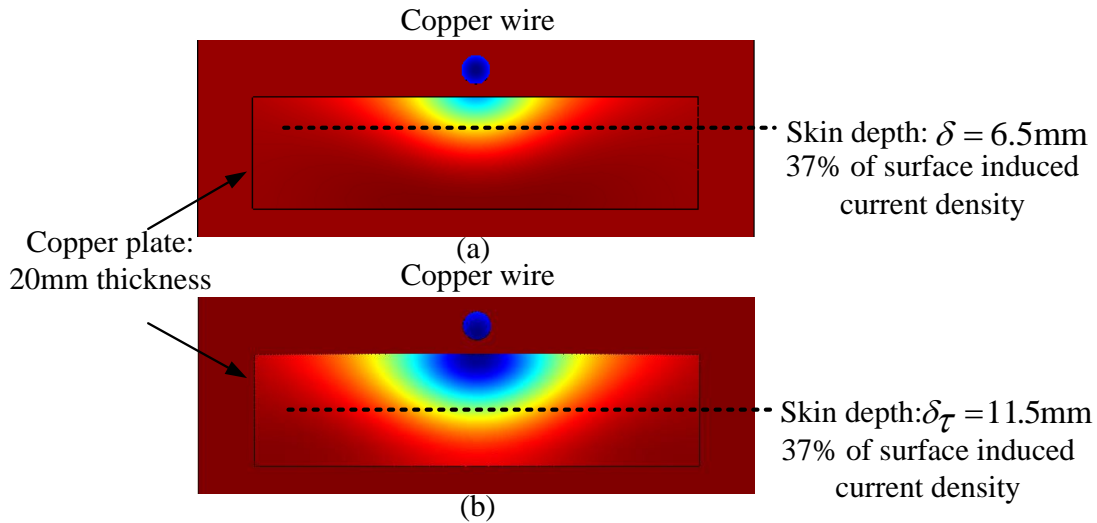


Figure 3.1 Skin depths of conventional EC and transient EC fields (Comsol 3.5 simulation): (a) Conventional 100Hz EC result: induced eddy current and skin depth and (b) 100Hz square-wave PEC result: induced eddy current and skin depth

3.2.2 Transient Signal Characteristics

Transient field can be generated by two modes, namely current driven or voltage driven [96]. In

the current driven mode, a constant current is provided regardless of the coil inductance (within a specified range). In the voltage driven mode, the driver applies a given voltage drop across the excitation coil. The voltage driven mode is generally less complicated in design and allows the adjustment of the current. However, the magnetic field generated by the excitation coil is proportional to the coil current not the voltage. Therefore, this dissertation uses the current driven mode to employ a transient source.

Similar to ultrasonic testing where the measured time of flight in the received signal can determine a defect's depth, transient eddy current propagation through the material and the transient shape of the response signal are related to discontinuities at different depths [52, 94-97]. Transient parameters and features allow flaw discrimination and characterization in the time domain [7, 52]. Interpreted in the time domain, the defects that are closer to a conductor surface activate PEC response earlier than those located further below the surface. The information about sub-surface flaws is mostly contained in the tail part of the transient signal.

The most common features in transient characteristics of PEC signals are the peak amplitude, time to peak amplitude and time to zero crossing [52, 94, 96-98]. The peak amplitude is used to determine the defect size. The time to zero crossing is popularly used to find the depth of a flaw, and the time to peak amplitude can be used to identify the defect depth or material thickness. However, a balancing procedure is required to make those features indicative of flaw presence [52, 94, 96-97]. A common balancing procedure used is to subtract a reference signal that is collected over a region without flaws. A typical reference-subtracted PEC signal and its features are demonstrated in Figure 3.2 (a).

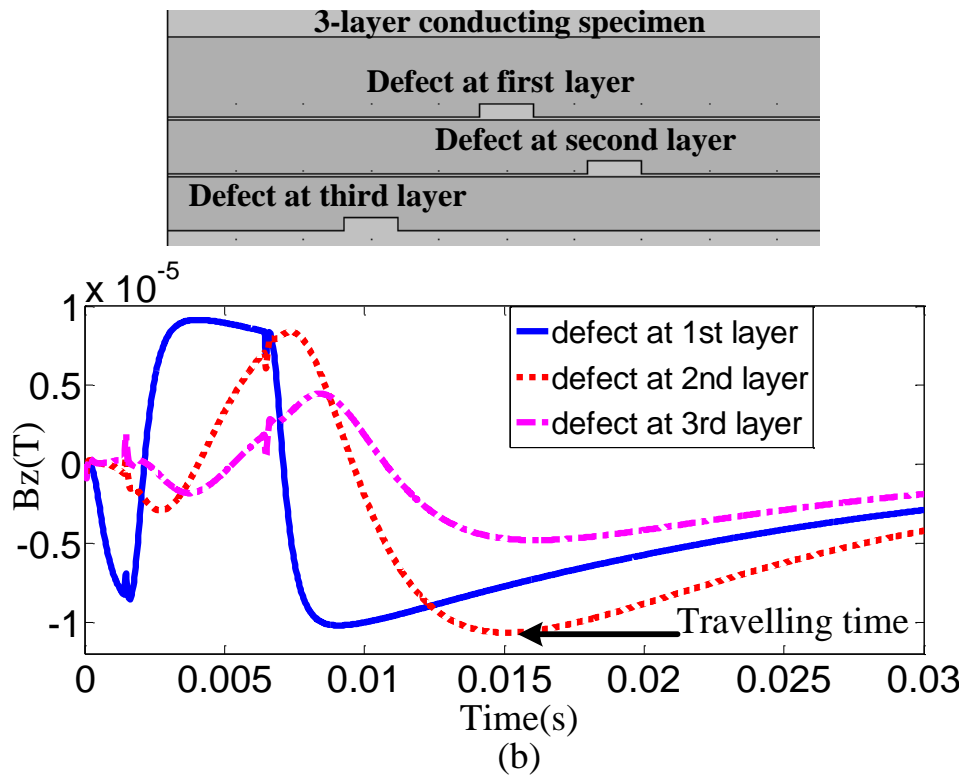
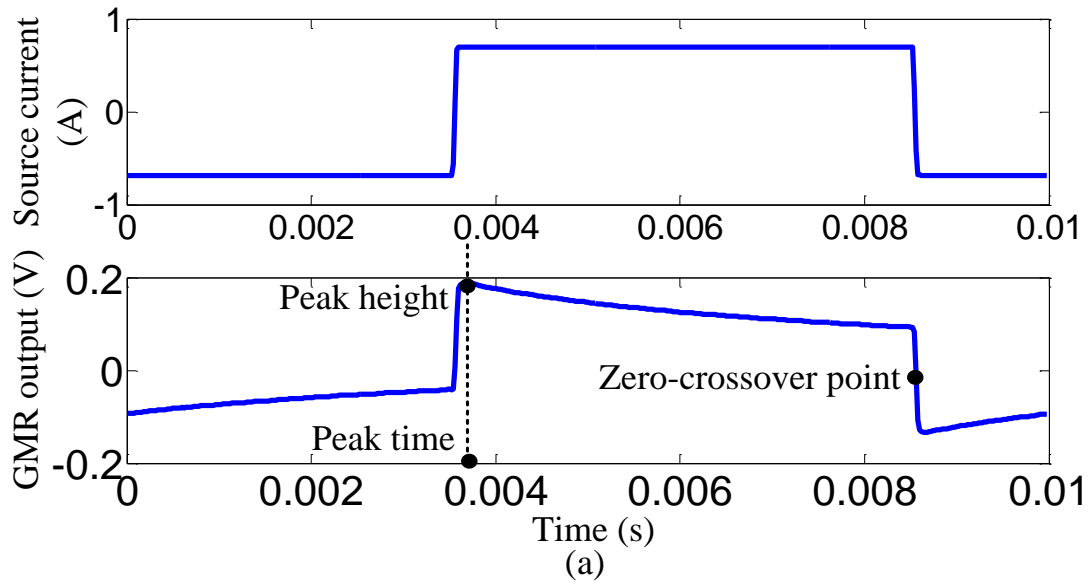


Figure 3.2 PEC signals: (a) A typical reference-subtracted transient response and typical features in the time domain and (b) Transient response associated with defective information at different depths (Comsol 3.5 simulation)

Since hidden discontinuities in a layered structure take longer time to interact with the attenuated transient signal, the depths or layers where flaws are present can be inferred from transient

signals. As shown in Figure 3.2 (b), the corrosion in the 3rd layer interacts with the transient field after deeper penetration and hence is indicated at a later time in the response signal. Furthermore, this deep defect also reduces the peak magnitude of transient signal.

As a result, the pulsed EC is able to detect discontinuities at different layers with a single transient excitation. It superimposes a range of frequencies in one spatial location, while the conventional EC needs to multiplex different frequencies to provide the information at various depths [5, 99].

3.2.3 Review of Transient EC NDE for Layered Structure

The earliest application of transient eddy current can be traced to the publication by Waidelich [100], where PEC was used to measure cladding thickness of reactor fuel elements. Furthermore investigation by Waidelich showed that transient signals presented characteristics that were independent of the distance between the probe and the specimen under test. This result was studied as a transient feature insensitive to lift-off [96] that has been investigated in the detection and characterization of corrosion by Lepine, Lefebvre and Giguere [46, 97, 101].

The earliest study of PEC for crack detection in layered structures with installed fasteners was conducted by Harrison [102-103]. Giguere also studied the detection of cracks beneath rivet heads using transient EC techniques [104].

Transient excitation of coil probes with two MR sensors or two Hall sensors in differential mode have been studied by Lebrun et al. [105-106], and used for characterizing crack parameters. Tai et al. [107] studied similar transient features for an inversion scheme to qualify the conductivity and thickness of samples. Moulder et al. [108] and Bieber et al. [109] developed quantitative

methods for crack and corrosion detection using C-scan images by the time gating of transient signals.

Papers by Smith et al. [110-111] presented a PEC technique named TRECSCAN system (QinetiQ product) for the inspection of aircraft structures. Other PEC techniques were reported for the examination of layered or riveted structures [112-118]. Table 3-1 summarizes different PEC systems developed by several research groups and their applications.

Pulsed EC imaging can be generated based on characteristics of the transient response [96]. Since an A-scan measurement refers the transient response at a single position, the mapping of a feature of each A-scan onto the probe position allows the construction of a C-scan image. Any time-dependent feature representing the dissipation of transient field associated different depths can be employed to produce the C-scan image. Therefore, the image produced contains information about the surface, near surface and subsurface [96, 119]. Data in the form of images is helpful if defects with complex shapes are encountered [23].

The C-scan measurement can be also generated by means of linear combinations of the parameters such as peak height, peak arrival time and zero crossing time [96]. The time gating method forms C-scan images by plotting those peak heights that have a zero crossing within a given time window. This technique was used for image information at various depths and discriminate signals from fastener structure against other interfering factors [108].

Table 3-1 PEC system summary.

PEC system	Excitation Coil	Sensing	Applications
QinetiQ (UK)	Conventional coil	Hall sensor	Corrosions at layered structures Cracks at riveted structures
Research Institute (France)	Conventional coil	Hall/GMR sensor	Cracks at riveted structures
Royal Military College & National Research Council (Canada)	Conventional Coil/ Planar coil	Pick-up coil	Corrosions at layered structures Cracks at riveted structures
Iowa State University (USA)	Conventional coil	Hall sensor/ Pick-up coil	Material characterization Corrosions at layered structures Cracks at riveted structures
University of Newcastle & Huddersfield (UK)	Conventional coil	Hall/GMR sensor	Corrosions & defects at single layer structures Cracks at riveted structures
National University of Defense Technology (China)	Conventional coil	Pick-up coil	Corrosions at layered structures
General Electric (USA)	Conventional coil	Hall sensor/ Pick-up coil	Corrosions at layered structures

3.2.4 Time Domain versus Frequency Domain

Considering $\omega = \frac{2\pi}{T} = \frac{2\pi}{2T_t} = \frac{\pi}{T_t}$, the transient skin depth in Eq. (3.8) is given by:

$$\delta_{PW} = \sqrt{\frac{2T_t}{\pi\sigma\mu}} \quad (3.10)$$

where δ_{PW} is called the pulse width based skin depth. Therefore, increasing the pulse width (duty cycle) enables deeper transient penetration [95]. The relationship between the width of a pulse source and the penetration depth of electromagnetic transient wave has been investigated by Sather [96]. Results indicate that the penetration depth is increased by lengthening the pulse duration.

In addition, the time interval between successive transient waveforms must be sufficient to allow each transient response to decay to zero. Since the diffusion velocity of the EC signal is heavily dependent upon the material, the transient response duration due to one pulse is also material dependent. Also, the transient response duration increases with the thickness of a specimen under test. According to Eq. (3.10), a higher value of T_t is required for a higher skin depth, i.e. a lower rate of pulse repetition is necessary for defect detection along deeper depth [97].

Studies of characteristics of the excitation pulse can be performed in the frequency domain. Two pulse sources in different forms using Discrete Fourier Transform (DFT) are presented in Figure 3.3. Time-dependent signals are decomposed into their harmonic components in the frequency domain, and this helps to design transient excitation waveform.

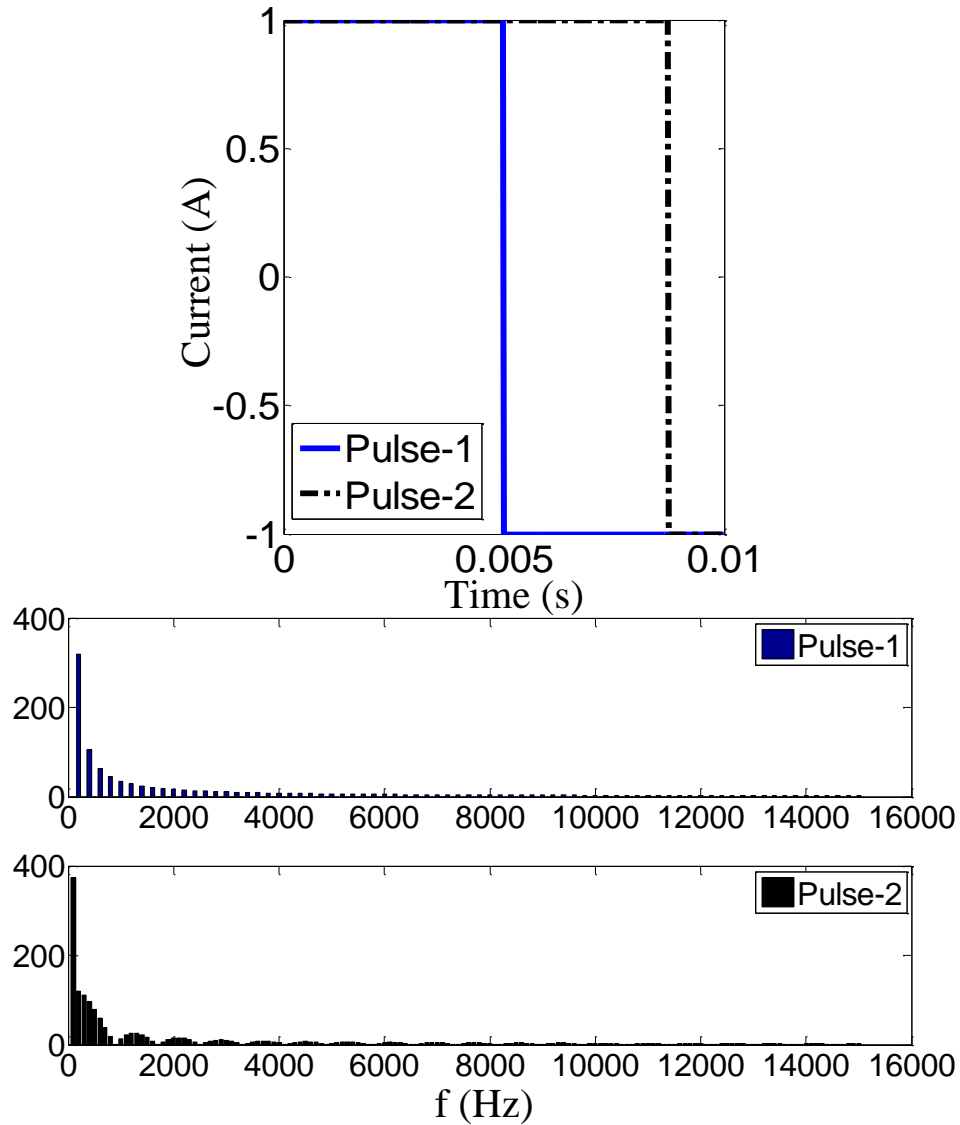


Figure 3.3 Time domain vs. frequency domain: Transient excitations in different pulse widths and their DFT spectrum results

Let the transient pulse source is a square waveform:

$$source(t) = \begin{cases} A_0 & kT < t < kT + T_t \\ 0 & kT + T_t < t < (k+1)T \end{cases} \quad (3.11)$$

where k is an integer, T is the pulse period, and T_t is the excitation pulse width shown in Figure

3.4. The Fourier series of this pulse source are expressed as:

$$source(t) = a_0 + \sum_{m=1}^{\infty} [a_n \cos \frac{2n\pi}{T} t + b_n \sin \frac{2n\pi}{T} t] \quad (3.12)$$

and the Fourier coefficients are evaluated as:

$$a_0 = \frac{1}{T} \int_0^T source(t) dt = \frac{1}{T} A_0 T_t$$

$$a_n = \frac{2}{T} \int_0^T source(t) \cos \frac{2n\pi}{T} t dt = \frac{A_0 T}{n2\pi} (\sin \frac{n2\pi T_t}{T})$$

$$b_n = \frac{2}{T} \int_0^T source(t) \sin \frac{2n\pi}{T} t dt = \frac{A_0 T}{n2\pi} (-\cos \frac{n2\pi T_t}{T} + 1) \quad (3.13)$$

If the cycle $T_t=1/2T$ (50% duty cycle), the source is represented in harmonics:

$$source(t) = \frac{A_0}{2} + \frac{A_0 T}{\pi} [\sin \omega t + \frac{1}{3} \sin 3\omega t + \frac{1}{5} \sin 5\omega t + \dots + \frac{1}{n} \sin n\omega t] \quad (3.14)$$

where n is odd and $\omega = \frac{2\pi}{T}$. Therefore, the square wave is approximated by a summation of odd

harmonics of the fundamental frequency with decreasing amplitude proportional to the harmonic

number. As shown in Figure 3.4, a better approximation is achieved when more sinusoidal

components are included in the summation. The transient field can be numerically studied in the

frequency domain or in the time domain [120-121].

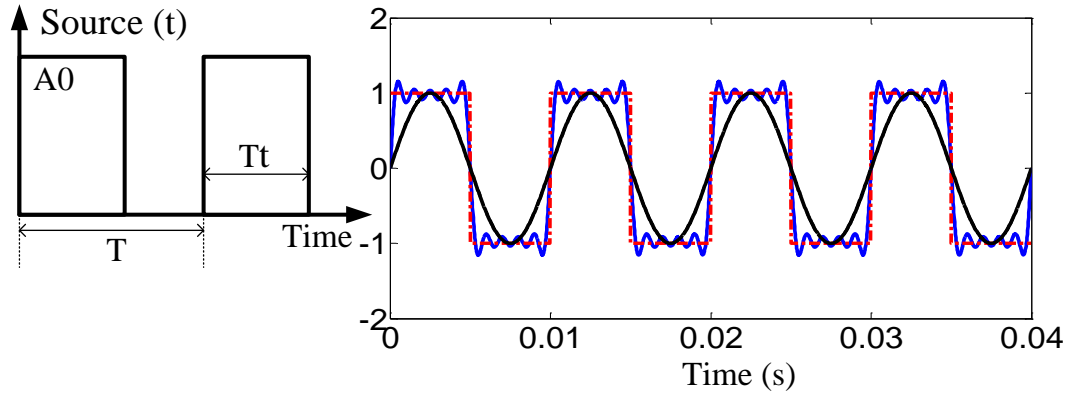


Figure 3.4 Square waveform as a source of pulse excitation (left) and the reconstruction of the waveform by adding Fourier series harmonics (right)

3.2.5 Review of Transient Field Numerical Modeling

Theoretical models play an important role to help understand the underlying physics and application of inspection strategy [122-123]. The landmark work for analytical solution of a single frequency EC testing and coil impedance calculation was studied in [124-125]. Analytical methods for solving transient EC testing were implemented in [126-127]. However, analytical approaches are, in general, conducted for relatively simple geometries such as a conducting half-space and hence have limited abilities to simulate complex structures. Numerical methods have therefore been the method of choice [5, 123, 128].

The popular numerical methods are FE analysis, finite difference analysis, integral analysis, boundary element method, and meshless method. Main contributions in numerical modeling of transient electromagnetic NDE are summarized in Table 3-2 [128, 129-144]. The approaches using transfer function or transient circuit method for modeling PEC system have been introduced in [132, 145-147]. The primary advantage of FE methods is the ability to study irregular or complex features of geometries in discretized elements [18].

Numerically, the transient field can be calculated by two methods: summation of harmonic components in the frequency domain and step marching in the time domain [120-121]. A strategy of interpolation in the frequency domain was proposed to reduce the required number of simulations by reducing the total number of harmonics [137]. However, FE techniques based on frequency selection or interpolation might suffer from low accuracy and need varying mesh size for low or high frequency components [126-127]. Therefore transient field modeling in the time domain is preferred [144, 148]. This dissertation investigates a scheme in the time domain for efficiently modeling the pulsed EC excitation and GMR sensor signals.

3.3 PEC Testing System with MR Sensor

Planar coils were also designed for the inspection of ferrous riveted airframes [22]. However, in these applications, conventional planar coils have limited SNR, and the sizes of detectable cracks are larger than 1 mm and the detected depths are limited to few millimeters below the surface. A design of a rectangular planar coil in differential symmetry with a GMR sensor array along the centric axis has been patented by Boeing company in 2008 [149]. The patented device was designed for scanning layered structures such as aircraft fuselage and wing components. As shown in Figure 3.5, it incorporates an excitation coil with multi-line conductors on a flexible membrane. In collaboration with the NDE laboratory at Michigan State University, this probe was studied for developing an effective EC-GMR imaging system [150]. This dissertation extends the multi-line probe for the use of a pulsed excitation to enhance the inspection capabilities.

Table 3-2 Summary of transient field modeling and simulation.

Modeling research	Modeling method	Solution domain	Applications
J. R. Bowler (USA)	Transfer function Integral method Analytical method	Frequency domain	Material characterization Conductor at half-space Crack profile inverse
T. Theodoulidis (Greece)	Integral method Analytical method	Frequency domain	Conductor at half-space
C. Mandache & T. W. Krause (Canada)	Transient circuit Method Comsol package (FE method)	Time domain	Layered structure Riveted structure
F. Thollon (France)	FE method Transfer function	Frequency domain	Riveted structure
G. Y. Tian (UK)	Comsol package (FE method) Analytical method	Frequency domain Time domain	Layered structure
T. Takagi & Z. Chen (Japan, China)	FE method Hybrid method	Frequency domain Time domain	Single layer structure Crack profile inverse

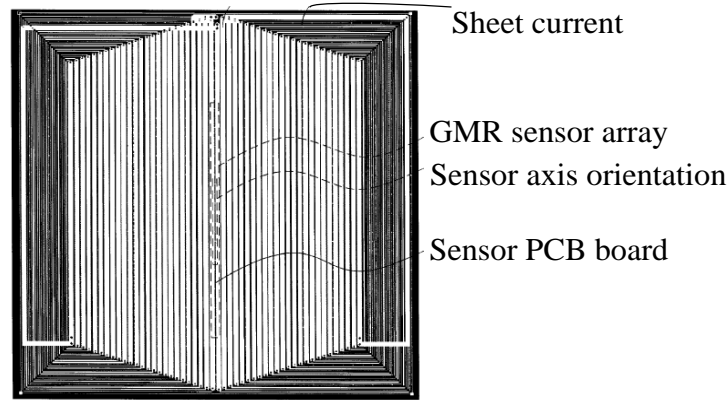


Figure 3.5 Schematic of the multi-line planar probe design [149]

3.3.1 Excitation Coil Configuration

To demonstrate the advantages of using planar coil as an excitation source, the induced fields due to a multi-line planar coil are compared to those due to a pancake coil. A riveted structure with two cracks in the 2nd and 3rd layers is studied. The distributions of the magnetic field and induced currents are investigated by numerical studies. Two coils are excited by a same 1A current source at 100Hz frequency. Figures 3.6-3.7 present the magnetic fields and eddy currents generated by the two coil configurations.

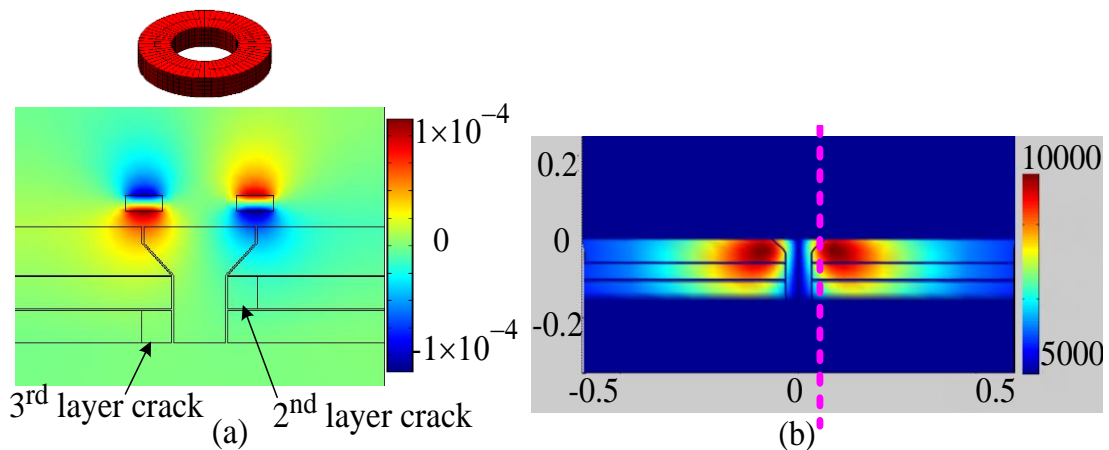


Figure 3.6 Simulation results of pancake coil: (a) Tangential component (B_x) of magnetic field

(T) and (b) Induced currents (A/m^2)

In Figure 3.6 (a), the pancake coil has 5mm inner radius and 10mm outer radius, and the eddy currents flow in circular paths and are parallel to the turns of the coil. As shown in Figure 3.6 (b), the case without crack is used for studying the skin depth associated with a coil configuration. The maximum density of eddy currents occurs close to coil windings that is also the edge of the fastener. In the central region of the structure under test, eddy currents are self-canceling. Meanwhile, eddy currents exponentially decay as the depth increases. The amplitude of currents induced at the sample surface is reduced by 34.71% at the bottom layer, and the skin depth (37% of the induced current density at the surface) is about 10mm.

In Figure 3.7 (a), the multi-line planar coil has a dimension of 98mm by 104mm with 2mm spacing between the wires, and the planar wire is 0.05mm thickness and 0.5mm height. The multi-line coil is driven by the current flowing in a same direction, and acts like a current sheet. The multi-line planar coil produces uniform and linear eddy currents. As shown in Figure 3.7 (b), the induced currents still keep 56.37 % of its energy after penetrating through all three layers. Therefore, a skin depth of more than 14mm is generated and this provides enhanced sensitivity to detect buried cracks. Additionally, the disturbances of eddy currents caused by the two defects around the fastener site generate a measurable magnetic field in the 2nd and 3rd layers that can be captured by a magnetic field sensor.

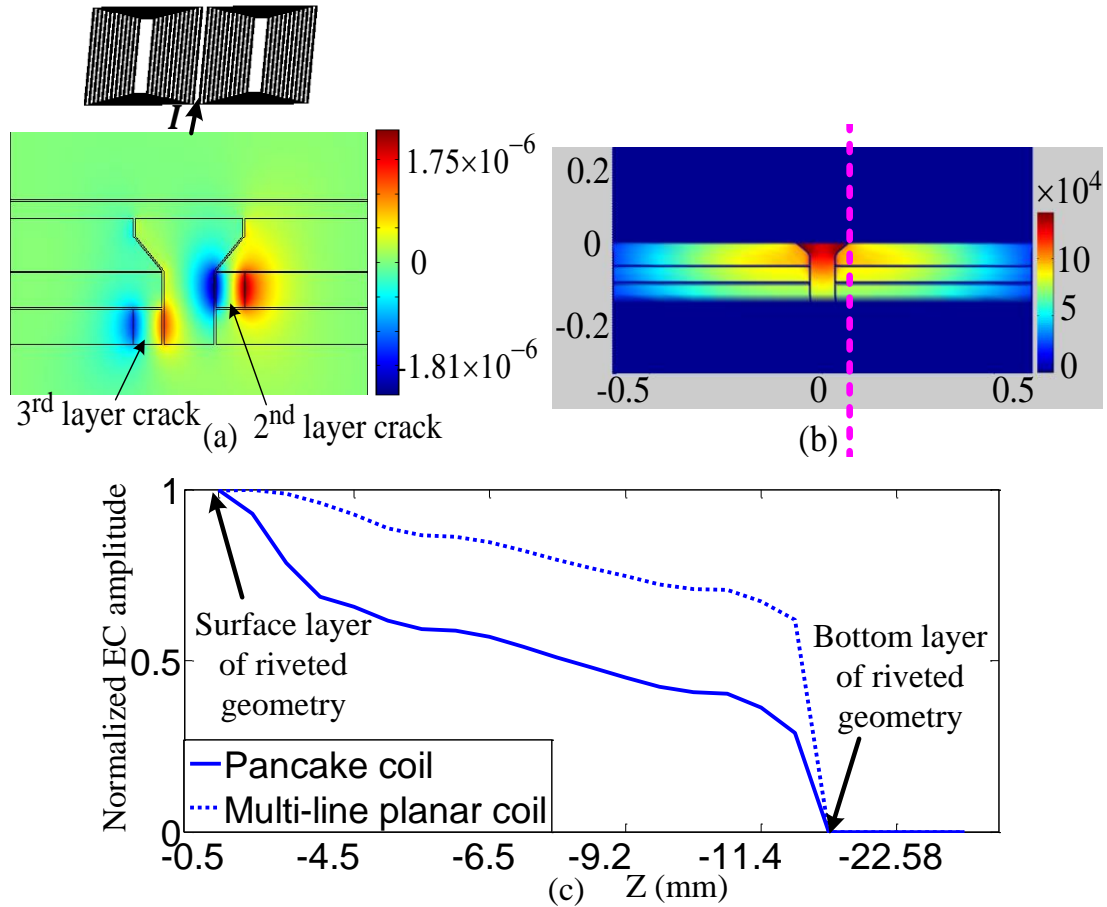


Figure 3.7 Simulation results of multi-line coil: (a) Normal component (B_y) of magnetic field (T) (b) Induced currents (A/m^2) (c) Comparison of induced currents due to two coil configurations

Furthermore, the induced currents along the depth due to these two coil configurations, as two dash lines shown in Figure 3.6 (b) and Figure 3.7 (b) are plotted in Figure 3.7 (c) using the normalized amplitude. It is seen that the multi-line coil generates stronger induced currents and provides deeper penetration of the induced field. In conclusion, the multi-line planar coil produces higher sensitivity to detect subsurface cracks hidden in riveted structures. Moreover, this coil configuration is relatively insensitivity to lift-off [52, 97, 149].

3.3.2 PEC-GMR Probe Operation

Numerical studies have validated the detection capability of the multi-line planar coil. This planar coil used for pulsed current excitation is studied in this chapter.

As described schematically in Figure 3.8, in the absence of any discontinuity, due to the symmetry of the coil geometry, the normal component of the magnetic field is zero on the line of symmetry at the center of the source coil. When the uniform distribution of induced currents is distorted by a fastener and/or a crack, the zero induced field on the line of symmetry is destroyed. A GMR sensor placed at this location is utilized to acquire the induced magnetic field. In the case of pulsed excitation, the induced transient currents diffuse into the test sample. A nonzero transient signal of the normal component is produced and captured by the GMR sensor. This measured signal represents information about cracks around fastener sites.

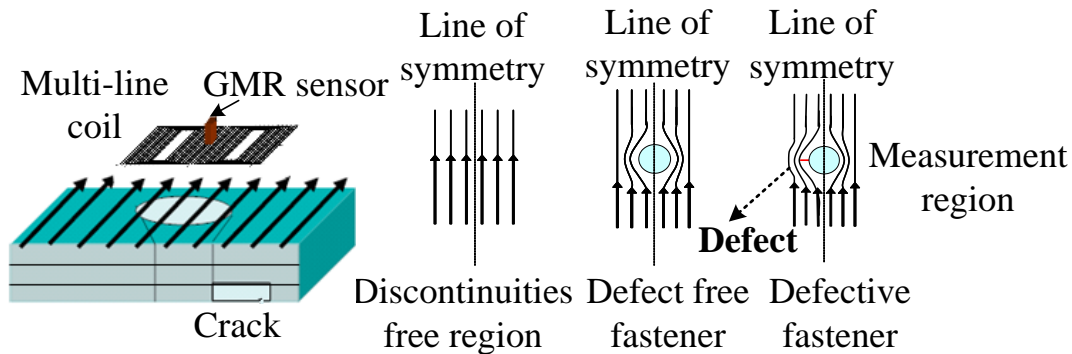


Figure 3.8 Schematic of the operation of multi-line planar probe

In this probe design, the induced field and eddy currents due to the return loop current at the edge sides of the probe are minor. Consequently, similar to MO imaging, but at much lower cost and simple design, single directional eddy currents in parallel pattern are induced around a fastener site. Subsurface discontinuities that distort these linear eddy currents are detected by the

GMR sensor that measures specific components of the magnetic field.

3.3.3 Giant Magnetoresistive Sensor

As described earlier, GMR sensors show large resistance changes when they are subjected to a magnetic field [51, 151]. The variation in resistance is about 2% for ferromagnetic materials and up to 300% for special materials [97]. GMR sensors have been used in low frequency EC testing [14-17, 21, 24, 76-77, 79-80, 92-93]. In this dissertation, the use of GMR sensors in conjunction with pulsed EC sensing is investigated. The advantages of this system are its high sensitivity, small dimension of field receiver, low cost, low power supply requirement, and linear sensitivity over a broad frequency range (from DC up to 1 MHz). Moreover, the front-end electronics are simple and relatively inexpensive [14, 152].

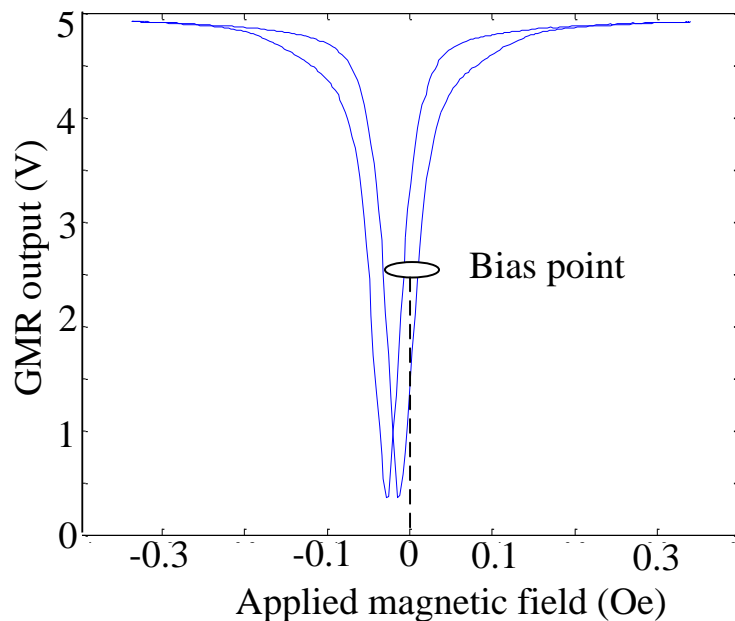


Figure 3.9 Characteristic curve for the calibration of the GMR sensor

Typical characteristic of the commercial AAH002 GMR sensor by NVE Corporation is obtained

experimentally and is shown in Figure 3.9. Due to its unipolar output, the GMR sensor needs to be biased appropriately to permit bipolar operation before it can be used for field measurements. Usually, the DC bias field is realized using a coil or a permanent magnet. Once the sensor is biased, the characteristic curve can be used for calibrating the output of the GMR sensor to achieve a reliable and quantitative estimate of the magnetic field.

3.3.4 Experimental Set-up

Experimental measurements are performed using a high resolution scanning system. A two-dimensional raster scan around each fastener is generated. At each scan position, the planar coil is excited by a pulse. The GMR sensor measures the normal component of the changing magnetic field due to induced eddy currents in the specimen. It should be noted that a single GMR sensor at the center of the symmetry line of the coil probe or an array of GMR sensors along the line symmetry could be used.

A schematic of the overall PEC-GMR inspection system is shown in Figure 3.10. The X-Y scanner is controlled by a PC, which produces a trigger signal to control the data acquisition at each scan position. The function generator supplies a square wave current excitation of frequency 100 Hz and 50% duty cycle as shown. The square waveform amplitude is adjustable by a power amplifier and it is fed into the multi-line excitation coil. A permanent magnet is used as a bias field for the GMR sensor. The DC bias is filtered out to get the pure response of the GMR sensor. A two-stage amplifier is used to amplify the output signal of the GMR sensor. The amplified output is connected to the data acquisition card in a differential mode to reduce the noise due to long connecting cables and interference from the environment. At each position, the

transient response of the GMR sensor is acquired at a sampling frequency of 50,000 samples per second for the duration of 2.56 seconds. The measurements are averaged over 256 cycles of the excitation waveform for further noise reduction.

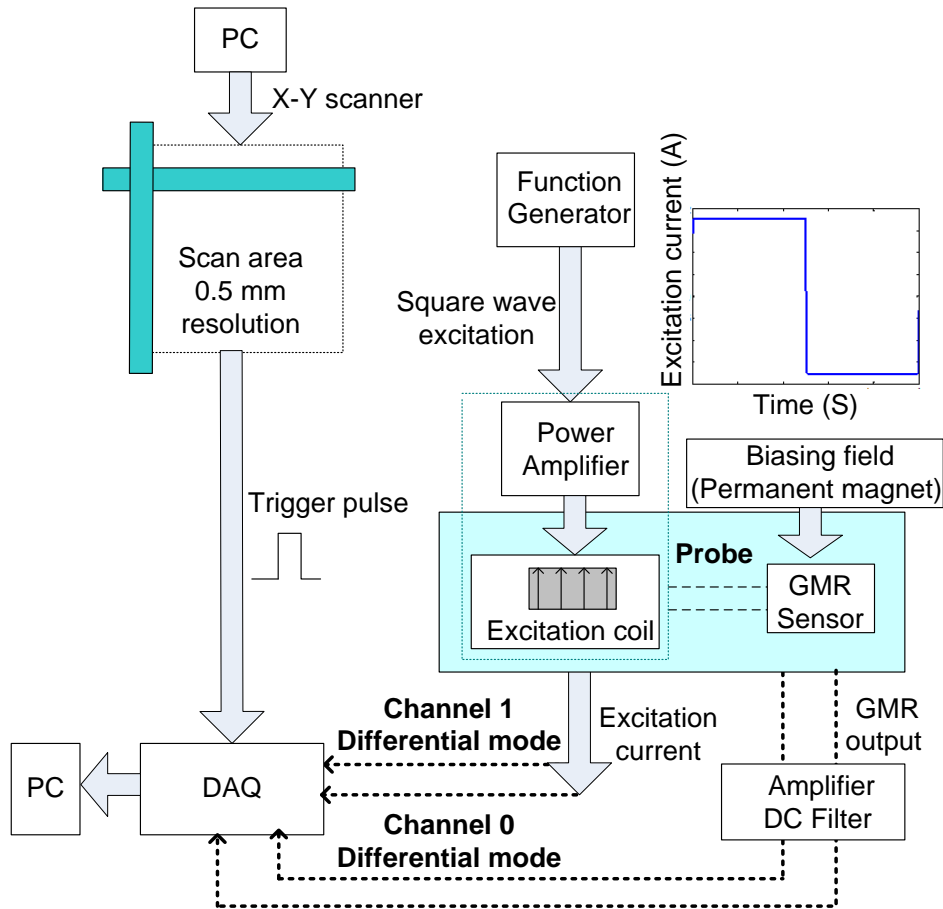


Figure 3.10 Schematic of the PEC-GMR inspection system

3.4 Inspection of Riveted Structures

The performance of the system was evaluated using multilayer riveted specimens with machined subsurface cracks.

3.4.1 A-scan Measurement of Transient Field

GMR measurements due to a crack located at a fastener site through the second layer of the

sample are illustrated in Figure 3.11. As in ultrasonic measurements, the A-scan signal is the time-dependent response collected at each scan point. A total of 19 scan positions above the fastener head are used to collect the GMR A-scan signals. These A-scan signals are the measurements of the normal transient field (B_z) at 2mm lift-off. Scan position 5 is located at the left edge of the fastener, scan position 11 is located at the fastener center, and scan position 17 is located at the right edge of the fastener. Scan positions 17-19 are located at the crack region.

As shown in Figure 3.11, the A-scan signals present a characteristic trend when the probe scans the fastener region. In the plots in Figure 3.11 (c), the peak magnitude of the GMR response presents an ascending trend when the probe moves towards the left edge of fastener (Scans 1-5). The response achieves the highest magnitude at the left edge location (Scan 5). The transient response magnitude decreases and reaches almost a null point at the center of the fastener (Scan 11). When the probe continues to move to away from the fastener center, the peak magnitude of transient response increases again and presents a maximum value at the right edge location (Scan 17). The plots in Figure 3.11 (d) show that the peak magnitude of the signal decreases as the probe moves away from the fastener's right edge.

The different characteristics of the signals are representative of the sample and defect geometry, and any discontinuity encountered at the corresponding scan position. Thus, the discriminations between transient signals at the two edges can be considered as a feature for the detection of embedded crack.

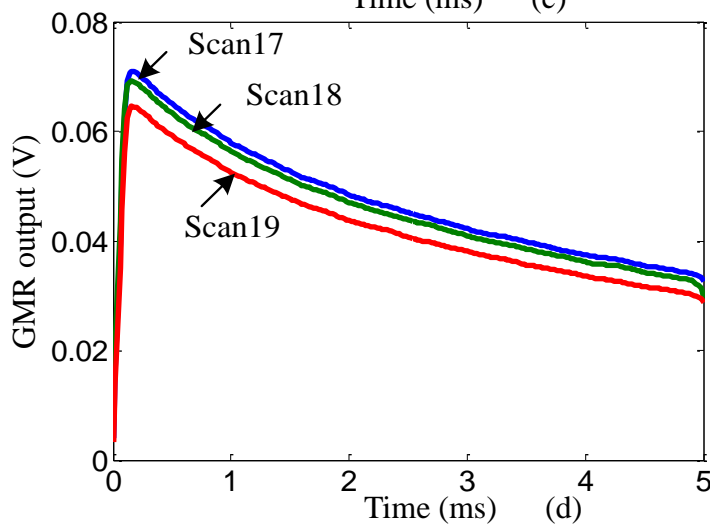
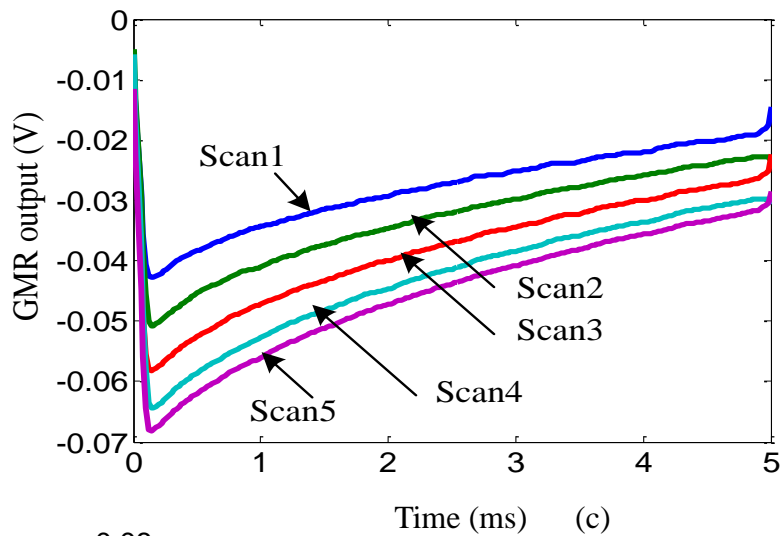
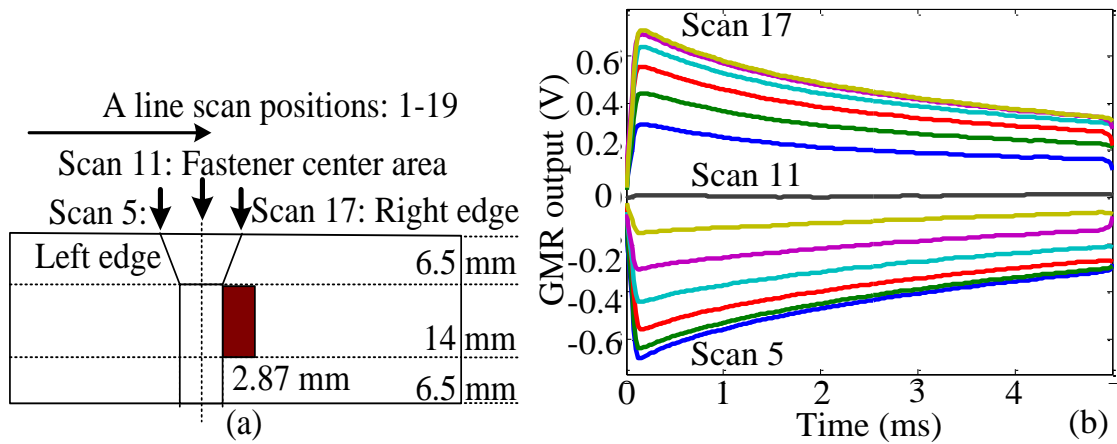


Figure 3.11 GMR measurements of the transient field B_z component along a line scan above a fastener with a subsurface crack: (a) Inspection Geometry (b) Sequence of A-scan signals within the fastener head region (c) Comparison of transient signals at the fastener head edge areas for crack indication

3.4.2 C-scan Image Measurement of Transient Field

The magnitude mapping using the peak value of each A-scan is performed to obtain the C-scan image. The experimental GMR measurements of A-scan signal along a line across a defective fastener shown in Figure 3.12 (a) and the corresponding C-scan data are presented in Figure 3.12 (b). The asymmetry observed in the C-scan image indicates the feasibility to infer the presence of a defect at the rivet site. The GMR response from multiple A-scan measurements or C-scan image data is utilized in this dissertation for data analysis and crack detection.

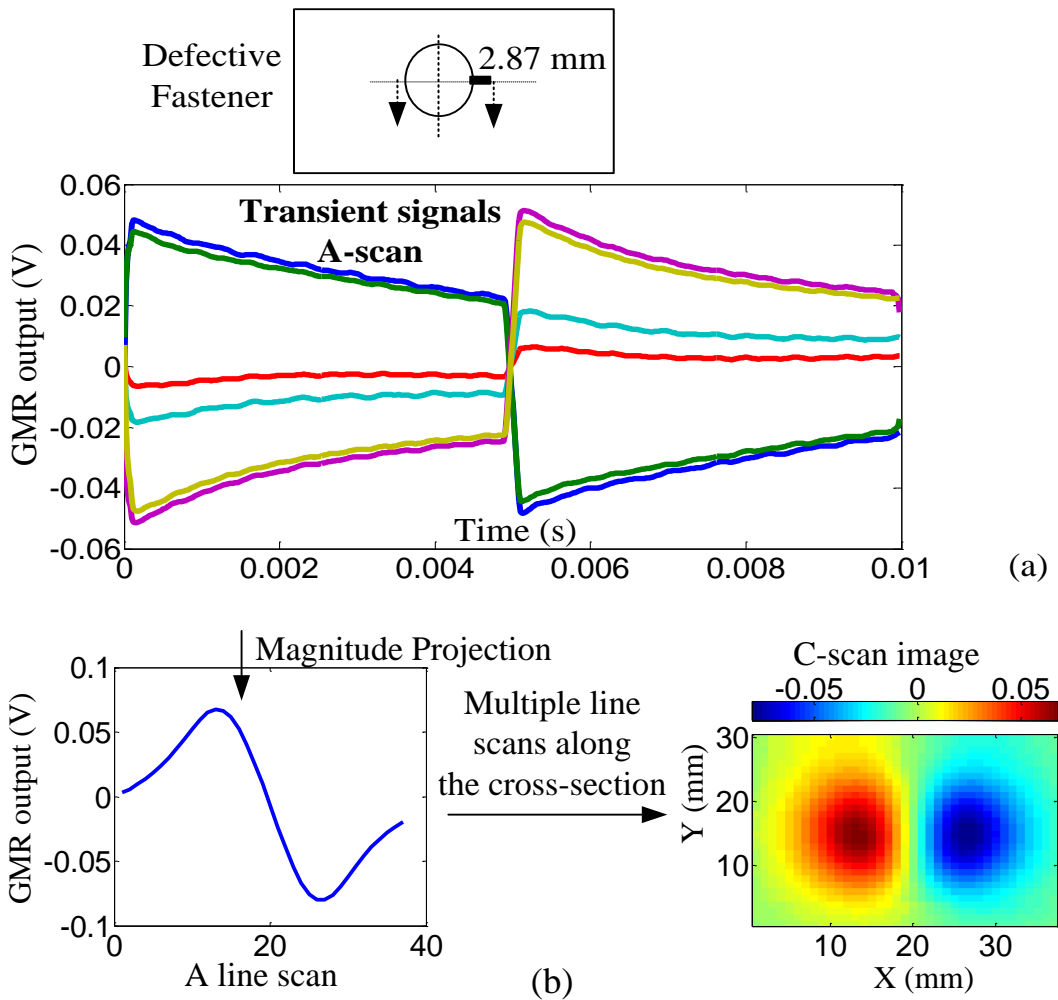


Figure 3.12 Three modes of PEC-GMR signals in the inspection of a riveted structure

3.5 Time-domain Modeling of PEC-GMR Testing

A time domain based FE model is studied for simulating the PEC-GMR inspection of multilayer aircraft frame. The proposed strategy provides a faster solution compared to the approach implemented in the frequency domain [137].

3.5.1 FE Modeling

FE methods based on magnetic vector potentials have been successful in modeling EC NDE problems [153-155]. In general, Maxwell's equations introduced in Chapter 2, Eq. (2.1) to Eq. (2.4) are formulated using vector potentials, along with the following continuity equation and the constitutive relationships:

$$\nabla \cdot \mathbf{D} = \rho \quad (3.15)$$

$$\nabla \cdot \mathbf{J} + \frac{\partial \rho}{\partial t} = 0 \quad (3.16)$$

$$\mathbf{B} = \mu \mathbf{H} \quad (3.17)$$

$$\mathbf{J} = \sigma \mathbf{E} \quad (3.18)$$

where the variables are:

\mathbf{D} : electric flux density (coulomb/meter³)

ρ : electric charge density (coulomb/ meter³)

μ : magnetic permeability, $4\pi \times 10^{-7}$ (henries/meter) for nonmagnetic materials

σ : electric conductivity (mhos/meter)

Various formulations have been used for modeling electromagnetic field, including the \mathbf{A} - \mathbf{V} - \mathbf{A} potential formulation, and the \mathbf{A}_r - V - \mathbf{A}_r reduced vector potential formulation.

I. FE Model: A-V-A Potential Formulation

In a typical EC testing problem, a solution region (Ω) is depicted in Figure 3.13 which consists of a nonzero conductivity region with eddy currents (Ω_1), the region free of eddy currents but with source currents (Ω_2), interface and boundary sections. The magnetic vector potential (\mathbf{A}) in the entire region is related to the magnetic flux density as:

$$\mathbf{B} = \nabla \times \mathbf{A} \quad (3.19)$$

And the magnetic field intensity is also expressed by \mathbf{A} :

$$\mathbf{H} = \frac{1}{\mu} \nabla \times \mathbf{A} \quad (3.20)$$

The electric scalar potential (V) in eddy currents region (Ω_1) is defined by the identity:

$$\nabla \times \nabla V = 0 \quad (3.21)$$

Substituting equation (3.19) into Maxwell's equation of Eq. (2.1), we get:

$$\nabla \times \left(\mathbf{E} + \frac{\partial \mathbf{A}}{\partial t} \right) = 0 \quad (3.22)$$

Combing Eq. (3.22) and Eq. (3.21):

$$\mathbf{E} = -\frac{\partial \mathbf{A}}{\partial t} - \nabla V \quad (3.23)$$

Considering the source currents, and using Ohm's law:

$$\mathbf{J} = \sigma \mathbf{E} + \mathbf{J}_s \quad (3.24)$$

Maxwell's equations are formed by the $\mathbf{A} - V - \mathbf{A}$ formulation as:

$$\begin{aligned} \nabla \times \left(\frac{1}{\mu} \nabla \times \mathbf{A} \right) + \sigma \left(\frac{\partial \mathbf{A}}{\partial t} + \nabla V \right) &= \mathbf{J}_s \\ \nabla \cdot \sigma \left(\frac{\partial \mathbf{A}}{\partial t} + \nabla V \right) &= 0 \end{aligned} \quad (3.25)$$

in the whole solution domain by neglecting the displacement current term $\frac{\partial \mathbf{D}}{\partial t}$, and

where \mathbf{J}_s presents the source current density.

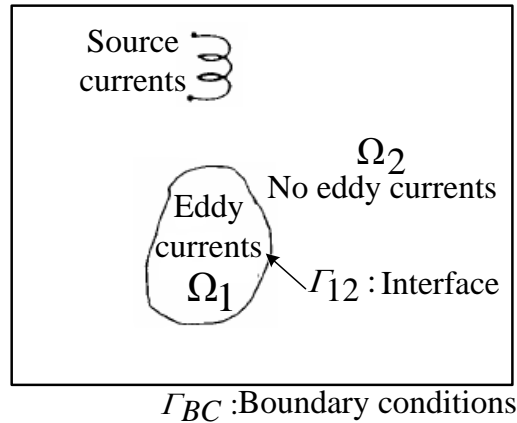


Figure 3.13 A typical EC problem with regions, boundary sections and interface

In the solution of Eq. (3.25), a gauge condition is necessary to ensure the uniqueness of \mathbf{A} . Two gauge conditions, Lorentz gauge and Coulomb gauge are generally used. The Lorentz gauge is expressed as:

$$\nabla \cdot \mathbf{A} + \frac{1}{c^2} \frac{\partial V}{\partial t} = 0 \quad (3.26)$$

where c is the speed of light in free space. Lorentz gauge leads the potentials suitable for a set of wave equations in high frequency problems. The Coulomb gauge, defined as:

$$\nabla \cdot \mathbf{A} = 0 \quad (3.27)$$

is usually utilized in low frequency problems due to the absence of the displacement current and the resulting equations are simplified.

II. FE Model: $\mathbf{A}_r - V - \mathbf{A}_r$ Reduced Vector Potential Formulation

Although the $\mathbf{A} - V - \mathbf{A}$ formulation has been widely studied for FE modeling of time-harmonic and transient electromagnetic NDE [126, 143, 150, 153-156], the meshing of the source coil probe becomes very cumbersome, particularly if the probe motion is to be taken into account [137, 153-154, 157-158]. Moreover, accurately meshing the complex coil structure at

each scan position associated with the test sample poses difficulties in mesh discretization. A scheme that helps to alleviate this problem using reduced vector potential formulation $\mathbf{A}_r - V - \mathbf{A}_r$ is introduced [153-154, 157-158].

The magnetic vector potential is decomposed into potentials due to excitation source and induced currents. Correspondingly the magnetic flux density \mathbf{B} is similarly split into two parts:

$$\mathbf{B} = \mathbf{B}_S + \mathbf{B}_r = \mu_0 \mathbf{H}_S + \mathbf{B}_r \quad (3.28)$$

where \mathbf{B}_S and \mathbf{H}_S are the flux density and field density due to the source current in free space, and \mathbf{B}_r is the flux density due to induced current or magnetization and μ_0 is the free-space permeability. Considering equation (3.19), the magnetic vector potential \mathbf{A} is defined as:

$$\mathbf{A} = \mathbf{A}_S + \mathbf{A}_r, \quad \nabla \times \mathbf{A}_S = \mathbf{B}_S \quad \text{and} \quad \nabla \times \mathbf{A}_r = \mathbf{B}_r \quad (3.29)$$

The vector potential \mathbf{A}_S in air is due to the excitation current and \mathbf{A}_r is due to the induced and/or magnetization currents. Furthermore, \mathbf{A}_S can be evaluated by Biot-Savart's law:

$$\begin{aligned} \nabla \times \mathbf{H}_S &= \mathbf{J}_S \\ \mathbf{A}_S &= \frac{\mu_0}{4\pi} \int_{\Omega'} \frac{\mathbf{J}_S(\mathbf{r}')}{|\mathbf{r} - \mathbf{r}'|} d\Omega \end{aligned} \quad (3.30)$$

Where Ω' is the volume of source currents, and \mathbf{r} and \mathbf{r}' denote the coordinates of observation and source points, respectively.

Correspondingly, the governing equations (3.25) can be expressed as:

$$\nabla \times \left(\frac{1}{\mu} \nabla \times \mathbf{A}_r \right) + \sigma \frac{\partial \mathbf{A}_r}{\partial t} + \sigma \nabla V = \nabla \times \mathbf{H}_S - \nabla \times \left(\frac{1}{\mu} \nabla \times \mathbf{A}_S \right) - \sigma \frac{\partial \mathbf{A}_S}{\partial t}$$

$$\nabla \cdot \left(\sigma \frac{\partial \mathbf{A}_r}{\partial t} + \sigma \nabla V \right) = -\nabla \cdot \sigma \frac{\partial \mathbf{A}_s}{\partial t} \quad (3.31)$$

The advantages of the reduced vector potential formulation are as follows [157-158]:

- 1) Mesh generation with complex coil shape becomes much easier because the excitation coil is discretized independently for computing the source potential.
- 2) Convergence of the iterative solver is faster because the current source can be modeled accurately.
- 3) Scanning of the coil over a sample involved in a typical EC testing process can be simulated without re-meshing. Computational errors due to remeshing are removed.
- 4) Incomplete factorization of the system matrix, which is the most time-consuming process in the solution phase, is performed only once.
- 5) Only the secondary field due to magnetization and/or induced currents is solved. Hence the solution time can be reduced because the secondary field is much smaller than the source field.
- 6) It is efficient for conducting parametric studies without changing the mesh, such as lift-off variation and tilt in angle.

III. FE Method Implementation

The numerical approximation of the potentials as unknowns is based on a discretized FE mesh.

The potentials can be expanded in terms of shape functions associated with the nodes of mesh:

$$\mathbf{A} \approx \sum_i A_{xi} N_i \hat{x} + A_{yi} N_i \hat{y} + A_{zi} N_i \hat{z} = \sum_k N_k \mathbf{A}_k \quad (3.32)$$

$$V = \sum_i N_i V_i \quad (3.33)$$

$$\mathbf{A}_r \approx \sum_i A_{rxi} N_i \hat{x} + A_{ryi} N_i \hat{y} + A_{rzi} N_i \hat{z} = \sum_k N_k \mathbf{A}_k \quad (3.34)$$

Where A_{xi}, A_{yi}, A_{zi} and V_i are the three Cartesian components of the potentials at node i , and N_i is the shape function associated with node i that assumes the value of one at this node and the value of zero at any other node. The vectors $\hat{x}, \hat{y}, \hat{z}$ are the Cartesian unit vectors.

The Galerkin formulation of weighted residual method [153-155] is implemented to solve Eq. (3.25) and Eq. (3.31) in two presented formulations:

$$\begin{aligned} \int_{\Omega} (\nu \nabla \times N_i \cdot \nabla \times \mathbf{A} + \sigma N_i \cdot \partial \mathbf{A} / \partial t + \sigma N_i \cdot \nabla V) d\Omega + \oint_{\Gamma} (\sigma N_i \nabla \cdot (\partial \mathbf{A} / \partial t + \nabla V)) \cdot \hat{n} d\Gamma \\ = \int_{\Omega} N_i \cdot \mathbf{J}_S d\Omega \end{aligned} \quad (3.35)$$

$$\begin{aligned} \int_{\Omega} (\nu \nabla \times N_i \cdot \nabla \times (\mathbf{A}_r + \mathbf{A}_s) + \sigma N_i \cdot \partial (\mathbf{A}_r + \mathbf{A}_s) / \partial t + \sigma N_i \cdot \nabla V) d\Omega \\ + \oint_{\Gamma} (\sigma N_i \nabla \cdot (\partial (\mathbf{A}_r + \mathbf{A}_s) / \partial t + \nabla V)) \cdot \hat{n} d\Gamma = \int_{\Omega} N_i \cdot \mathbf{J}_S d\Omega \end{aligned} \quad (3.36)$$

where N_i ($i=1,2,\dots,N$ with N the number of nodes) are shape functions, Ω the solution domain, and $\nu=1/\mu$ is reluctivity. Γ is the conductor surface and \hat{n} is the unit outward normal vector of Γ . By neglecting the surface integral in Eq. (3.35) or Eq. (3.36), we implicitly set the normal component of induced currents on the conductor surface to zero.

The FE procedure results in a linear algebraic system of equations that must be solved to determine the unknown coefficients of the shape functions. The global stiffness matrix is obtained by assembling each element matrix together. The value at each entry is the sum of values contributed by all the connected elements:

$$GA = S \quad (3.37)$$

where G is a complex, symmetric sparse matrix, A is the vector of unknowns consisting of the electric scalar potential and the three components of the magnetic vector potential or the

magnetic reduced vector potential at each node, and S is the load vector incorporating the current source.

The equations can be solved using either direct or iterative methods. Either Dirichlet boundary conditions or Neumann boundary conditions need to be specified. Since Neumann boundary conditions are usually included implicitly in the FE formulation, one only needs to impose Dirichlet boundary conditions. Current continuity conditions will be explicitly imposed at the interface boundaries to avoid spurious solutions.

3.5.2 Time-domain Modeling Schemes

The $A_r - V - A_r$ formulation is used as the basis for the time domain modeling scheme. The backward difference method is used to treat time and the transient values are evaluated by iterations $t^{n+1} = t^n + \Delta t$. The time derivative term $\frac{\partial \mathbf{A}}{\partial t} = \frac{\mathbf{A}^{n+1} - \mathbf{A}^n}{\Delta t}$ is implemented by considering A_s and A_r separately:

$$\frac{\partial \mathbf{A}_s}{\partial t} = \frac{\mathbf{A}_s^{n+1} - \mathbf{A}_s^n}{\Delta t}, \quad \frac{\partial \mathbf{A}_r}{\partial t} = \frac{\mathbf{A}_r^{n+1} - \mathbf{A}_r^n}{\Delta t} \quad (3.38)$$

The governing equations of this formulation can be written as:

$$\begin{aligned} \nu \nabla^2 \mathbf{A}_r^{n+1} \Delta t + \sigma \mathbf{A}_r^{n+1} + \sigma \nabla V^{n+1} \Delta t &= (1 - \nu_r) \nabla \times \mathbf{H}_s^{n+1} \Delta t - \sigma (\mathbf{A}_s^{n+1} - \mathbf{A}_s^n) \\ &\quad + \sigma \mathbf{A}_r^n \\ \nabla \cdot (\sigma \mathbf{A}_r^{n+1} + \sigma \nabla V^{n+1} \Delta t) &= -\nabla \cdot \sigma (\mathbf{A}_s^{n+1} - \mathbf{A}_s^n) + \nabla \cdot \sigma \mathbf{A}_r^n \end{aligned} \quad (3.39)$$

I. Interpolation based Time-domain Modeling

The simulation of PEC signals using an interpolation scheme in the time domain is proposed to increase the simulation efficiency. As shown in Figure 3.14, the geometry for this simulation

study is a 3 mm thick aluminum plate with a fastener hole of 10 mm diameter. A 1 mm crack is included at the right edge of the fastener hole. Transient signals of the normal component at three positions are simulated with the multi-line current excitation: position 1 (P1) is at hole center, position 2 (P2) is at the left edge, and position 3 (P3) is directly above a crack near the right edge.

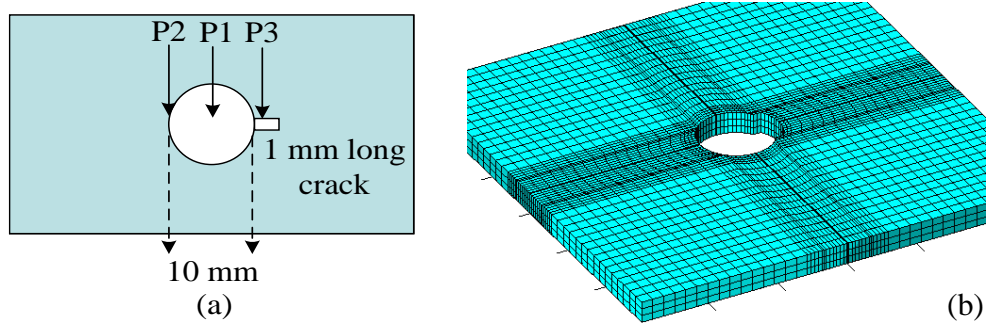


Figure 3.14 A geometry used in the time-domain modeling: (a) Simulation geometry and three scan positions and (b) Geometry FE mesh

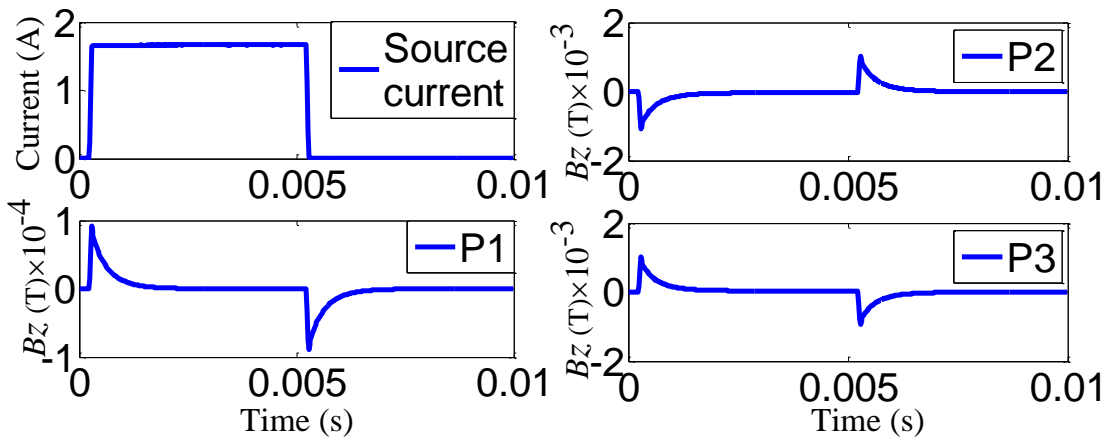


Figure 3.15 The excitation source signal (upper left), and the simulation results of B_z in time-domain modeling at positions P1, P2, and P3

A 100 Hz 50% duty cycle square waveform, with a total duration of 10 ms, is applied as source, shown in Figure 3.15. Solutions to Eq. (3.39) at the three positions in Figure 3.14 are calculated

over 500 time steps ($\Delta t = 2e-5$ s). Transient signals simulated at three positions P1, P2 and P3 are shown in Figure 3.15. A zoomed representation of the three signals is shown in Figure 3.16. These signals are used as a reference for comparison with other implementation of the time domain model.

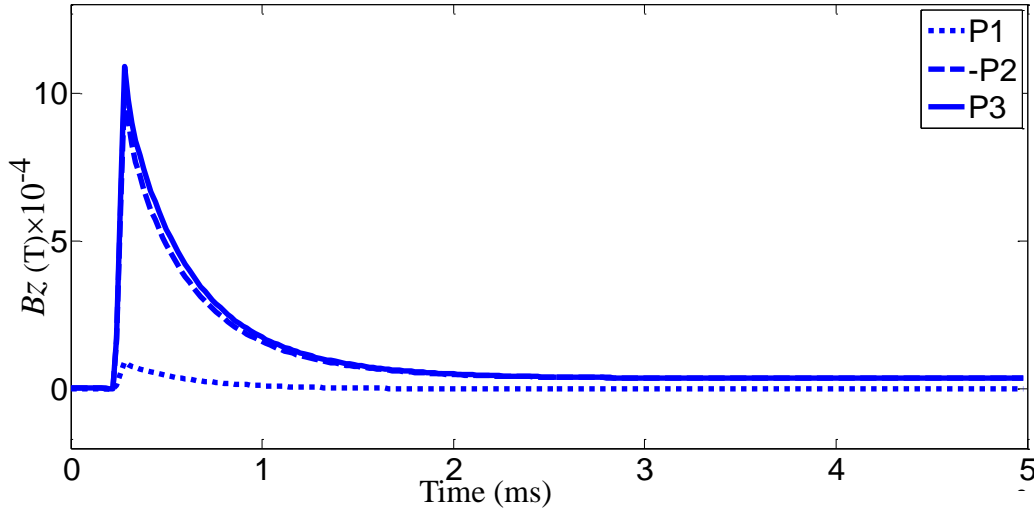


Figure 3.16 The first peak of B_z in the simulation results at positions P1, P2, and P3

The use of a larger sampling time step Δt with linear interpolation is investigated. Two cases, namely, 125 time steps ($\Delta t_1 = 2\Delta t = 4e-5$ s), and 50 time steps ($\Delta t_2 = 5\Delta t = 1e-4$ s) are simulated. These simulation results are interpolated such that $\Delta t = 2e-5$ s. Figure 3.17 shows the results at positions P1, P2, and P3, before and after interpolation. Compared to the reference signals in Figure 3.16, the error in interpolated signals is listed in Table 3-3.

$$\text{error} = \left| \frac{B_{\text{reference}}(f) - B_{\text{interpolation}}(f)}{B_{\text{reference}}(f)} \right| \times 100\% \quad (3.40)$$

The results in Table 3-3 show that a larger time step produces higher simulation error.

Table 3-3 Simulation error analysis of the interpolation modeling in time-domain.

Number of time steps	Position	Relative error to reference signal
125	P1	1.64%
	P2	1.38%
	P3	1.39%
50	P1	7.58%
	P2	6.68%
	P3	6.59%

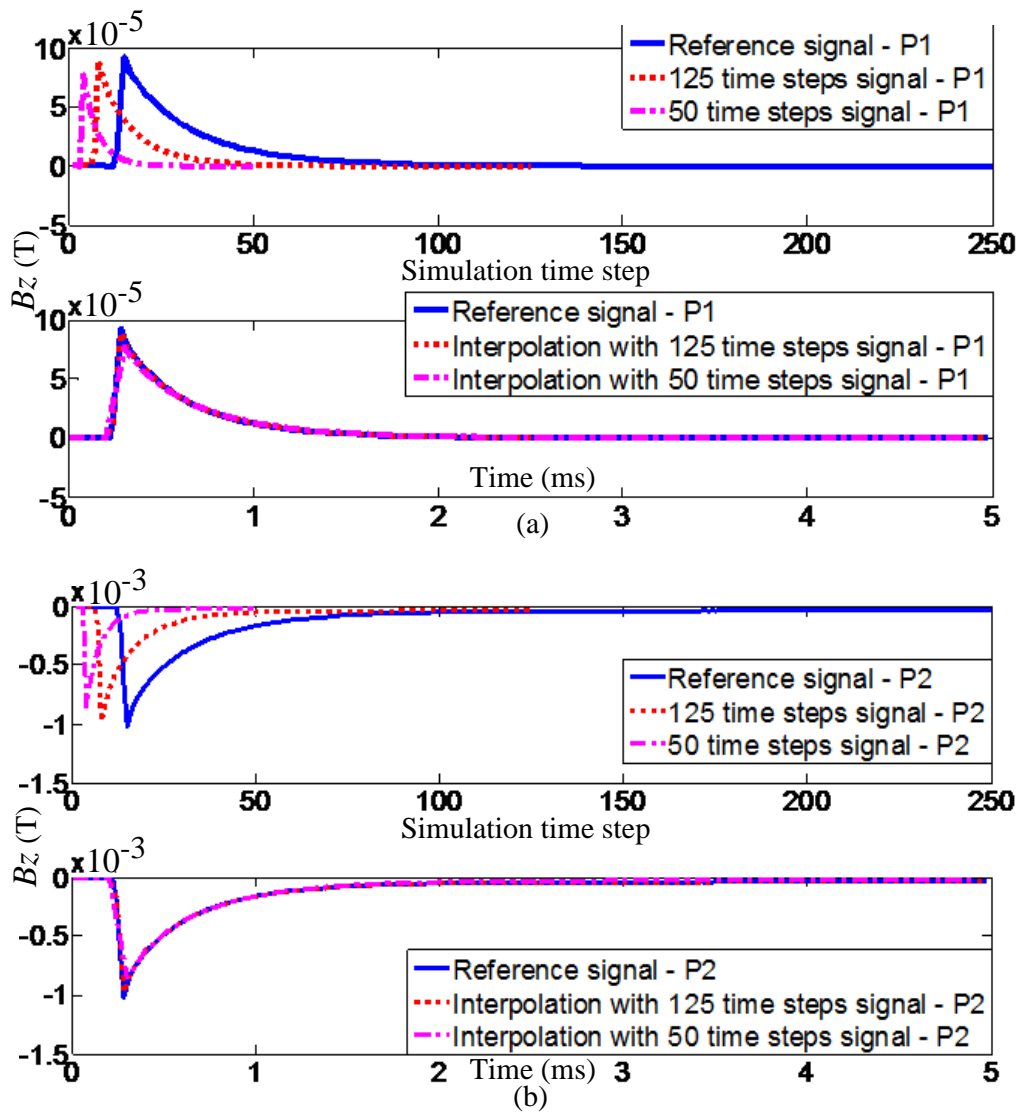
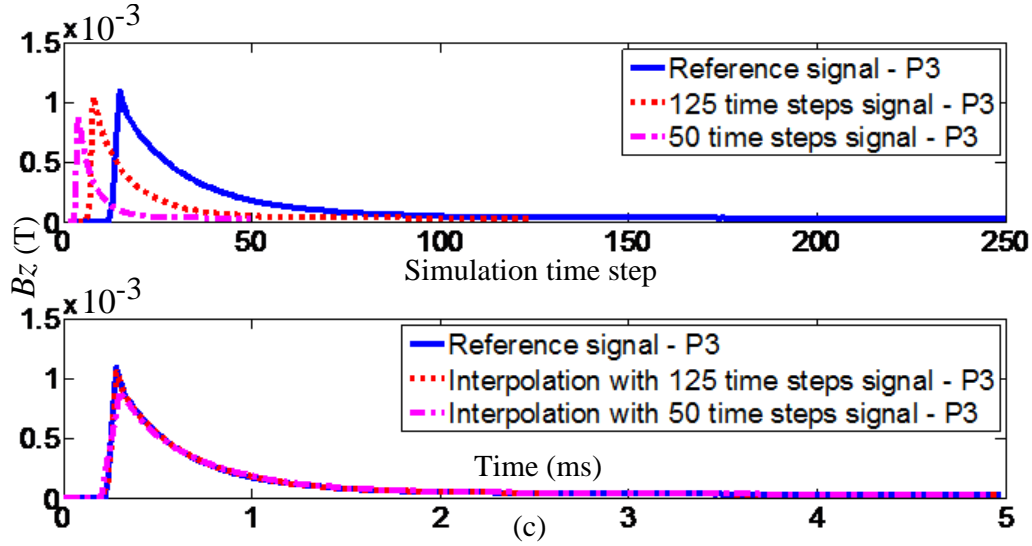


Figure 3.17 Simulation results of B_z using the time-domain interpolation modeling: (a) PEC-GMR signals at P1 (b) PEC-GMR signals at P2 (c) PEC-GMR signals at P3

Figure 3.17 (cont'd).



II. Impulse Response based Time-domain Modeling

A linear and time-invariant (LTI) system can be described by its impulse response [146-147]. In an LTI system, the response due to an arbitrary excitation is a convolution of an impulse response with the arbitrary excitation function [159-160]. Using this approach, results from different excitation signals could be calculated from a single simulation of the impulse response. Additionally, since less number of time steps is required for impulse response based time domain modeling, this strategy uses less computation time compared to conventional methods in time or frequency domain.

The impulse response approach is depicted in Figure 3.18. An impulse $\delta(t-2)$ excitation source is applied to the FE time domain solver:

$$\delta(t-2) = \begin{cases} 0 & t = 1, 3, \dots, t_1 \\ 1 & t = 2 \end{cases} \quad (3.41)$$

where t is the discrete time. The output $f(t)$ is the impulse response obtained due to the excitation

$\delta(t)$, and t_I is the number of time steps used in the simulation.

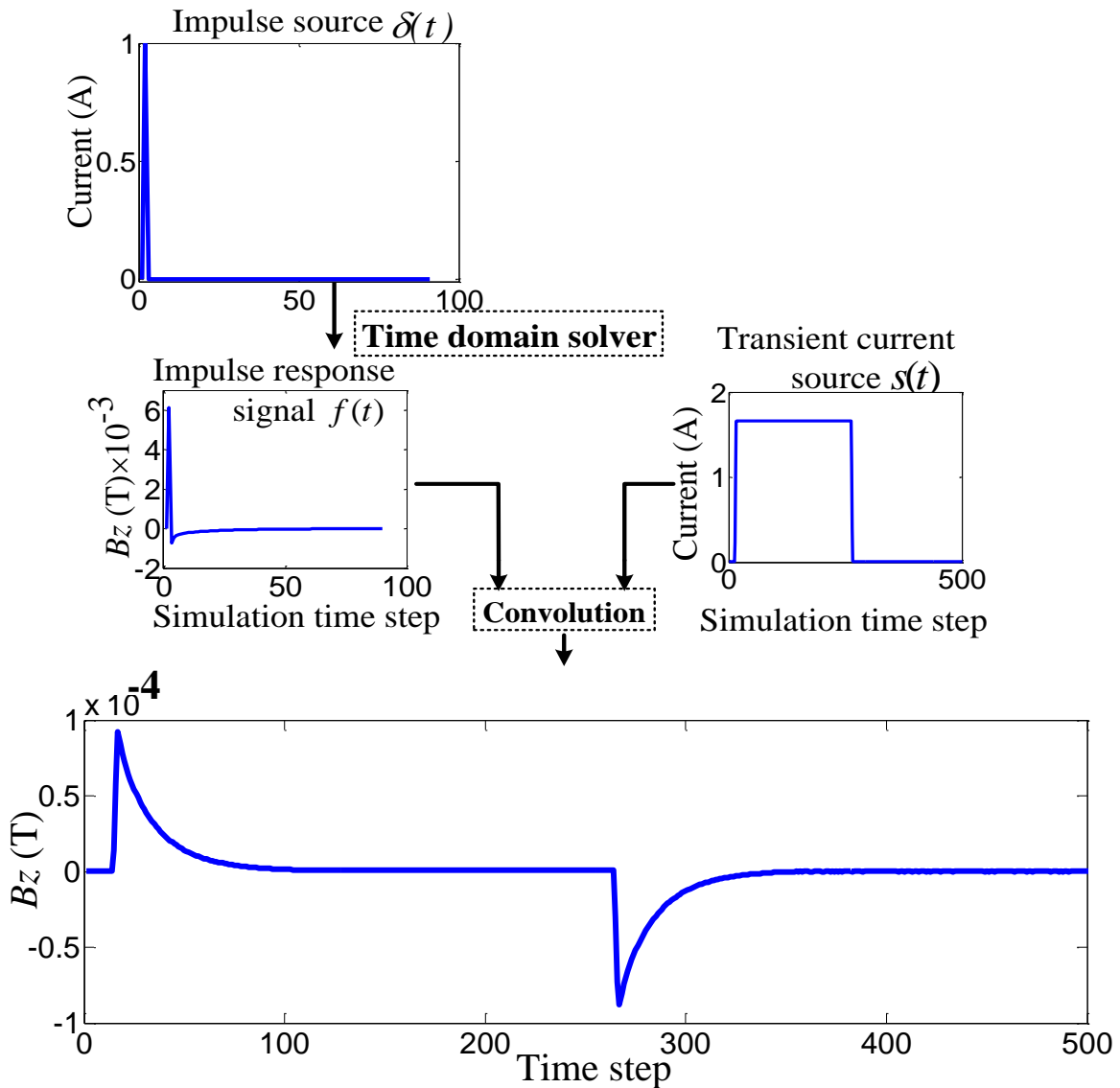


Figure 3.18 The strategy for impulse response based time-domain simulation

A square waveform is given as a current source $s(t)$, which is sampled at Δt_2 time intervals, and with a total of $t_2 = 500$ time steps, the system response $p(t)$ can be computed by convolving $f(t)$ with $s(t)$:

$$\begin{aligned}
p(t) = f(t) * s(t) &= \int_{-\infty}^{\infty} f(t-\tau) s(\tau) d\tau = f(1 \cdots t_1) * s(1 \cdots t_2) \\
&= \sum_j f(j) s(i-j)
\end{aligned} \tag{3.42}$$

where the transient signal $p(t)$ is response due to the pulsed current source $s(t)$. The indices i, j are time steps and the length of $p(t)$ is $t_1 + t_2 - 1$.

This approach is applied for the simulation of pulsed EC-GMR testing. The transient signals at the three positions P1, P2 and P3 are shown in Figure 3.19, and they are compared to the reference signal (250 time steps) in Figure 3.16. The simulation errors relative to different number of time steps are presented in Table 3-4. It is observed that the error in simulated signal depends on the number of time steps used in convolution.

In order to increase the simulation accuracy using less number of simulation time steps, the result obtained with 30 time steps is extended by padding the signal with the last time-step value $f(30)$ as:

$$\begin{aligned}
f'(t) &= [f(1), f(2), \dots, f(30) \underbrace{f(30) f(30) f(30) \cdots f(30)}_{\text{extra 20 time steps}}] \\
p'(t) &= f'(t) * s(t) = [f'(1), f'(2), \dots, f'(50)] * [s(1), s(2), \dots, s(500)]
\end{aligned} \tag{3.43}$$

The simulation error relative to the reference signal in Figure 3.16 is shown in Table 3-5. Using this padding procedure has effectively reduced the simulation error shown in Table 3-4, when only 30 time steps are used.

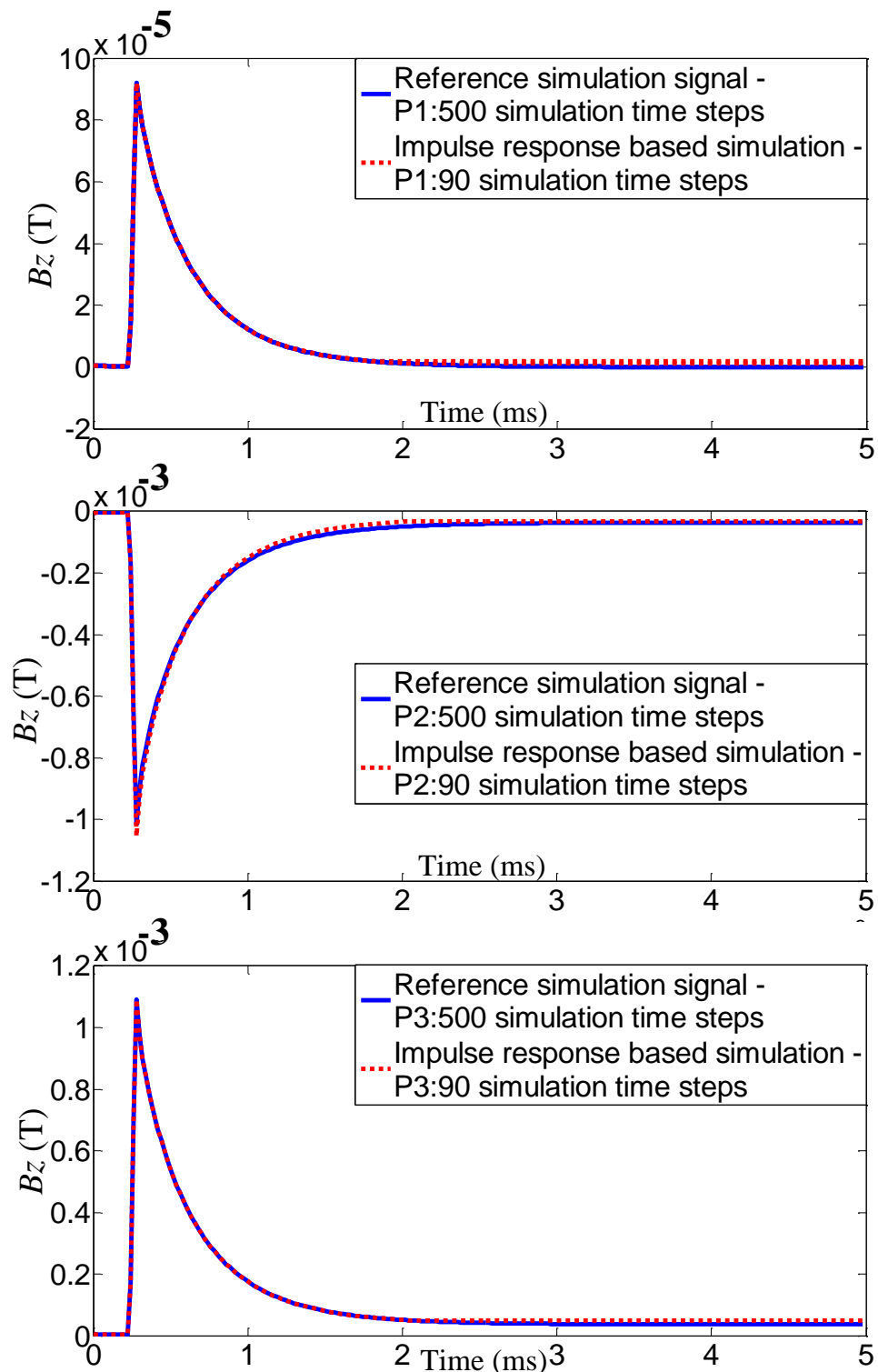


Figure 3.19 Impulse response based simulation results vs. the reference signal for the positions P1, P2, and P3

Table 3-4 Simulation error analysis of the impulse response based modeling.

Impulse response based modeling		Relative error to reference signal
Number of time steps	GMR sensor location	
90	P1	0.04%
	P2	0.58%
	P3	1.01%
70	P1	0.13%
	P2	1.69%
	P3	2.26%
50	P1	0.75%
	P2	5.16%
	P3	6.07%
30	P1	5.22%
	P2	17.80%
	P3	19.73%
25	P1	8.69%
	P2	25.09%
	P3	27.55%

Table 3-5 Simulation signal accuracy enhancement.

GMR sensor location	Relative error to reference signal
P1	1.79%
P2	2.81%
P3	2.61%

3.5.3 Modeling in Frequency-domain vs. Time-domain

The simulation of PEC testing is also evaluated using a frequency domain model presented in [137]. For position P1 in the geometry of Figure 3.14, the predicted transient response is shown in Figure 3.20 using 250 harmonic components ranging from 100 Hz to 25,000 Hz in 100 Hz step. Simulation accuracy is decided by the total number of frequency components representing

the spectrum of excitation pulse in Figure 3.15. The simulation results have an error of 2.37% relative to the reference signal in Figure 3.16.

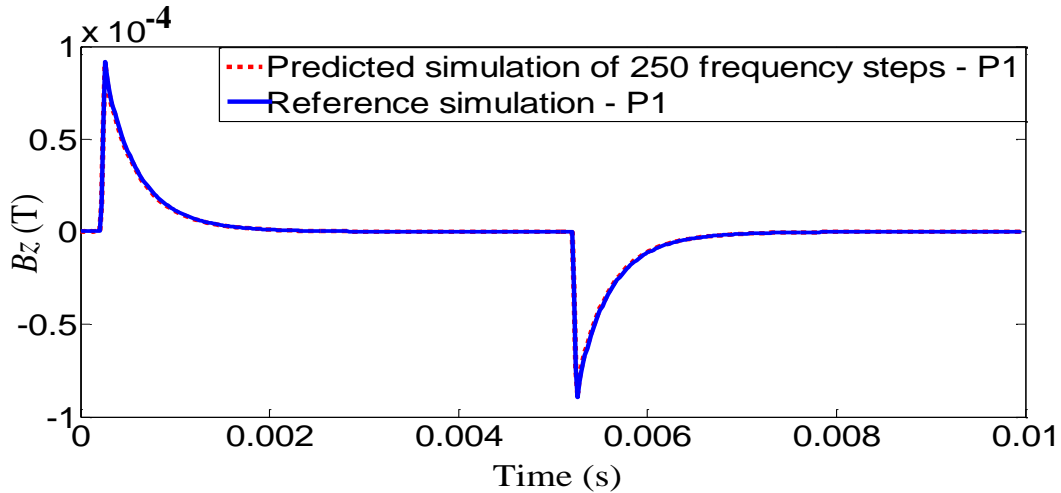


Figure 3.20 Simulations of PEC signals using FE solver in frequency-domain: Predicted transient signal of 250 frequency steps vs. the reference signal simulated in time-domain

In order to reduce computation time, results were predicted with less number of harmonics and interpolation was used to compensate for the missing harmonics. Simulation results of the transient response using interpolation with only 100 and 50 uniformly spaced harmonic components from 100Hz to 25000Hz are predicted in Figure 3.21. The accuracy deteriorates when less harmonics are used in the modeling. The error is 0.44% for 100 harmonic components and 5.93% for 50 harmonic components. In contrast, the proposed approach provides a more accurate solution using 30 simulations in time domain.

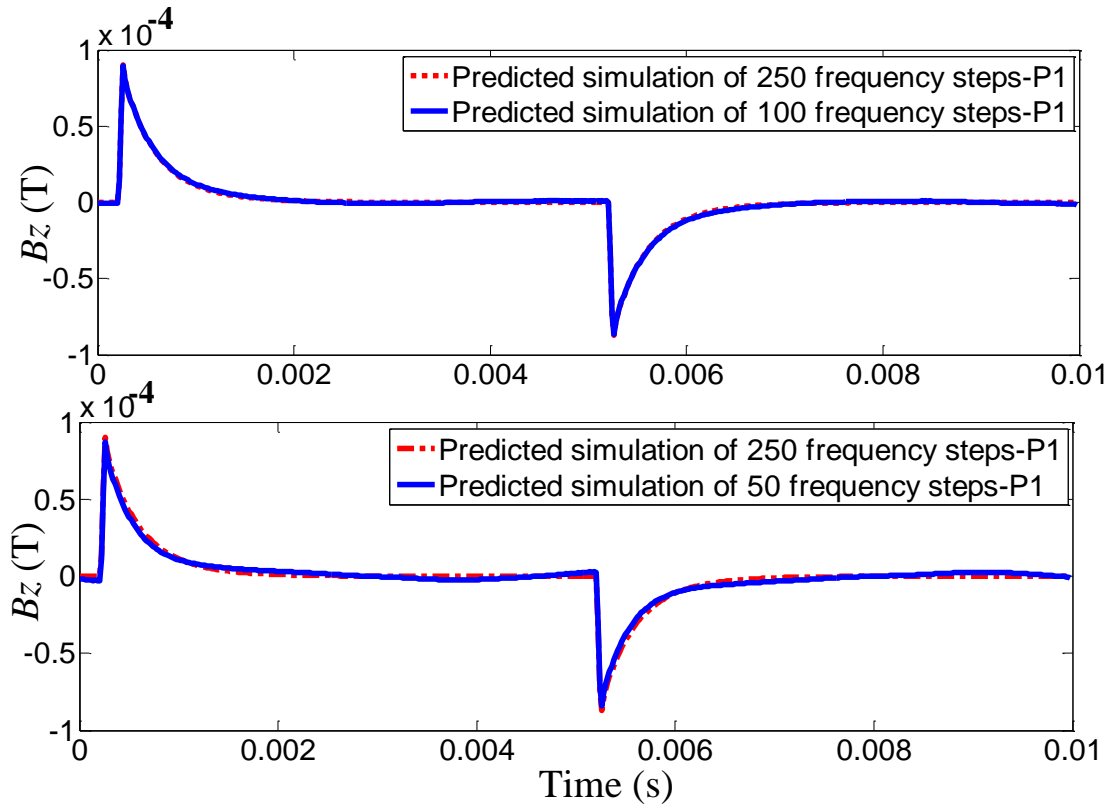


Figure 3.21 Simulations of PEC signals: predicted transient signal of 250 frequency steps vs. predicted transient signals with interpolation of 100 and 50 frequency steps

Additionally, the simulation in time domain uses a fixed computation time at each time step, while the computation time increases with higher harmonic components used in frequency domain simulation method as seen in Table 3-6. Therefore, the presented FE model based on the convolution with the impulse response is superior in speed and accuracy relative to the frequency domain model in [137].

Table 3-6 Computation time comparison.

FE model	Solve domain	Simulation steps	Computation time (each step)	Relative error	Node
Proposed method	Time domain	30	4 mins	1.79%	12996
Reference method	Frequency domain	50	4 mins:20 mins	5%	0

3.5.4 Time-domain Model Validation

The time-domain modeling strategy described in this section is validated using experimental PEC-GMR measurements of the specimen shown in Figure 3.14. The validation of the signals at three probe positions corresponding to P1, P2, and P3 is presented in Figure 3.22.

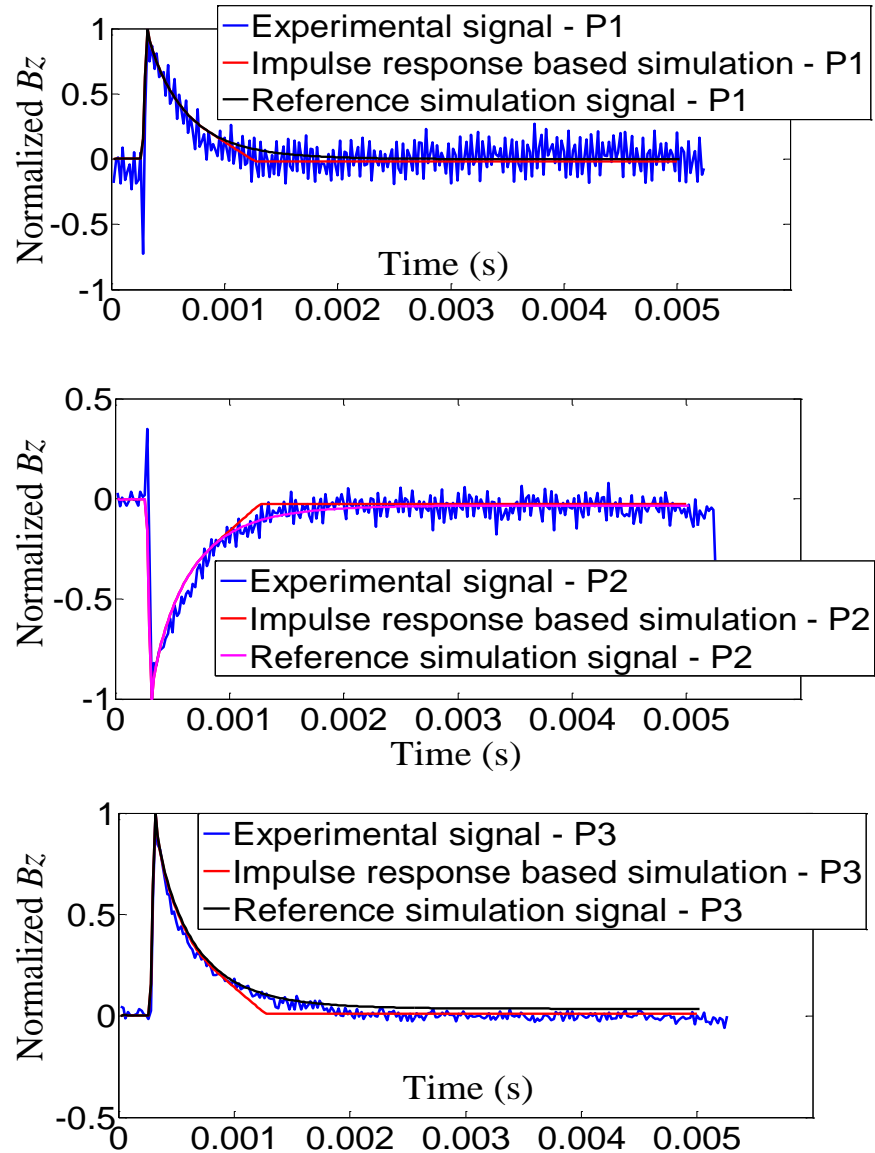


Figure 3.22 Model validation: Simulation signals of 250 time steps and signals of the impulse response based modeling (30 time steps) vs. experimental signals

The proposed FE model is then applied to multilayer riveted structure inspection. A three-layer aluminum plates with a 5 mm crack in the 3rd layer around the aluminum fastener is modeled. The three dimensional geometry is meshed using hexahedral elements with 8 nodes. A narrow air gap is introduced around the fastener structure and also in between plate layers. The cross-sectional geometry of the model is shown in Figure 3.23. The simulation of PEC-GMR measurements at three positions displayed in Figure 3.24 is performed. The B_z component signals are studied using the impulse response based time-domain modeling. The experimental PEC-GMR measurements of the B_z component are presented for comparison.

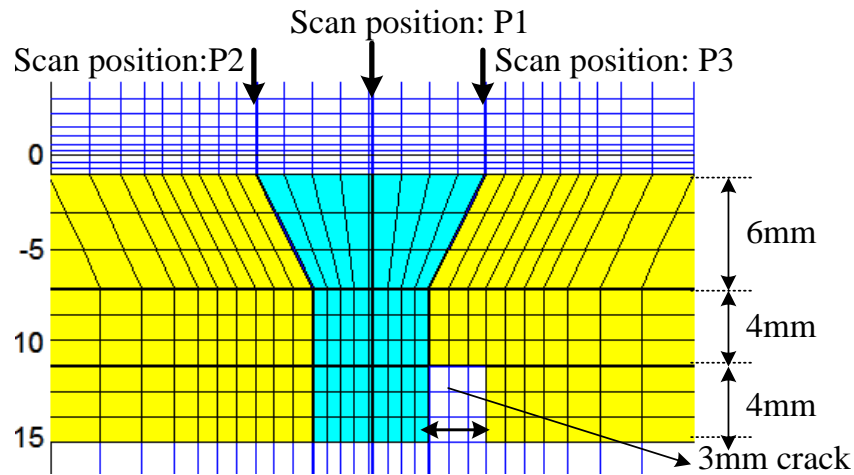


Figure 3.23 Modeling geometry of a three layer riveted plate with a 3rd layer crack at aluminum fastener site

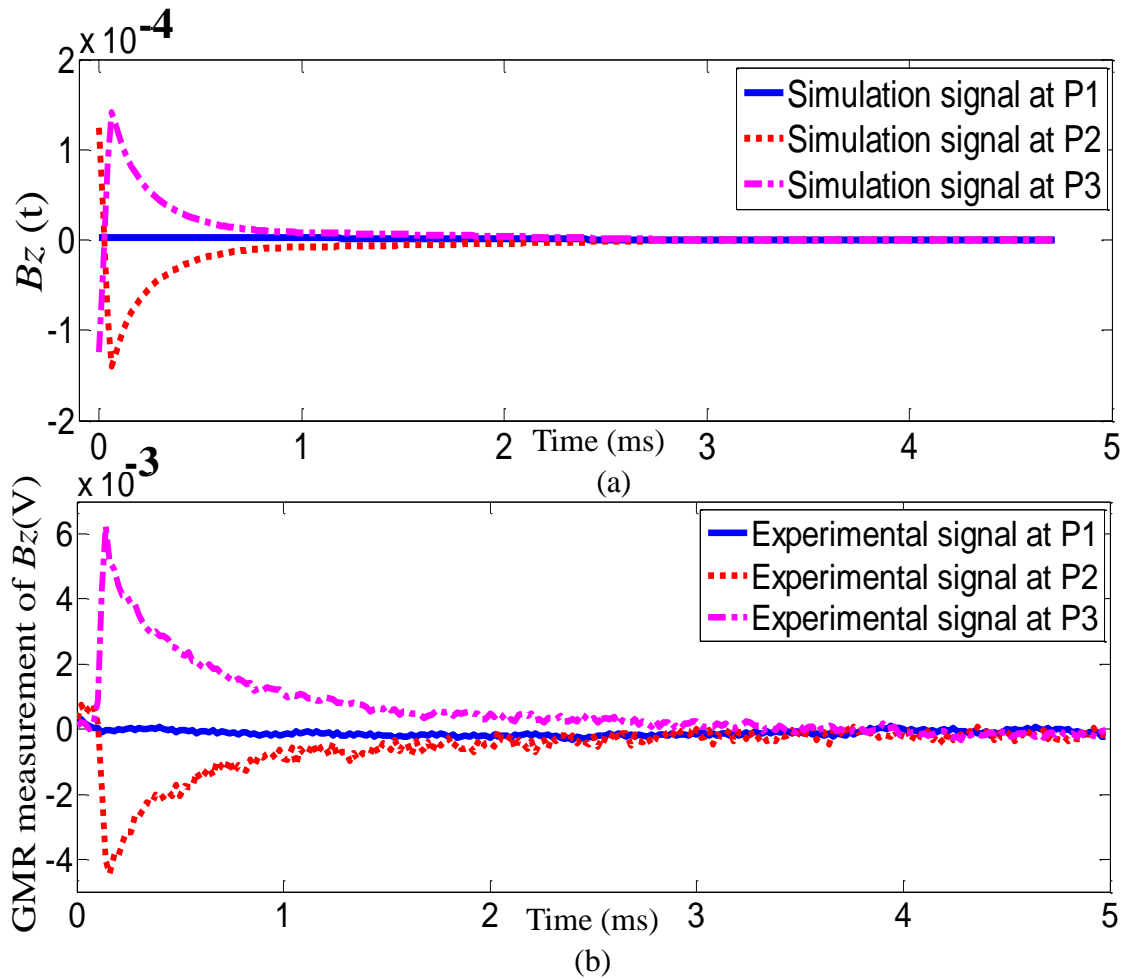


Figure 3.24 PEC-GMR signals at three scan positions: (a) Simulation signals and (b) Experimental signals

3.6 MR Measurements of 3-component Transient Fields

In order to resolve the challenges of detecting cracks under steel fasteners, measurement of all 3-components of the magnetic field (normal component- B_z , tangential components- B_x, B_y) using MR sensors is proposed. The model-based study in [161] reports the enhanced detection of defective steel fastener using the additional information in the tangential components in low frequency EC-GMR inspection.

3.6.1 Ferrous Fastener Inspection

Due to ferromagnetism, ferrous fasteners become the areas of flux concentration, even for a relatively low applied field intensity [7, 21]. Consequently, the response due to ferrous fastener can mask small defect indications as seen in the distributions of the magnetic flux density for aluminum and steel fasteners in Figure 3.25 (a-b).

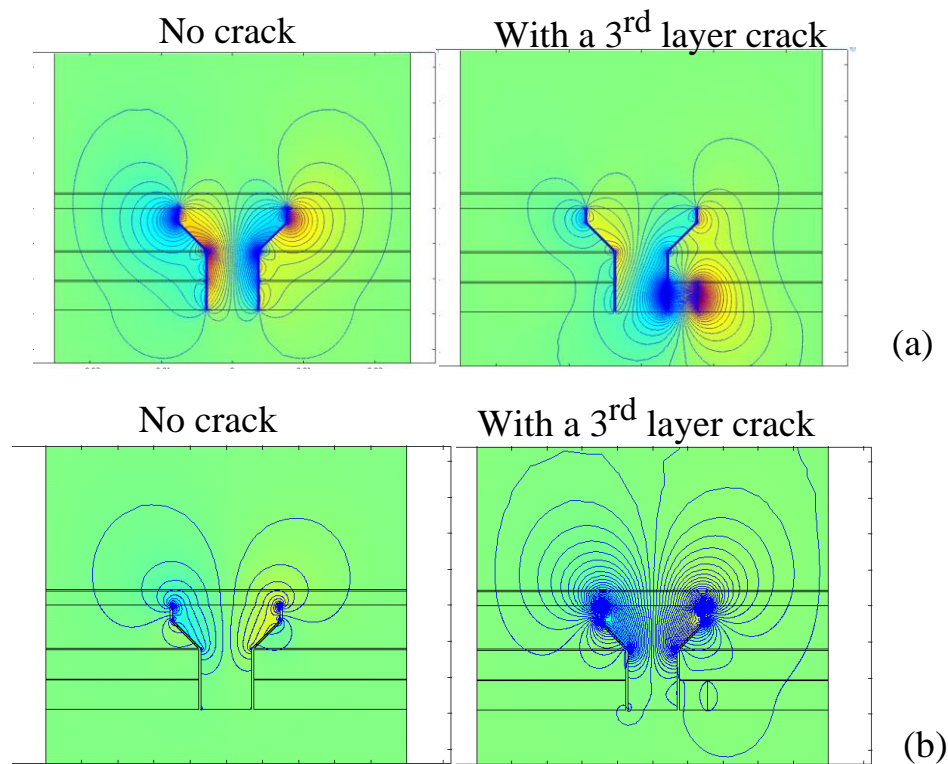
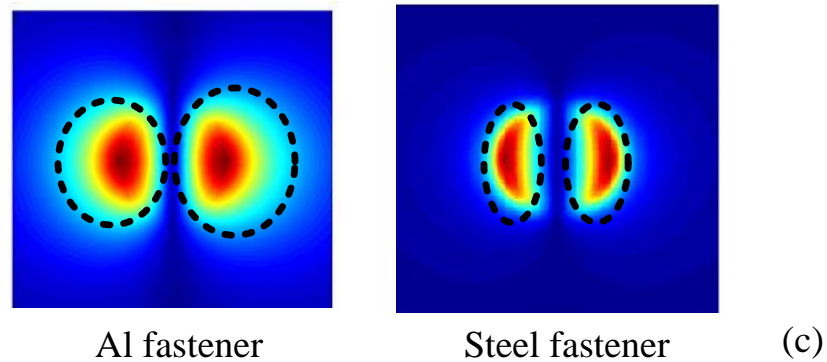


Figure 3.25 Numerical results illustrating the challenge of ferrous fastener inspection when measuring the normal magnetic field component (B_z): (a) Induced field at an aluminum fastener without crack (left image) and with crack (right image) (b) Induced field at a steel fastener without crack (left image) and with crack (right image) (c) C-scan image in the presence of a subsurface 8mm notch a at aluminum fastener site (left image), and at steel fastener site (right image)

Figure 3.25 (cont'd).



The C-scan images of normal component data also demonstrate the difficulty in detecting a subsurface crack around steel fastener hole (Figure 3.25 (c)). That the C-scan image of a defective aluminum fastener demonstrates an observable asymmetry in the left and right lobes, however, this asymmetry is not easily detected in a defective steel fastener.

Little study is done for ferrous fastener examination using transient EC methods. The study in [21] is limited to relatively large crack sizes (8mm, under surface up to 6mm), and one-dimensional transient signal analysis. The reliable detection of cracks under steel fasteners in layered structures is studied in this dissertation using GMR measurements of the three components of magnetic field.

3.6.2 Simulation Study of 3-component Measurements

The FE model developed in the time domain is employed to study the 3-component measurements in a layered geometry with a steel fastener. Using the impulse response based scheme, the formulation in Eq. (3.39) is solved in the time domain. The three components of the magnetic flux density are calculated from the solution vector as:

$$B_z = dA_y / dx - dA_x / dy \quad (3.44)$$

$$B_x = dA_z / dy - dA_y / dz \quad (3.45)$$

$$B_y = dA_x / dz - dA_z / dx \quad (3.46)$$

The mesh for the FE model, and the geometrical dimensions of sample and crack are shown in Figure 3.26. The sensing position is shown to be at the right edge of the fastener head. The measured B_z , B_y , and B_x components for the defect and no defect cases are shown in Figure 3.27 (a), (b), and (c) respectively. Figure 3.27 (d) shows the 3-components after baseline subtraction. It can be seen that the B_x components give a large difference compared with B_z . In this study, the FE model is used as a tool to generate signals for a variety of defective rivet geometries.

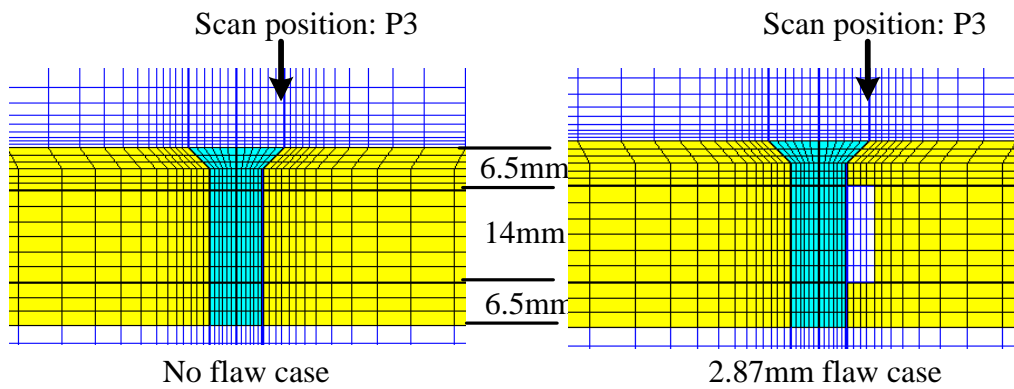


Figure 3.26 Simulation for steel fastener structures-Test sample: no crack vs. with 2.87mm notch

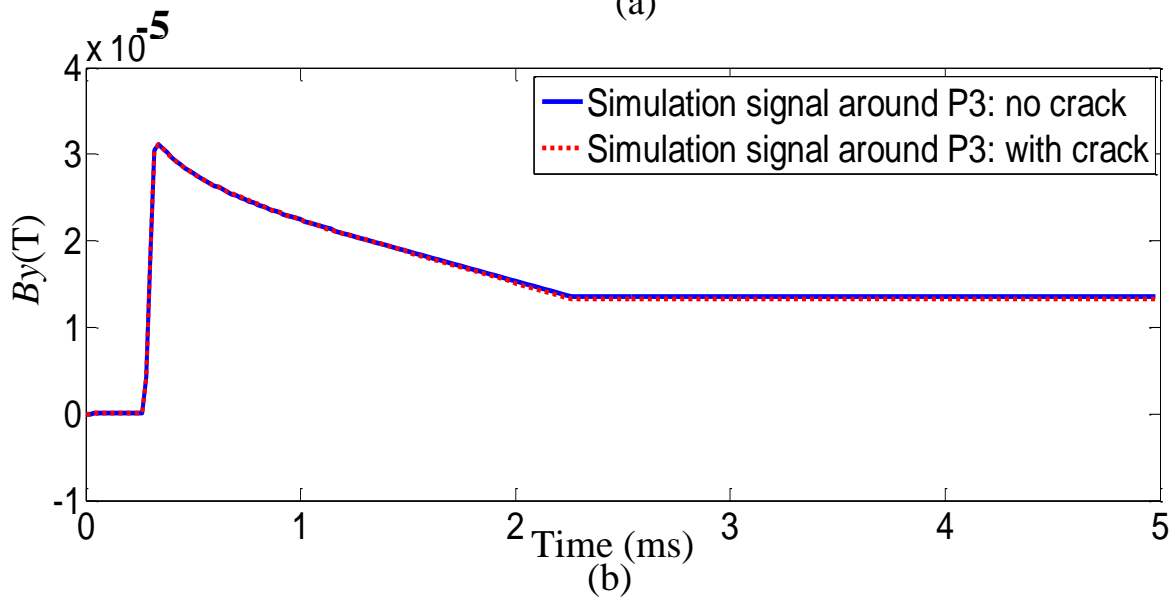
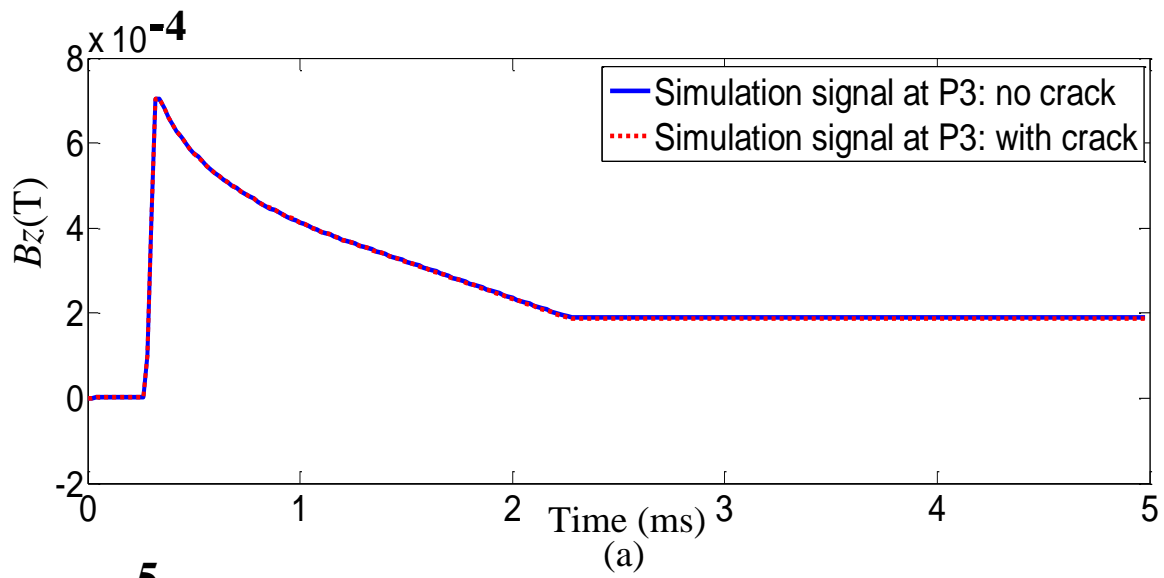
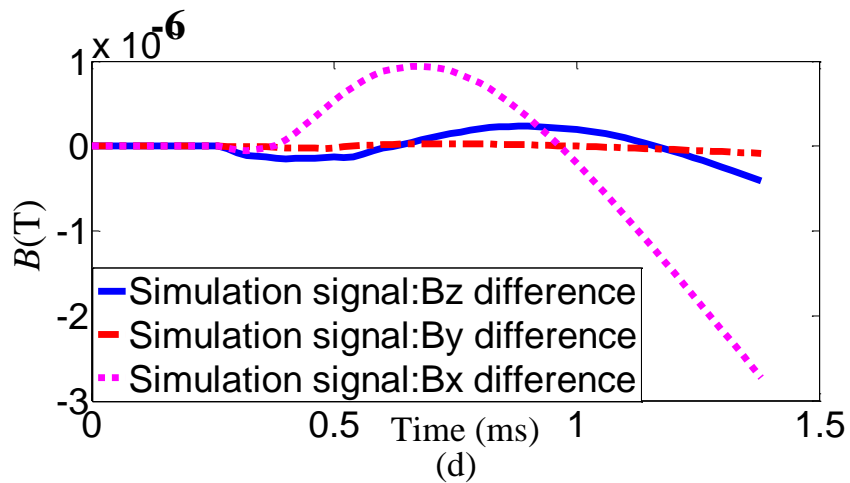
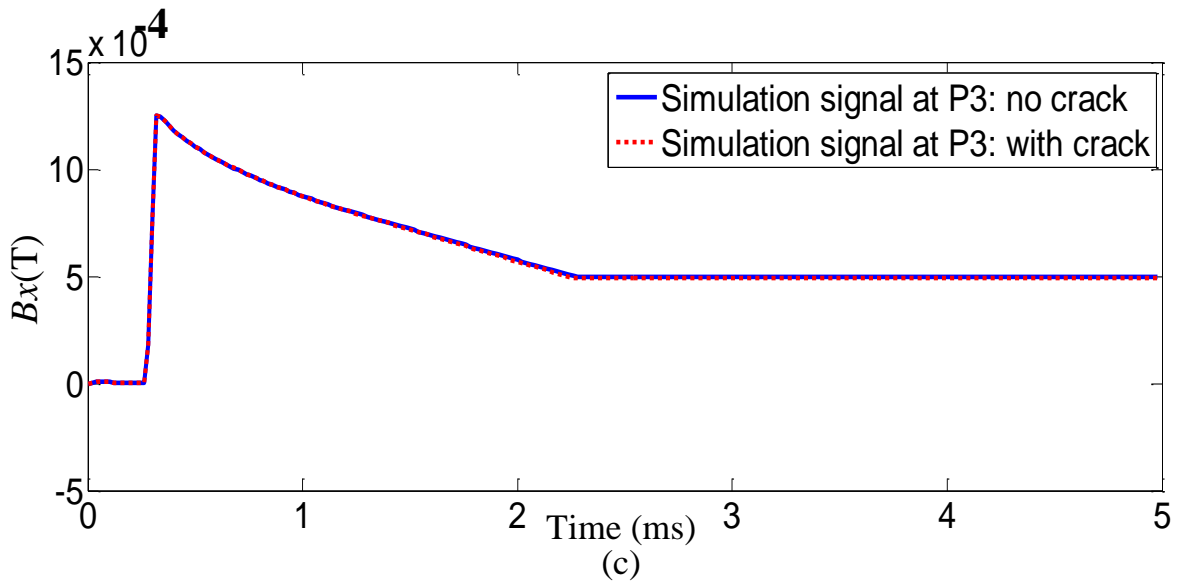


Figure 3.27 Simulation of 3-component measurements for steel fastener structures: (a)-(c) Simulation signals of B_z , B_y , B_x components respectively (d) Subtraction of the no flaw measurements from the 2.87 mm flaw measurements for each component

Figure 3.27 (cont'd).



3.6.3 Experimental Study of 3-component Measurements

The GMR sensor, as presented in Figure 3.28, placed at the center can be oriented to be sensitive to a selected component of the magnetic field. The experimental measurement of the three components in the case of a steel fastener with a subsurface 2.87 mm notch through the 2nd layer is conducted. Two types of NVE GMR sensors (AAH002 for the normal component and AA002 for the tangential components) are used with different linear response ranges.

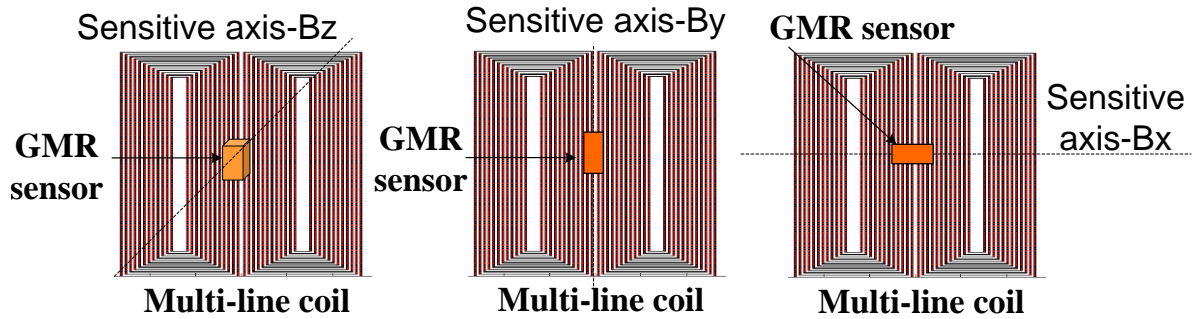


Figure 3.28 GMR sensing 3-component of the magnetic field

The C-scan images of these inspection data are shown in Figure 3.29. The application of PEC inspection of laboratory samples with 3D GMR measurements, and features from the C-scan images of 3-component data and signal processing algorithms for automatic crack detection will be implemented in Chapter 4.

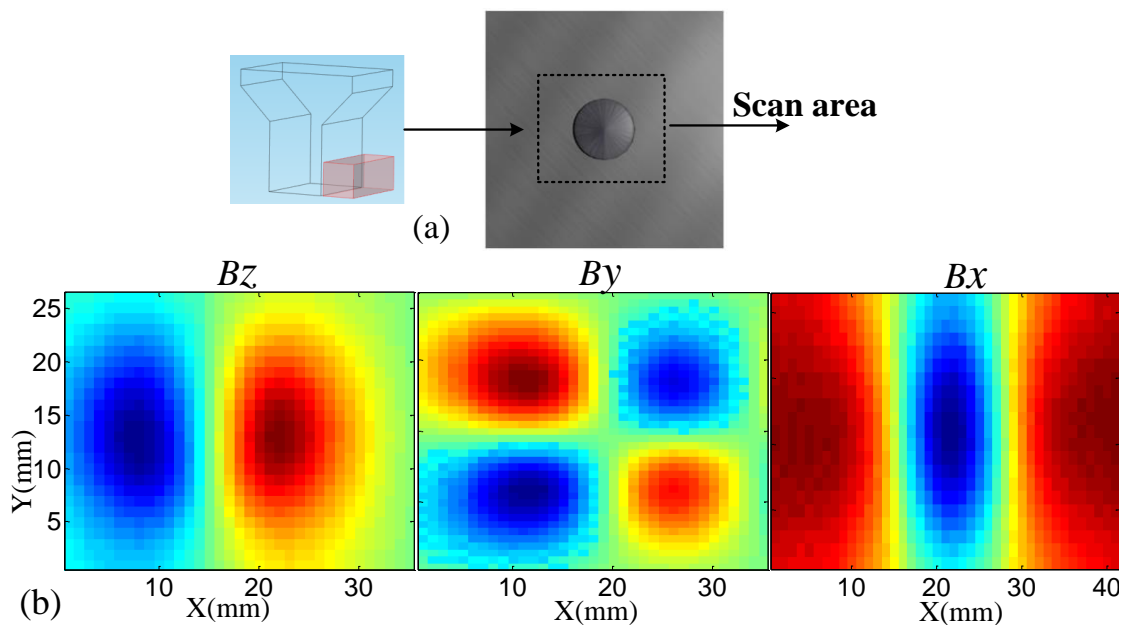
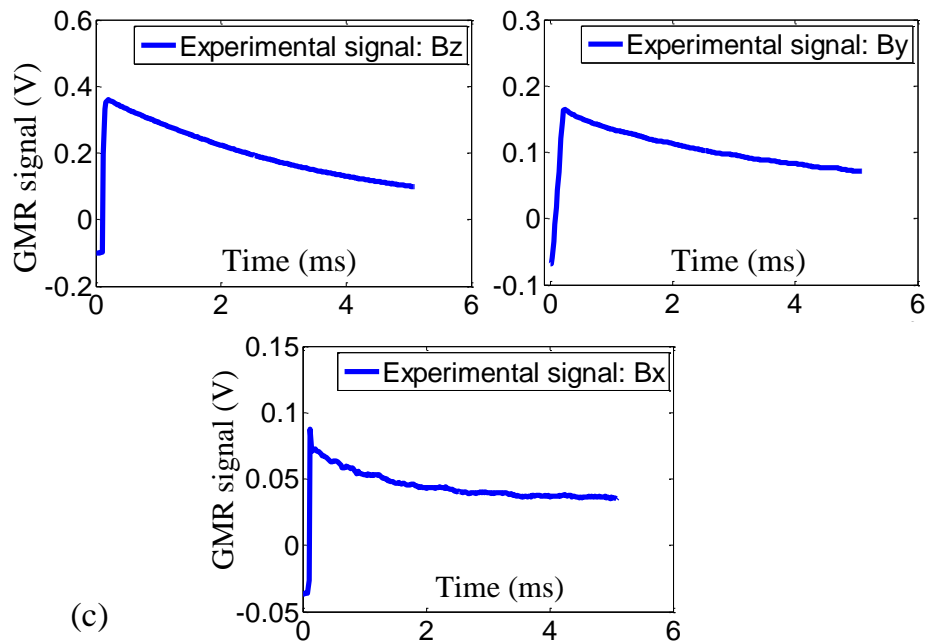


Figure 3.29 PEC-GMR measurement of a steel fastener with a 2.87 mm notch using three components: (a) Test geometry (b) C-scan images of B_z , B_y , B_x (c) Transient A-scan signals of B_z ,

B_y , B_x

Figure 3.29 (cont'd).



3.7 Summary

This chapter presents the development of an EC-GMR inspection system, which uses a pulsed excitation applied to a planar multi-line coil to generate a transient field that is detected using GMR sensor. The transient skin depth of electromagnetic field associated with the diffusing fields is shown to be greater than that associated with steady state case. A novel simulation strategy is developed to model the PEC system in the time domain and validated by experimental results. The scheme that measures 3-component of transient fields is numerically and experimentally demonstrated as a feasible approach for the inspection of ferromagnetic fasteners.

CHAPTER 4 ANALYSIS OF PEC-GMR INSPECTION DATA

4.1 Introduction

This chapter describes methods for the analysis of PEC-GMR data obtained from the inspection of multilayer riveted structures. C-scan image data of GMR response is collected experimentally. A strategy using principal component analysis (PCA) method is adopted to process the C-scan image for crack detection near fastener sites. Initial results show feasibility for detecting the embedded cracks at steel fastener sites using 3D GMR measurements.

4.2 Review of Signal Enhancement for PEC Inspection

Signal transformation methods have been studied to represent transient signals in different domains, such as frequency domain, time-frequency domain, and wavelet transform [162-167]. Another study found in [168] used a Fisher discriminative model for defect classification in PEC testing.

Although Safizadeh [165] studied the time-frequency distribution of PEC signals for the removal of interlayer gap and lift-off noise, the analysis of A-scan signals is not reliable to detect embedded cracks in riveted or layered structures [18, 23].

Signal processing using PCA and independent component analysis (ICA) techniques were introduced as strategies for new feature extraction in [98, 163, 169-171]. The time series constituting transient signals were reduced to single points in principal component space for defect detection [171]. The detection schemes need training data and a training model to classify the data.

4.3 Multilayer Riveted Specimen

Three laboratory specimens consisting of multilayer aluminum plates with aluminum or steel fasteners are used in this work. Sample 1 is a three-layer aluminum plate (aluminum alloy 3003 and 1145) with mushroom-head aluminum fasteners drilled through the plates. The layer thicknesses are: 6 mm (top layer), 4 mm (middle layer) and 4 mm (bottom layer). The fasteners are of diameter 6 mm at the top and tapering to 3 mm diameter at the bottom layer. Cracks of various radial dimensions located at fastener sites in the 2nd layer (Row 1) and the 3rd layer (Row 2) of the sample are machined. A schematic of Sample 1 is shown in Figure 4.1.

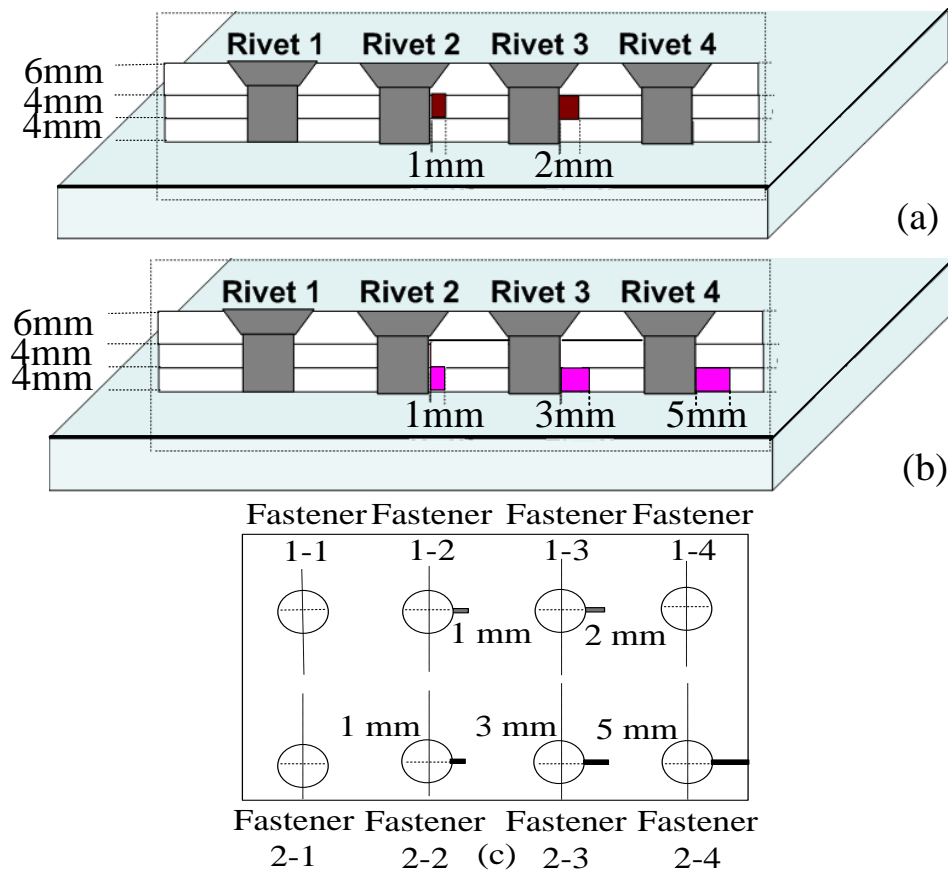


Figure 4.1 Schematic of Sample 1: three layers aluminum plate with aluminum fasteners and cracks in second and third layers (a) Side view of cracks in the second layer (b) Side view of cracks in the third layer (c) Top view of Sample 1

Sample 2 is a layered aluminum (aluminum 7075-T6) plate containing steel fasteners. This sample consists of a three layer aircraft skin structure. The thicknesses of the three layers are: 6.5 mm (top layer), 14 mm (middle layer) and 6.5 mm (bottom layer). The steel fasteners are of 14.5 mm top diameter and 7.9 mm bottom diameter. Through-wall notches in the 2nd layer with different radial lengths are machined at Rows 2 and 4. Corner notches of four sizes are installed in Rows 1 and 3. Sample 2 is illustrated in Figure 4.2.

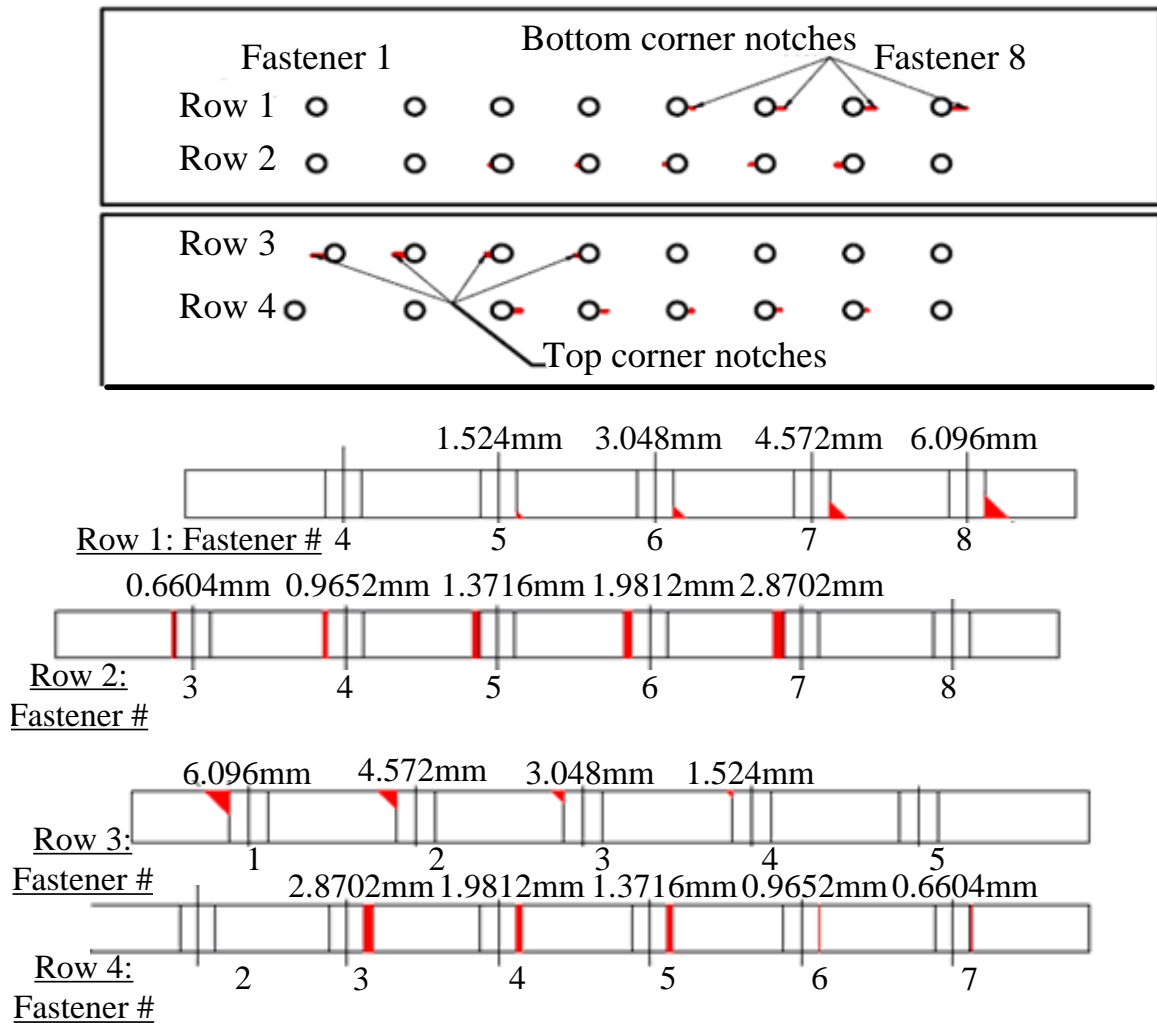


Figure 4.2 Schematic of Sample 2: top view of a three layers aluminum plate with four rows of steel fasteners, and cracks dimensions in the second layer at each fastener site in every row

Sample 3 is a two-layer aluminum sample (aluminum alloy 3003 and 1145) with small cracks in the bottom layer around the fasteners. The layer thicknesses are 4 mm (top layer) and 2 mm (bottom layer) with drilled aluminum fastener of 6mm top diameter, 5mm bottom diameter in the first row, and 3mm bottom diameter in the second row. The machined cracks are less than 1mm long, as shown in Figure 4.3. Fastener 1-2 contains a radial crack of length 0.2 mm, and fastener 2-3 has a 0.5mm crack. Fastener 1-3 has two radial cracks of lengths 0.8 mm and 0.7 mm extending at diametrically opposite sides.

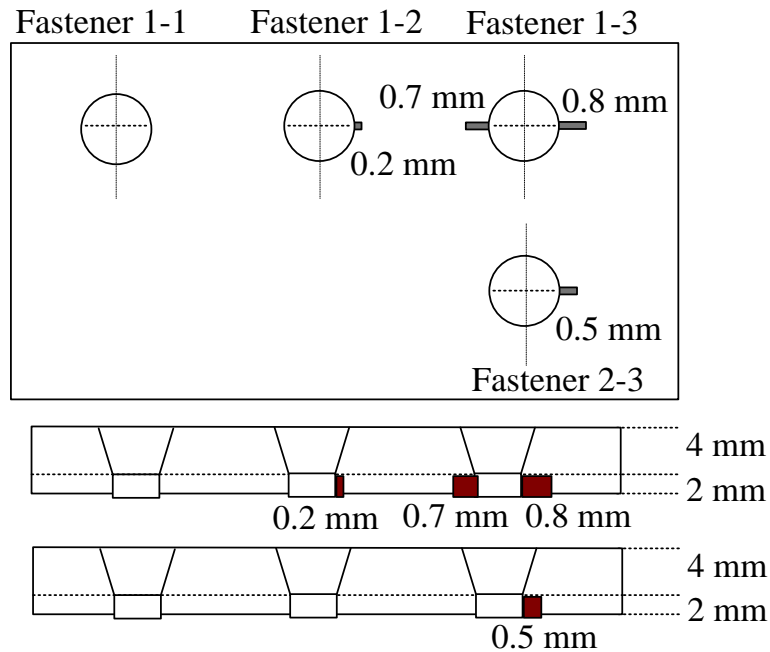


Figure 4.3 Schematic of sample 3: two layers aluminum sample with aluminum fasteners and cracks in the bottom layer

The three samples are inspected using the PEC-GMR system, and the measured A-scan signals are used to generate C-scan images using the maximum value of transient signals. The three components of magnetic fields associated with induced eddy currents are measured for the inspection of steel riveted structures.

4.4 Automatic Analysis of PEC-GMR C-scan Images

Image based data analysis is more reliable than the treatment of individual A-scan and line scan measurements. In this chapter, a strategy exploiting underlying statistical characteristics of C-scan image data is developed for automatic crack detection in the presence of fastener signals. Automatic damage detection using PEC-GMR measurements is performed using unsupervised classification.

4.4.1 Principal Component Analysis

Principal component analysis is an eigenvector-based multivariate analysis tool for analyzing and structuring data sets. It is applied to the image data of PEC-GMR measurements for reducing the dimensionality of measured data. This allows easier interpretation of the data in a lower dimensional space [172-173]. The PCA analysis is also known as the Karhunen Loeve (KL) transform or the Hotelling transform. The PCA technique is known for its ability to generate independent features. This data transformation is particularly useful for classification and compression [162, 174]. In the case of multi-frequency EC signal analysis, the PCA method has been used as a source separation algorithm [175-176].

In PCA processing, the procedure seeks to retain the maximum variance in the processed data. PCA method decorrelates the data sets to find the orthogonal principal components (PCs), and maps the original data onto the PCs subspace using a linear transformation. This is done by finding the eigenvectors of the covariance matrix of input data [172-173].

Let measured signals be represented by $X = [x_1, x_2, \dots, x_n]^T$, the mean of the signals is:

$$\mu = E[X] \quad (4.1)$$

where n is the number of sampled signals, $E[.]$ is the expected value. The covariance of the data X is calculated as matrix C :

$$C = E(X - \mu)(X - \mu)^T \quad (4.2)$$

The algorithm performs a singular value decomposition of matrix C , and computes eigenvectors as the rows of matrix V that diagonalizes the covariance matrix:

$$V^{-1}CV = D \quad (4.3)$$

where D is the diagonal matrix.

The matrix decomposition defines the k^{th} principal component (PC) of X as the normalized eigenvector v_k corresponding to the eigenvalue λ^k of matrix C_x , which is obtained by solving:

$$C_x v_k = \lambda_k v_k \quad (4.4)$$

where $k = 1, 2, \dots, n$. This is equivalent to finding the solutions of the characteristic equation:

$$|C_x - \lambda I| = 0, \quad v_k = \lambda_k v_k \quad (4.5)$$

where I is the unity matrix.

PCA method finds the directions that decorrelate the input data. Principal components are formed by projecting the data on the eigenvectors which are arranged according to descending eigenvalues. The first eigenvector has the direction of the largest variance of X and it determines the direction with the most significant amount of energy.

4.4.2 Flaw Detection

The PCA method is applied for the automatic flaw analysis of PEC-GMR measurements. A $n \times m$ C-scan image is obtained at each fastener site, and the image data of all fasteners machined in a row of a sample are used in PCA. As demonstrated in Figure 4.4, the C-scan images of the 7 fasteners from row 1 of sample 2 are formed. The image data D are formed by 287 points (pixels) in each row, and with a total of 40 line scan, resulting in 40 pixels in each column. The zero-mean data of D is represented by a matrix M with a size of 40×287 . Each 40×41 data set in matrix M represents the measurements from a single fastener.

The eigenvector decomposition is performed on the covariance matrix C of M and the eigenvectors are calculated as the vectors V_i in matrix $V = \{V_1, V_2, \dots, V_{40}\}$. A new representation of data M is implemented by the linear projection into a lower dimensional space:

$$S = V^T M \quad (4.6)$$

where the vector S is in PCs coordinates. Each row of S is the component

$$PC_k = V_k^T M, k = 1, \dots, 40.$$

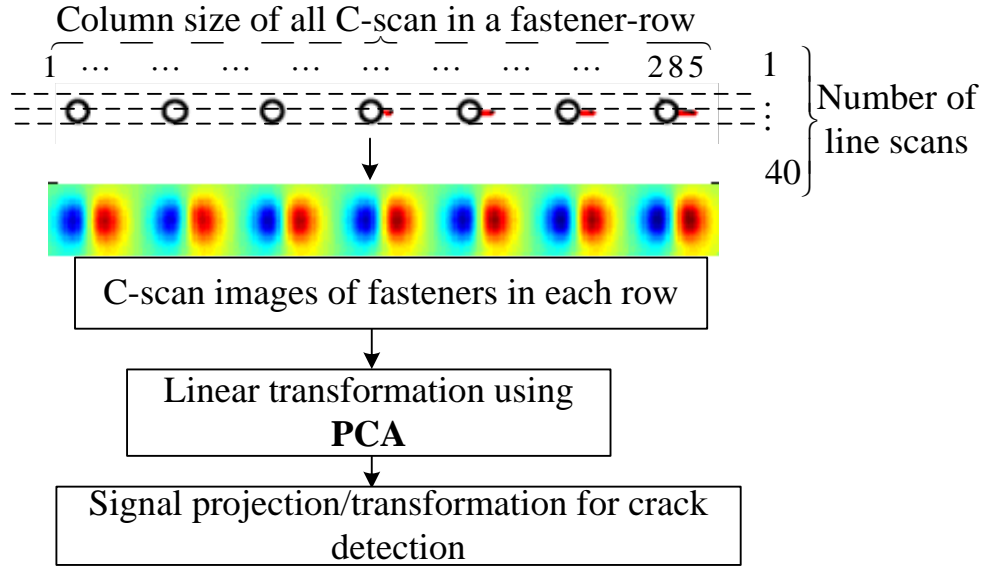


Figure 4.4 Flaw detection using the image analysis

From a geometrical standpoint, the PCA procedure rotates the coordinate system so that the axes follow the directions of the largest variances of the analyzed data in the new space. These axes are referred to as principal axes [174]. In general, the dimensionality of the PCs subspace is selected to retain at least 90% of the energy in original data. The energy in 3 PCs is calculated as:

$$\alpha = \sum_{i=1:3} \lambda_i / \sum_{i=1:k} \lambda_i \quad (4.7)$$

The first three PCs: PC1 to PC3 are found to carry $\alpha = 95\%$ energy of input data presented in Figure 4.4. Therefore, the first three PCs with $k = 3$ are used in this chapter for the image data processing and analysis.

The C-scan data of two fasteners without cracks and one defective fastener are processed following the procedure demonstrated in Figure 4.4. As shown in Figure 4.5 (a), the first two PCs (PC1 and PC2) are plotted for each pixel row in the C-scan image (this corresponds to column size of the image). Since the fastener information is the dominant energy in the input data, the plot of PC1 that is relative to the largest eigenvalue represents the fastener signals.

The plot of PC2 that is calculated by the smaller eigenvalue represents the residual energy, and indicates the signal variation relative to defect response. In Figure 4.5 (b), the components PC1 vs. PC2 are represented by a phase-magnitude polar plot. It is observed that the data due to fasteners and cracks correspond to different regions in the plot.

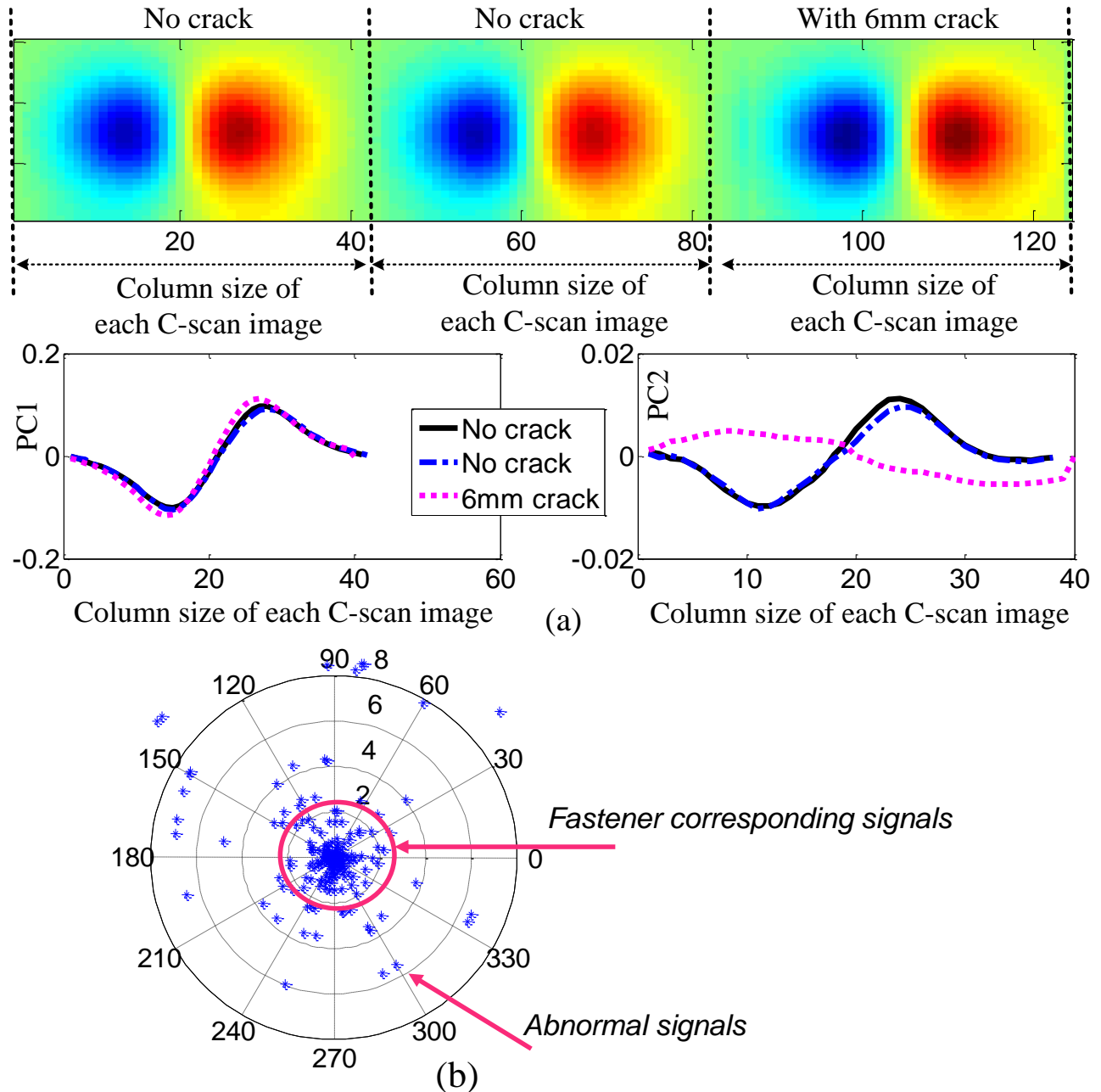


Figure 4.5 Principle of applied PCA analysis

Therefore, crack detection is implemented by exploiting the uncorrelated PCs to represent the fastener data and crack signals in different directions in PC subspace. In This scheme does not need training data. Automatic crack detection is performed by plotting the data in the PCs subspace.

4.5 Results of PEC-GMR Inspection

4.5.1 Detection of 2nd and 3rd Layer Cracks in Sample 1

Experimental measurements of Sample 1 are presented as the C-scan images in Figure 4.6. For each row, 40 line scans are measured with 215 points at 1mm interval in each line scan. The excitation current source is a 100Hz and 1.4A square waveform. The normal component B_z of the transient field is measured. The peak value of each A-scan signal is utilized to generate the C-scan image. Defects machined in Sample 1 are summarized in Table 4-1.

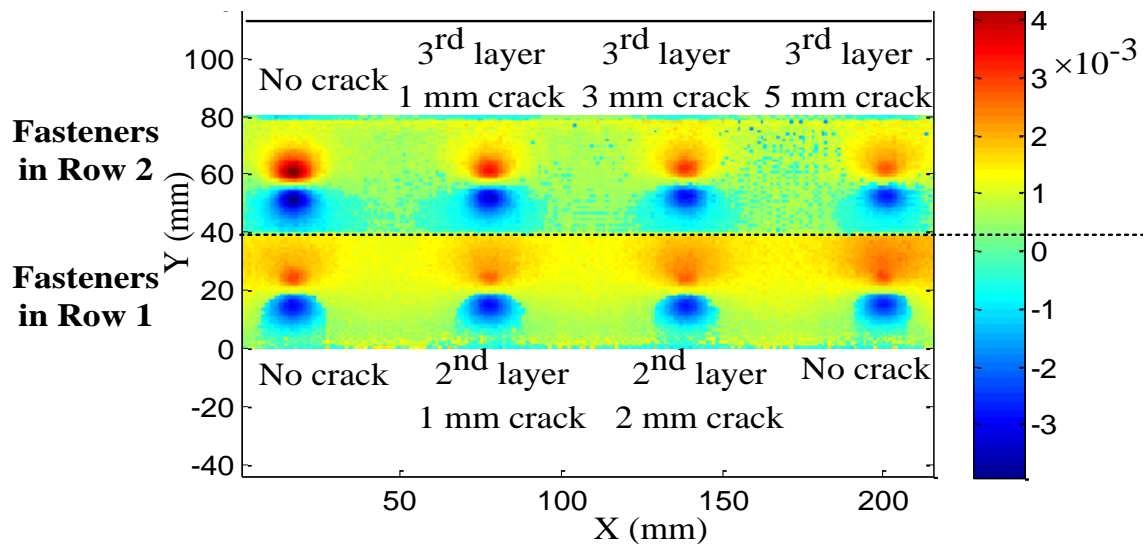


Figure 4.6 C-scan images of aluminum fasteners in Sample 1 using PEC-GMR measurements

Although the asymmetry observed in the C-scan images of aluminum fasteners with cracks, it is not a reliable indication in the case of 2nd or 3rd layer crack. In addition, it is also possible to get an asymmetric image in the case of improper fastener installation or sensor tilt.

Table 4-1 Sample 1 – aluminum fastener.

Sample1	Defect size	Location
Fastener1-1	0	2 nd layer
Fastener1-2	1 mm	2 nd layer
Fastener1-3	2 mm	2 nd layer
Fastener1-4	0	2 nd layer
Fastener2-1	0	3 rd layer
Fastener2-2	1mm	3 rd layer
Fastener2-3	3mm	3 rd layer
Fastener2-4	5mm	3 rd layer

PCA method for crack detection is performed on the C-scan images of aluminum fasteners (Figure 4.6) in Row 1 (2nd layer cracks) and Row 2 (3rd layer cracks) of Sample 1. The C-scan images of Sample 1 are first processed for mean removal and are represented by a matrix M of size (40×215). A denoising linear spatial filter represented by a ‘gaussian’ 10 by 10 mask is used for de-noising.

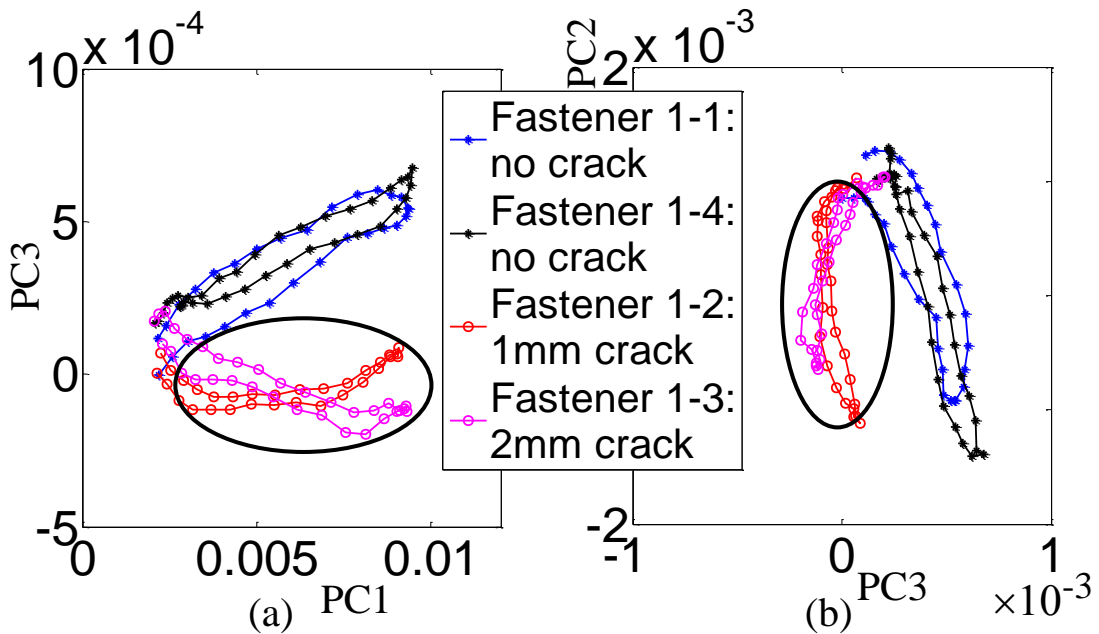


Figure 4.7 Detection of cracks in the 2nd layer of Sample 1 using the PCA method (a) Detection results by PC1 vs. PC3 representations (b) Detection results by PC3 vs. PC2 representations

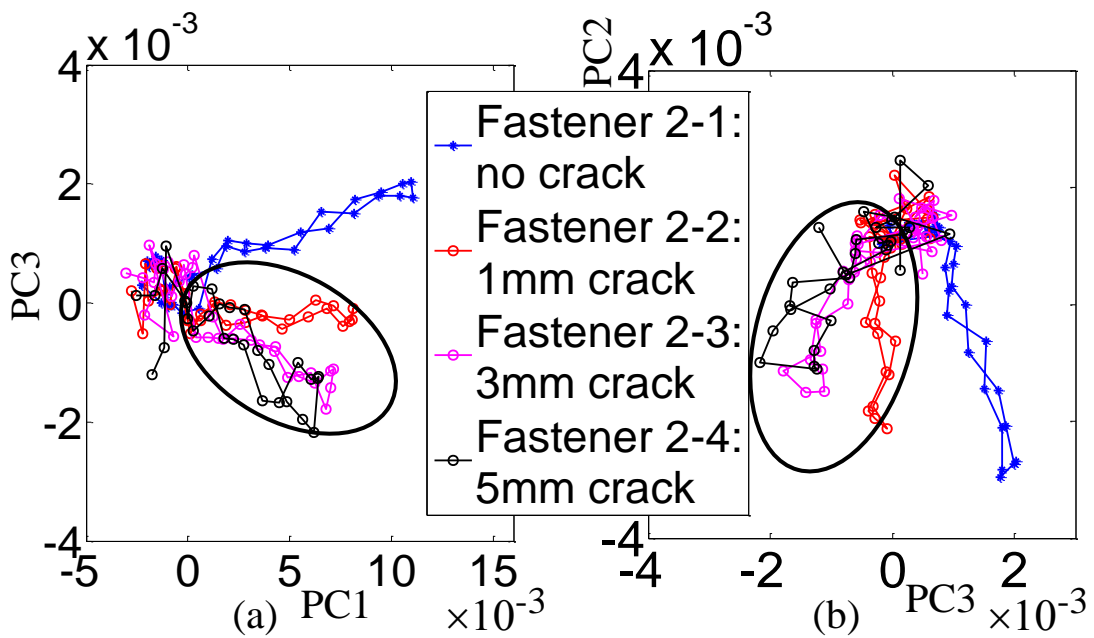


Figure 4.8 Detection of cracks in the 3rd layer of Sample 1 using the PCA method (a) Detection results by PC1 vs. PC3 representations (b) Detection results by PC3 vs. PC2 representations

Projection of input data into PC1 vs. PC3, and PC3 vs. PC2 subspace domains is shown in

Figure 4.7 and 4.8. It is seen that discriminatory information about cracks are successfully found in PC3 vs. PC1 or PC3 vs. PC2 plots. As shown in Figures 4.7-4.8, the uncorrelated PCs have significantly suppressed fastener signals and enhanced the crack information contained in the collected image data.

4.5.2 Detection of 2nd Layer Cracks in Sample 2

The PEC-GMR experimental C-scan images of sample 2 are shown in Figure 4.9. Table 4-2 describes the cracks machined in sample 2.

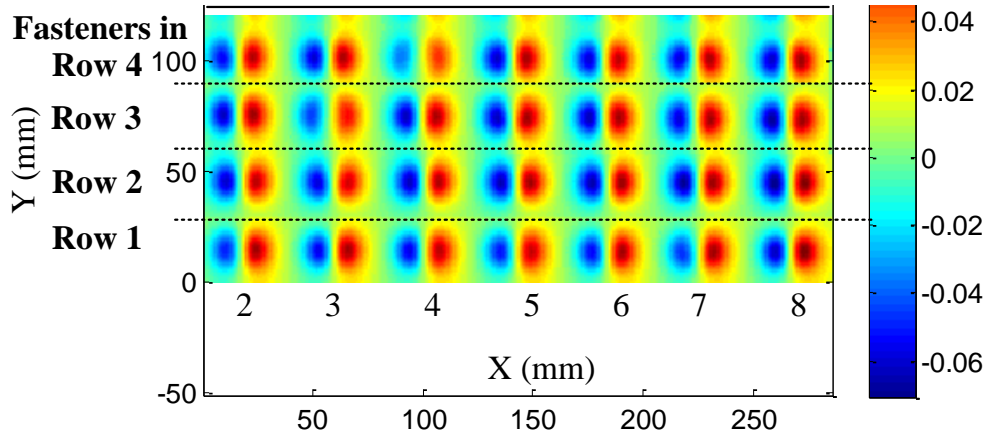


Figure 4.9 C-scan images of steel fasteners in Sample 2 using PEC-GMR measurements

Table 4-2 Sample 2 – steel fastener with 2nd layer cracks.

Row1 Fastener	Crack size (mm)	Row2 Fastener	Crack size (mm)	Row3 Fastener	Crack size (mm)	Row4 Fastener	Crack size (mm)
1-2	0	2-2	0	3-2	4.572	4-2	0
1-3	0	2-3	0.6604	3-3	3.048	4-3	2.8702
1-4	0	2-4	0.9652	3-4	1.524	4-4	1.9812
1-5	1.524	2-5	1.3716	3-5	0	4-5	1.3716
1-6	3.048	2-6	1.9812	3-6	0	4-6	0.9652
1-7	4.572	2-7	2.8702	3-7	0	4-7	0.6604
1-8	6.096	2-8	0	3-8	0	4-8	0

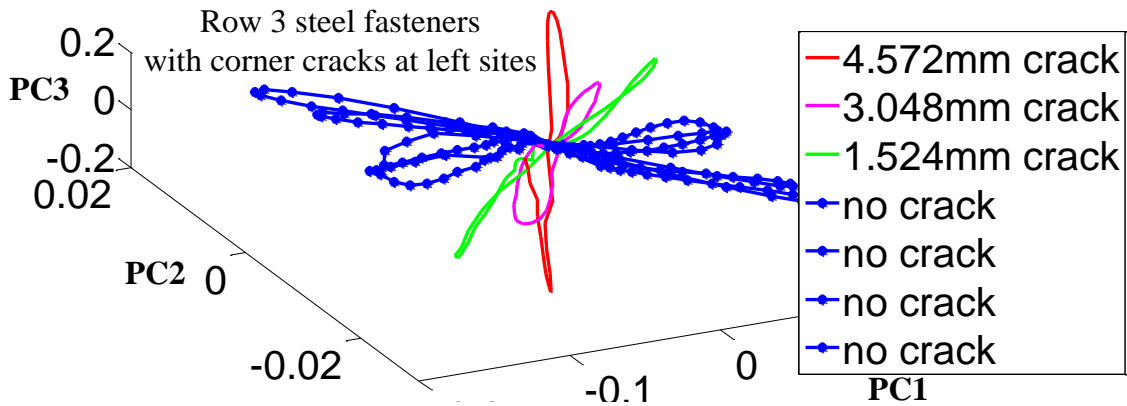
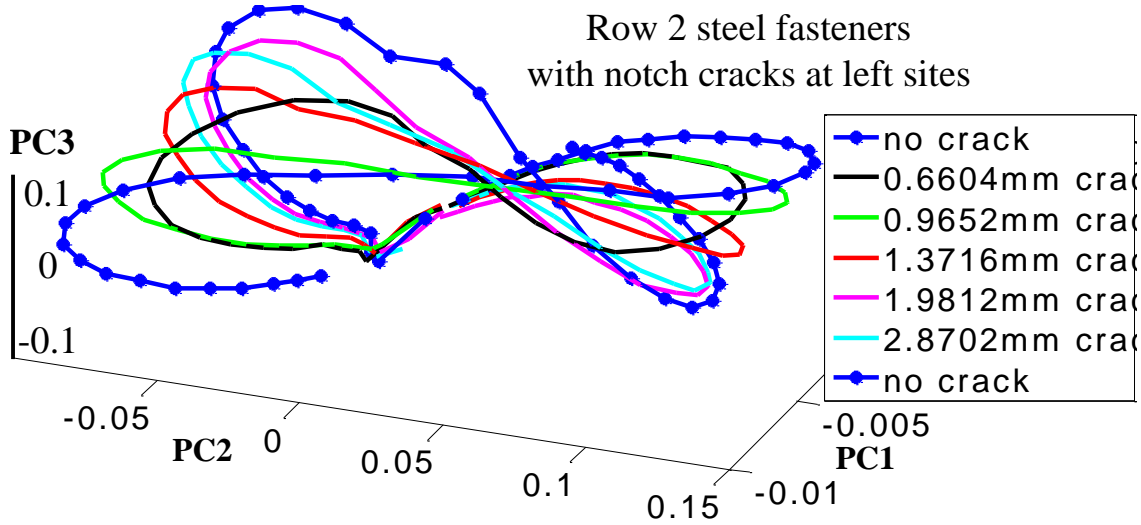
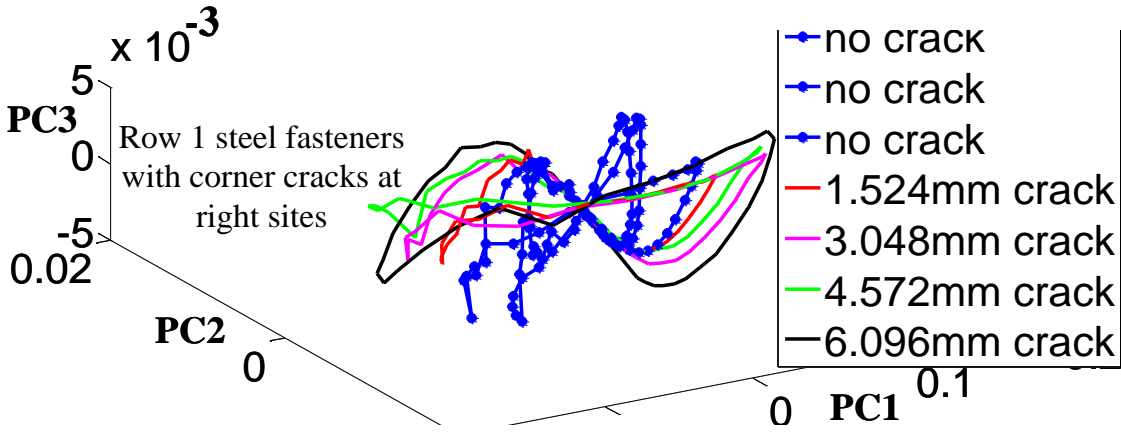
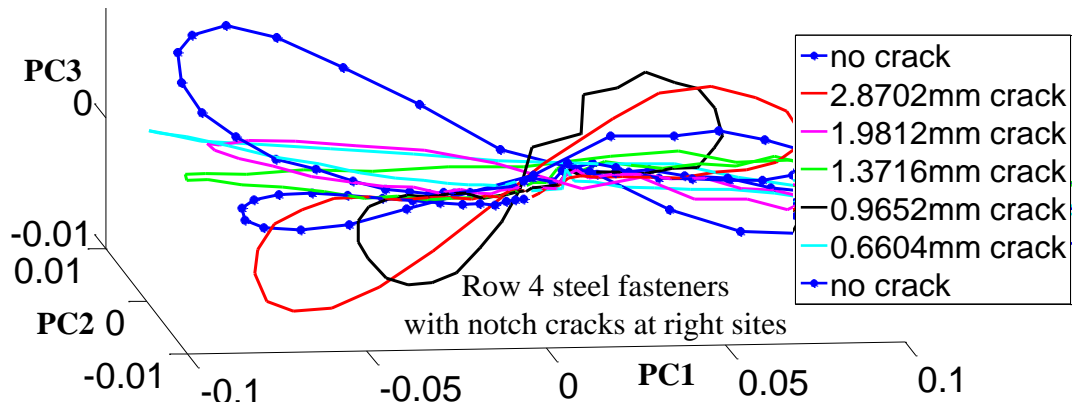


Figure 4.10 Detection of cracks around steel fasteners in Row 1 to Row 4 of Sample 2 using the 3D plots of PC1 to PC3: B_z component

Figure 4.10 (cont'd).



C-scan images of steel fasteners in Row 1 to 4 (Figure 4.9) are processed using PCA method. Linear transformations of image data into PC1 to PC3 subspace are shown in Figure 4.10. The signal representations in PC1 vs. PC2 domain are found to exhibit the trajectories that can discriminate the steel fasteners without cracks from the fasteners with radial cracks. Therefore, the signals in PC1 vs. PC2 representations are employed for automatic crack detection and the results are shown in Figure 4.11.

In this case, few false calls are observed: the image data of steel fastener #8 (no flaw) in Row 2, and steel fasteners #2 and #3 (2.87mm and 1.98mm) and #8 (no flaw) in Row 4. These false identifications were attributed to possible variations in lift-off, and a limited sensitivity of a single component of the magnetic field.

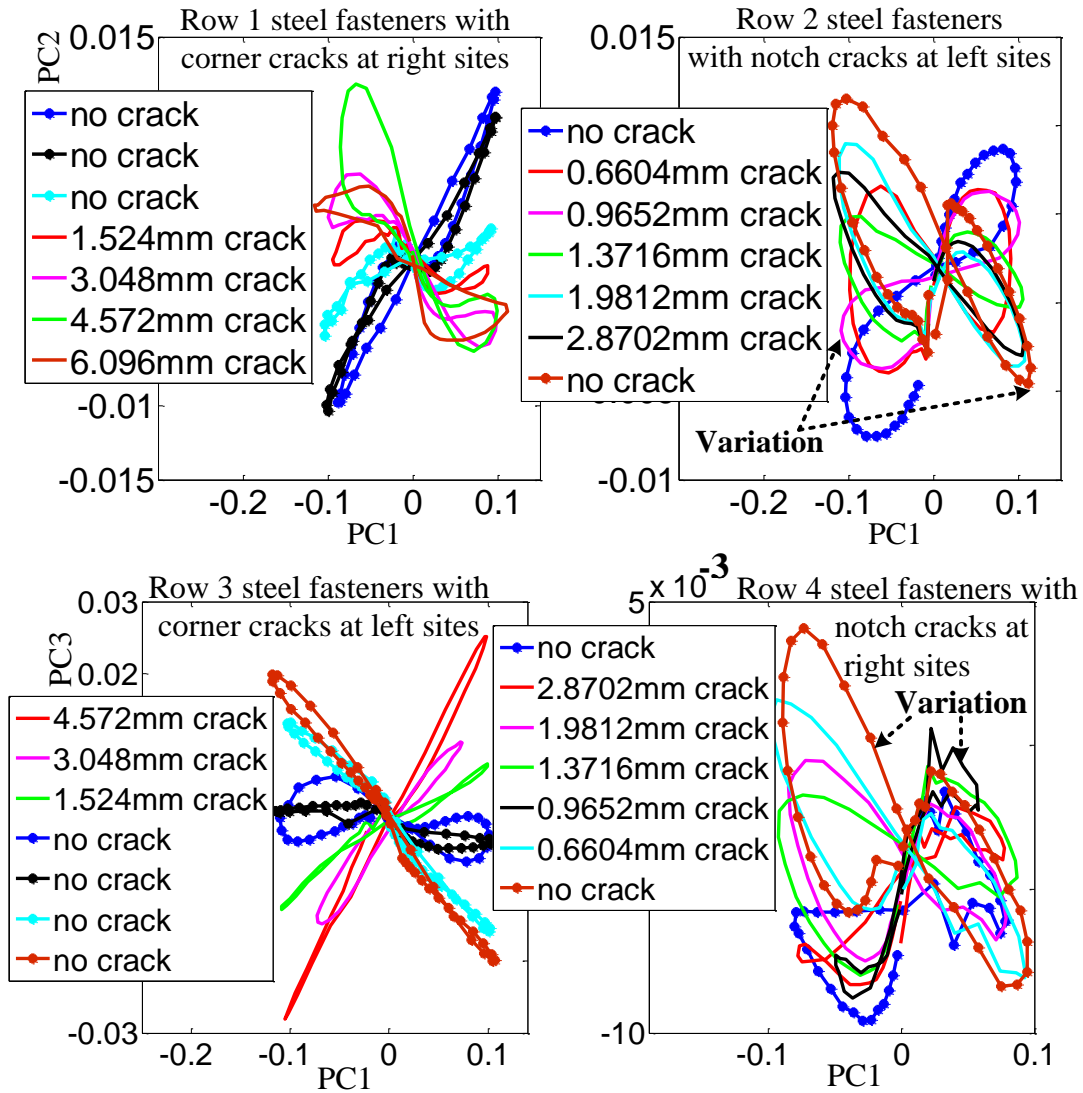


Figure 4.11 Detection of cracks in the 2nd layer of Sample 2 using the PCA method (steel fasteners in Row 1 to Row 4): B_z component

4.5.3 Flaw Detection using Tangential-component Measurements

Data analysis using PEC-GMR measurements of B_y and B_x components are investigated in this section. Tangential-component measurements of steel fasteners in Sample 2 are presented in the C-scan images of Figure 4.12.

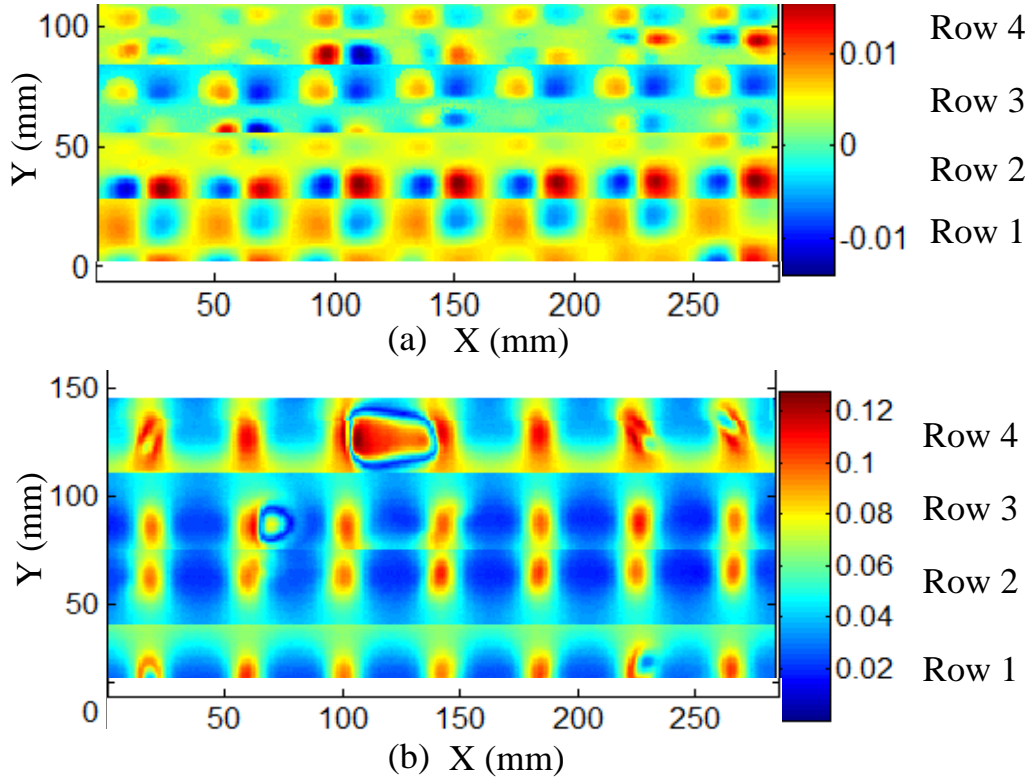


Figure 4.12 PEC-GMR tangential-component measurements of steel fasteners (a) C-scan images of B_y measurements (b) C-scan images of B_x measurements

Image data of B_y and B_x measurements are processed using PCA technique, and the results are presented in Figures 4.13-4.14 (B_y component) and Figures 4.15-4.16 (B_x component). The 3D plots using the first three PCs are studied, and the signal representations in the PCs subspace are exploited to detect defective steel fasteners with cracks in the 2nd layers.

PCA applied to measurements of B_y component are seen to be effective in detecting cracks at steel fastener sites in Rows 2 and 4. The smallest crack (0.66mm length) is missed. The measurements of B_x component are sensitive to all cracks in four rows. Hence, the tangential components of the magnetic field are validated as a reliable option for the inspection of steel fasteners.

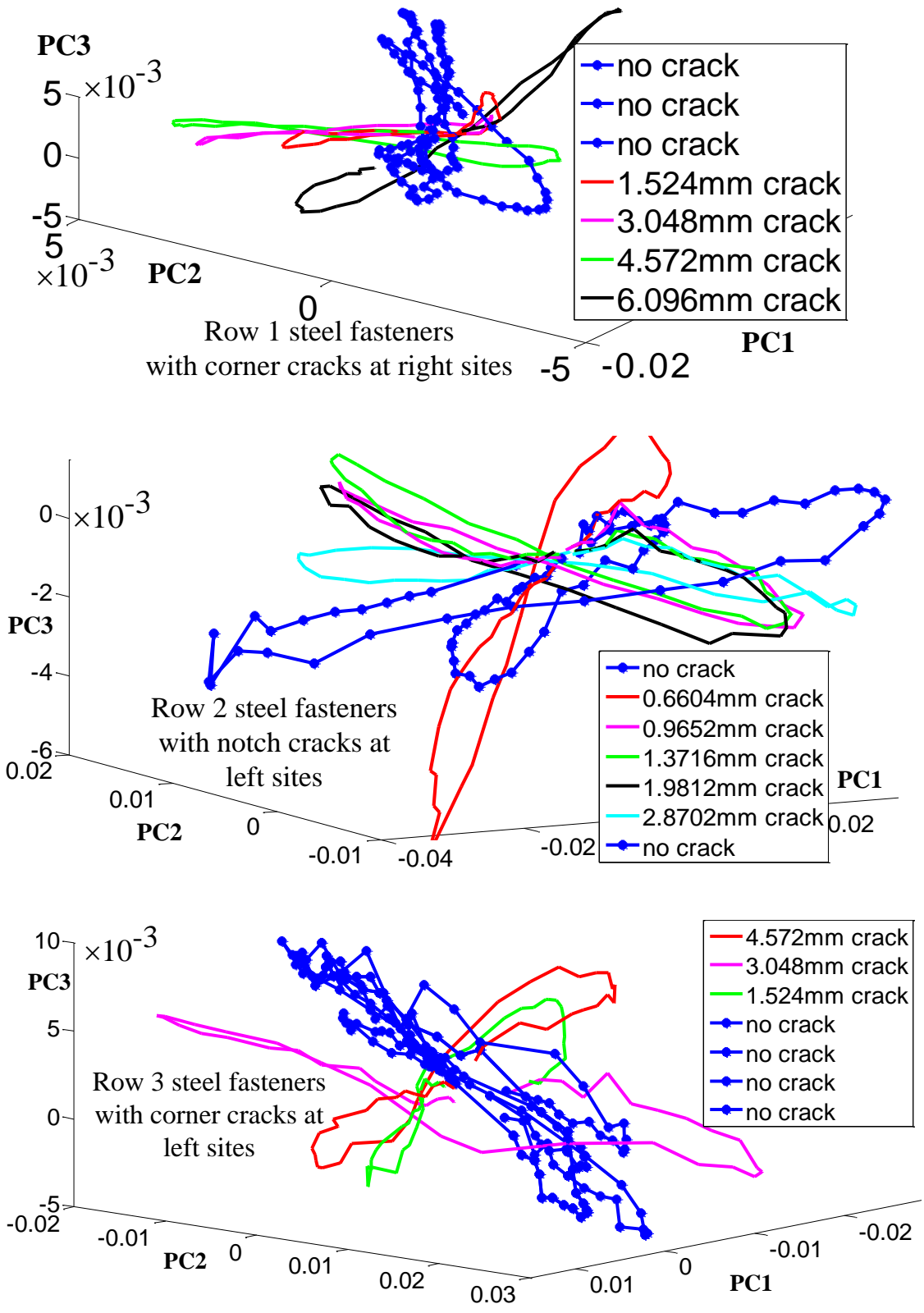


Figure 4.13 Detection of cracks around steel fasteners in Row 1 to Row 4 of Sample 2 using the 3D plots of PC1 to PC3: By component

Figure 4.13 (cont'd).

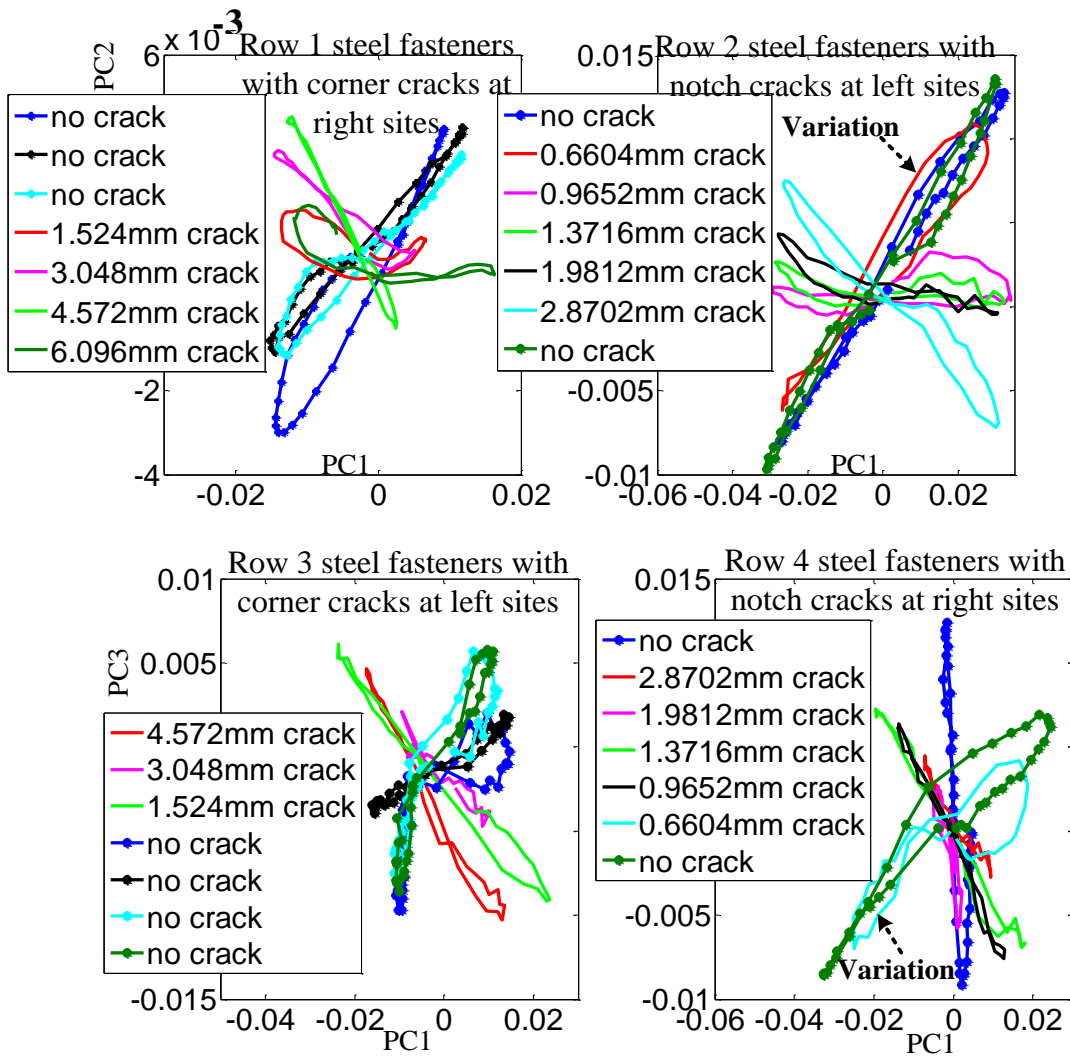
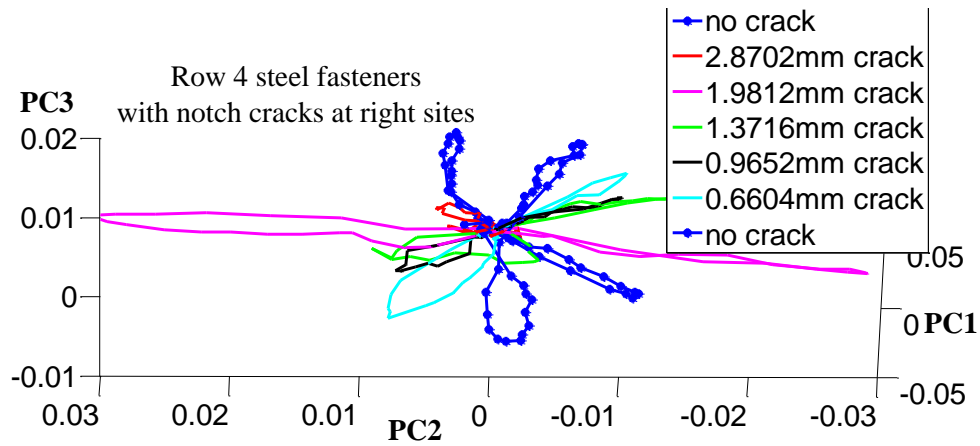


Figure 4.14 Detection of cracks in the 2nd layer of Sample 2 using the PCA method (steel fasteners in Row 1 to Row 4): *By component*

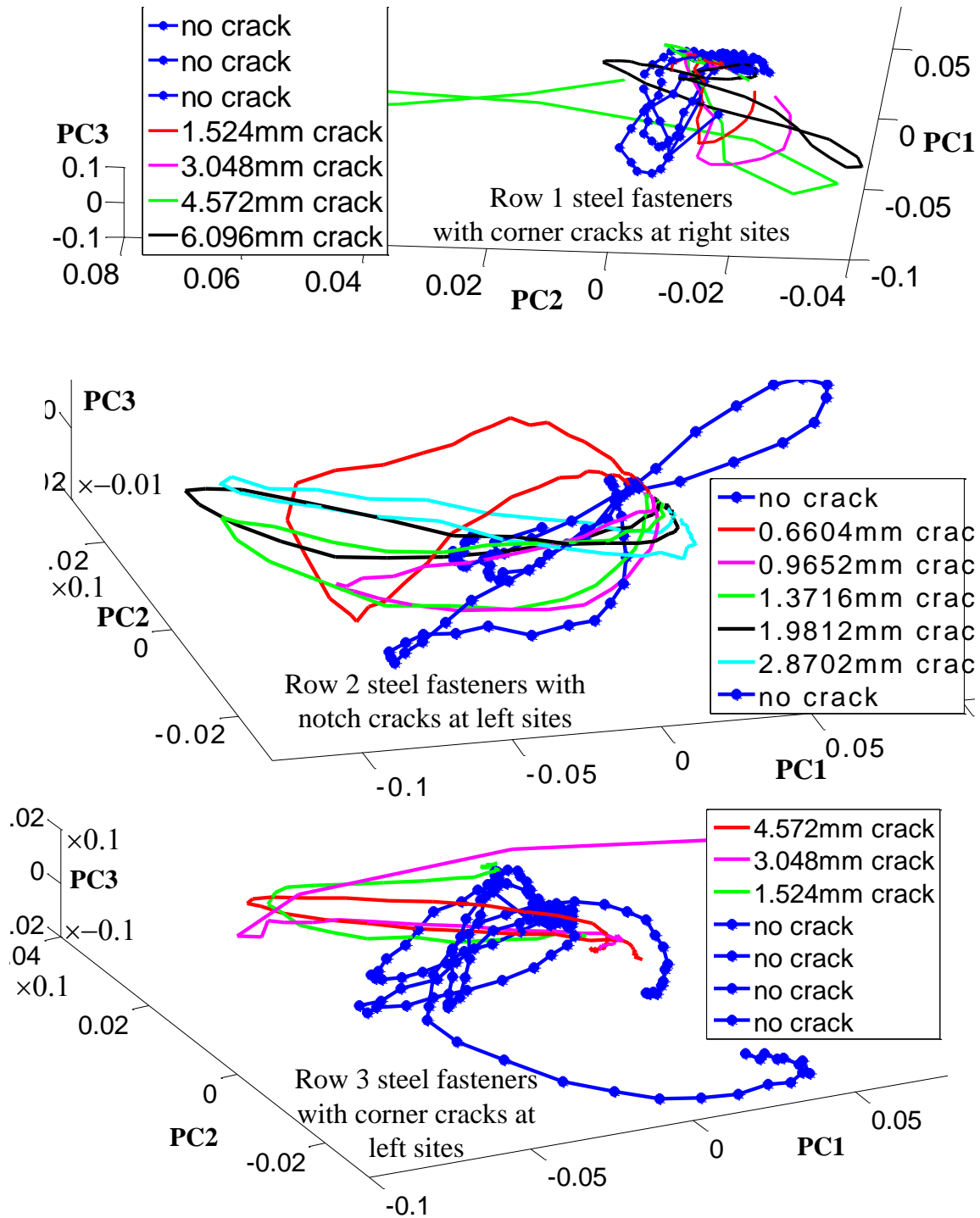


Figure 4.15 Detection of cracks around steel fasteners in Row 1 to Row 4 of Sample 2 using the 3D plots of PC1 to PC3: B_x component

Figure 4.15 (cont'd).

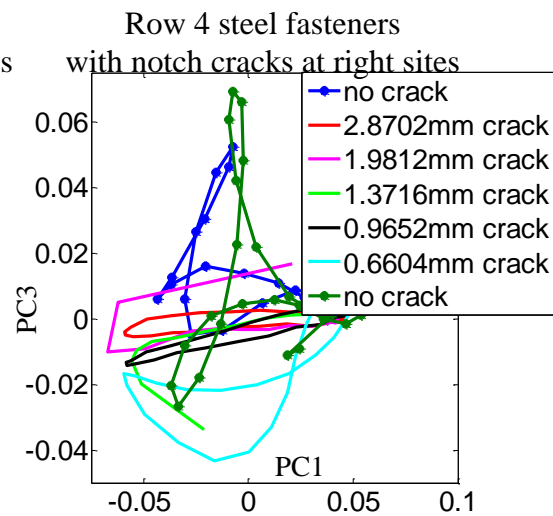
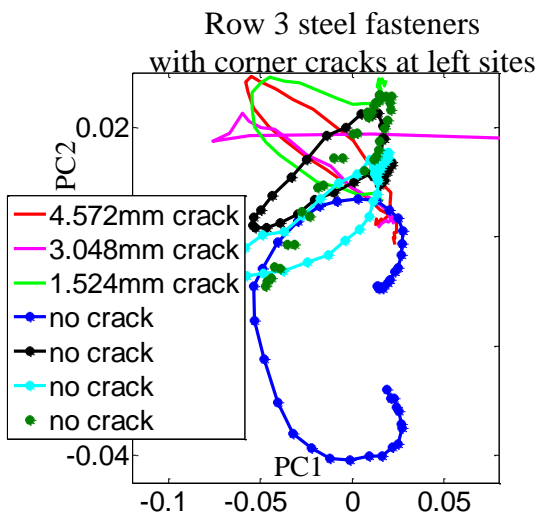
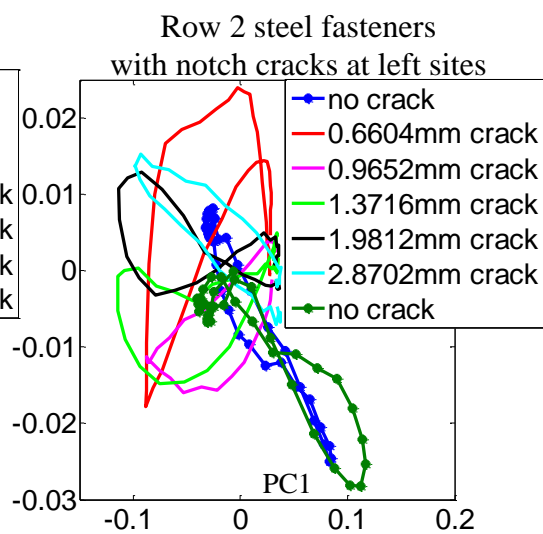
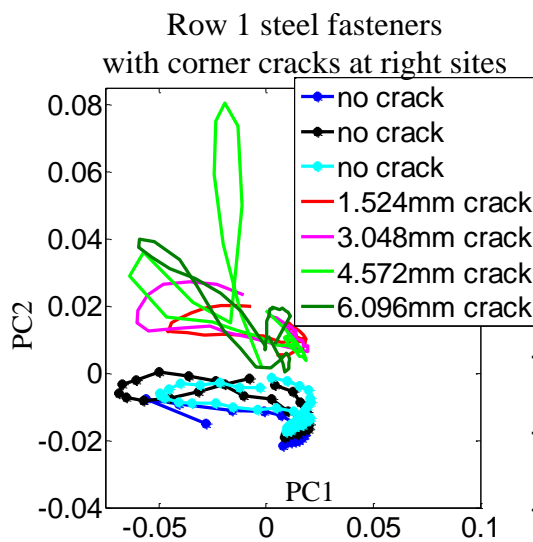
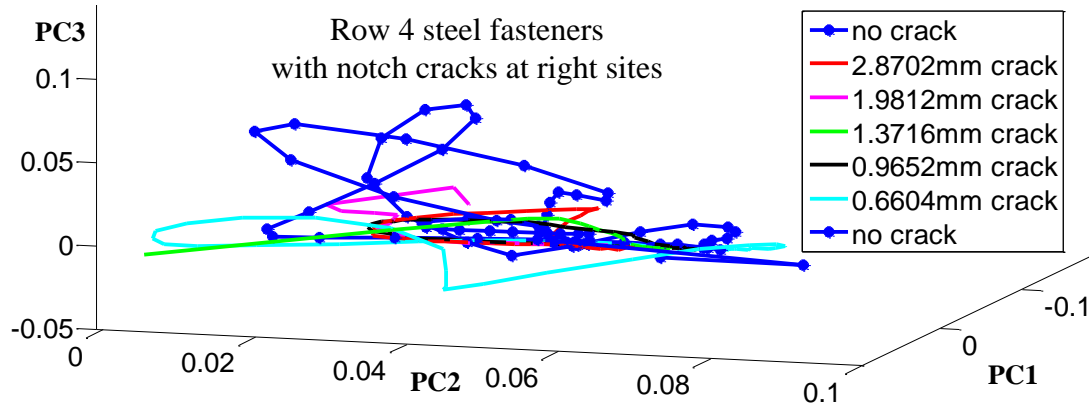


Figure 4.16 Detection of cracks in the 2nd layer of Sample 2 using the PCA method (steel

fasteners in Row 1 to Row 4): B_x component

4.6 Automatic Crack Detection using 3-component GMR Images

This section describes the design of quantitative signal analysis and classification developed to utilize information contained in the three components of the magnetic flux density with respect to feature based detection.

4.6.1 Feature Extraction

PCA based automated crack detection has proved to be promising in discriminating between signals from fasteners with and without cracks. A quantitative feature set is derived for reliable automatic crack detection. Three types of signal features containing discriminatory information are defined for automated classification.

Orientations of corresponding signals in projected PC subspace are first studied. As shown in Figure 4.17, the orientations of signals in PCs representation are extracted quantitatively as:

$$ori = \text{atan}[(y_2 - y_1) / (x_2 - x_1)] \quad (4.8)$$

where (x_1, y_1) and (x_2, y_2) are coordinates of the signal maximum and minimum in PC1 vs. PC2 or PC1 vs. PC3 subspace.

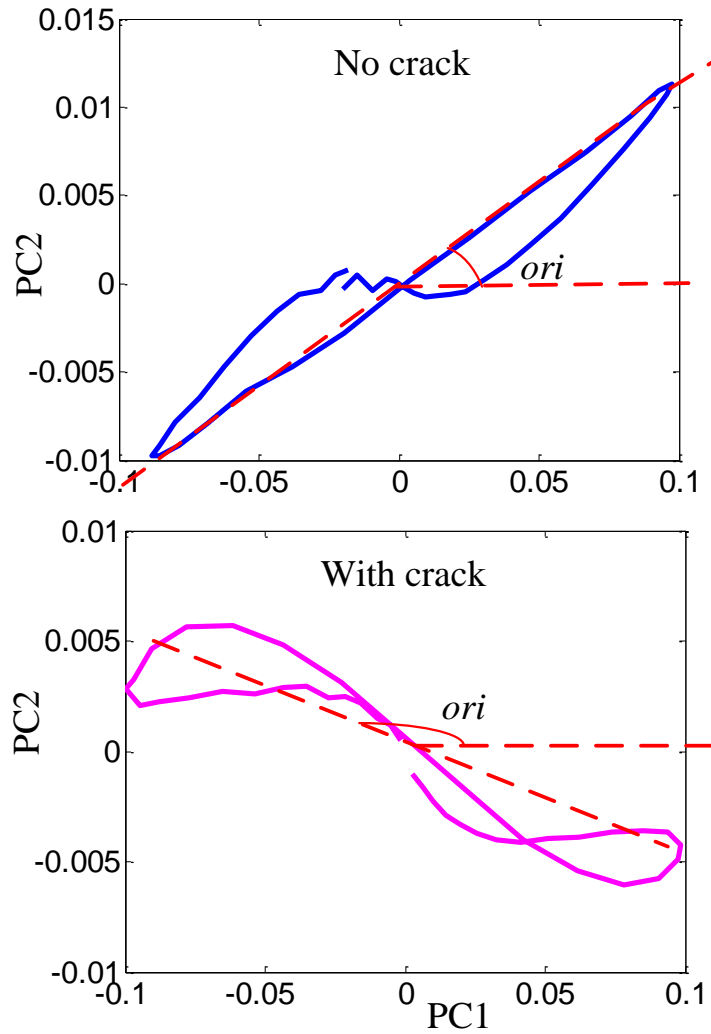


Figure 4.17 Orientation based feature extraction

A feature quantifying asymmetry calculated by the 3rd order moment, and a feature quantifying sharpness calculated by the 4th order moment are defined next. As shown in Figure 4.18, the two features s and k quantify the asymmetry associated with the crack in PC subspace. These two features based on the statistical moments skewness and kurtosis [24, 89, 156, 177] and are defined as:

$$s = \frac{\sum_{i=1}^p (sig_i_{PC} - \overline{sig_i_{PC}})^3}{(p-1)std^3}$$

$$k = \frac{\sum_{i=1}^p (sig_i_{PC} - \overline{sig_i_{PC}})^4}{(p-1)std^4} \quad (4.9)$$

where sig_i_{PC} is the fastener image data associated with the 2nd PC component, and $\overline{sig_i_{PC}}$ is the mean and p is number of signal data points. The term std is the standard deviation of the signal.

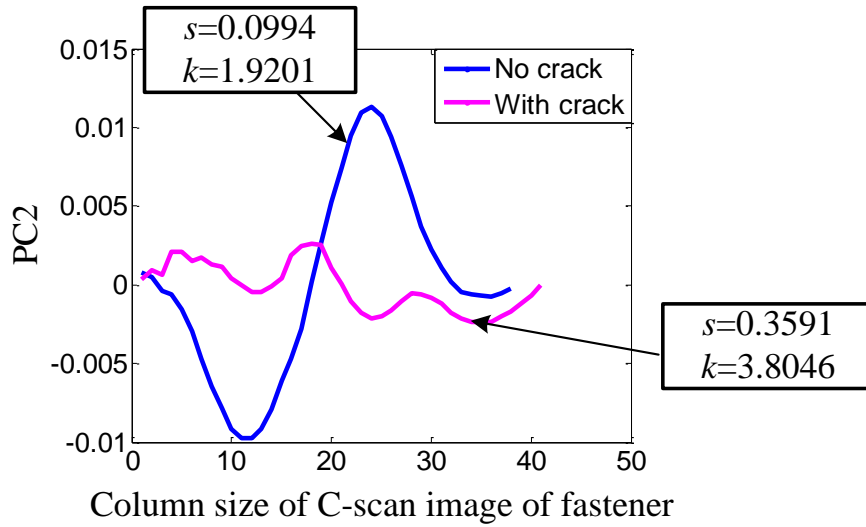


Figure 4.18 Asymmetry quantification using moment based features (3rd & 4th orders)

4.6.2 Crack Detection Scheme

The overall approach for automated fastener classification is depicted in Figure 4.19. Data from each row of the C-scan images from the 3-component EC-GMR system are applied to the PCA processor for enhancing the indications due to cracks present at fastener sites. GMR images of

three components are analyzed sequentially. Corresponding signals represented in PC1 vs. PC2 or PC1 vs. PC3 domain are used for feature extraction.

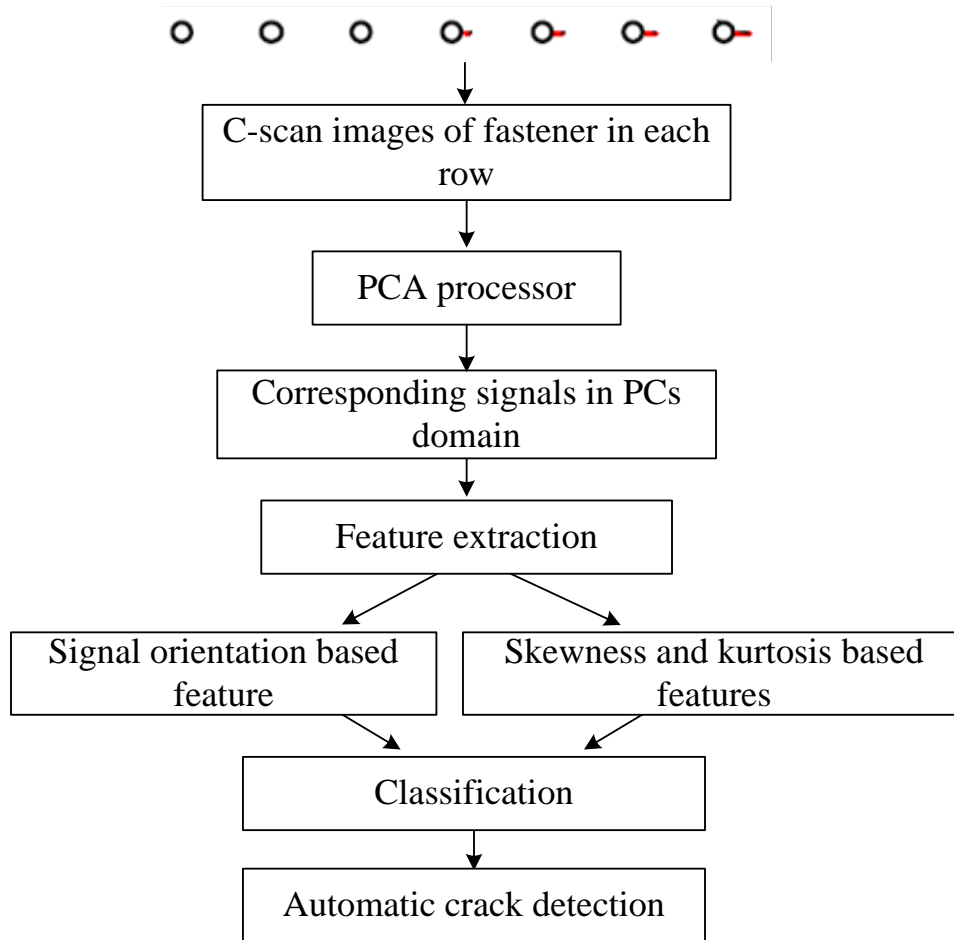


Figure 4.19 Overall approach for automated crack detection

Classification results of B_z , B_y , B_x measurements using three features are performed. As presented in Figures 4.20-4.23 (B_z measurements) and Figures 4.24-4.27 (B_y measurements), the automatic classification and crack detection are implemented using the plots of features ori vs. k and features ori vs. s . Figures 4.28 presents the automatic classification and crack detection for B_x measurements using feature s vs. k .

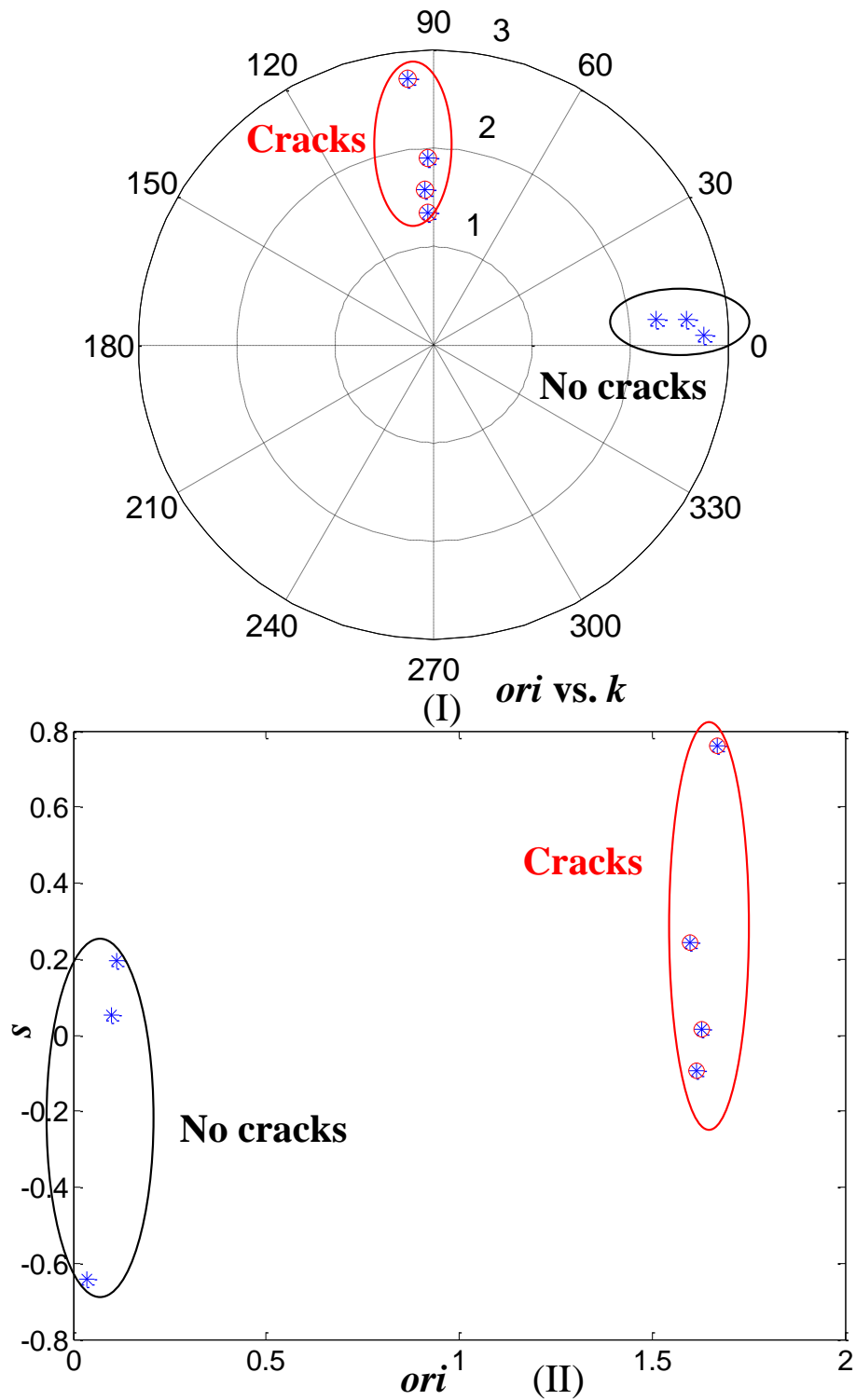


Figure 4.20 Classification results of steel fasteners in Row 1 using features ori calculated from PC1 and PC2, s and k calculated from PC2: PEC-GMR measurements of B_z component

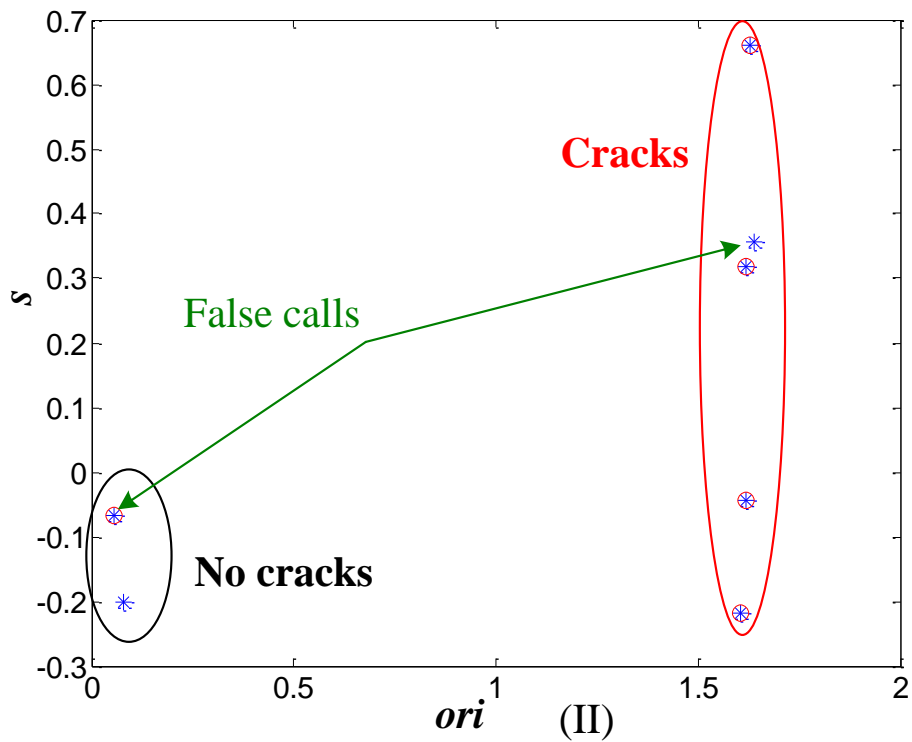
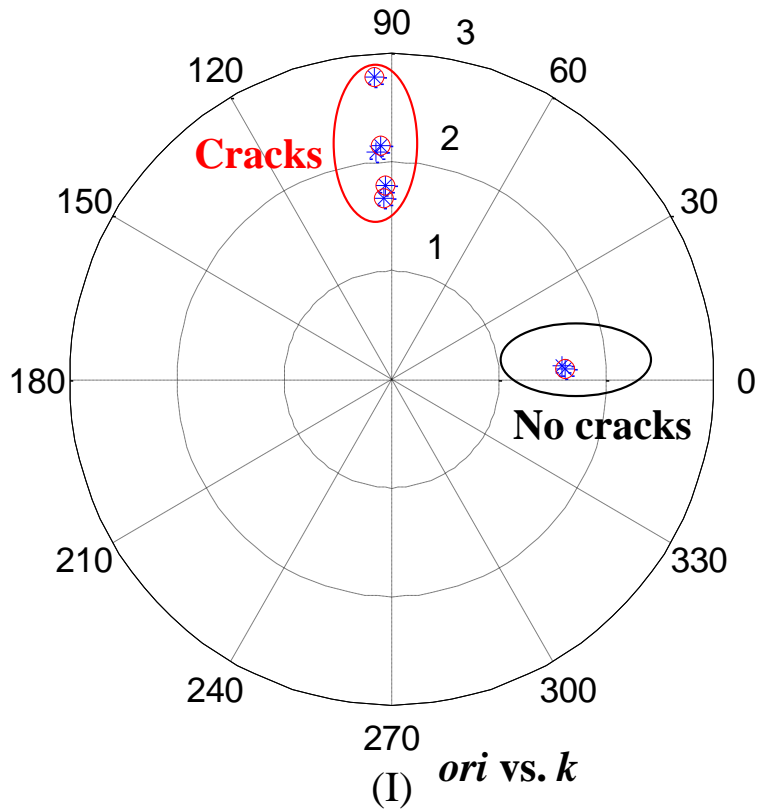


Figure 4.21 Classification results of steel fasteners in Row 2 using features *ori* calculated from PC1 and PC2, *s* and *k* calculated from PC2: PEC-GMR measurements of B_z component

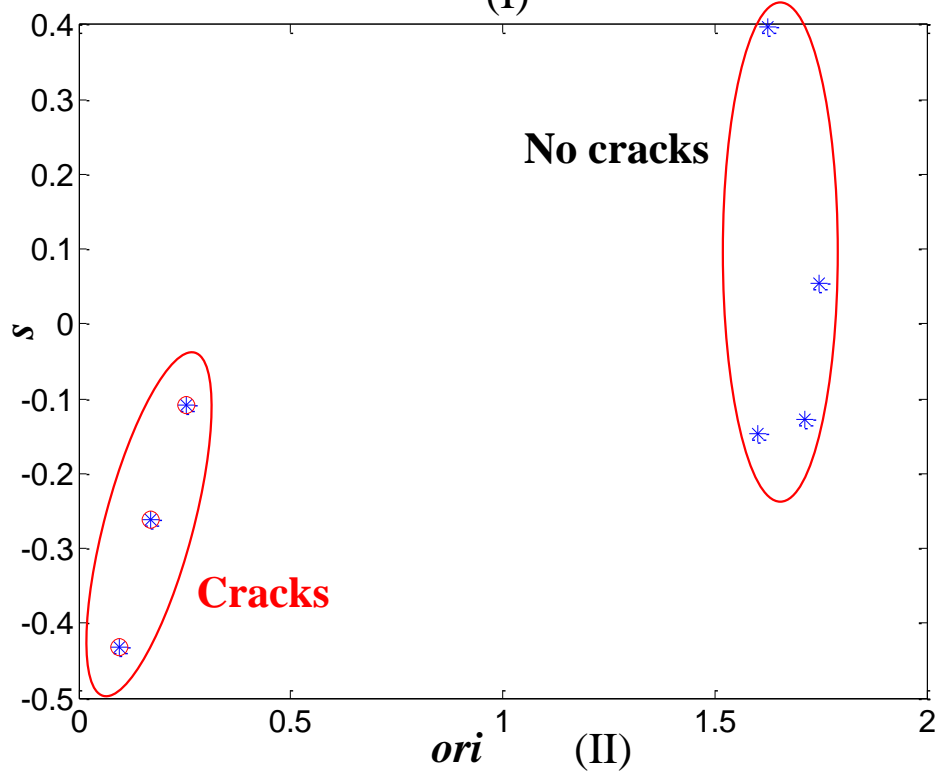
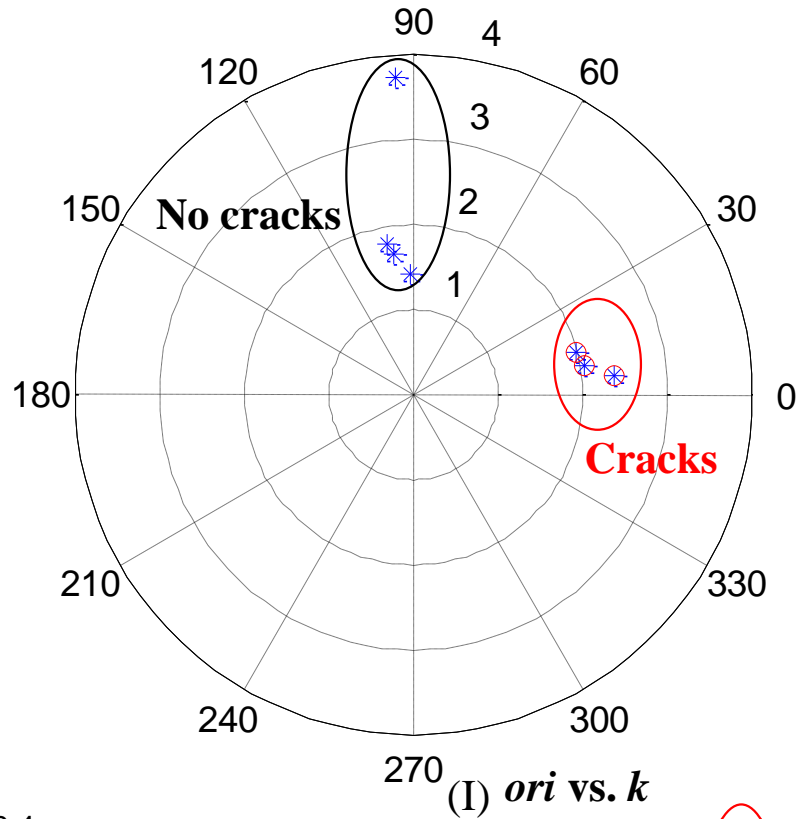


Figure 4.22 Classification results of steel fasteners in Row 3 using features *ori* calculated from PC1 and PC2, *s* and *k* calculated from PC2: PEC-GMR measurements of B_z component

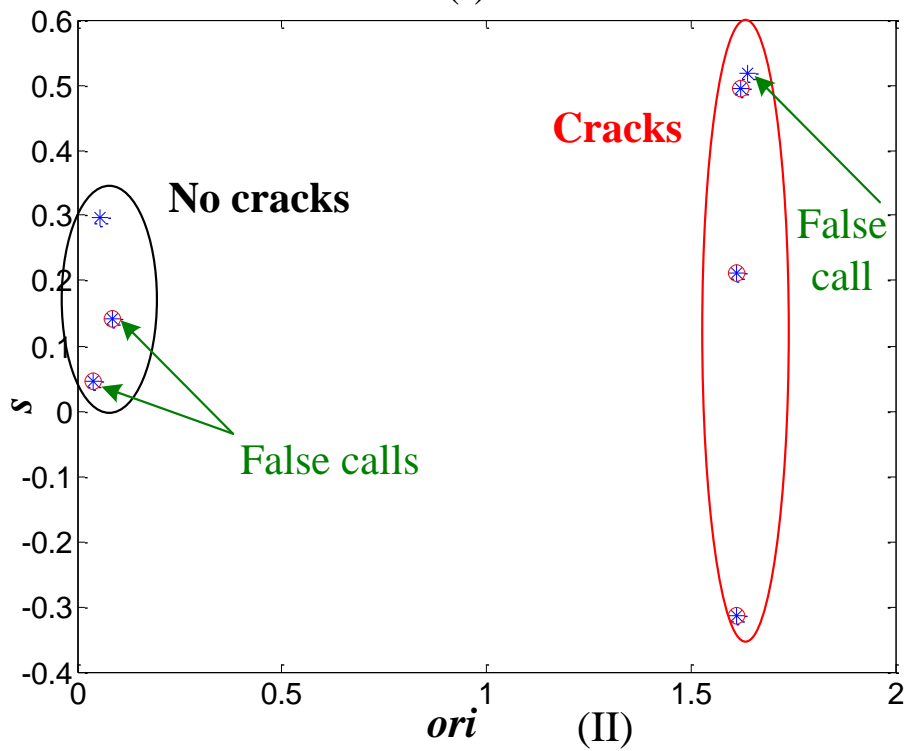
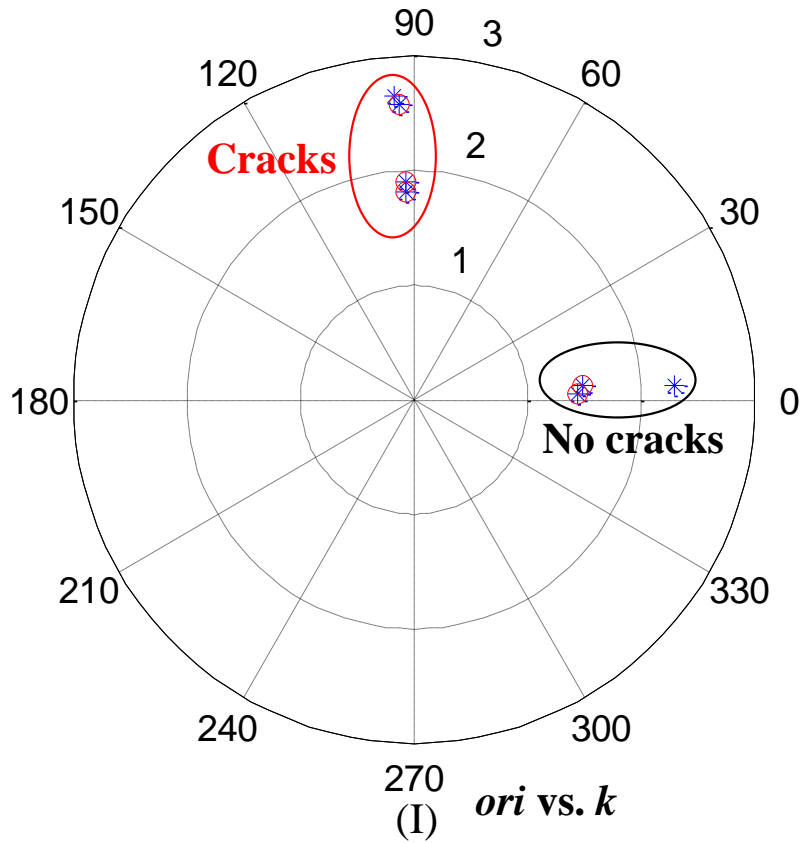


Figure 4.23 Classification results of steel fasteners in Row 4 using features ori calculated from PC1 and PC2, s and k calculated from PC2: PEC-GMR measurements of B_z component

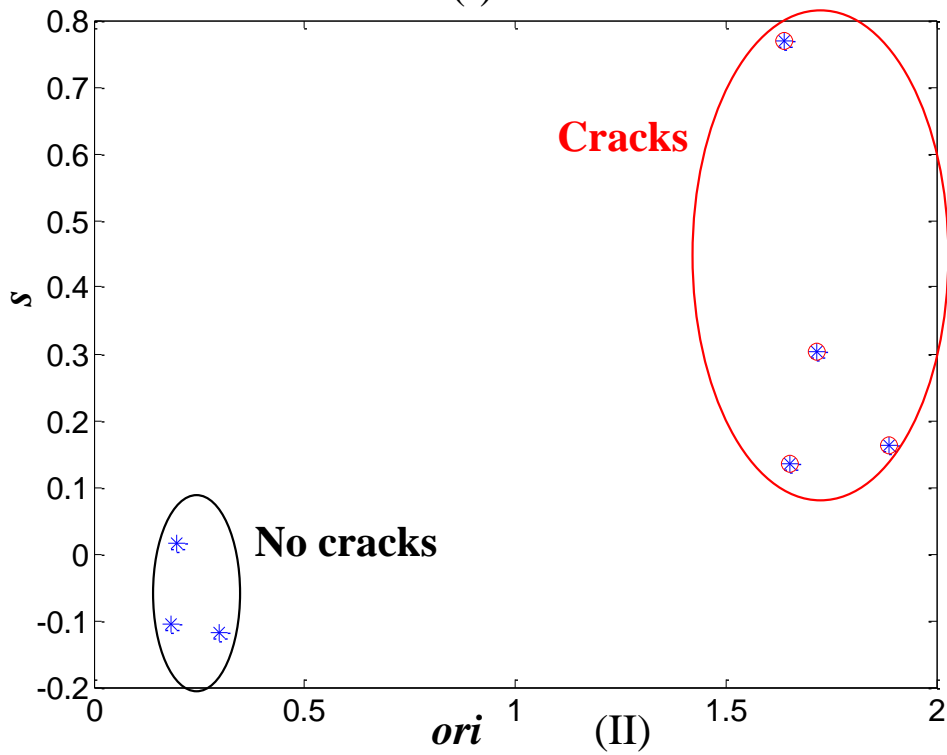
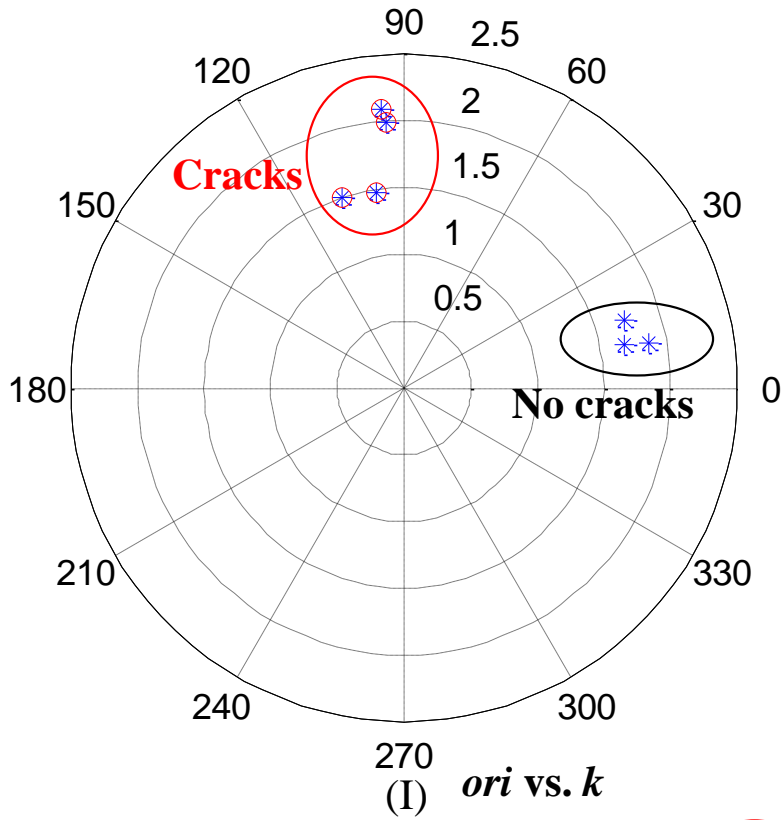


Figure 4.24 Classification results of steel fasteners in Row 1 using features *ori* calculated from PC1 and PC2, *s* and *k* calculated from PC2: PEC-GMR measurements of B_y component

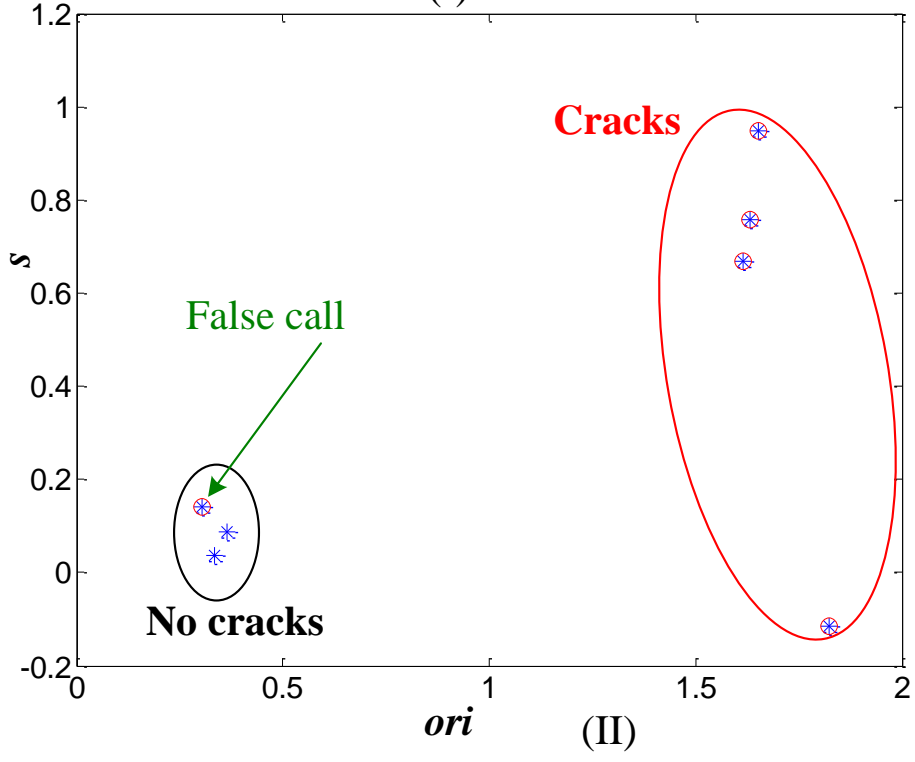
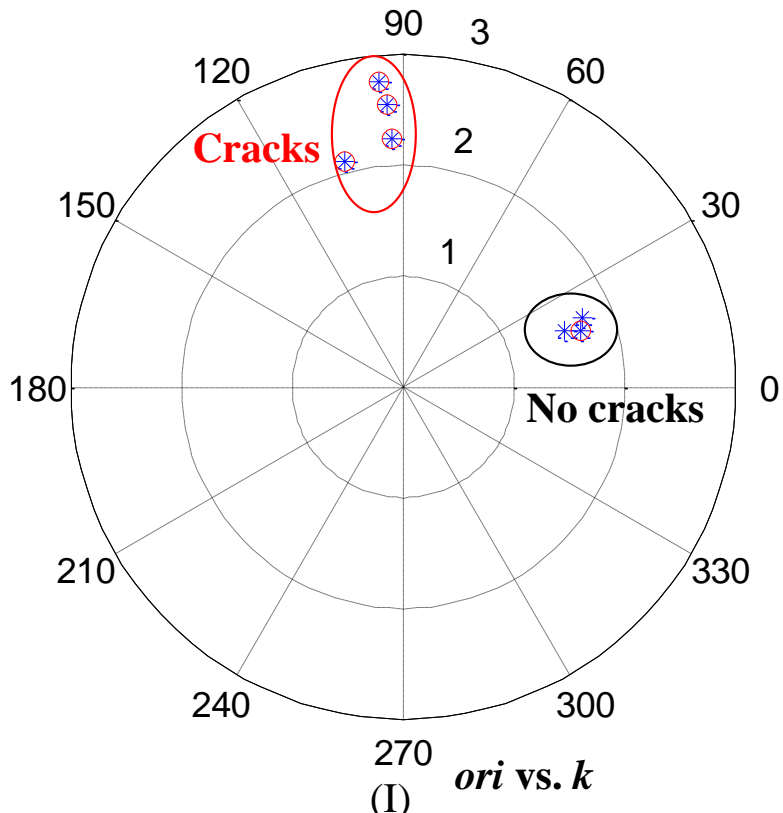


Figure 4.25 Classification results of steel fasteners in Row 2 using features *ori* calculated from PC1 and PC2, *s* and *k* calculated from PC2: PEC-GMR measurements of B_y component

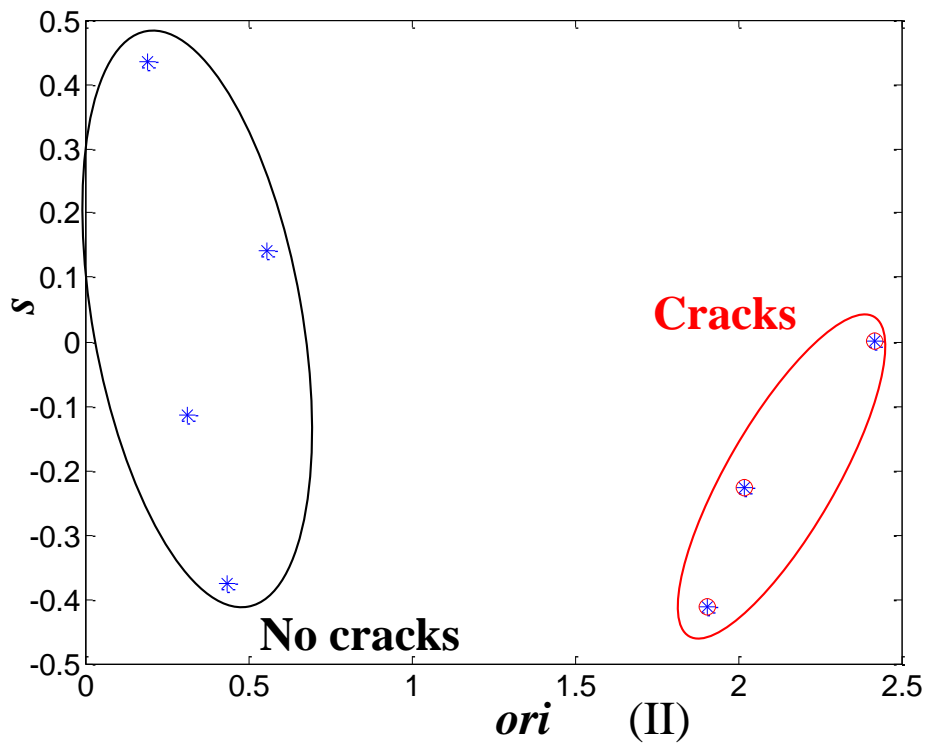
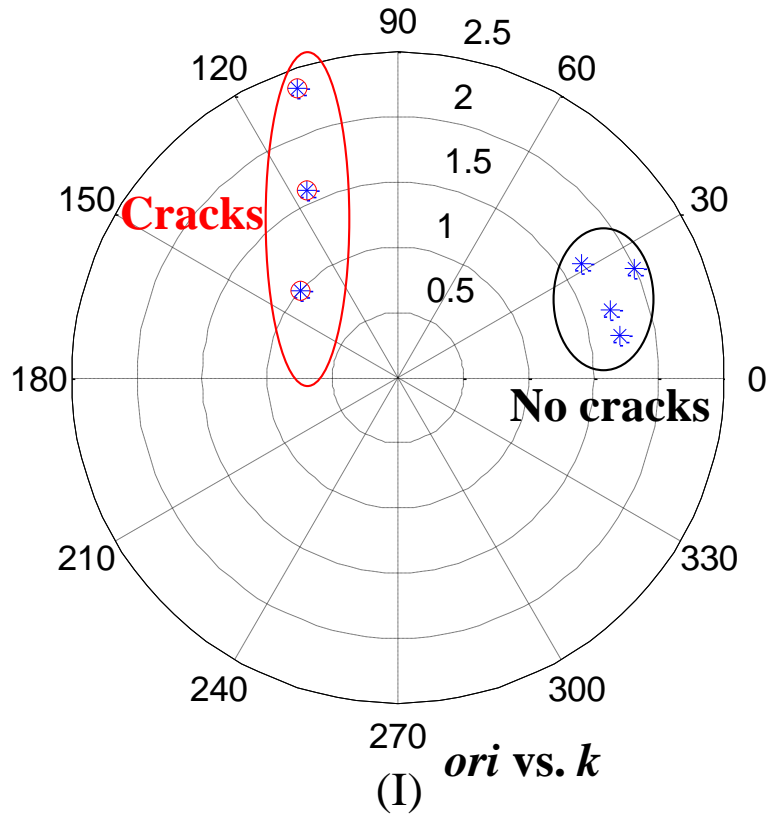


Figure 4.26 Classification results of steel fasteners in Row 3 using features *ori* calculated from PC1 and PC2, *s* and *k* calculated from PC2: PEC-GMR measurements of B_y component

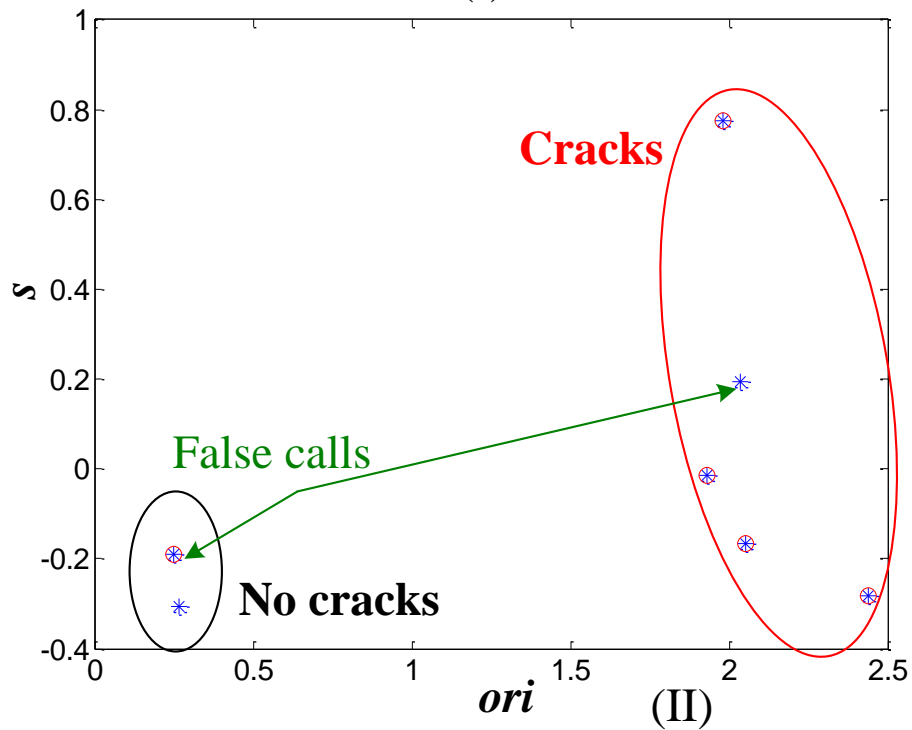
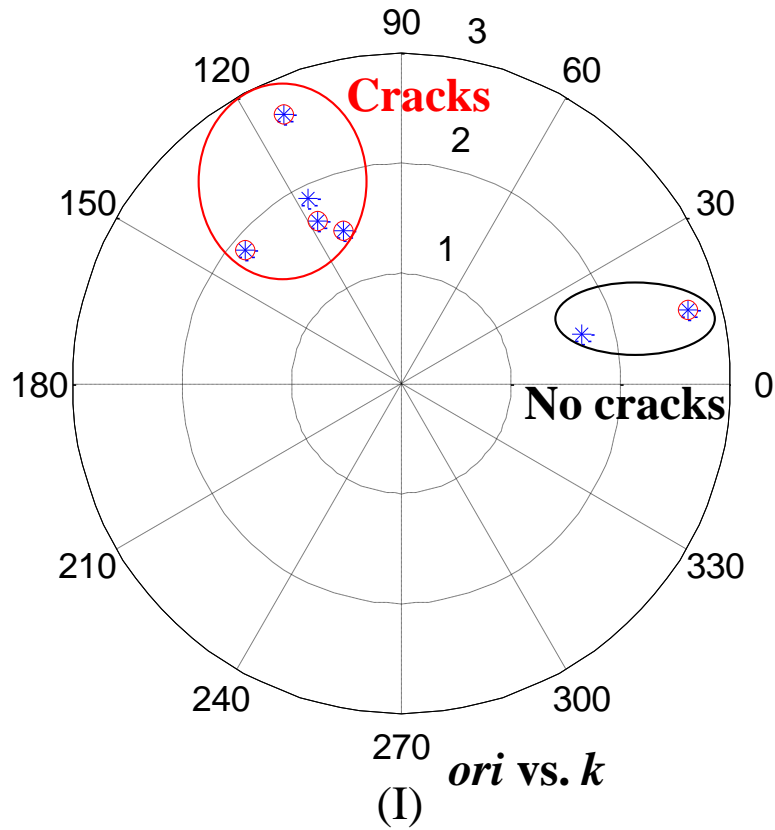


Figure 4.27 Classification results of steel fasteners in Row 4 using features *ori* calculated from PC1 and PC2, *s* and *k* calculated from PC2: PEC-GMR measurements of B_y component

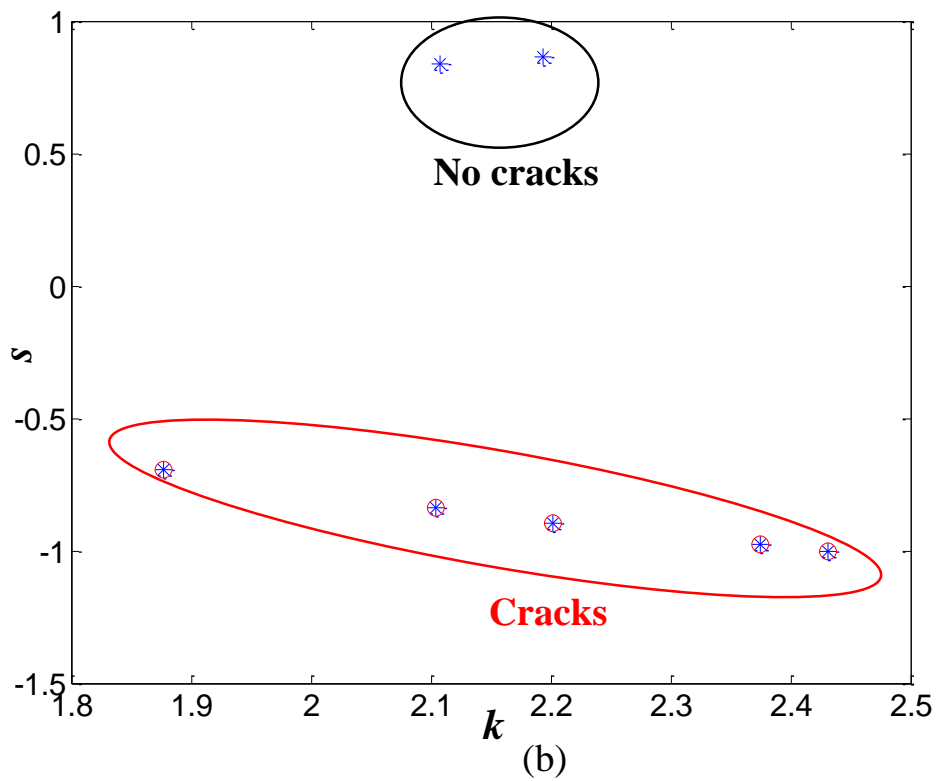
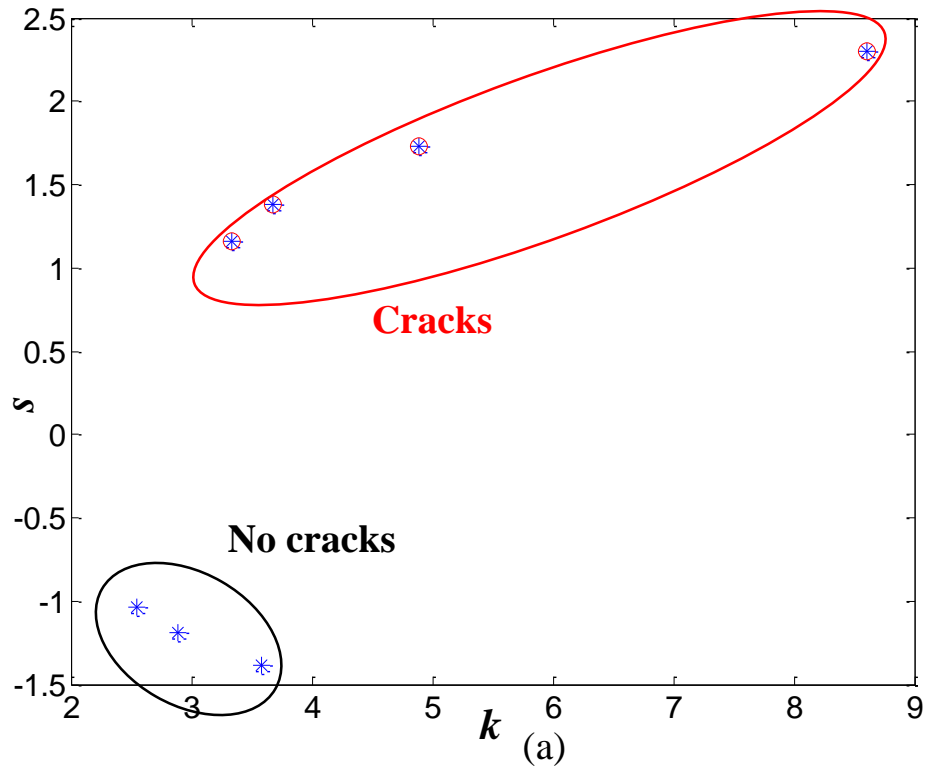
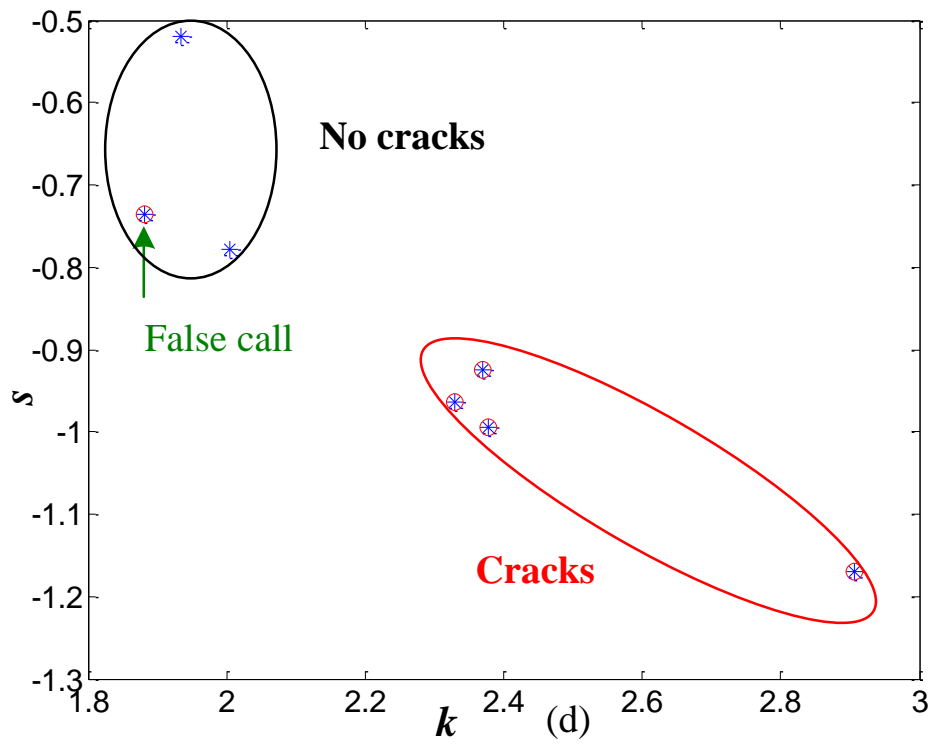
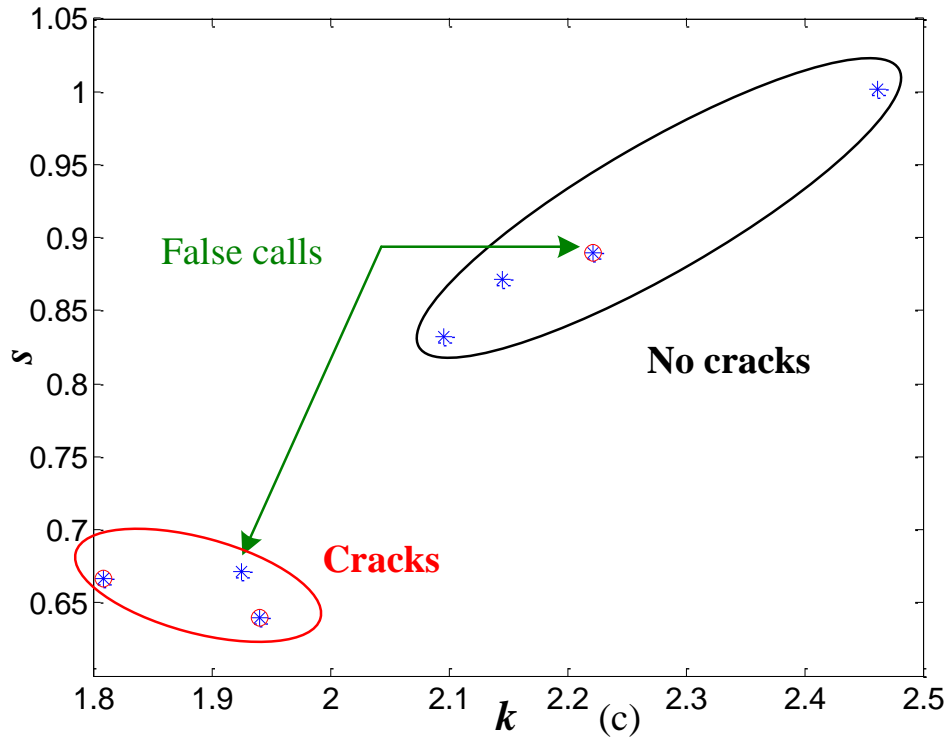


Figure 4.28 Classification results of steel fasteners in (a) Row 1 (b) Row 2 (c) Row 3 (d) Row 4 using feature s and k calculated from PC1: PEC-GMR measurements of B_x component

Figure 4.28 (cont'd).



4.7 Summary

Crack detection using the PCA analysis has been explored for the automatic inspection of defective fasteners. A feature set has been derived for quantifying asymmetry in GMR images. A strategy using 3-component GMR measurements has been validated for detecting subsurface cracks at steel fastener sites in layered structures.

CHAPTER 5 EC-MR SENSOR SYSTEM – LOW FREQUENCY EXCITATION

5.1 Introduction

The inspection of multilayer structures with buried cracks is examined using a low frequency EC testing with 3D GMR sensors. The experimental inspection of subsurface cracks under steel fastener heads is presented. A FE model that is validated with the experimental EC-GMR images is used to develop data fusion algorithms using 3-component measurements of the magnetic flux density.

5.2 Low Frequency EC-MR Sensing

The multi-line coil in presented in Chapter 3 is excited by a low frequency (100Hz) sinusoidal waveform, which generates a time-harmonic uniform field and linear EC currents. A GMR sensor placed on the line of symmetry measures the single component of magnetic field.

5.2.1 Experimental Set-up

The EC-GMR system consists of signal excitation, signal modulation, signal preparation and signal demodulation. In this section, an analog in-phase/quadrature (I/Q) detection scheme is used. The complex components of a GMR signal can be directly computed. The I/Q detection scheme exploits synchronous AM demodulation which results in a baseband signal whose bandwidth is a function of flaw characteristics. The raw GMR signal is processed for SNR enhancement and then fed into the I/Q detector to calculate in phase (real) and quadrature (imaginary) parts simultaneously. This system diagram is shown in Figure 5.1 (a).

The implementation of I/Q detection is based on the mathematical equations:

$$\begin{aligned} S_s &= A_0 \sin(\omega t) \\ S_{GMR} &= A_n \sin(\omega t + \Phi_n) \end{aligned} \quad (5.1)$$

where S_s is the input excitation signal (also the reference signal) at frequency ω and amplitude A_0 . S_{GMR} is the measured GMR signal at the same frequency but different amplitude A_n and phase Φ_n . The complex sinusoidal field is expanded as:

$$\begin{aligned} A_n \sin(\omega t + \Phi_n) B \sin(\omega t) &= \frac{A_n B}{2} [\cos(2\omega t + \pi) + \cos(\Phi_n)] \\ A_n \sin(\omega t + \Phi_n) B \cos(\omega t) &= \frac{A_n B}{2} [\sin(2\omega t + \pi) + \sin(\Phi_n)] \end{aligned} \quad (5.2)$$

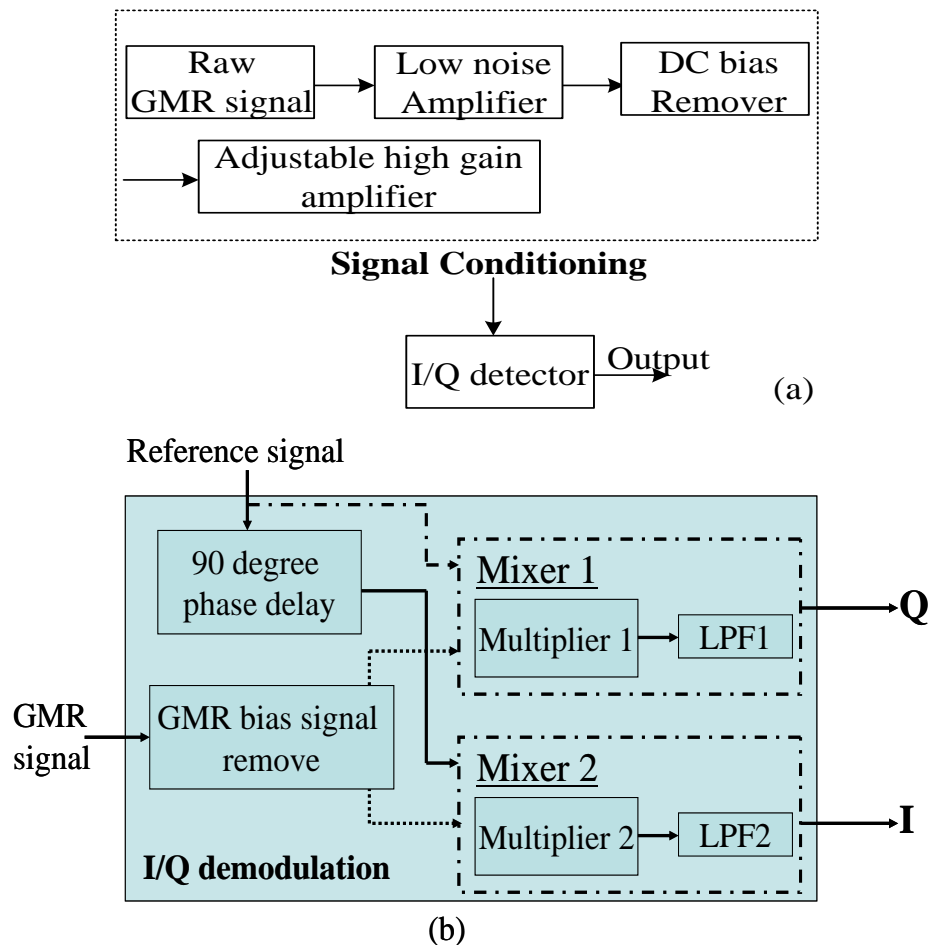


Figure 5.1 Schematic of low frequency EC-GMR system: (a) Experimental Set-up and (b) Signal demodulation

By multiplying the GMR signal with $\sin(\omega t)$ and $\cos(\omega t)$, in-phase and quadrature components are obtained along with a high frequency sinusoidal terms at 2ω frequency. Low pass filtering is used to filter out the AC component ($\cos(\Phi_n), \sin(\Phi_n)$). The Lock-in amplifier is employed to “lock” onto the input signal and maintain the reference output at the proper frequency. The schematic of I/Q demodulation system is displayed in Figure 5.1 (b).

5.2.2 Inspection of Cracks around Steel Fasteners –Normal component

Two rows of steel fasteners in Sample 2 (described in Chapter 4, Figure 4.2) are examined experimentally. Row 1 has corner cracks at right fastener sites and Row 2 has notch cracks through the 2nd layer at left fastener sites. The C-scan images of the normal component B_z are measured at 100Hz excitation frequency and shown in Figure 5.2.

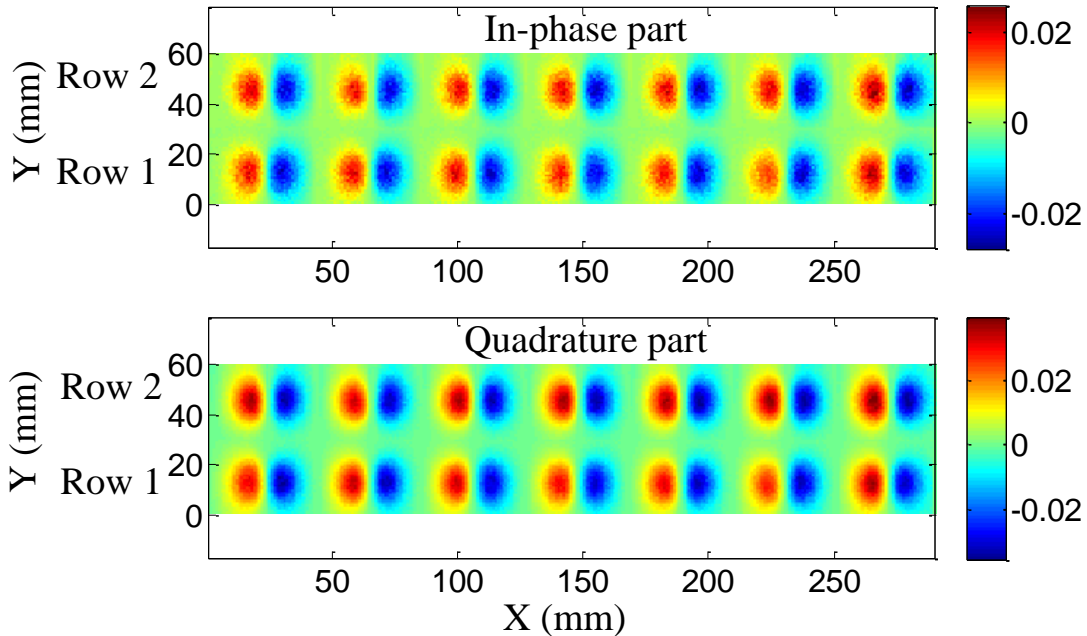


Figure 5.2 C-scan images of steel fasteners in Sample 2 using low frequency EC-GMR measurements: B_z component

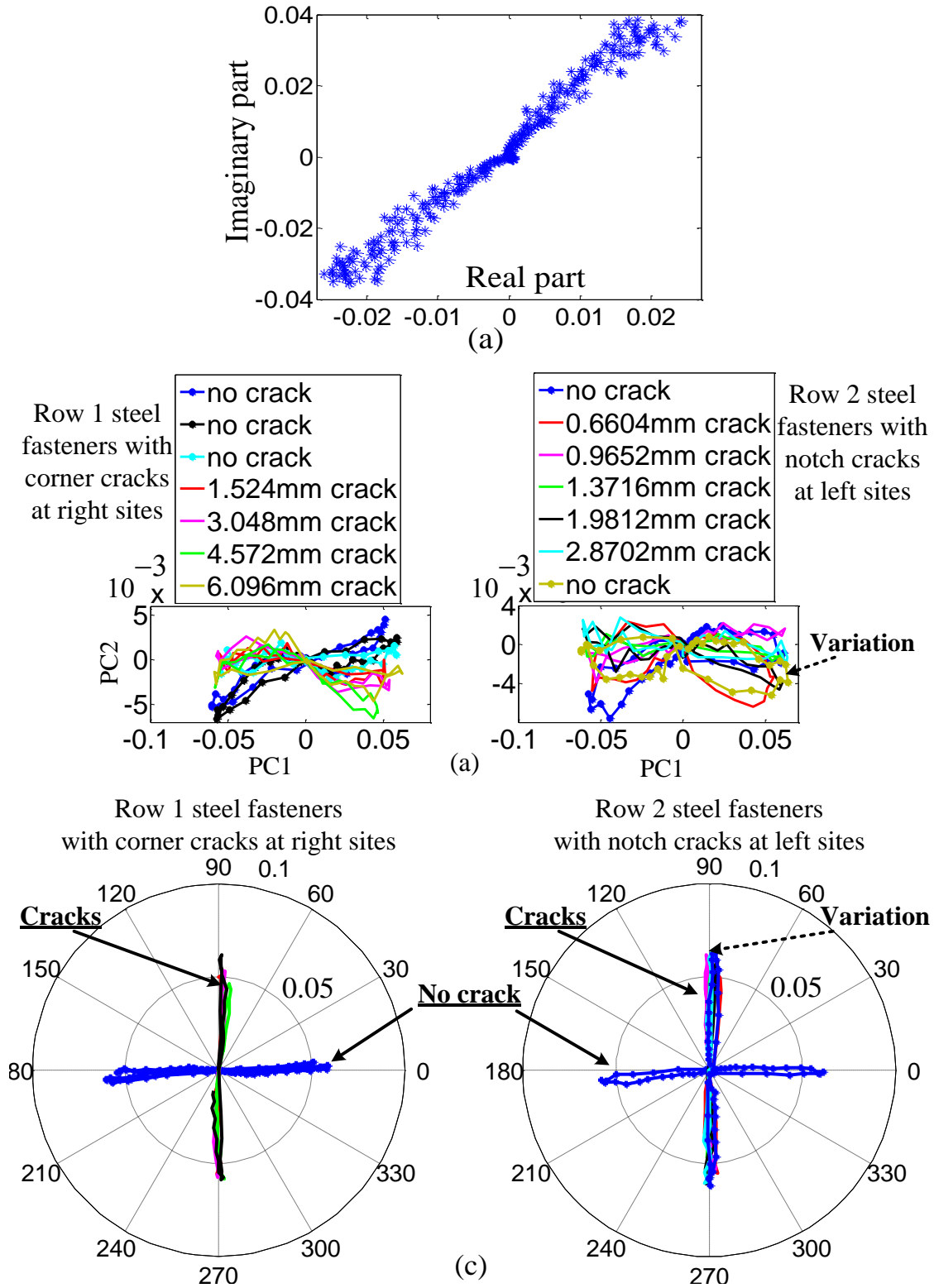


Figure 5.3 Inspection of steel fasteners in Sample 2 using EC-GMR detection: B_z measurements
 (a) Plots of conventional complex trajectories (b) Detection of hidden cracks around steel fastener sites using the PCA method (c) Polar plots with data rotation for automatic detection

Using the conventional method that interprets EC signals in the impedance plane, the Lissajous plots of in-phase part vs. quadrature components are presented in Figure 5.3 (a). These Lissajous plots are from the line scans across the peak value of C-scan images in the complex plane. The defect indications are not easily detectable from these plots. Consequently, the PCA scheme described in Chapter 4 is employed.

The crack detection using the PCA method is applied to the C-scan images of quadrature parts, and the results are shown in Figure 5.3 (b). The data representations in PCs subspace (PC1 and PC2 components) are rotated so that crack data is at 90° and plotted in Figure 5.3 (c). Two clusters that represent fasteners without cracks and fasteners with subsurface cracks are achieved although false calls are also found.

5.2.3 Inspection of Cracks around Steel Fasteners –Tangential component

The results in Figure 5.3 have shown the feasibility of flaw detection in the presence of steel fasteners, using the PCA processing of B_z measurements with a low frequency excitation. In this section, tangential components of low frequency EC field are examined.

The GMR sensor placed at the center of the source coil can be oriented to be sensitive to a selected component of the magnetic field, as displayed in Figure 3.28. The C-scan images of Sample 2 using tangential component B_y at a 100Hz excitation are presented in Figure 5.4.

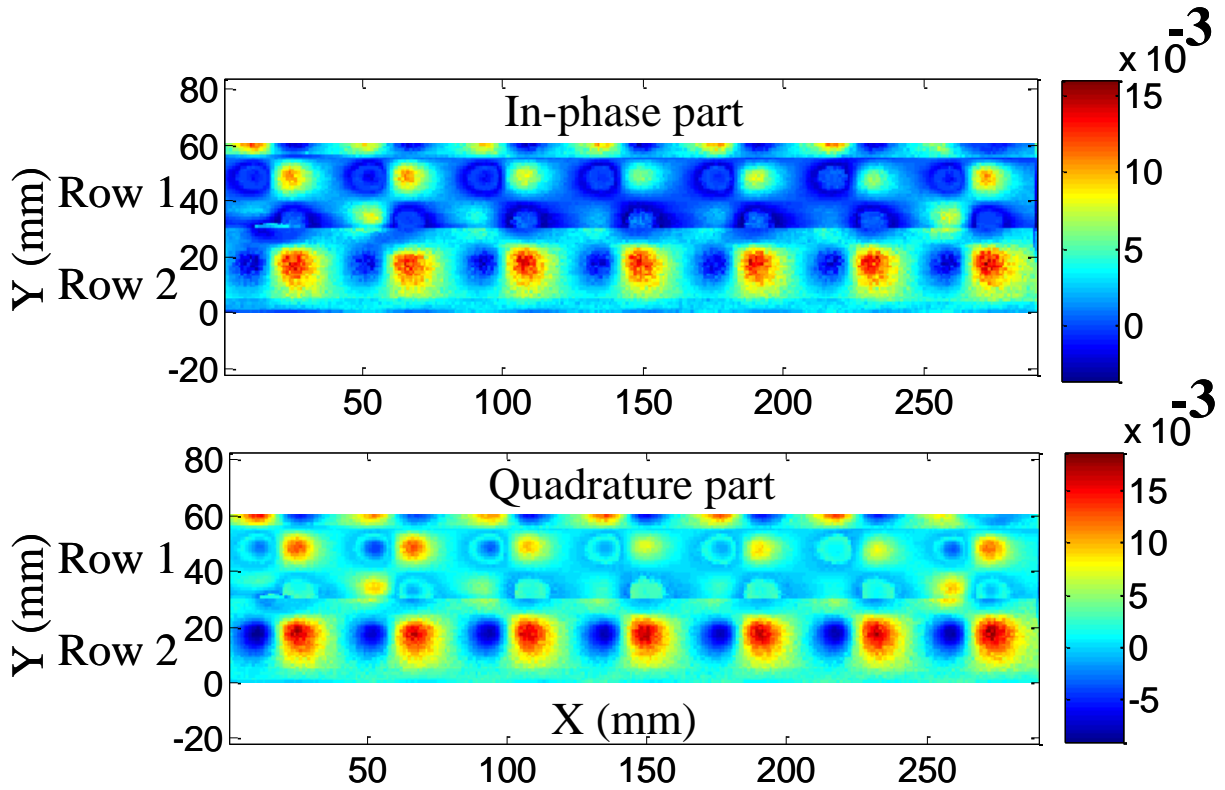


Figure 5.4 C-scan images of steel fasteners in Sample 2 using low frequency EC-GMR measurements: B_y component

The same procedure using the PCA method is applied to enhance the data analysis. Automatic detection is implemented and presented in Figure 5.5. Similarly, the crack information is recovered in the B_y images of quadrature parts of GMR signals, and is indicated after data processing. In summary, it is feasible to use low frequency EC and GMR measurements to detect defective steel fasteners with embedded cracks.

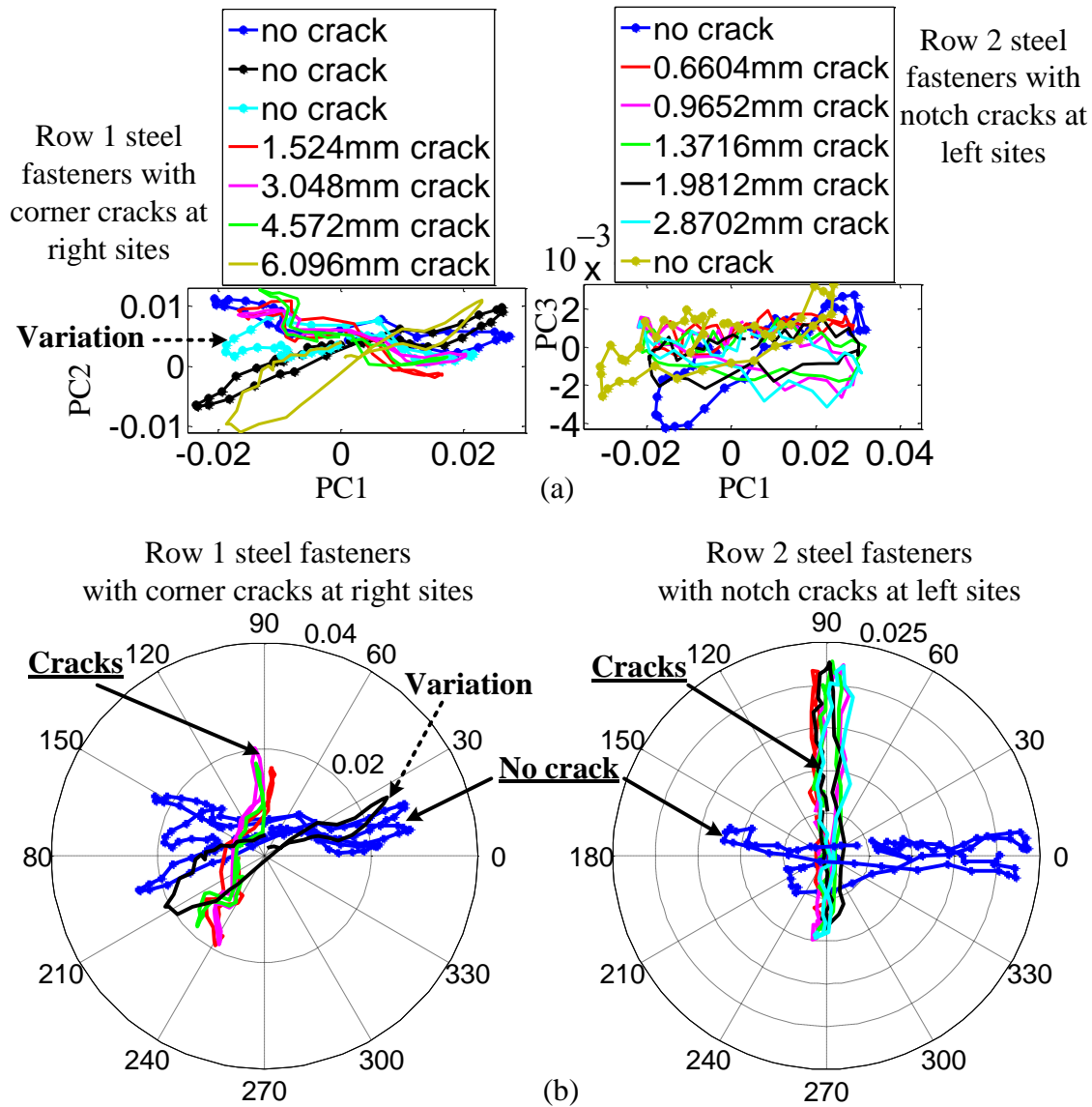


Figure 5.5 Inspection of steel fasteners in Sample 2 using EC-GMR detection: B_y measurements
 (a) Detection of hidden cracks around steel fastener sites using the PCA method (b) Polar plots with data rotation for automatic detection

5.3 Model-based Study of Low Frequency 3D EC-GMR Measurements

The FE model based investigations are performed to enhance the analysis of EC-GMR image data associated with crack identification. C-scan image fusion of three components of time-harmonic magnetic flux density is developed.

5.3.1 FE Model of EC-GMR Imaging

A FE model developed in [26, 156] is used to simulate 3D GMR inspection with low frequency excitation of the multi-line coil. This model employs an infinite sheet coil in place of the used finite and planar coil, which eliminates the need for scanning the sample and meshing the source coil. The $A - V - A$ formulation is used in this FE model.

As shown in Figure 5.6 (a), the excitation current source is a waveform of 100 Hz frequency with a current density J_s along the \hat{y} direction (Y-axis). The infinite current sheet is located at 1 mm above the sample. Homogeneous Dirichlet boundary conditions (values of A or V on the boundary) are imposed to obtain a unique solution. The riveted geometry consisting of a three layer structure is studied. The top layer and the bottom layer are 6.5 mm thick respectively. The 2nd layer is 14 mm thick. The material properties of steel fastener and aluminum plate are incorporated in the model.

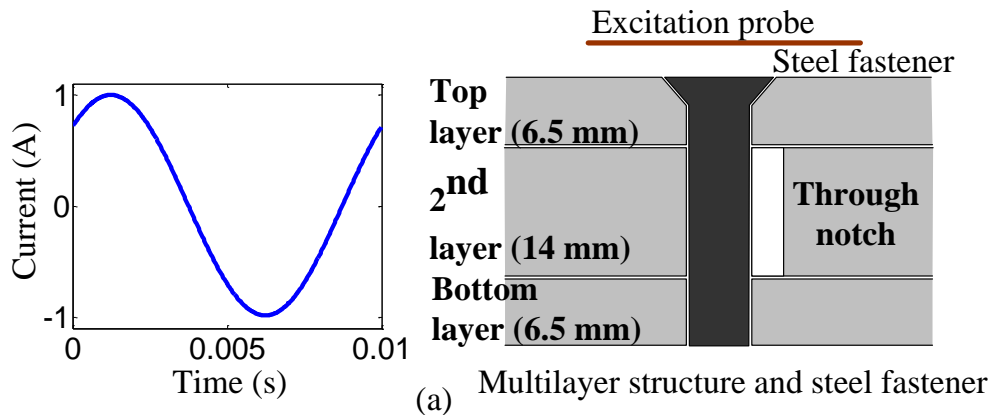
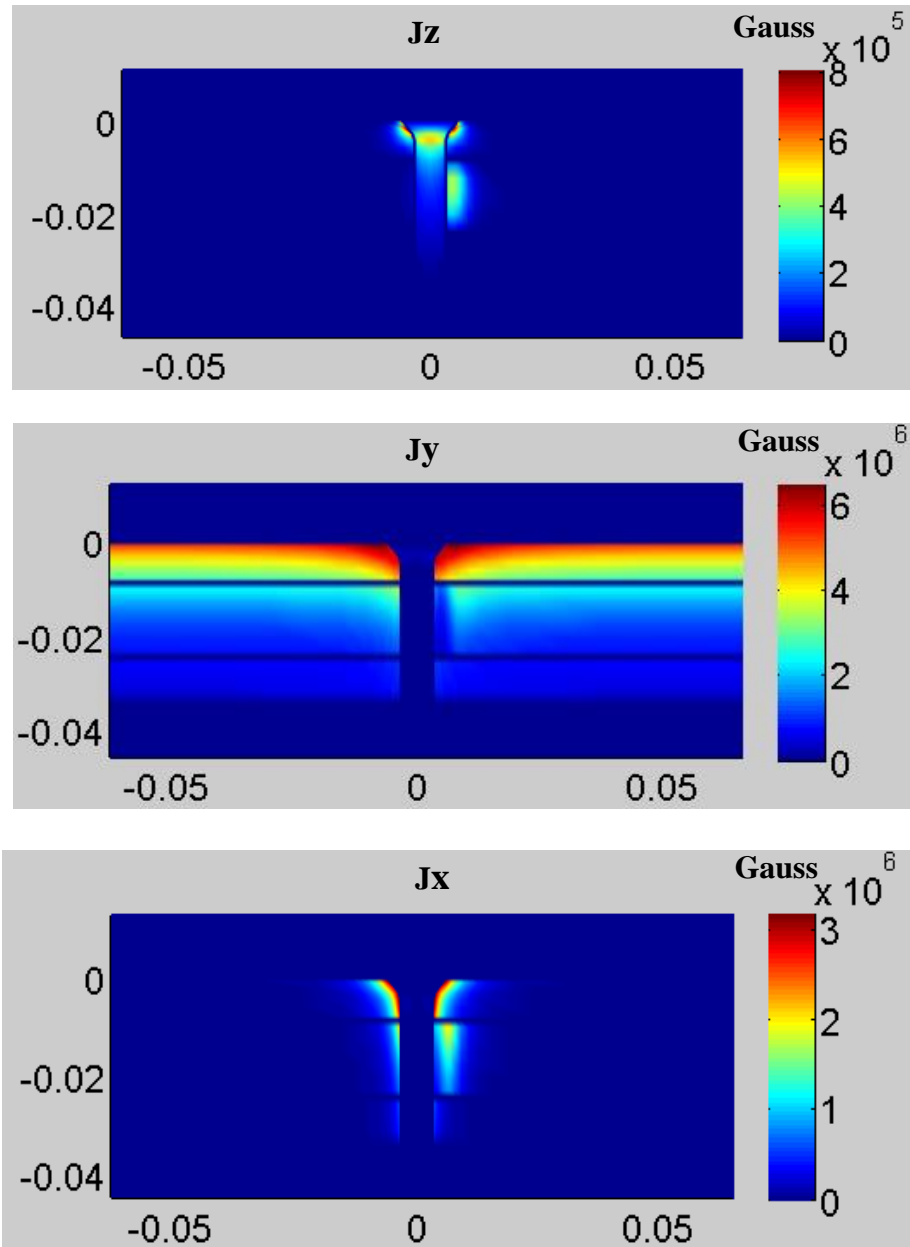


Figure 5.6 Modeling study of a three layers riveted aircraft structure: (a) Test geometry and (b) Distributions of 3D induced currents

Figure 5.6 (cont'd).



(b)

The $\mathbf{A} - \mathbf{V} - \mathbf{A}$ formulation presented in Eq. (3.35) is solved for the unknown nodal quantities.

The induced currents inside the specimen are calculated by Eq. (5.3), and their 3D distributions are

displayed in Figure 5.6 (b)-(d).

$$J_{ind} = \sigma \mathbf{E} \quad (5.3)$$

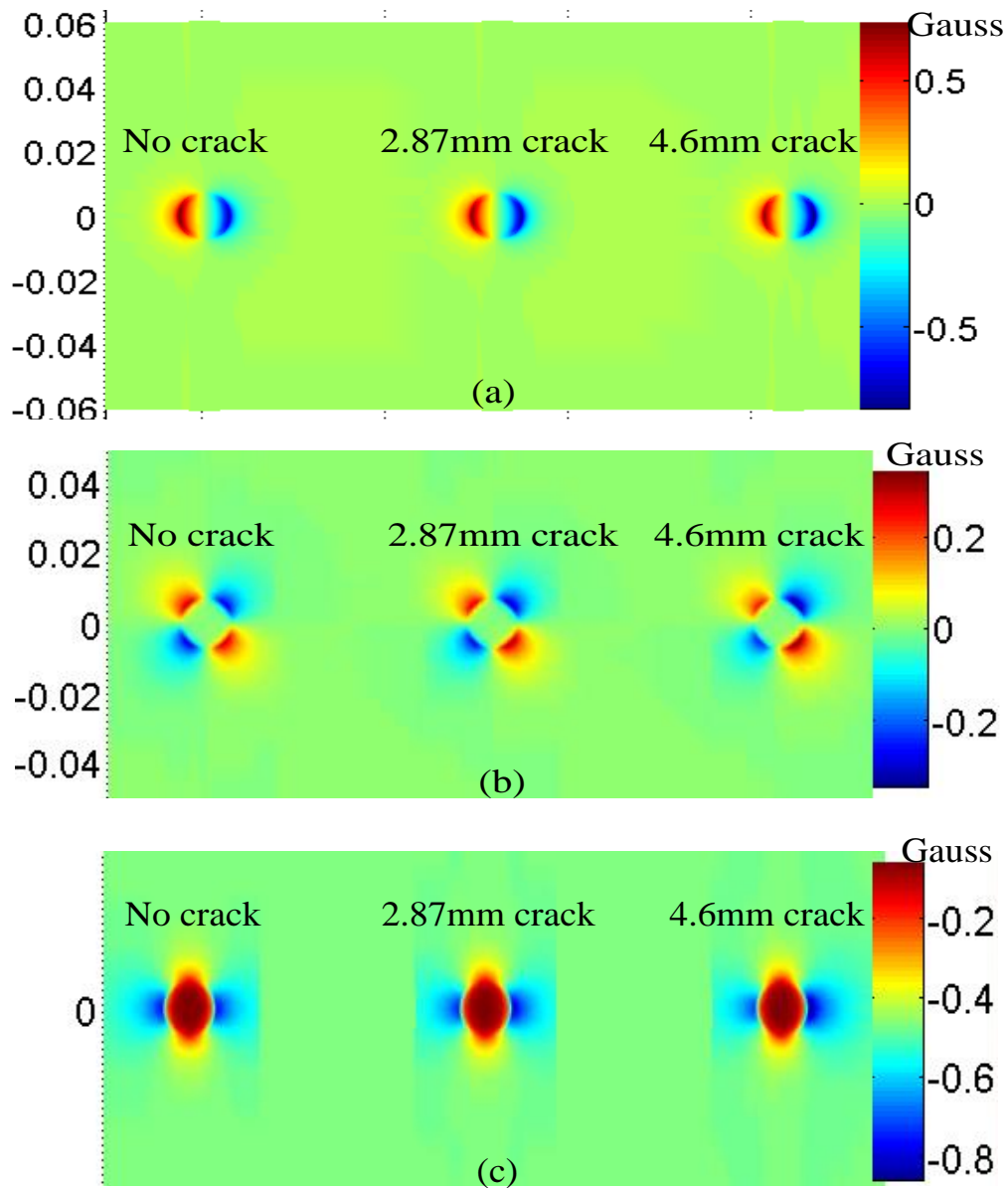


Figure 5.7 Simulation of 3-component C-scan images of three cases: (a) Quadrature part of B_z (b) Quadrature part of B_y (c) Quadrature part of B_x

The C-scan images of 3D magnetic flux density associated with three steel fasteners R1 (no defect), R2 (2.87 mm radial long defect) and R3 (4.6 mm radial long defect) are plotted in Figure

5.7 (a), (b) and (c) respectively. It is observed that the cracks at fastener sites magnify the asymmetry in C-scan images, particularly in the images of tangential components. Additionally, the degree of asymmetry is also related to the length of the crack.

5.3.2 Experimental Validation

The model predictions of 3-component fields are compared with experimental measurements on the defective steel fastener in Figure 5.6. The C-scan images (normalized values of in-phase and quadrature) of B_z, B_y, B_x components are presented in Figures 5.8-5.10 respectively. These results provide a qualitative validation of the FE simulation model for EC-GMR inspection, allowing the use of this model for further investigation of 3-component signals.

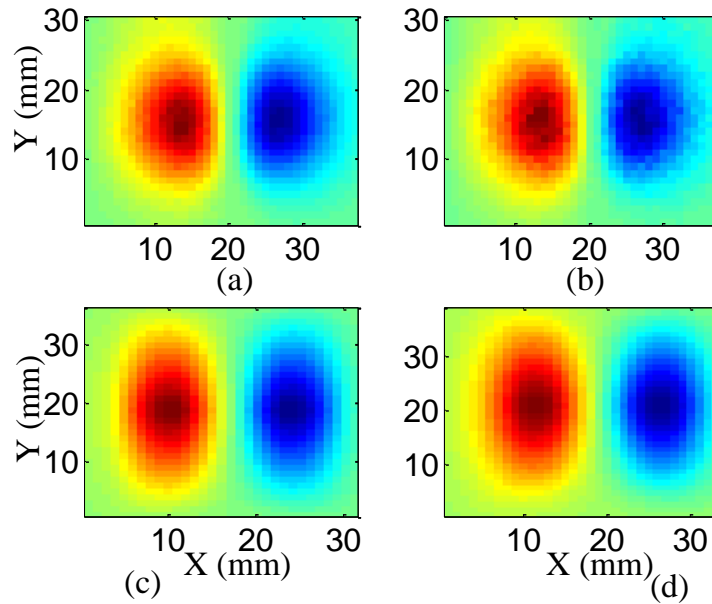


Figure 5.8 Qualitative comparison of experimental and simulation C-scan images of B_z component for a steel fastener with 2.8 mm notch: (a)-(b) Experimental in-phase and quadrature parts (c)-(d) Simulation in-phase and quadrature parts

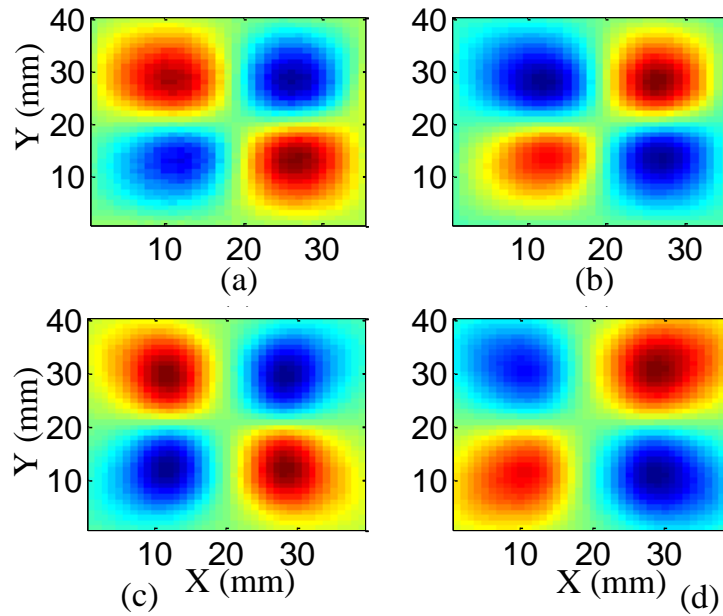


Figure 5.9 Qualitative comparison of experimental and simulation C-scan images of B_y component for a steel fastener with 2.8 mm notch: (a)-(b) Experimental in-phase and quadrature parts (c)-(d) Simulation in-phase and quadrature parts

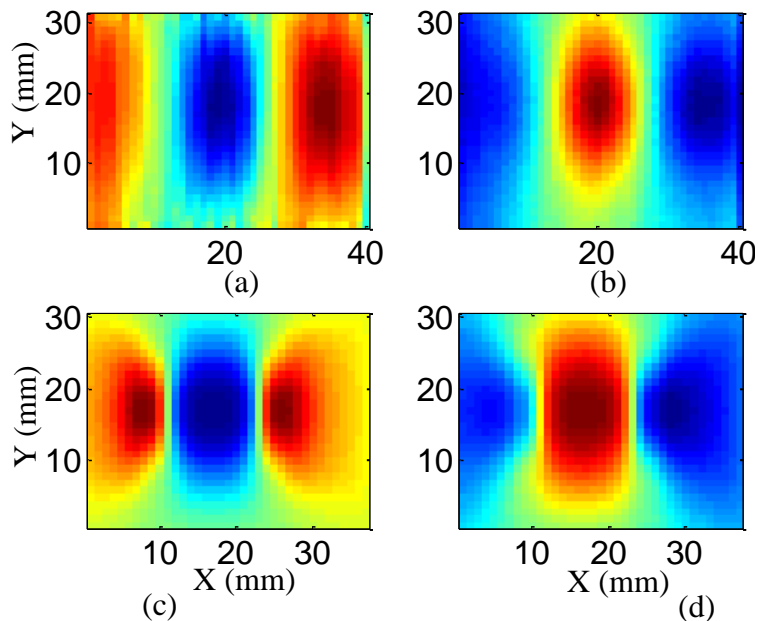


Figure 5.10 Qualitative comparison of experimental and simulation C-scan images of B_x component for a steel fastener with 2.8 mm notch: (a)-(b) Experimental in-phase and quadrature parts (c)-(d) Simulation in-phase and quadrature parts

5.3.3 Image Fusion Method

Based on the prior analysis, a simple image fusion method is investigated to combine the quadrature parts in C-scan images of 3-component data. A simple approach for this fusion is shown schematically in Figure 5.11. Two issues are studied using this linear data processing.

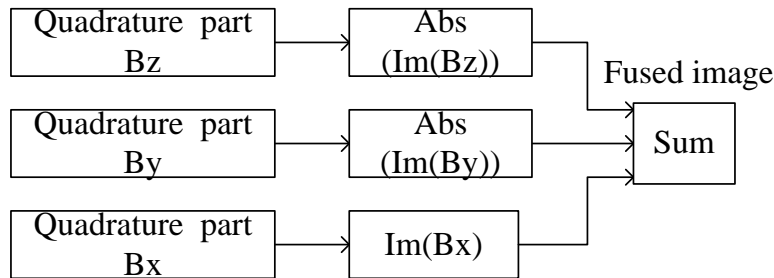


Figure 5.11 Fusion of quadrature parts of the 3-component GMR measurements

5.3.4 Model-based Study – Inspection of Non-ideal Fasteners

A commonly encountered problem in riveted structures is the non-ideal case of a tilted fastener or off-center fastener as shown in Figure 5.12. These imperfect geometric factors also produce asymmetric responses during the inspection, which can be erroneously interpreted as a crack signal [26, 28].

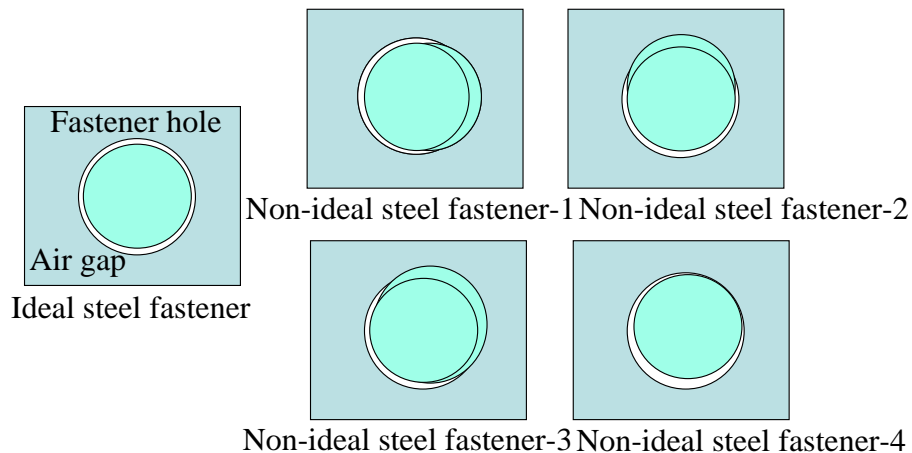
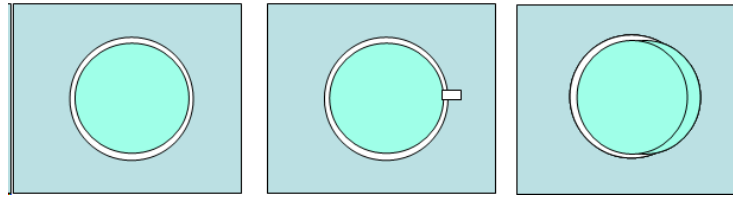


Figure 5.12 Geometries of steel fastener structures: ideal and non-ideal fasteners



No notch steel fastener 2.8 mm notch at steel fastener bottom Non-ideal steel fastener
(a)

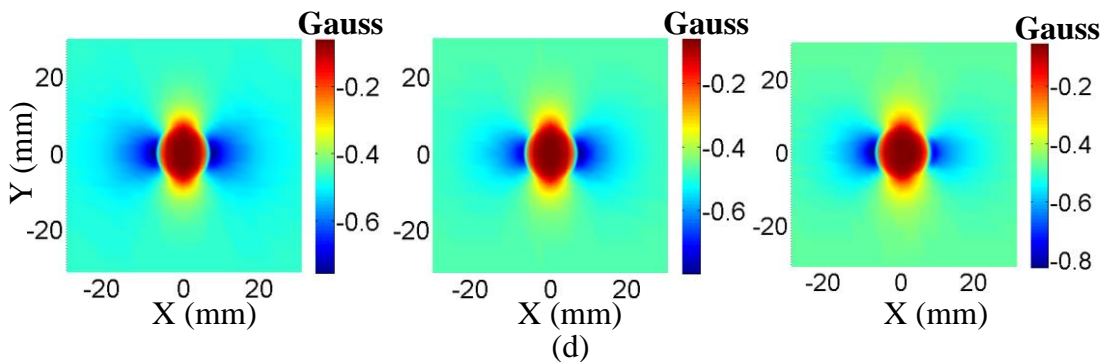
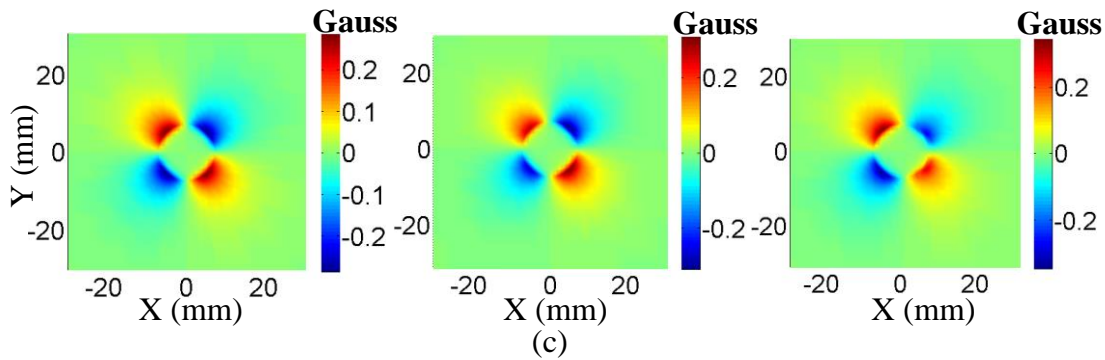
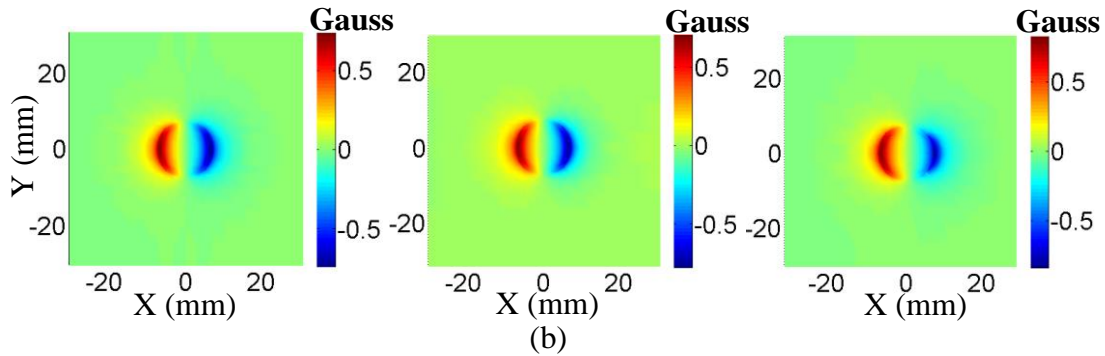


Figure 5.13 Simulation geometries and results: (a) Geometries of three cases: steel fastener without defect (left), with a 2.8 mm notch (middle) and off-centered fastener without defect (right)
(b)-(d) B_z , B_y and B_x components (quadrature parts) for the corresponding cases

Simulation results of the three field components for the cases depicted in Figure 5.13 (a) were computed. The test cases are 1) Ideal fastener with no defect, 2) Ideal fastener with 2.8 mm notch in the 2nd layer and 3) Non-ideal (off-centered) fastener with no defect. The quadrature components of the corresponding simulation fields are shown in Figure 5.13 (b)-(d).

The fused image of three field components is designed to enhance the asymmetry information useful for crack detection relative to the conventional single component method. As seen in Figure 5.14, the results of image fusion serve to suppress the contribution from steel fasteners and enhance the signals due to defect. Figure 5.14 (a) has no features once the fastener contribution is eliminated. In Figure 5.14 (b), an asymmetric image is produced in the presence of a defect. Non-ideal steel fastener yields a fused image in Figure 5.14 (c) with substantially different characteristics from that of a crack.

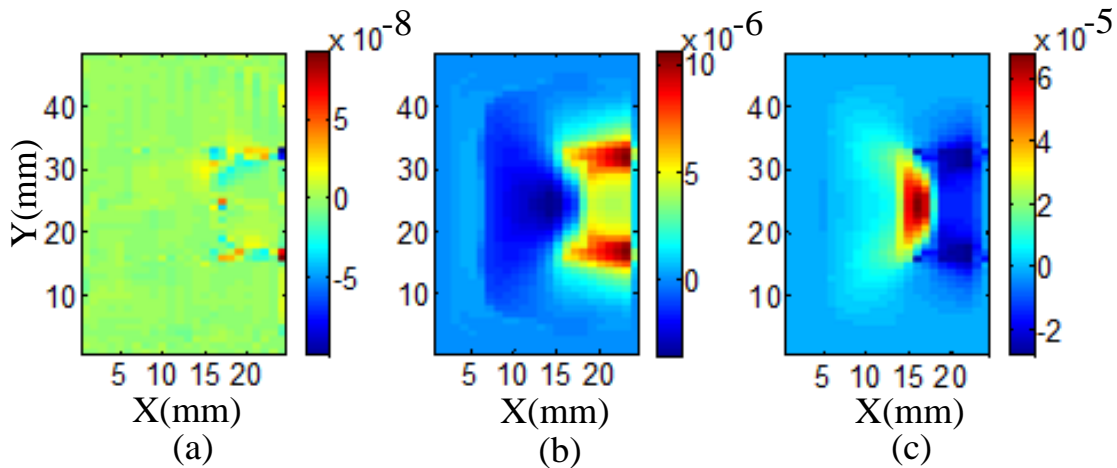


Figure 5.14 Fused images: (a) Defect-free steel fastener (b) Steel fastener with a 2.8 mm notch (c) Off-centered steel fastener

These differences are captured and quantified by means of an algorithm based on PCA method. Specifically, the components PC1 and PC2 corresponding to two largest eigenvectors of the

covariance matrix are computed, which have been utilized for signal representation and crack detection in Chapter 4 and Sections 5.2. Here, the asymmetry of fused image is quantified using the function F_r , defined by the ratio as:

$$F_r = \min(\text{abs}(PC_1 / PC_2)) \quad (5.4)$$

Table 5-1 presents the comparison of feature values for the case of defect-free, defective and non-ideal steel fasteners. It is seen that the fused image of defect-free case produces a feature value close to 0, whereas the asymmetric image of fastener with 2.8 mm notch results in larger values of F_r . In the case of a non-ideal steel fastener, the values of F_r are significantly smaller than that due to a defect.

Table 5-1 Feature F_r quantifying the defective steel fastener.

Steel fastener	Defect size	Ratio feature F_r
Fastener1	0	0.03
Fastener2	2.8 mm	1.1
Fastener3	4.6 mm	2.62
Fastener4	Non-ideal-1	0.57
Fastener5	Non-ideal-2	0.03
Fastener6	Non-ideal-3	0.55
Fastener7	Non-ideal-4	0.001

5.4 Summary

Eddy current testing at low frequency with 3D GMR sensors is studied for the detection of embedded cracks under steel fastener heads. Experimental inspection of a layered aircraft structure has been used to validate the FE model utilizing infinite coil source. Model based studies are then

conducted to effectively study the 3-component measurements of induced magnetic fields.

Signal processing and image fusion of B_z, B_x, B_y data are further investigated to enhance SNR for detecting cracks around steel fastener sites. The inspection of improperly installed fasteners is performed with promising initial results, but more extensive studies are needed using simulation and experimental measurements.

CHAPTER 6 EC-MR SENSOR SYSTEM – ROTATING FIELD EXCITATION

6.1 Introduction

The EC-GMR sensor system presented so far have one drawback in that it is sensitive largely to cracks that are perpendicular to induced current direction. The multi-line uniform coil cannot detect cracks that are parallel to the direction of linear currents [6-7]. Mechanically rotating EC probes around fastener sites can be used to capture flaws in all directions [91-93]. Alternatively, a rotating current excitation can be designed to rotate the fields and currents electrically that generates the uniform sensitivity to cracks at all directions around fastener sites.

6.2 Orthogonal Current Excitation

6.2.1 Rotating Field

The EC-GMR probe is developed in a rotating field mode using two multi-line coils with linear currents in orthogonal directions carrying currents with 90° phase shift. As presented in Figure 6.1, a simple design of linear current sources that are excited in two orthogonal directions is introduced. A rotating current field is generated by the 90° phase difference of the current in two multi-line coils:

$$\mathbf{J}_{rot} = \hat{y}J_0 \pm \hat{x}jJ_0 \quad (6.1)$$

where \hat{y} and \hat{x} are unit vectors along Y- and X-axis, and $j = \sqrt{-1}$ represents the 90° phase shift. These two orthogonal coils are on top and bottom sides of a planar PCB film and share the same geometrical center. The GMR sensor placed at the center of this probe measures the normal component of the total rotating field due to \mathbf{J}_{rot} currents.

$$\mathbf{B}_{rot} = (B_{1r} + jB_{1j}) + j(B_{2r} + jB_{2j}) \quad (6.2)$$

where B_{1r}, B_{1j} are the real and imaginary parts of the field due to $\hat{y}J_0$ and B_{2r}, B_{2j} are the corresponding fields produced by $j\hat{x}J_0$.

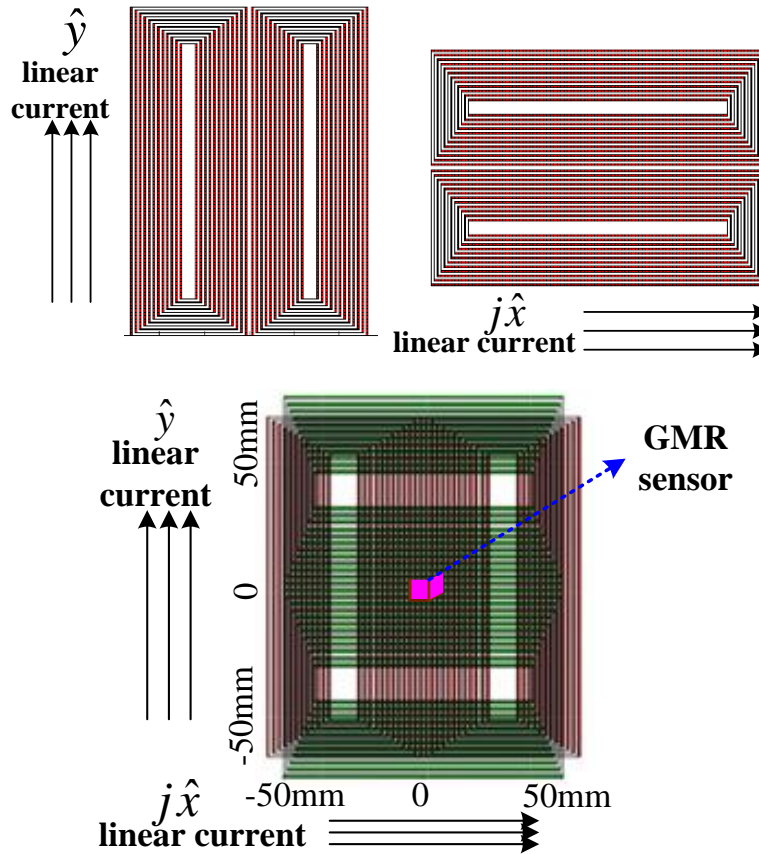


Figure 6.1 Planar multi-line current field: (a)-(b) linear current excitation: linear current field (c) rotating current excitation: rotating current field

6.2.2 Experimental Set-up

The low frequency EC-GMR system in Chapter 5 is extended to two orthogonal coils excited by two sinusoidal sources with 90° phase shift, produced by a function generator. The sinusoidal waveform in 0° phase is locked in as the reference for the I/Q detector. The normal component of the induced flux of the rotating field is sensed by the GMR sensor. The real and imaginary

parts of GMR response are obtained after signal conditioning and demodulation, as show in Figure 6.2.

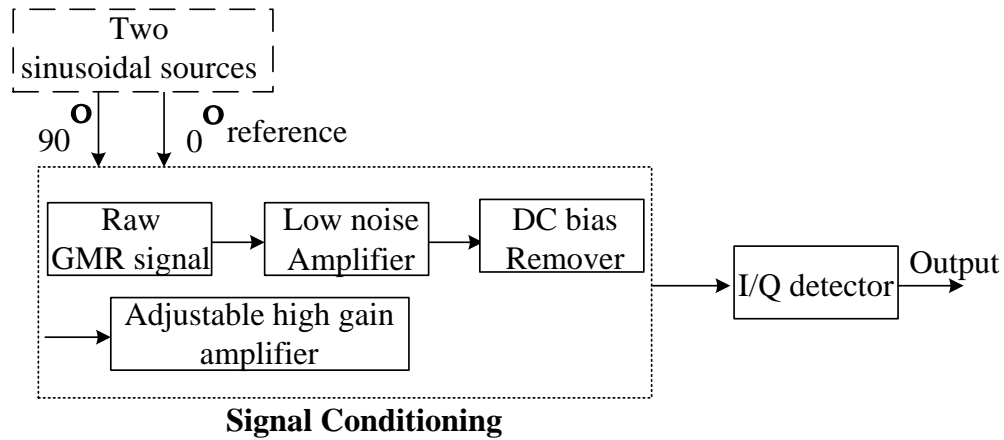


Figure 6.2 Experimental set-up of the rotating current field

6.3 Detection of Crack Orientation at Rivet Site

6.3.1 Parameters in a Practical Design

The rotating field operation is studied with respect to its sensitivity to cracks parallel in direction as shown in Figure 6.3. From the image data in Figure 6.3 (a)-(b), it is seen that the rotating EC-GMR sensor captures the crack orientation successfully. However, the practical design of the rotating current excitation has challenges in that the two orthogonal multi-line coils are located at different lift-off from the specimen surface. Therefore, the magnetic fields generated by two coils need to be normalized or calibrated corresponding to a reference lift-off.

The model-based study of the geometry used in Figure 6.3 addresses this issue and the corresponding results are shown in Figure 6.4. The FE model developed for simulating the EC-GMR system in Chapter 5 is employed in this study. Two cases are considered: Case 1) Ideal rotating current probe - the two coils are at the same lift-off of 1 mm. Case 2) Practical rotating

current probe - coil 1 is at 1mm lift-off and coil 2 is at 2 mm lift-off. The sensor is always considered to be at 2 mm lift-off. Aluminum fastener without a flaw and with a 90° orientation crack is simulated. Crack-free fastener signals for the two cases are used to calibrate the signal from the practical probe (Case 2) as shown in Figure 6.4 (a). This calibration is applied to Case 2 signal from an Aluminum fastener with 90° orientation crack. The calibrated signal from a practical probe is compared to that of an ideal probe signal in Figure 6.4 (b).

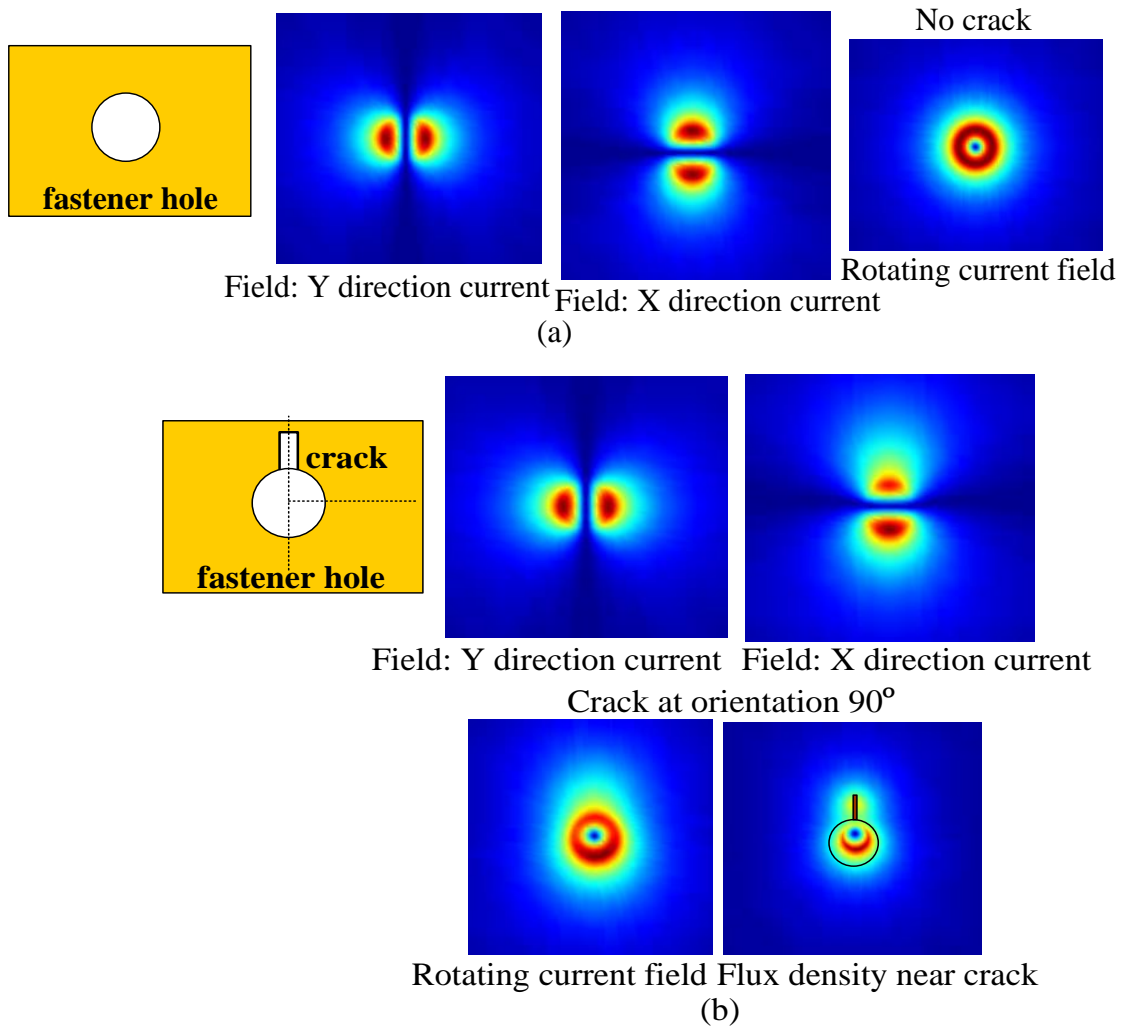


Figure 6.3 Demonstration of crack detection using the rotating field: (a) No crack case and (b) Crack at orientation 90° (parallel to Y direction current)

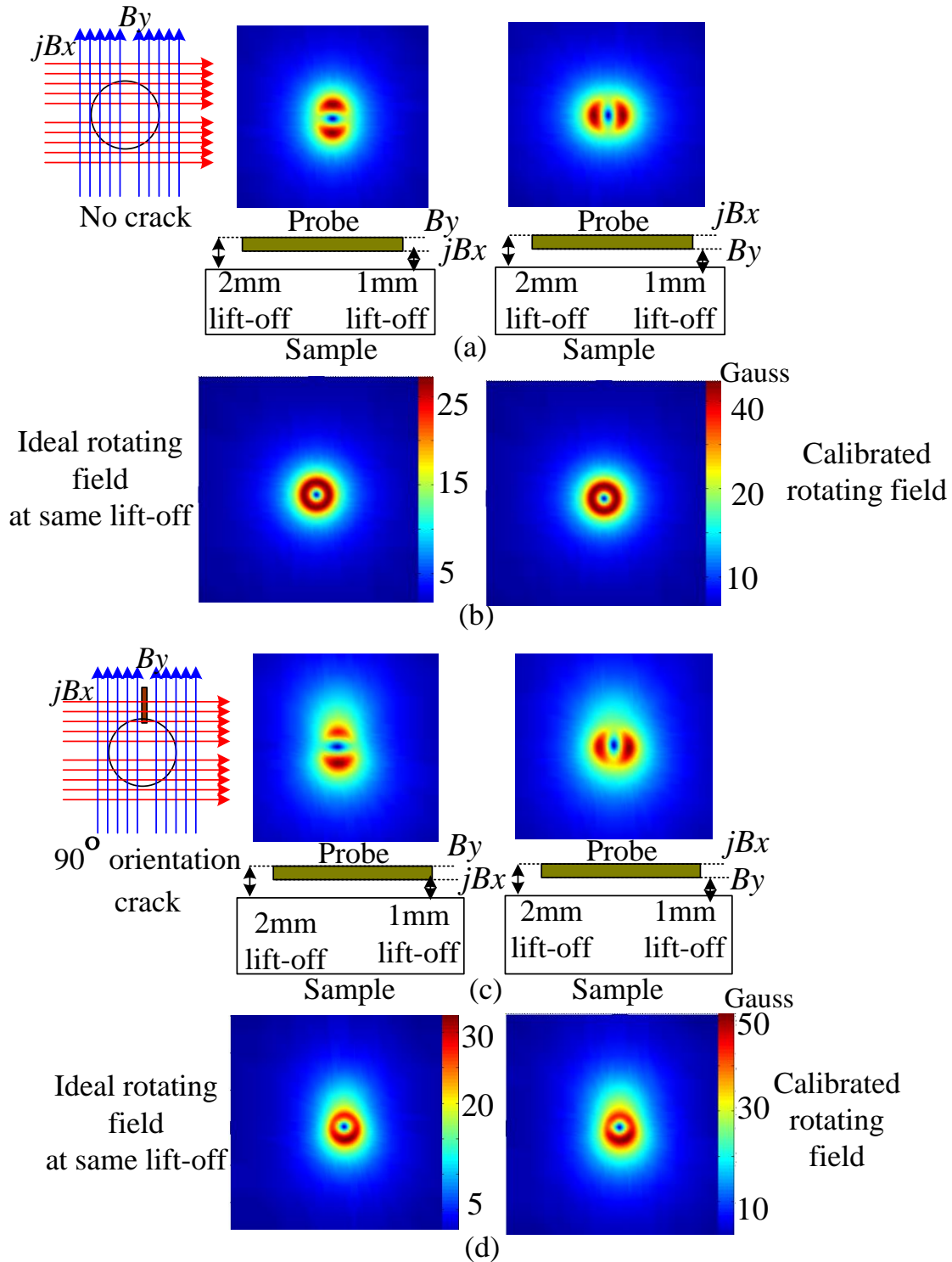


Figure 6.4 Probe lift-off study: (a) Model-based study of rotating field variations for the crack case (b) Model-based study of rotating field variations for the no crack case (c) Calibrated vs. ideal rotating current field for the crack case (d) Calibrated vs. ideal rotating current field for the no crack case

6.3.2 Model-based Investigation of Crack Orientation Detection

Model-based investigations for detecting crack orientations in three-layer riveted lap-joint samples are described in this section. The model uses a low frequency (10Hz) excitation and studies the detection of 8mm cracks through the 2nd layer in all orientations. The simulation results of rotating fields for aluminum and steel fasteners are studied and displayed in Figure 6.5 respectively.

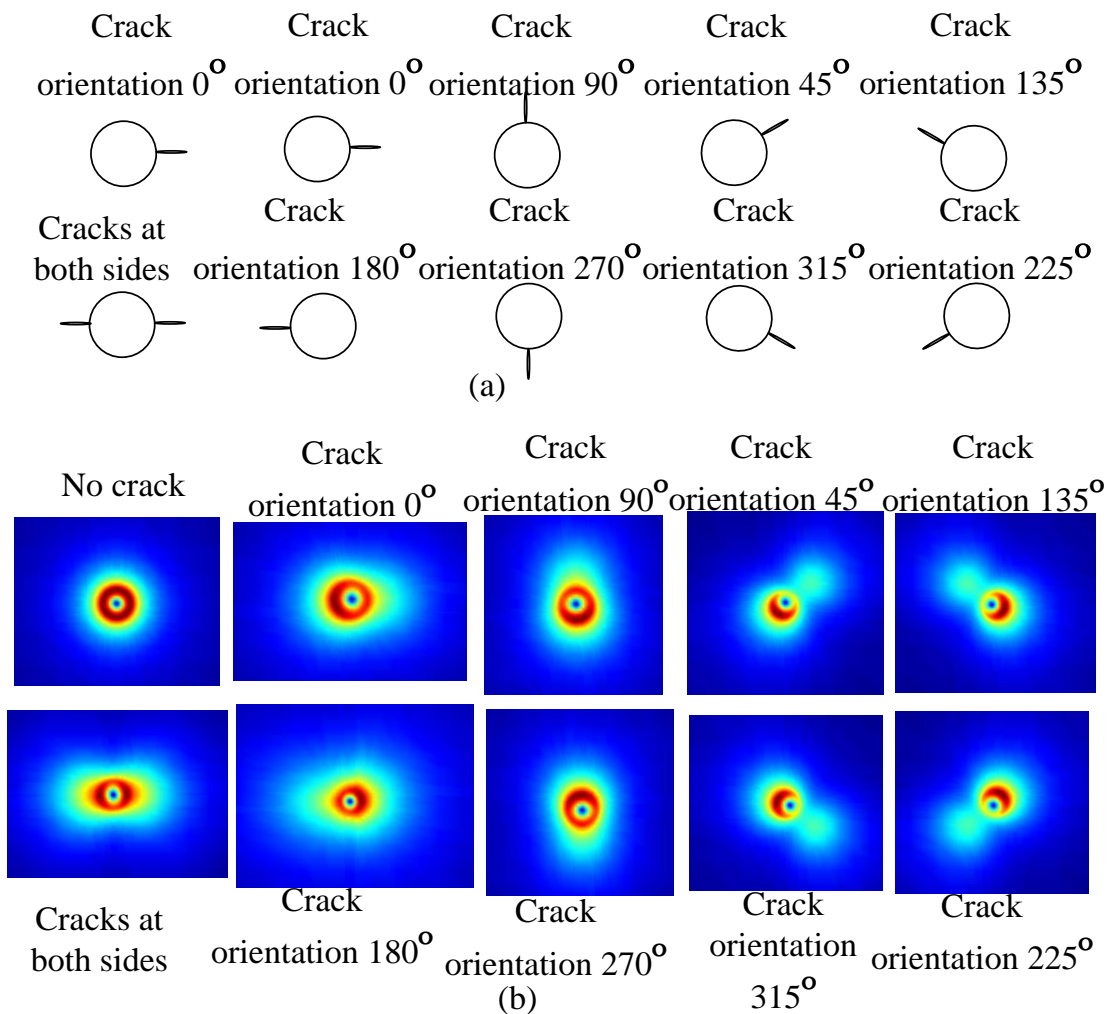
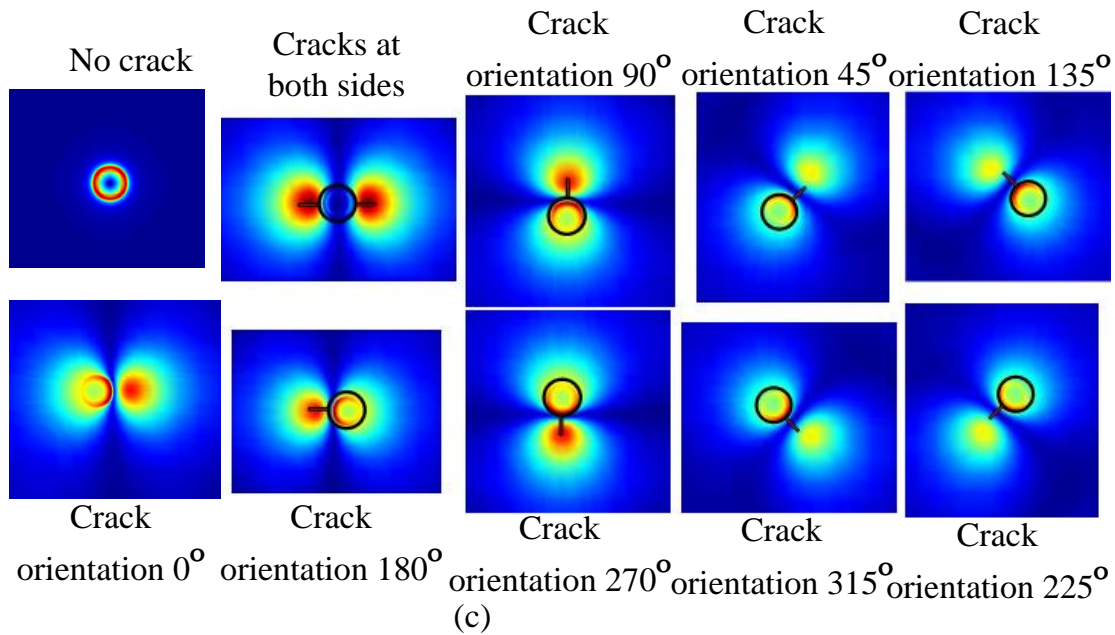


Figure 6.5 Detection of crack orientations: (a) Cracks geometry in all directions (b) Rotating field from cracks around aluminum fasteners (c) Rotating field from cracks around steel fasteners (steel fastener effect removed)

Figure 6.5 (cont'd).



Although the cracks are not easily visible with a single current excitation, cracks in different orientations are captured with rotating current excitation, validating the hypothesis. It should be noted that the data from steel fasteners are first processed to suppress the fastener response.

6.4 Experimental Validation

6.4.1 Experimental Detection of Crack Orientations

EC-GMR measurements using rotating field excitation is first calibrated. In order to compensate for the varying liftoff of the two orthogonal coils on top and bottom sides of a film, two sinusoidal currents with 90° phase shift but different amplitudes are used. In Figure 6.6, a defective steel fastener is tested. The two source currents are operated individually or simultaneously and the GMR sensor located at the center measures the normal component of magnetic field.

C-scan image of single coil operation-top coil is shown in Figure 6.6 (a), and that of the bottom

coil is shown in Figure 6.6 (b). The total rotating field using two simultaneous excitations can detect crack orientation as seen in Figure 6.6 (c).

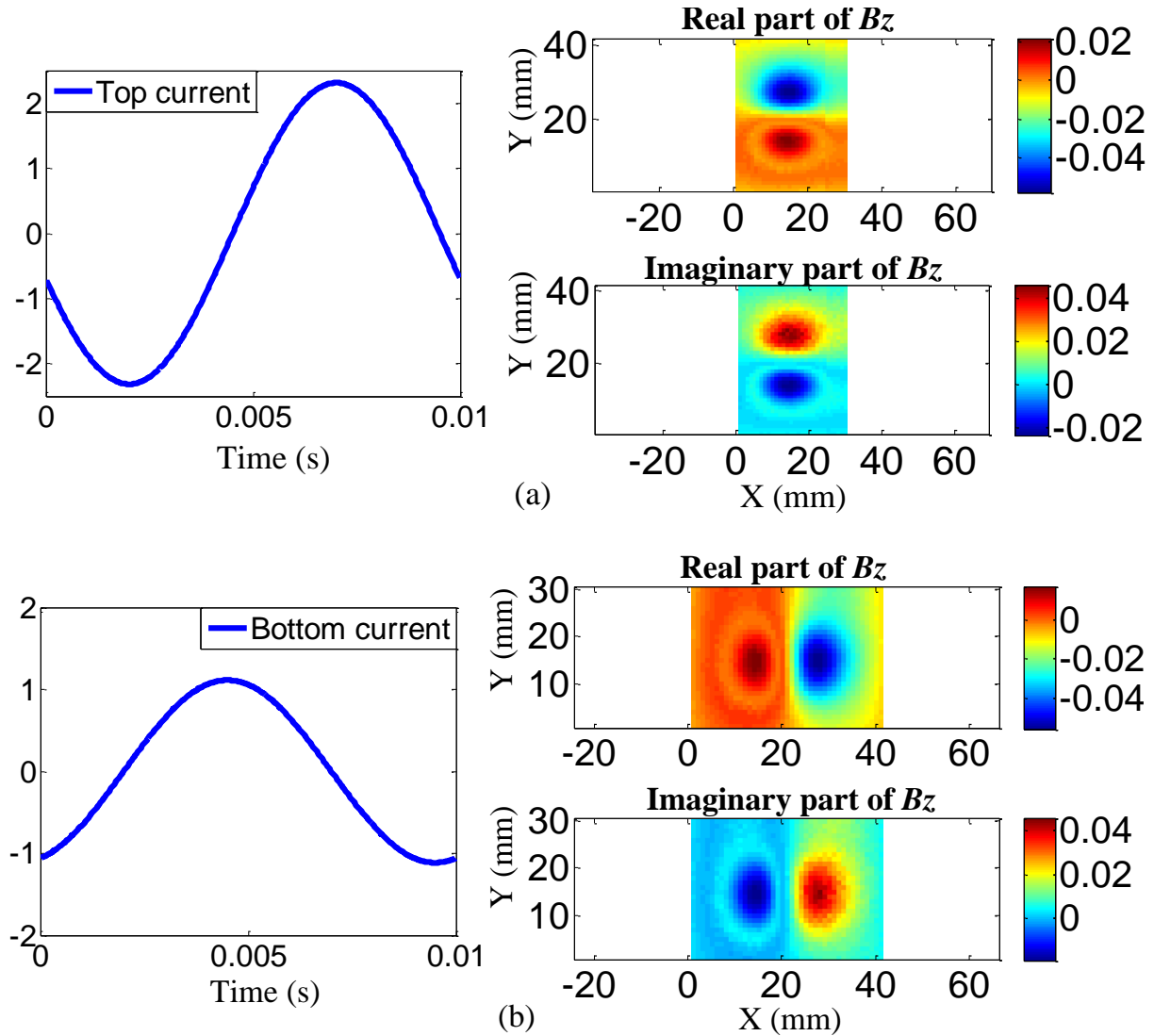
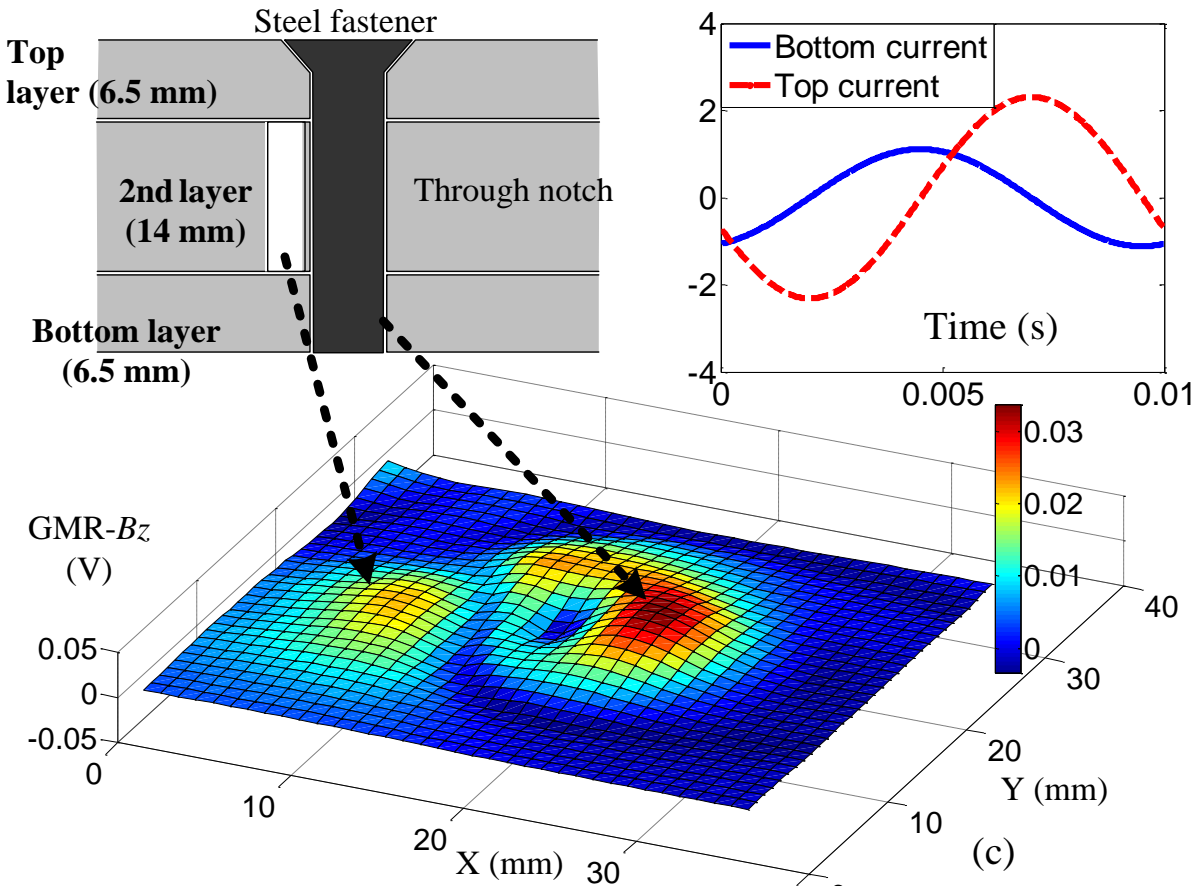


Figure 6.6 Experimental study of rotating field: (a) Field measurement due to the top source coil (b) Field measurement due to the bottom source coil (c) Total rotating field sensitive to a crack

around steel fastener site: absolute value of B_z

Figure 6.6 (cont'd).



Experimental validation of the model-based study was carried out using Sample 2 with steel fasteners. Rotating fields sensitive to different crack orientations are presented in Figure 6.7. The measurements demonstrate the feasibility of the proposed rotating field sensor to detect cracks of all orientations, in a qualitative manner.

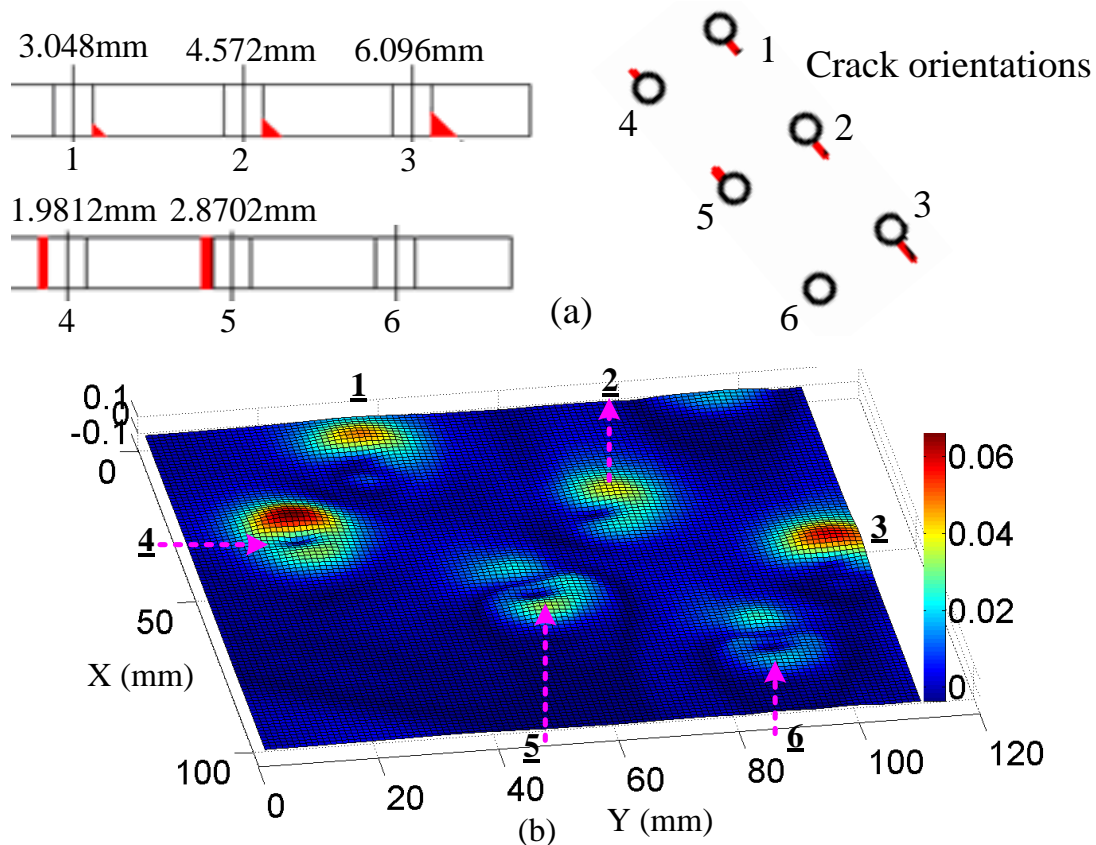


Figure 6.7 Experimental data from cracks with different orientations: (a) Geometry of crack in different orientations and (b) Rotating field measurement

6.4.2 Design of Array Receiver to Crack Orientations

The use of a GMR array receiver is investigated for rapid imaging without moving the probe. The simulation of GMR array measurement is performed using the infinite coil modeling (FE model in Chapter 5), which generates the measured C-scan image of array receiver. Using the single coil excitation on the top side, GMR array measurement of B_z field in the fastener area $40\text{mm} \times 30\text{mm}$ is performed experimentally. The top coil of the rotating current probe is excited and the corresponding GMR images are obtained without probe scan.

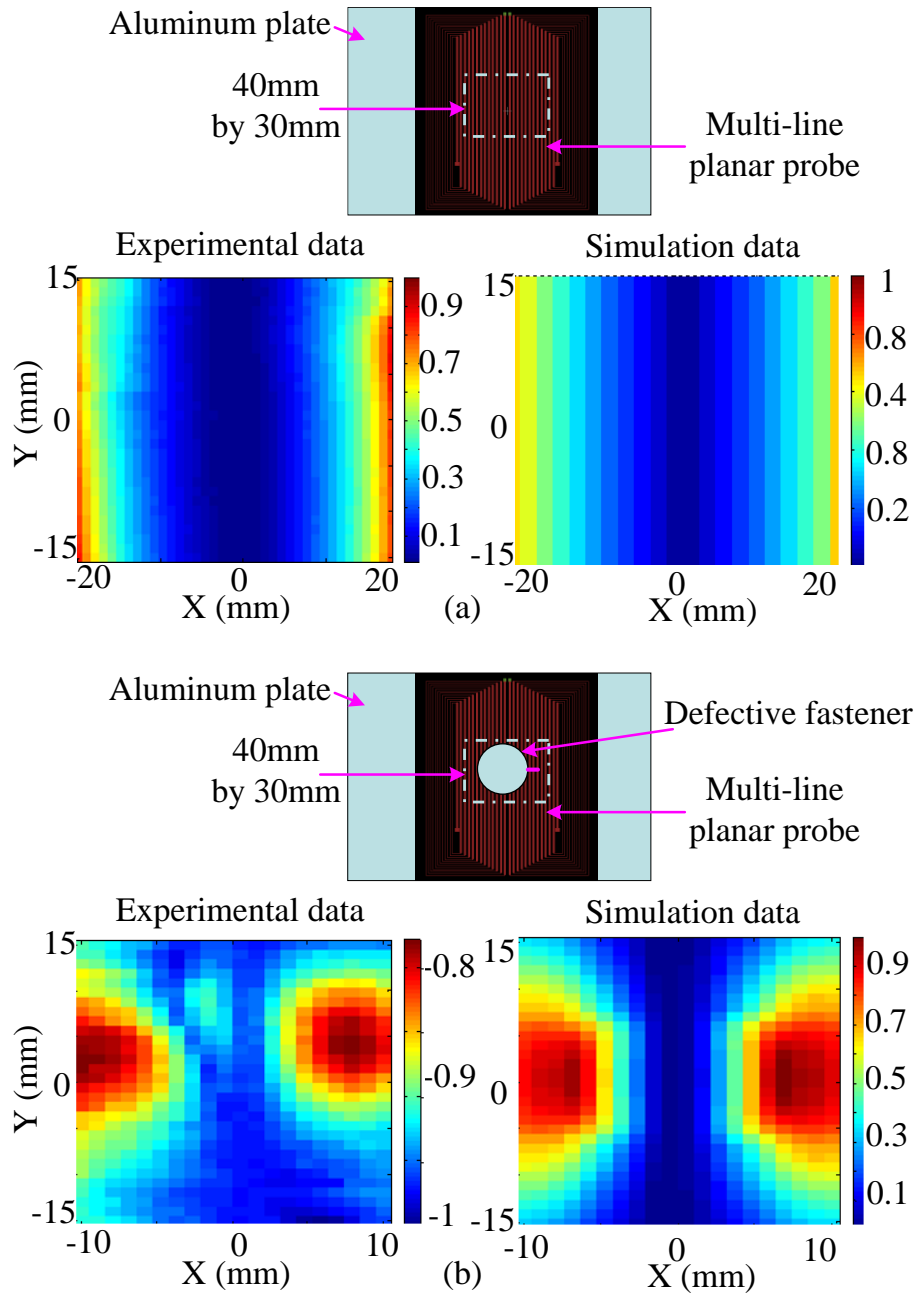


Figure 6.8 GMR image measurement without probe motion: (a) B_z measurement of aluminum plate and (b) B_z measurement of a defective steel fastener

As presented in Figure 6.8, in the case of an aluminum plate (Figure 6.8 (a)) and defective steel fastener (Figure 6.8 (b)), the comparisons between the experimental and simulation data have

presented the feasibility of introducing the GMR array sensors for measuring the normal component of the magnetic field. The image response of the rotating current excitation is sensitive to all crack orientations and can be measured by the GMR array receiver, as demonstrated in Figure 6.9.

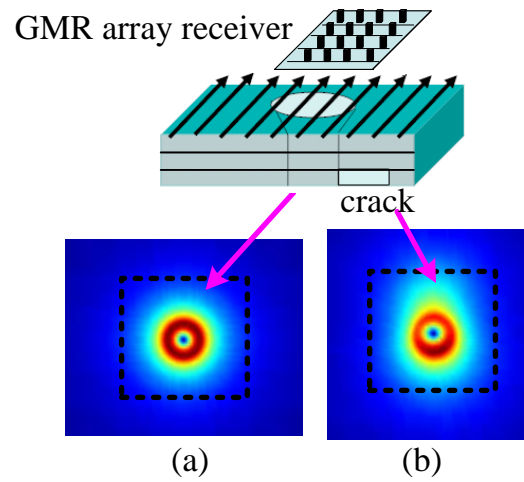


Figure 6.9 Application of GMR array receiver: B_z fast image measurement of fastener using rotating field (a) Without crack and (b) With crack at 90° orientation

6.5 Summary

An EC-GMR system with orthogonal current excitation, that produces rotating currents, is developed for inspecting thick riveted multilayer structures with cracks in all directions. Capability of the sensor to detect cracks of all orientations at fastener sites was demonstrated using simulation and experiments. FE model based studies and experimental measurements validate the hypothesis. The model based study was used to optimize the design of a practical probe. More extensive experimental work to detect subsurface flaws in all directions need to be performed in the future.

CHAPTER 7 PARAMETRIC STUDY OF EC-GMR DETECTION SYSTEM

7.1 Introduction

In a practical inspection scenario, signals measured by GMR sensors depend on several parameters such as lift off, sensor tilt, top and bottom layer conductivity, and edge effect. In particular, the signals are affected by slight tilts of the sensor which alters the probability of detection of subsurface defects. A parametric study is conducted to analyze variations in signal due to sensor tilt. The FE model is applied to investigate changes in defect signals in the presence of sensor tilt. A procedure for rendering the signals invariant under sensor-tilt is also proposed.

7.2 Sensor-tilt Study

7.2.1 Sensor-tilt of GMR Sensing

During the inspection of riveted samples, variations in EC-GMR probe lift-off from the sample and sensor wobble resulting in sensor tilt can occur. As illustrated in Figure 7.1, this affects the fields measured by the sensor since only the component of B_z normal to the sensor is measured according to Eq. (7.2). Also, induced magnetic fields associated with eddy currents through the sample are no longer uniform distributions. Consequently, some asymmetry of image data is seen to occur even when no crack is present.

$$V_{GMR} \propto B_{GMR} = B_z \quad (7.1)$$

$$V_{GMR} \propto B_{GMR} = B_z \times \cos(\theta) - B_x \times \sin(\theta) \quad (7.2)$$

7.2.2 Model-based Investigation of Sensor-tilt

A systematic study of the effect of GMR sensor-tilt is performed using the FE model. In this study, the application of an infinite coil that is used for modeling the multi-line coil in Chapter 5 obviates the need for simulating the scan operation. Therefore, the FE model using $A_r - V - A_r$ formulation is implemented to study the finite coil and its sensor-tilt scenario.

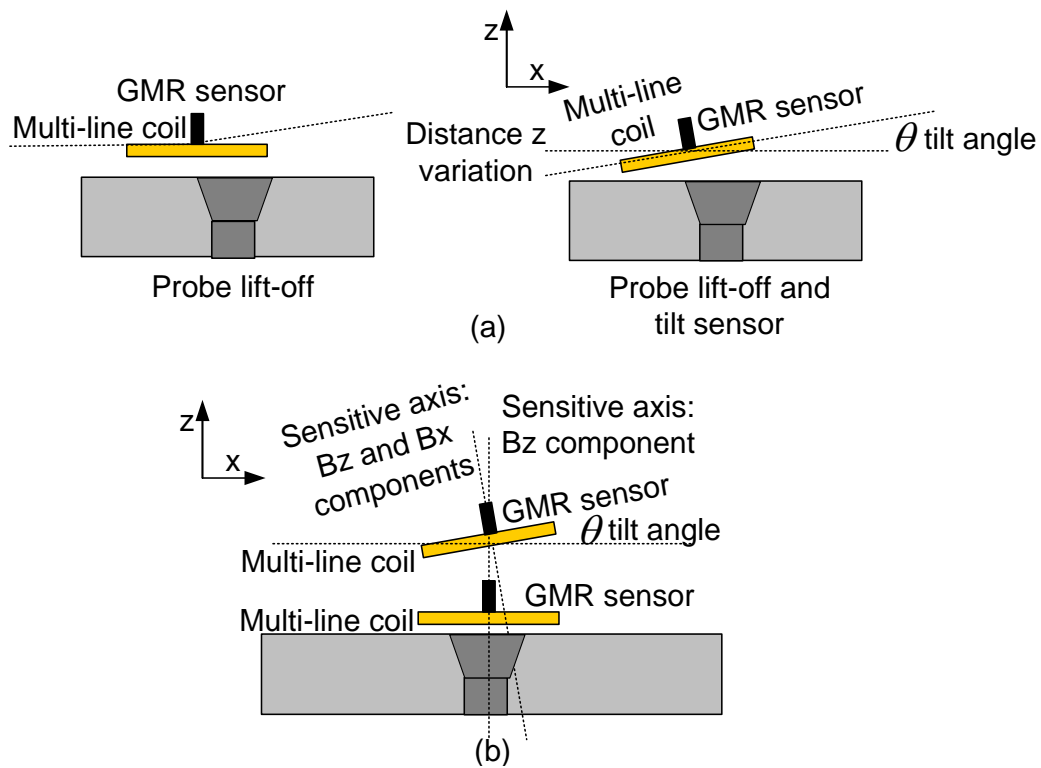


Figure 7.1 Sensor-tilt variations: (a) Probe lift-off and tilt sensor and (b) GMR sensor measurements of magnetic field components

Model-based study is conducted using a three-layer aluminum sample with aluminum fasteners. The sample thicknesses are 6.5 mm (top layer), 14mm (middle layer) and 6.5mm (bottom layer). Excitation frequency is 100 Hz and current density J_s is along \hat{y} direction. The cracks are 2nd layer through-wall Electrical Discharge Machined (EDM) notches of different lengths in x

direction. GMR sensor measures the normal component under normal (0^0) and tilted ($-2.5^0 : 2.5^0$) states, as shown in Figure 7.2. The magnetic field measured by the GMR sensor is calculated by Eq. (7.2) for normal, positive and negative tilt angles.

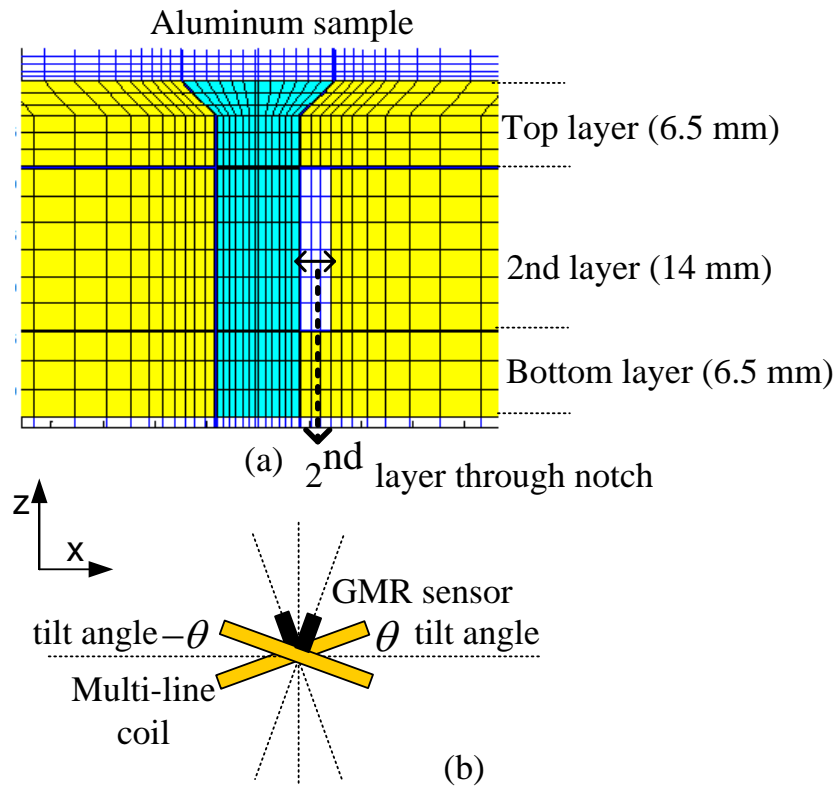


Figure 7.2 Sensor-tilt measurement: (a) Geometry and FE mesh of tested sample: three-layer riveted structure and (b) Definition of tilt degrees in two directions

Figure 7.3 presents the real and imaginary parts of GMR signals under tilt variations for the case of a crack-free fastener geometry. It is seen that the measurements of both normal and tangential components introduce asymmetric image data that is normally interpreted as existence of a flaw. This could potentially results in false calls. It is hence necessary to render GMR signals insensitive to sensor tilt while preserving sensitivity to defects.

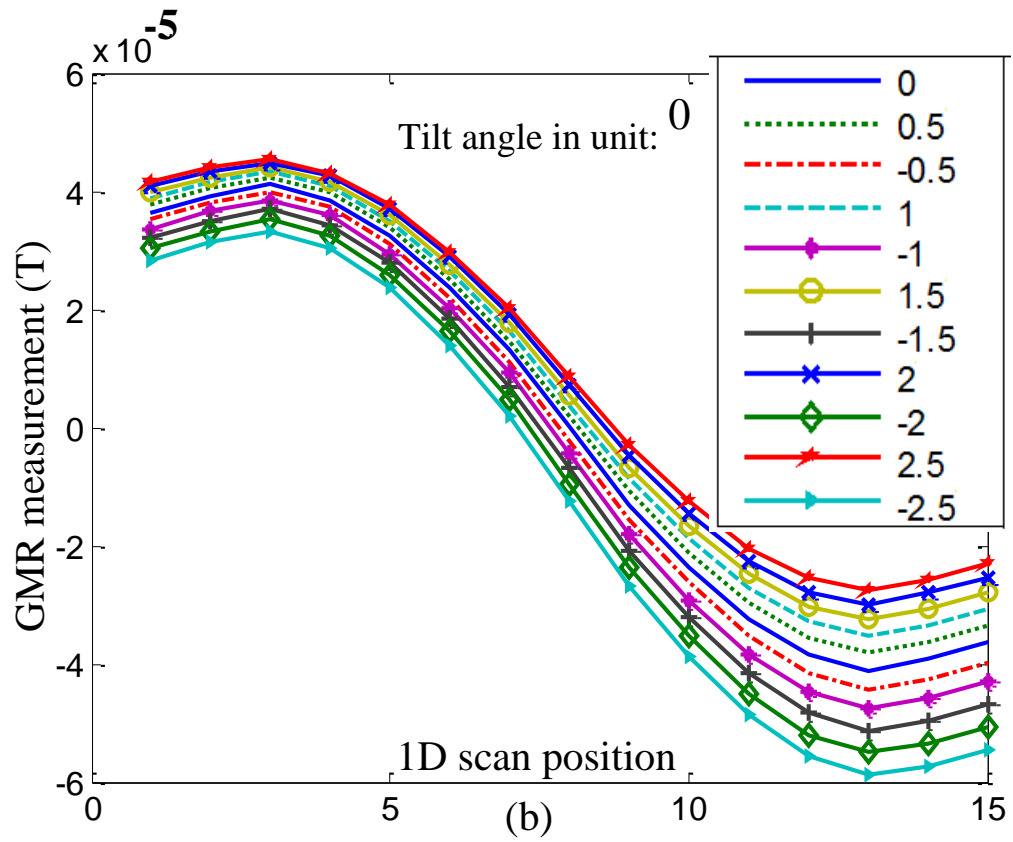
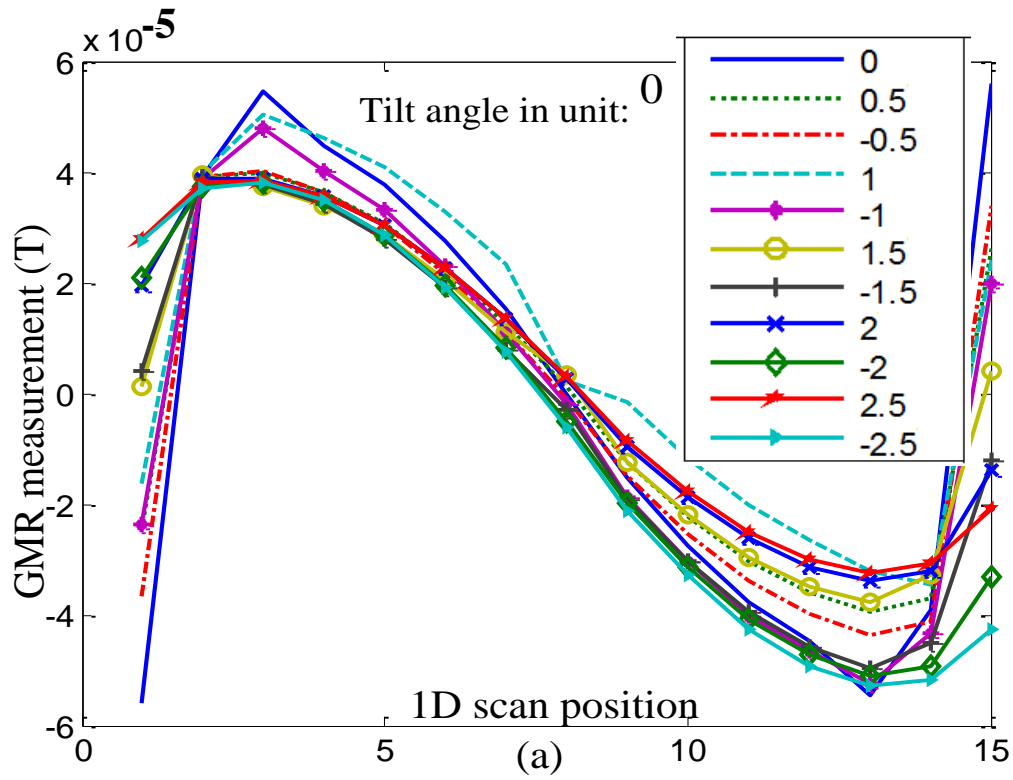


Figure 7.3 Magnetic field measured under tilt GMR sensor for a crack-free fastener: (a) Real part of signals and (b) Imaginary part of signals

7.3 Invariant Analysis

Techniques for invariant pattern recognition have been studied to achieve invariance to specified operational parameters and preserve crack information in NDE applications [180-182]. Invariance schemes have been developed in magnetostatic flux leakage and eddy current NDE, to eliminate sensitivity to permeability or lift-off variations respectively. A novel invariance analysis with regard to sensor tilt is explored here.

7.3.1 Transformation for Invariance to Sensor-tilt

Independent component analysis [183-184] is a useful signal-processing tool to separate multiple unknown sources [171, 177]. In this section, the ICA analysis is applied to transform the GMR measurements insensitive to sensor-tilt variations. Assuming the GMR measurements under n tilt states to be composed of multiple signal components, the GMR signal g_j at the j th tilt state is expressed as a linear combination of m independent components (ICs):

$$g_j = a_{j1}s_1 + a_{j2}s_2 + \dots + a_{jm}s_m, \quad j = 1, 2, \dots, n \quad (7.3)$$

where components s_1, s_2, \dots, s_m are zero mean random variables that are mutually independent and elements $a_{j1}, a_{j2}, \dots, a_{jm}, j = 1, 2, \dots, n$ are mixing coefficients. A vector-matrix notation of Eq. (7.3) is represented as:

$$G = AS \quad (7.4)$$

where A is coefficient matrix and row components of S are estimated ICs.

The scheme for invariant transformation is depicted in Figure 7.4. Simulations of 11 GMR signals are measured with tilt angles in the range $[-2.5^0 : 0.5^0 : 2.5^0]$ and 15 scan positions. Tilt signals are computed by Eq. (7.2). Linear interpolation is used to generate signals from other

sensor-tilt angles to get a dense set of measurements. After the interpolation, the GMR measurements are re-sampled as an input vector $T = [t_1, t_2, \dots, t_p]$, where p is the total number of signals for ICA analysis. The RobustICA Matlab module is used for ICA decomposition. The measured GMR signal (with or without sensor-tilt effect) is expressed as a linear weighted sum of ICs with weight coefficients.

$$\begin{bmatrix} t_1 \\ t_2 \\ \vdots \\ t_p \end{bmatrix} = \begin{bmatrix} a_1 & a_2 & \dots & a_p \\ & & & \vdots \end{bmatrix} \times \begin{bmatrix} s_1 \\ s_2 \\ \vdots \\ s_p \end{bmatrix} \quad (7.5)$$

Invariance transformation is obtained by projecting GMR signals T onto the ICs domain to generate transformed signals D .

$$D = \begin{bmatrix} d_1 \\ d_2 \\ \vdots \\ d_p \end{bmatrix} = \begin{bmatrix} t_1 \\ t_2 \\ \vdots \\ t_p \end{bmatrix} \times \begin{bmatrix} a_1 & a_2 & \dots & a_p \\ & & & \vdots \end{bmatrix} \quad (7.6)$$

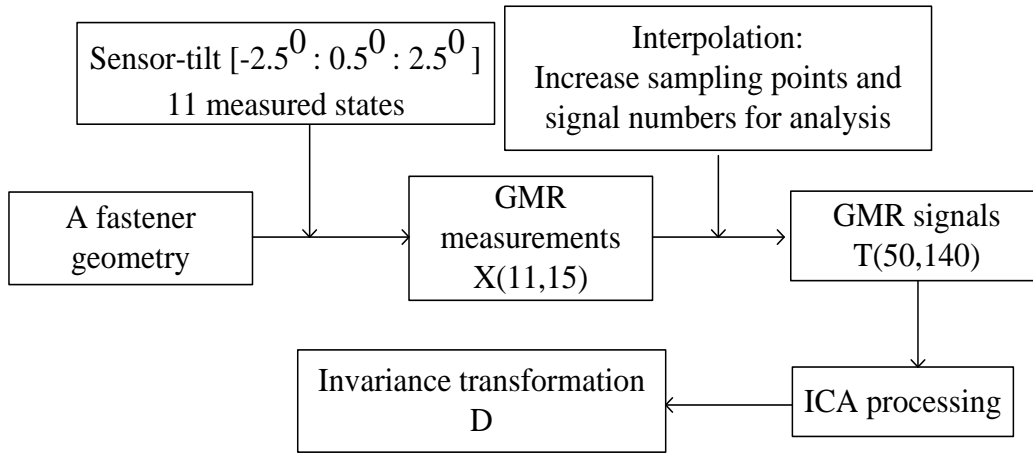


Figure 7.4 Diagram of ICA based transformation invariant to sensor-tilt

7.3.2 Invariance Transformations of GMR signals

The invariance processing is implemented on the signals in Figure 7.3 and the results are presented in Figure 7.5. The GMR signal is a linear combination of conventional measurement and signal caused by sensor tilt. Hence sensor-tilt effects serve as an interference source that should be suppressed relative to crack indication. The results of suppression of the contributions of sensor tilt are shown in Figure 7.5 (a) for the real part and Figure 7.5 (b) for the imaginary part.

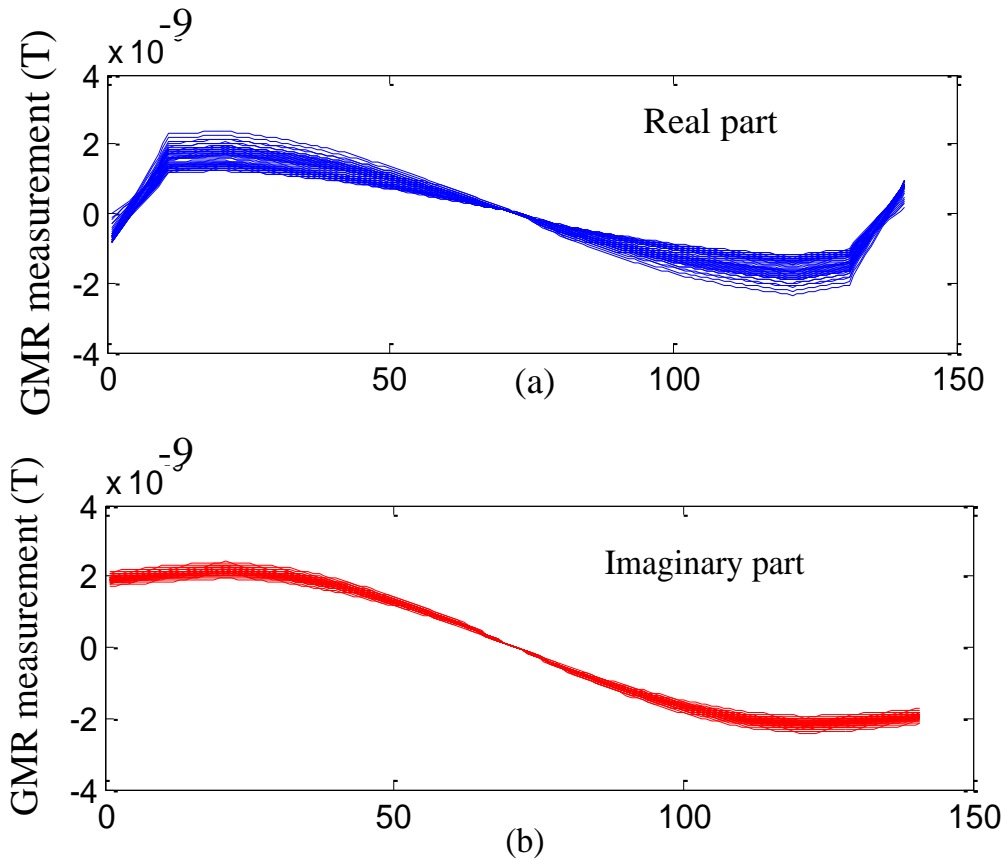


Figure 7.5 Transformed signals invariant to sensor-tilt in the inspection of a crack-free aluminum fastener: (a) Real part of signals and (b) Imaginary part of signals

The ICA scheme for tilt invariance is applied to data from fastener geometries in Figure 7.6, which include fasteners with different crack sizes or locations. The invariance transformations of GMR measurements are presented in Figures 7.7-7.8.

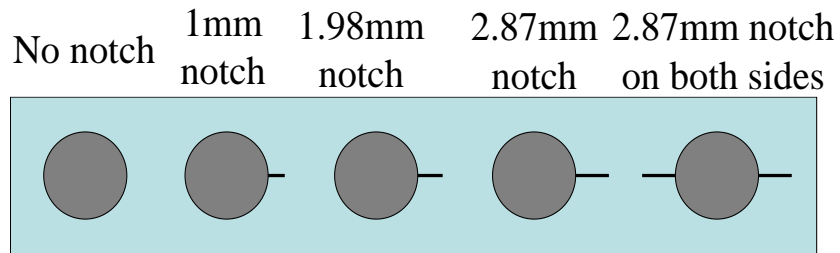


Figure 7.6 Studied riveted geometries

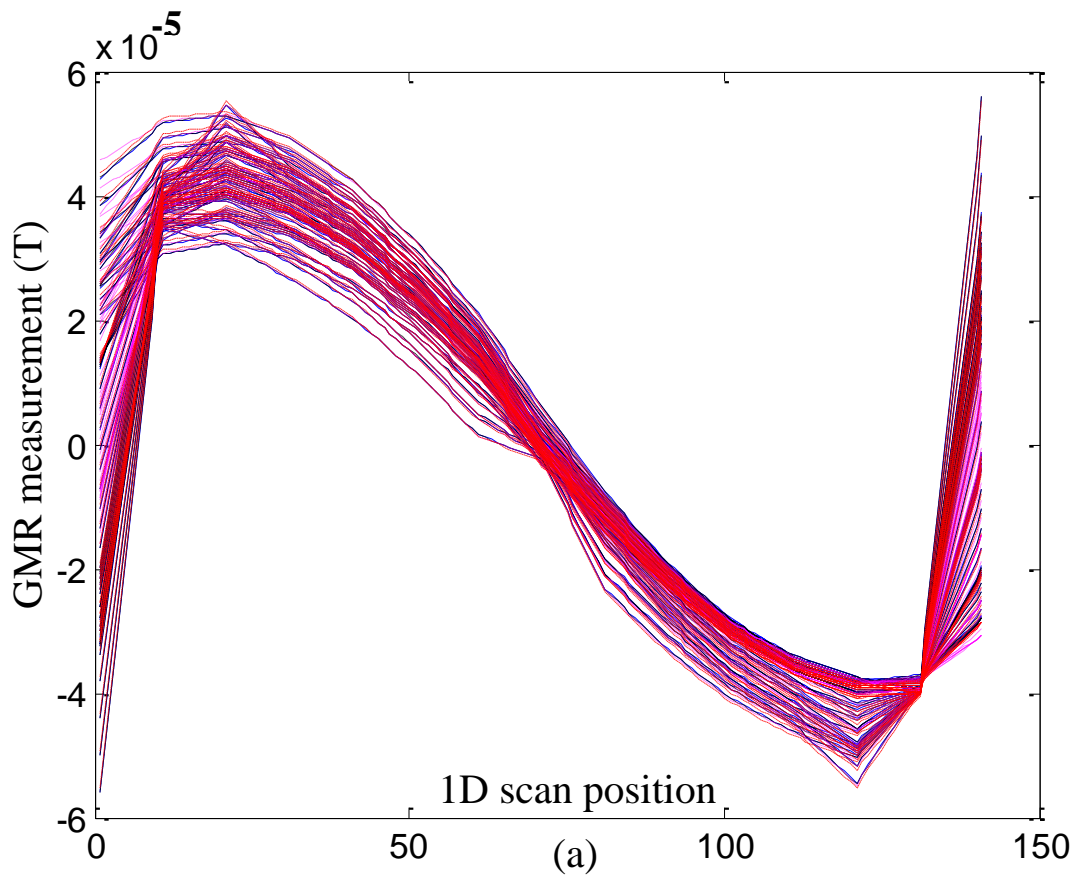
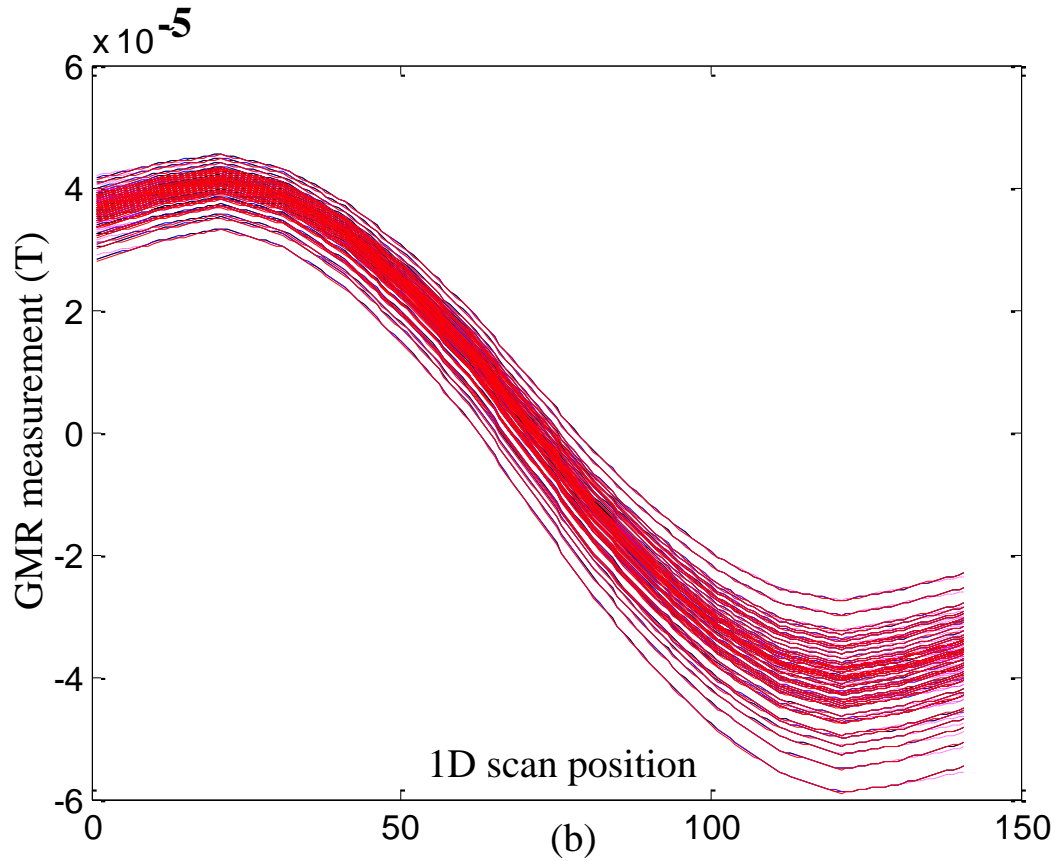


Figure 7.7 Measured GMR complex signals of defect-free and defective fasteners:
 (a) Real parts of signals and (b) Imaginary parts of signals

Figure 7.7 (cont'd).



As seen in Figures 7.7, the interpretation of signals is rather difficult. However, the transformed signals in Figure 7.8 have successfully ameliorated this difficulty and enhanced the contributions from different cracks. The distinguishable characteristics of transformed signals indicate the potential for crack detection.

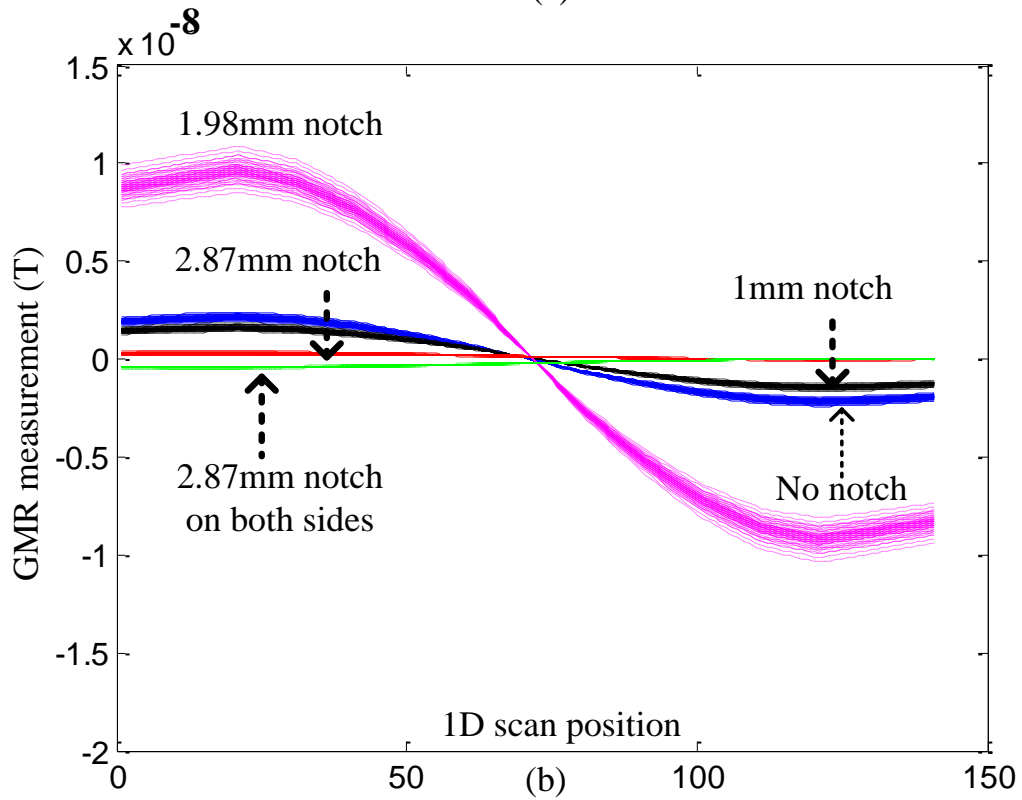
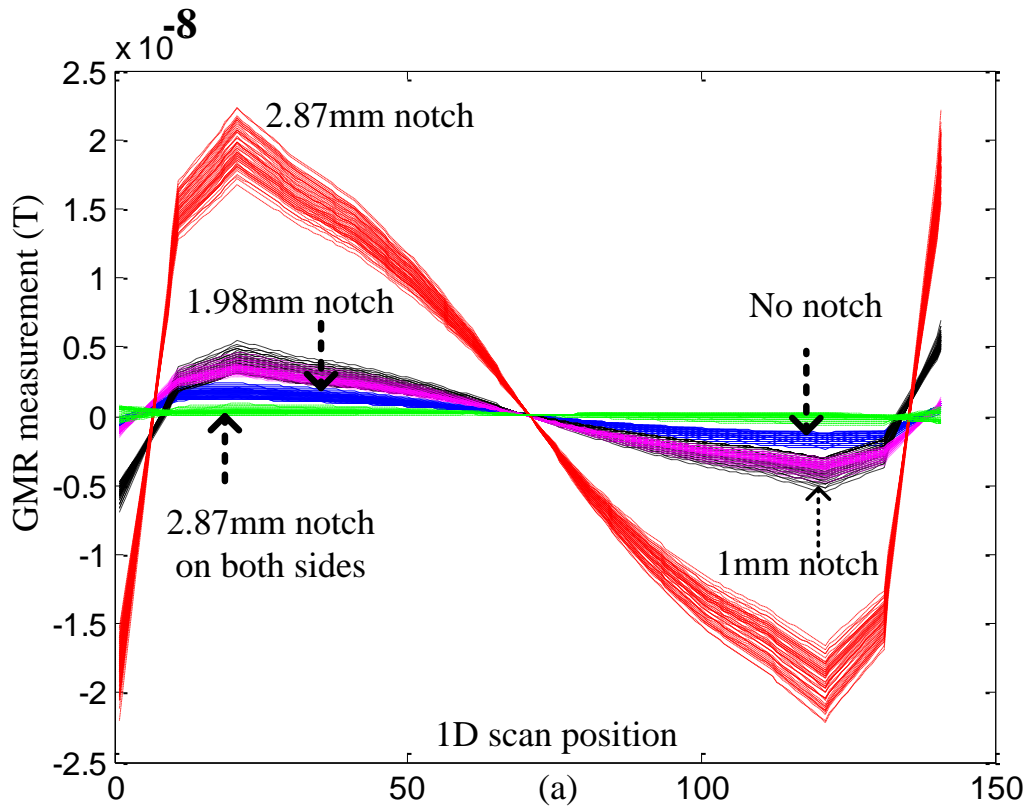


Figure 7.8 Transformed GMR complex signals of defect-free and defective fasteners: (a) Real parts of signals and (b) Imaginary parts of signals

7.3.3 Invariance Features and Crack Detection

Signal features that are insensitive to sensor-tilt variations are extracted from the data after ICA transformation. Features based on skewness and kurtosis that were described in Chapter 4 are utilized to detect cracks in the presence of sensor tilt. The skewness values of real parts of transformed GMR signals in Figure 7.8 (a) are calculated. The skewness curves in Figure 7.9 (a) are seen to follow a constant curve demonstrating their insensitivity to changes in sensor-tilt angles during inspection.

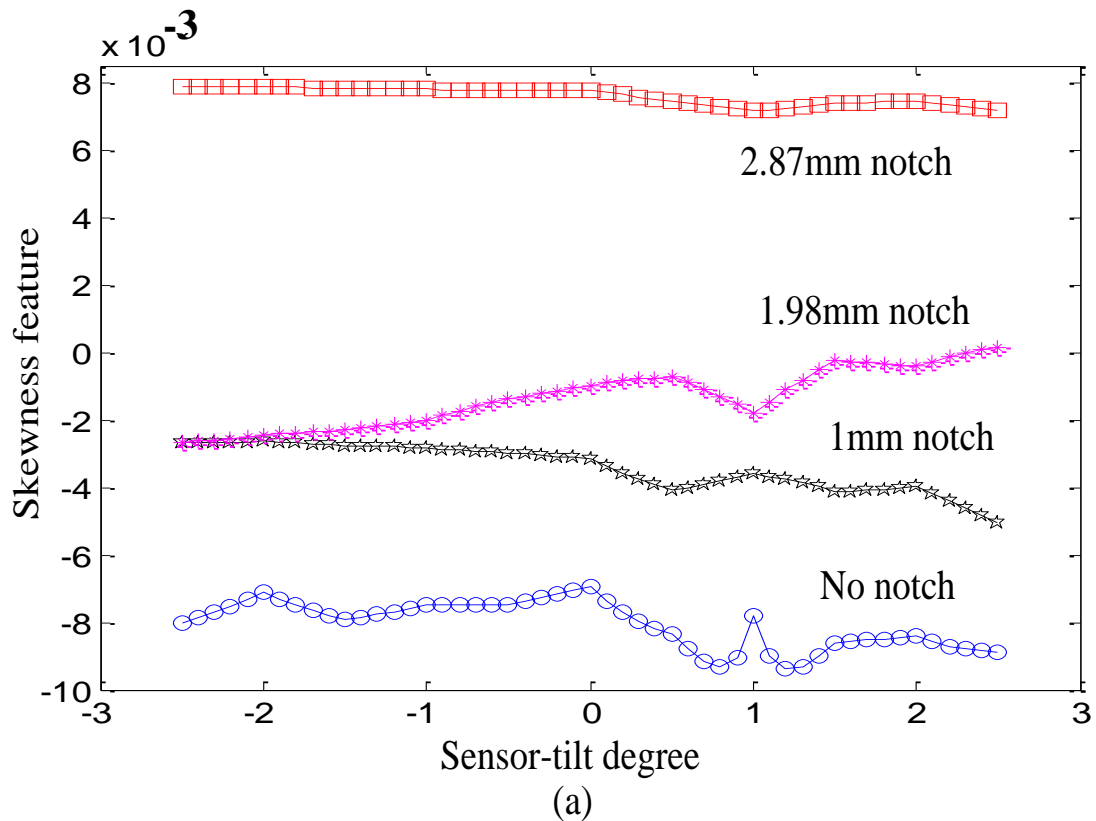
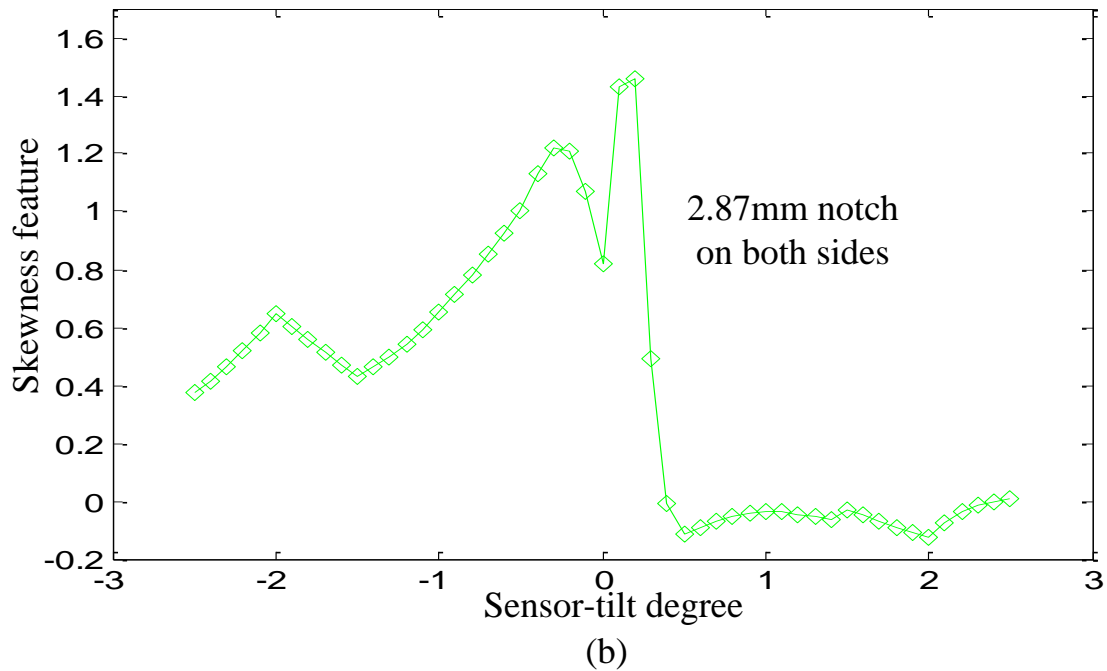


Figure 7.9 Invariance feature analysis: (a) Skewness curves of transformed GMR signals regarding different fastener states: single cracks vs. no crack (b) Two cracks on both sides

Figure 7.9 (cont'd).



It is also found that the used feature is able to identify the signals due to cracks at rivet sites from the case without crack. An interesting phenomenon is observed in Figure 7.9 (b). In the case of two cracks on both sides of the rivet, the skewness values vary from positive to negative numbers with respect to sensor-tilt changes, while the signals due to single cracks yield consistent skewness value. A similar phenomenon is observed in the study of kurtosis values.

Therefore, skewness and kurtosis are employed as invariance features for signal classification, as shown in Figure 7.10. Considering the performance of skewness feature in Figures 7.9-7.10, work was done on effectiveness of higher-order moments. Moments of order 5^{th} , 6^{th} ... 11^{th} ... were investigated with respect to their behavior with sensor tilt and defects. The classification using 5^{th} order moments is displayed in Figure 7.11 where insensitivity to sensor-tilt is achieved, while detection of cracks is retained.

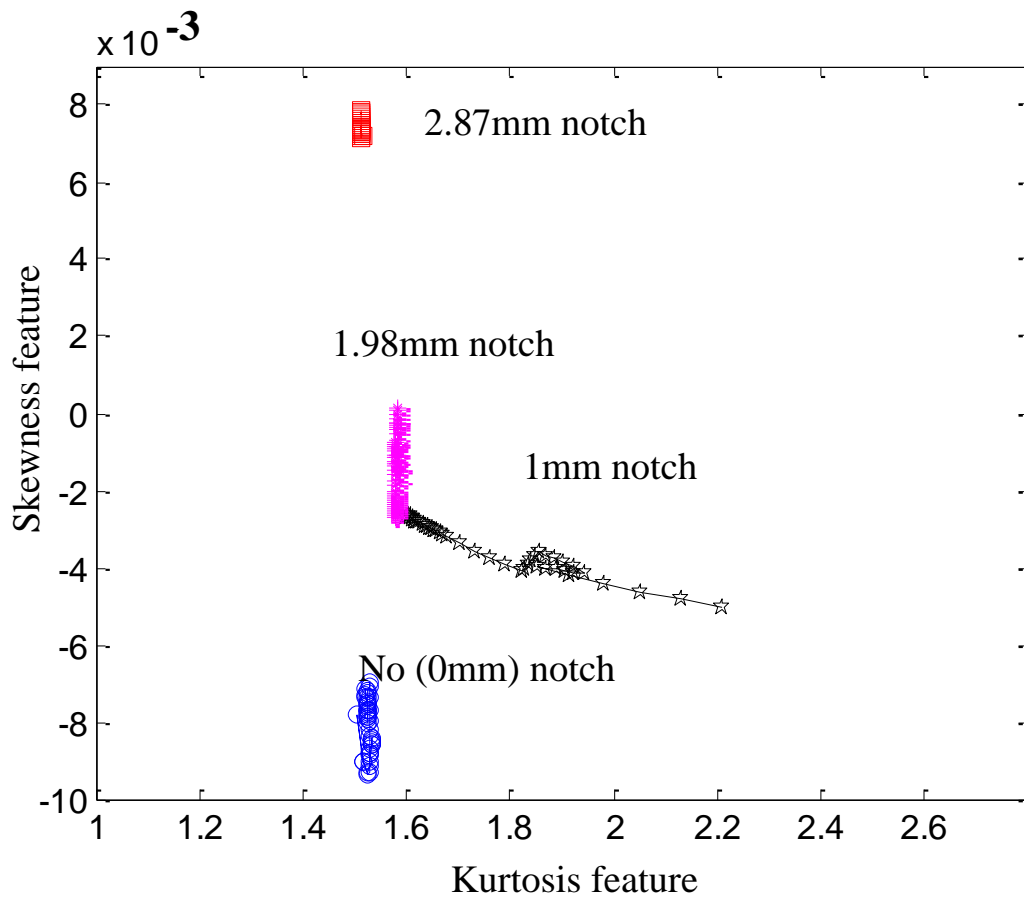


Figure 7.10 Crack detection: classification of GMR signals (the real part) using invariance features

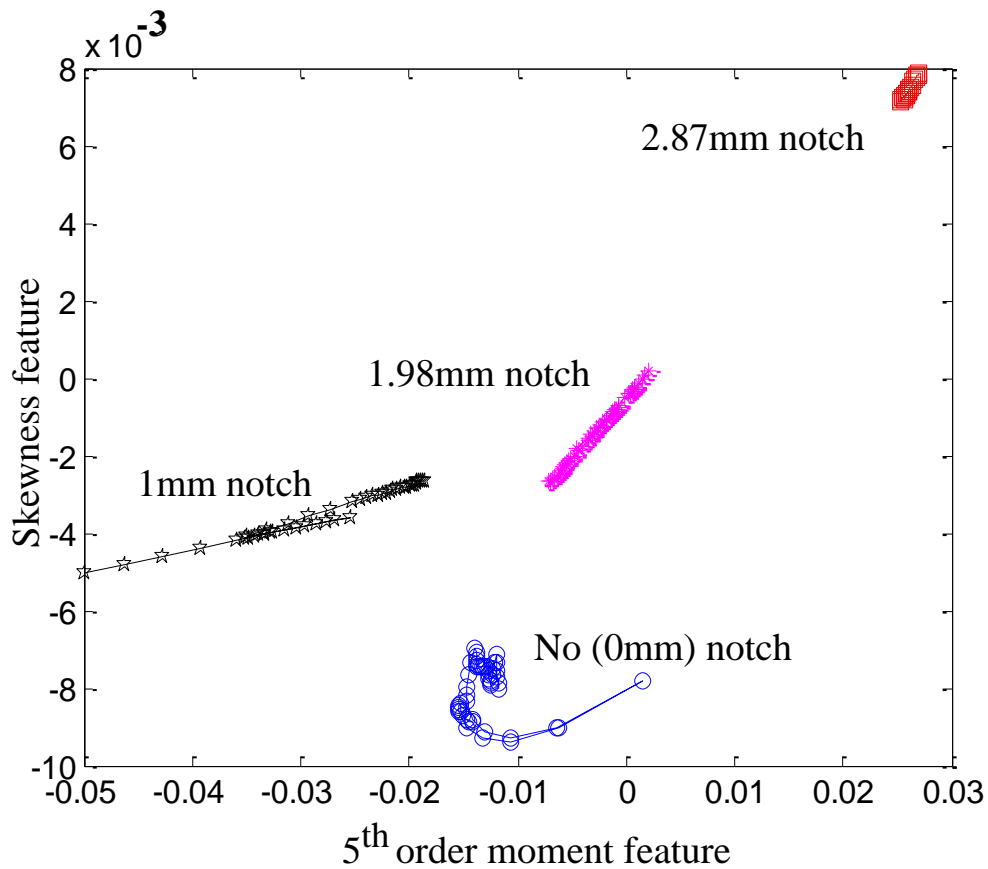
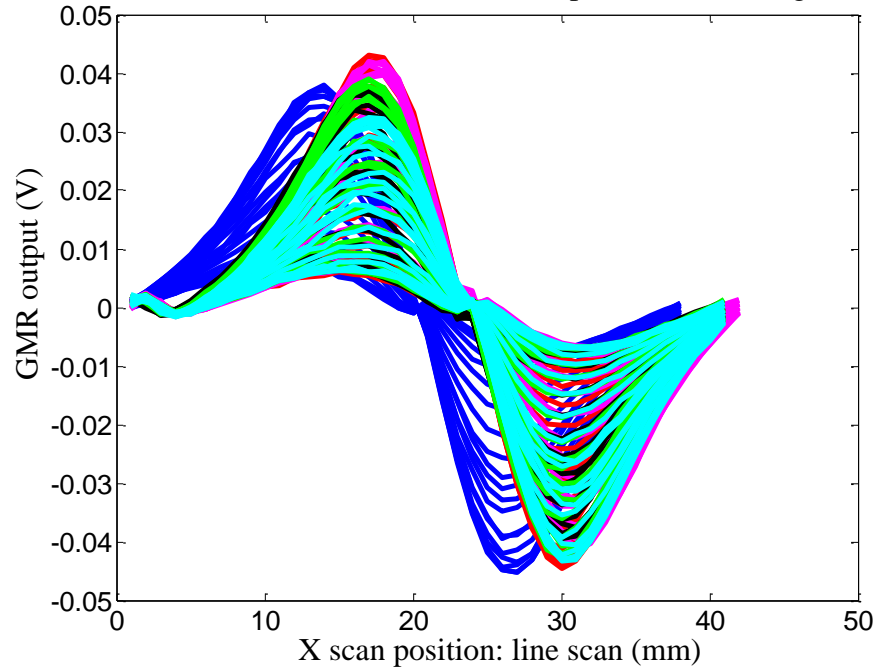


Figure 7.11 Classification of GMR signals in Figure 7.10 using higher order invariance features

7.3.4 Implementation to Experimental Data

The strategy described above is implemented on the experimental data from Sample 2. As shown in Figure 7.12, GMR measurements of line scan signals along the center of steel fasteners in Row 1 are collected under two sensor-tilt conditions. Transformed experimental signals after ICA processing are presented in Figure 7.13 (a). Invariance analysis and classification of GMR signals are shown in Figure 7.13 (b), which demonstrates the potential use of the scheme for EC-GMR signal analysis in the presence of sensor-tilt.

Measurements of fasteners in Row 1 of Sample 2 under tilt angle_1



Measurements of fasteners in Row 1 of Sample 2 under tilt angle_2

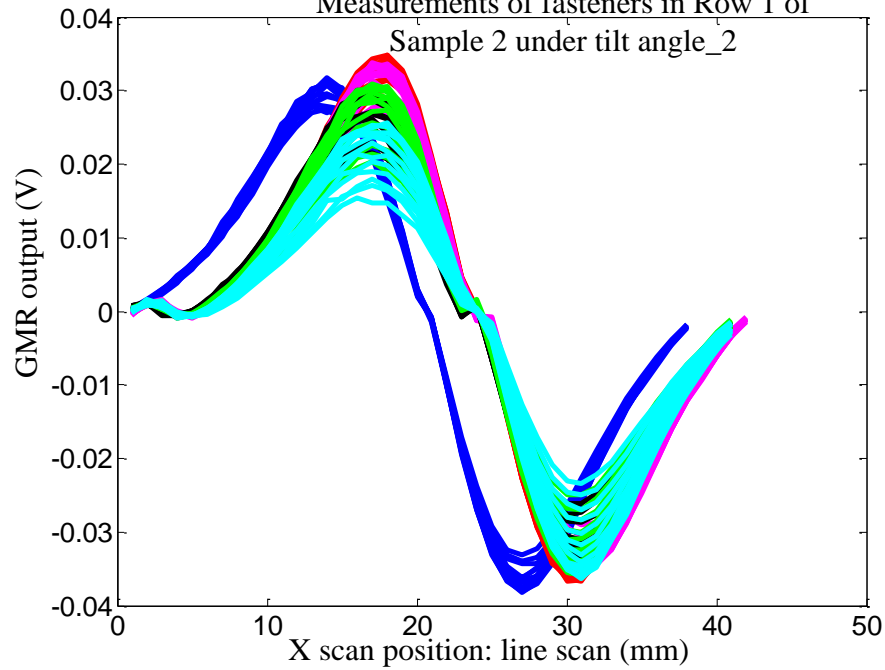


Figure 7.12 GMR signals collected under two sensor-tilt states

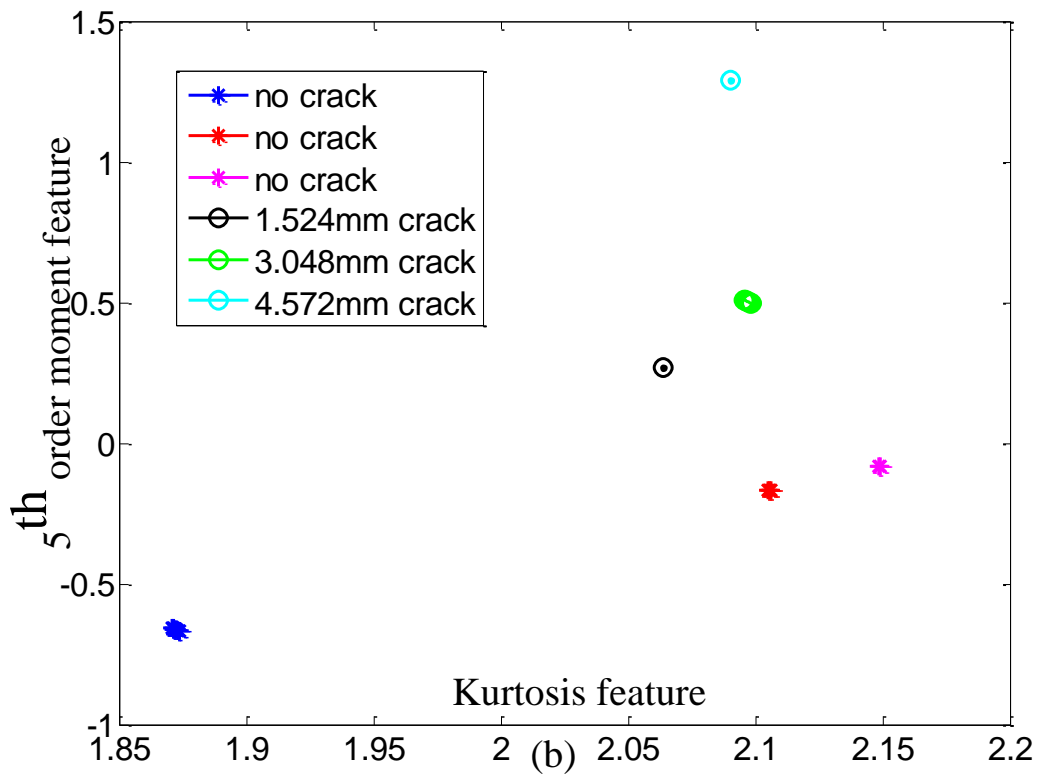
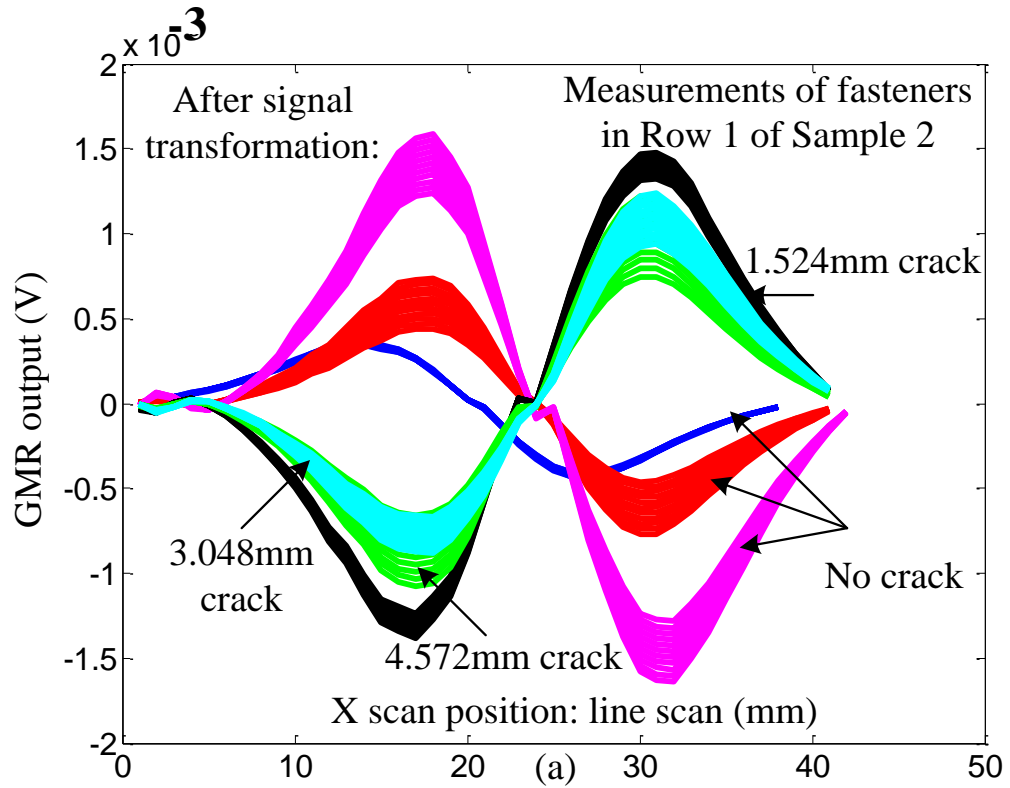


Figure 7.13 Results of invariance analysis: (a) Transformations of measured GMR signals and (b) Classification result using invariance features

7.4 Summary

Sensor-tilt is a major source of error in the proposed EC-GMR sensor. A novel invariance analysis scheme based on independent component analysis is studied and validated in this chapter. Model-based parametric studies successfully validated the performance of proposed invariance transformation. Invariance features are extracted from transformed GMR signals and their ability to detect defective fastener in the presence of sensor-tilt noise is demonstrated. The results of the experimental data validate the feasibility of proposed strategy.

CHAPTER 8 CONCLUSIONS AND FUTURE WORK

8.1 Accomplishments and Conclusions

The research carried out during the course of this dissertation resulted in the following contributions to the field of electromagnetic NDE:

(1) The applications of electromagnetic field GMR sensors in EC technique have been studied extensively. Image measurements using three-component MR sensors are proposed and GMR measurements of three-component magnetic flux density have been experimentally and numerically validated for improving the detection of subsurface cracks under steel fastener sites.

The overall optimization was done using model-based studies for sensor design and signal processing algorithms for data analysis and classification.

(2) Inspection systems using pulsed excitation and low frequency excitation are developed and studied for the inspection of buried cracks at fastener sites. These studies comprise, model-based simulation results validated by experimental measurements and development of signal processing techniques for classification of measurements.

(3) Design of rotating field using two orthogonal-current excitations has enhanced the system capability to detect cracks of all orientations at fastener sites. Crack orientations in all radial directions around fastener site can be detected using appropriate signal processing algorithms.

(4) A statistical signal processing scheme is developed for automated analysis of measured data.

(5) An invariance analysis strategy is developed and evaluated and experimentally validated for crack detection under sensor-tilt conditions.

(6) FE models that compute electromagnetic fields associated with the EC-GMR sensor

geometry are investigated in time and frequency domains. A fast numerical model for pulsed EC technique is developed in time domain.

8.2 Future Work

Although a number of signal processing algorithms have been proposed, these algorithms have not been tested with a lot of experimental data. The proposed probe design and signal analysis algorithms must be tested more extensively. In addition, the remaining work can be pursued in the coming years:

- (1) More quantitative feature extraction for crack sizing.
- (2) 3-component GMR measurement and data fusion for crack profile in riveted structure.
- (3) More experimental validation of the rotating field probe and array receiver.
- (4) Extension of proposed techniques to inspect other geometries.
- (5) Effect of coil size to reduce edge effect. An initial study of this effect is presented. In order to alleviate edge effects, the coil size is reduced. The system capability to inspect a riveted structure is studied with decreasing the size of multi-line planar coil. Sample 3 with small subsurface cracks (less than 1mm size) is examined using an excitation coil with just two turns, as shown in Figure 8.1.

The C-scan images of the normal component are measured in Figure 8.1 (b)-(c), and the analysis results are shown in Figure 8.1 (d) after the PCA processing. Initial results indicate feasibility of the approach. Decreased coil size is beneficial in reducing artifacts due to edges. A more systematic study is warranted.

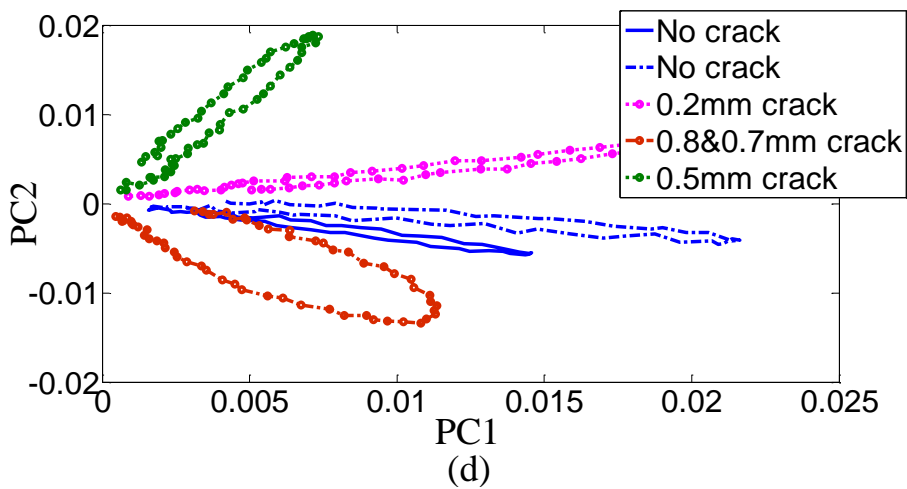
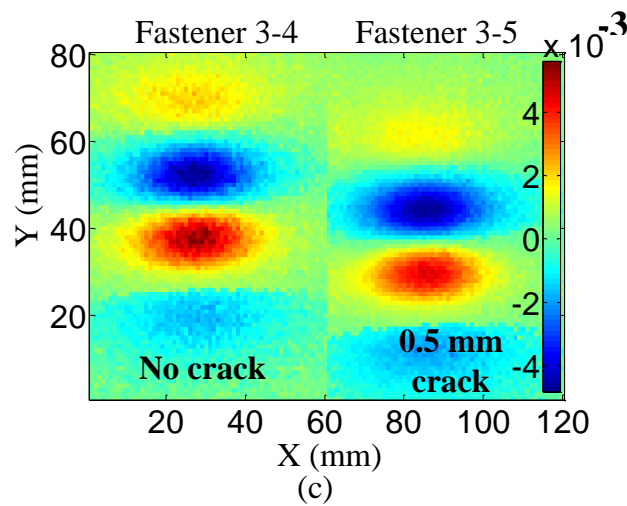
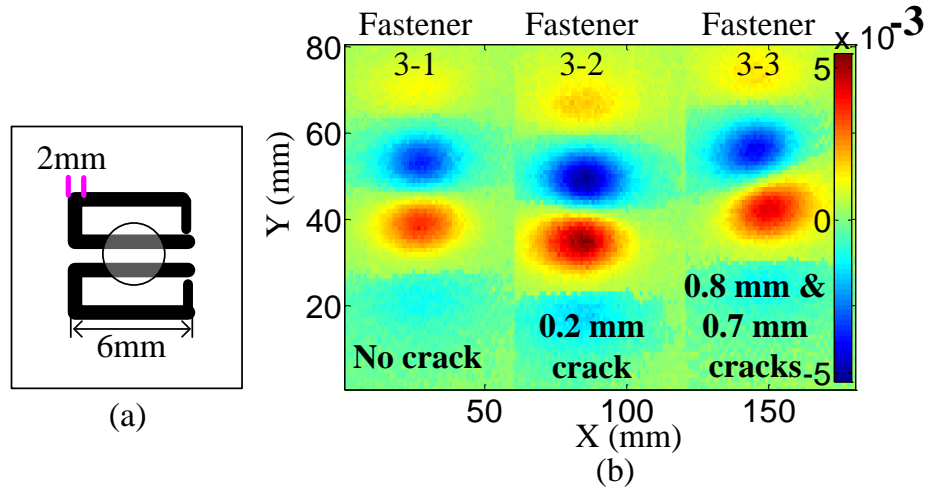


Figure 8.1 Detection of the subsurface cracks (less than 1mm) around aluminum fasteners in Sample 3: (a) Schematic of probe in a reduced size (b-c) C-scan images of normal component (d) Automatic detection using the PCA processing

BIBLIOGRAPHY

BIBLIOGRAPHY

- [1] Nondestructive Evaluation and Quality Control, *ASM Handbook*, vol. 17.
- [2] G. M. Javier, G. G. Jaime and V. S. Ernesto, "Non-Destructive Techniques Based on Eddy Current Testing," *Sensors*, pp. 2525-2565, Nov. 2011.
- [3] Course 30001 Reader: Non-destructive Testing, *online resource*.
- [4] Non-destructive Testing book, *online resource*.
- [5] S. S. Udpa and O. P. Moore, *Nondestructive testing handbook: eletromagnetic testing*, American Society for Nondestructive Testing, 2004.
- [6] S. S. Udpa and L. Udpa, "Eddy current nondestructive evaluation," *Encyclopedia of Electrical and Electronics Engineering*, John G Webster, Editor, John Wiley, vol. 6, pp. 149-163, Dec. 1999.
- [7] H. L. Libby, *Instruction to Electromagnetic Nondestructive Test Methods*, John Wiley and Sons, New York, 1971.
- [8] Y. Deng and X. Liu, "Electromagnetic imaging methods for nondestructive evaluation applications," *Sensors*, pp. 11774-11808, Nov. 2011.
- [9] D. J. Hagemaiier, *Fundamentals of Eddy Current Testing*, ASNT, 1990.
- [10] D. C. Latia, *Nondestructive testing for aircraft*, Jeppesen, 1994.
- [11] National Research Council Final Report, *Aging of U.S. Air Force aircraft*, National Academy Press, Washington, D.C. (United States), 1997.
- [12] "Eddy Current Testing of Aerospace Materials," *NASA Report*.
- [13] P. I. Beda and V. M. Sapunov, "Experience in eddy-current testing of mounting holes in aircraft components," *Russian Journal of Nondestructive Testing*, vol. 36, no. 4, pp. 241-245, 2000.

- [14] A. Jander, C. Smith, and R. Schneider, "Magnetoresistive sensors for nondestructive evaluation," *Proceedings of 10th SPIE International Symposium, Nondestructive Evaluation for Health Monitoring and Diagnostics*, vol. 5770, pp. 1-13, 2003.
- [15] O. Hesse and S. Pankratyev, "Usage of magnetic field sensors for low frequency eddy current testing," *Measurement Science Review*, vol. 5, no. 3, pp. 86-93, 2005.
- [16] T. Dogaru, C. H. Smith, R. W. Schneider, and S. T. Smith, "Deep crack detection around fastener holes in airplane multi-layered structures using GMR-based eddy current probes," *Proceedings of AIP Conference*, vol. 700, pp. 398–405, 2004.
- [17] W. F. Avrin, "Eddy-current measurements with magnetoresistive sensors: third-layer flaw detection in a wing-splice structure 25 mm thick," *Review of Progress in QNDE*, vol. 3994, pp. 29-36, 2000.
- [18] J. S. Knopp, J. C. Aldrin, and K. V. Jata, "Computational methods in eddy current crack detection at fastener sites in multi-layer structures," *Nondestructive Testing and Evaluation*, vol. 24, pp. 103-120, 2009.
- [19] J. M. Buckley and J. H. Calvert, "Improved eddy current techniques for the aerospace industry," *Air Transport Association Non-Destructive Testing Forum*, 1995.
- [20] S. Natht, B. Wincheskii, J.P. Fultont and M. Namkung "Study of the new eddy current non-destructive testing sensor on ferromagnetic materials," *IEEE Transactions on Magnetics*, vol. 30, No. 6, pp. 4644-4646, Nov. 1994.
- [21] R. T. Ko and G. J. Steffes, "Deep defect detection within thick multilayer aircraft structures containing steel fasteners using a giant-magneto resistive (GMR) sensor," *Review of Progress in QNDE*, vol. 27, pp. 865-851, 2008.
- [22] P. P. Whalen, "Transient eddy current inspection in the presence of ferrous fasteners in multi-layered aluminum structures," M. S. thesis, Royal Military College of Canada, 2010.
- [23] B. P. C. Rao and T. Jayakumar, "Recent trends in electromagnetic NDE techniques and future directions," *Proceedings of 18th World Conference on Nondestructive Testing*, Apr. 2012, South Africa.
- [24] Project final report, "Advanced nondestructive evaluation sensor modeling for multi-site inspection," 2008.

- [25] Y. Deng, X. Liu, Z. Zeng, B. Koltenbah, R. Bossi, G. Steffes, and L. Udpa, "Automated analysis of eddy current giant magneto-resistive data," *Review of Progress in Quantitative Nondestructive Evaluation*, vol. 1096, pp. 588-595, 2009.
- [26] Z. Zeng, Y. Deng, X. Liu, L. Udpa, S. S. Udpa, B. Koltenbah, R. Bossi, and G. Steffes, "EC-GMR data analysis for inspection of multilayer airframe structures," *IEEE Transactions on Magnetics*, vol. 47, No. 12, pp. 4745-4752, 2011.
- [27] W. F. Avrin, "Magnetoresistive eddy-current sensor for detection deeply buried flaws," *Review of Progress of Quantitative Nondestructive Evaluation*, vol. 15, pp. 1145-1150, 1996.
- [28] J. C. Aldrin, G. Steffes and J. S. Knopp, "Simulation and automated data classification for eddy current inspection of fastener sites using a GMR sensors array with sheet current excitation," *Review of Progress of Quantitative Nondestructive Evaluation*, vol. 28, pp. 342-349, 2009.
- [29] J. C. Aldrin, J. S. Knopp, E. A. Lindgren and K. V. Jata, "Model-based Inversion in Eddy Current Image Processing," *Review of Progress in Quantitative Nondestructive Evaluation*, vol. 28, pp. 719-726, 2009.
- [30] C. Hellier, *Handbook of Nondestructive Evaluation*, McGraw-Hill, Mar., 2001.
- [31] J. D. Jackson, *Classical Electrodynamics*, John Wiley & Sons, New York, 1998.
- [32] B. Bos, S. Sahlén and J. Andersson, "Automatic scanning with multi-frequency eddy current on multilayered structures," *Aircraft Engineering and Aerospace Technology*, vol. 75, pp. 491-496, 2003.
- [33] T. J. Davis and C. B. Perry, "Digitally controlled multi-frequency eddy current test apparatus and method," *Unite States Patent*, 1981.
- [34] J. D. Young, K. H. Hedengren and D. C. Hurley, "Method and apparatus for a multi-channel multi-frequency data acquisition system for nondestructive eddy current inspection testing," *Unite States Patent*, 1983.
- [35] B. Sasi, B. P .C. Rao, and T. Jayakumar, "Dual-frequency eddy current non-destructive detection of fatigue cracks in compressor discs of aero engines," *Defence Science Journal*, vol. 54, no. 4, pp. 563-570, Oct. 2004.
- [36] P. Xiang, "Automatic multi-frequency rotating-probe eddy-current data analysis," Ph.D. dissertation, Iowa State University, 2005.

- [37] G. Scheer, L. Frische and T. Meier, "Multi-frequency eddy current inspection of rivet rows on aircraft structures," *ECNDE*, 2006.
- [38] Avanindra, "Multifrequency eddy current signal analysis," M. S. thesis, Iowa State University, 1997.
- [39] Z. Liu, M. S. Safizadeh, D. S. Forsyth, and B. A. Lepine, "Data fusion method for the optimal mixing of multi-frequency eddy current signals," *Review of Progress in QNDE*, vol. 22, no. pp. 577-584, 2003.
- [40] H. J. Jung, Y. B. Kong, S. J. Song, C.H. Kim, Y. H. Choi, S.-C. Kang and M. H. Song, "Investigation of frequency mixing techniques for eddy current testing of steam generator tubes in nuclear power plants," *Review of Progress in QNDE*, vol. 26, pp. 603-610, 2007.
- [41] W. Yin, S. J. Dickinson and A. J. Peyton, "A multi-frequency impedance analyzing instrument for eddy current testing," *Measurement Science and Technology*, vol. 17, pp. 393-402, 2006.
- [42] C. V. Dodd, W. E. Deeds, and L. D. Chitwood, "Eddy current inspection of ferromagnetic materials using pulsed magnetic saturation," *Material Evaluation*, vol. 46, pp. 1592-1597, Nov. 1988.
- [43] R. E. Beissner, J. H. Rose, and N. Nakagawa, "Pulsed eddy current method: An overview," *Review of Progress in QNDE*, vol. 18A, pp. 469-475, 1998.
- [44] J. C. Bowler and M. Johnson, "Advances in transient eddy current nondestructive evaluation," *Nonlinear Electromagnetic Systems*, pp. 623-627, 1996.
- [45] Y. Bar-Cohen, "Emerging NDT technologies and challenges at the beginning of the third millennium, part I," *Materials evaluation*, vol. 58, pp. 17-30, 2000.
- [46] B. A. Lepine, J. S. R. Giguere, D. S. Forsyth, J. M. S. Dubois, and A. Chahbaz, "Applying pulsed eddy current NDI to the aircraft hidden corrosion problem," *Proceedings of 5th NASA/FAA/DoD Conference Aging Aircraft*, Sep. 2001.
- [47] T. Hocking, F. Spears, and Y. Plotnikov, "Pulsed eddy current technology and aerospace application," *GE Research, GEIT*, Nov. 2005.
- [48] T. J. Cadeau, "Increased field depth penetration with pulsed eddy current," M. S. thesis, Royal Military College of Canada, 2008.

[49] NDT resource center:

<http://www.ndt-ed.org/EducationResources/CommunityCollege/EddyCurrents/ProbesCoilDesign/ProbesConfig.htm>.

[50] Institut Dr. Foerster Home Page. Available online: <http://www.foerstergroup.com> (accessed on June 2012).

[51] J. E. Lenz, "A Review of Magnetic Sensors," *Proceedings of the IEEE*, vol. 78, no. 6, pp. 973-989, June 1990.

[52] C. L. Wendland, "Optimization of flexible coils for embedded detection and monitoring of cracks in aluminum structures using pulsed eddy current," M. S. thesis, Royal Military College of Canada, June 2005.

[53] R. J. Filkins, J. P. Fulton, T. C. Patton and J. D. Young, "Recent advances and implementation of flexible eddy current probe technology," *Review of Progress in QNDE*, vol. 17, pp. 1809-1816, 1998.

[54] D. C. Hurley, K. H. Hedengren, P. J. Howard, W. P. Kornrump, G. E. Sutton and J. D. Young, "An eddy current array system for aircraft engine inspection," *Review of Progress in QNDE*, vol. 13, pp. 1111-1118, 1994.

[55] J. P. Fulton, K. H. Hedengren, J. D. Young, R. J. Filkins and T. C. Patton, "Optimizing the design of multilayer eddy current probes-a theoretical and experimental study," *Review of Progress in QNDE*, vol. 16, pp. 973-980, 1997.

[56] J. Melcher, "Apparatus and methods for measuring permeability and conductivity in materials using multiple wave number magnetic interrogations," *Unite States Patent*, May 1991.

[57] N. Goldfine, V. Zilberstein, A. Washabaugh, D. Schlicker, I. Shay and D. Grundy, "Eddy current sensor networks for aircraft fatigue monitoring," *ASNT Materials Evaluation, Aerospace Health Monitoring*, vol. 61, no, 7, pp. 1-13, Jul. 2003.

[58] T. Yentzer, S. Kramer et al, "High-resolution eddy current sensor arrays for detection of hidden damage including corrosion and fatigue cracks," *NASA/FAA/DoD Conference on Aging Aircraft*, pp. 1-13, Sep. 2001, Florida.

[59] V. Zilberstein, D. Schlicker, K. Walrath, V. Weiss and N. Goldfine, "MWM eddy current sensors for monitoring of crack initiation and growth during fatigue tests and in service," *International Journal of Fatigue*, vol. 23, pp. 477-485, 2001.

- [60] V. Zilberstein, K. Walrath, D. Grundy, D. Schlicker and N. Goldfine, "MWM eddy current sensors for monitoring of crack initiation and growth," *International Journal of Fatigue*, vol. 25, pp. 11477-1155, 2003.
- [61] S. Yamada, M. Katou, M. Iwahara and F. P. Dawson, "Eddy current testing probe composed of planar coils," *IEEE Transactions on Magnetics*, vol. 31, no. 6, pp. 3185-3187, Nov. 1995.
- [62] S. Yamada, M. Katou, M. Iwahara and F. P. Dawson, "Defect images by planar ECT probe of meander-mesh coils," *IEEE Transactions on Magnetics*, vol. 32, no. 5, pp. 4956-4958, Sep. 1996.
- [63] S. C. Mukhopadhyay, "A novel planar mesh-type microelectromagnetic sensor. Part I. Model formulation," *Sensors Journal, IEEE*, vol. 4, no. 3, pp. 301-307, 2004.
- [64] A. Rakow, "A structural health monitoring fastener for tracking fatigue crack growth in bolted metallic joints," Ph.D. dissertation, Stanford University, 2008.
- [65] A. Rakow and F. Chang, "A structural health monitoring fastener for tracking fatigue crack growth in bolted metallic joints," *Structural Health Monitoring*, vol. 11, pp. 253-267, 2012.
- [66] L. Rosado, "Non-destructive testing based on eddy currents," M. S. thesis, Instituto Superior Técnico, Nov. 2009.
- [67] J. Fava, M. Ruch and A. E. Obrutsky, "Design and construction of eddy current sensors with rectangular planar coils," *Non-Destructive Testing Condition Monitoring*, vol. 46, pp. 268-274, 2004.
- [68] T. Dogarl, "Giant magnetoresistance based eddy current probes for nondestructive testing," Ph.D. dissertation, University of North Carolina, 2002.
- [69] T. Dogaru, C. H. Smith, R. W. Schneider and S. T. Smith, "New directions in eddy current sensing," Albany Instruments, NVE Corp. and UNC Charlotte.
- [70] T. P. Theodoulidisa and E. E. Kriezisb, "Impedance evaluation of rectangular coils for eddy current testing of planar media," *NDT & E International*, vol. 35, no. 6, pp. 407-414, Sep. 2002.
- [71] R. J. Ditchburn, S. K. Burke and M. Posada, "Eddy-Current Nondestructive Inspection with Thin Spiral Coils: Long Cracks in Steel," *Journal of Nondestructive Evaluation*, vol. 22, no. 2, pp. 63-77, June 2003.

- [72] R. J. Ditchburn and S. K. Burke, "Planar rectangular spiral coils in eddy-current non-destructive inspection," *NDT & E International*, vol. 38, no. 8, pp. 690-700, Dec. 2005.
- [73] M. J. Caruso, T. Bratland, C. H. Smith and R. Schneider, "A new perspective on magnetic field sensing," Honeywell and NVE Corp.
- [74] M. Spies, "Course on Electromagnetic NDT Methods," *Online resource*.
- [75] S. Cherepov, O. Hesse, G. Mook, S. Pankratyev and V. Uchanin, "Optimisation of low frequency eddy current sensors using improved inductive coils and highly sensitive AMR and GMR sensor modules," *Online resource*.
- [76] J. K. Na, M. A. Franklin and J. R. Linn, "Detection of hidden cracks on aircraft lap joints with GMR based eddy current technology," *Review of Progress in QNDE*, vol. 25, pp. 345-352, 2005.
- [77] E. S. Boltz, D. W. Cutler and T. C. Tiernan, "Low-frequency magnetoresistive eddy-current sensor for NDE of aging aircraft," *Proceedings of SPIE*, vol. 3397, pp. 39-49, 1998.
- [78] C. Reig, M. D. Cubells-Beltrán and D. R. Muñoz, "Magnetic field sensors based on giant magnetoresistance (GMR) technology: applications in electrical current sensing," *Sensor*, vol. 9, no. 10, pp. 7919-7942, 2009.
- [79] Carl H. Smith and Robert W. Schneider, "Low-field magnetic sensing with GMR sensors," NVE Corp.
- [80] T. Dogaru and S. T. Smith, "Giant magnetoresistance-based eddy-current sensor," *IEEE Transactions on Magnetics*, vol. 37, no. 5, pp. 3831-3838, Sep. 2001.
- [81] F. Di Iorio, "Low field magnetic sensing with giant magneto resistive sensors," Ph.D. dissertation, University of Naples "Federico II", 2007.
- [82] Y. Sun, T. Ouyang and S. Udpa, "Multi-layer aircraft structure inspection using super-sensitive Remote-Field Eddy-Current system," *Review of Progress in QNDE*, vol. 20, pp. 1906-1913, 2001.
- [83] R. A. Smith and D. Edgar, "Advances in transient eddy-current imaging for aerospace applications," *Proceedings of World Conference on NDT*, 2004.
- [84] M. Gibbs and J. Campbell, "Pulsed eddy current inspection of cracks under installed fasteners," *Materials Evaluation*, vol. 49, no.1, pp. 51-59, Jan. 1991.

- [85] G. L. Fitzpatrick, D. K. Thome, R. L. Skaugset, E. Y. C. Shih and W. C. L. Shih, "Magneto-optic/eddy current imaging of aging aircraft: A new NDI technique," *Material Evaluation*, vol. 51, pp. 1402-1407, 1993.
- [86] I. Elshafiey and L. Udpa, "Sensitivity analysis of magneto-optic imaging in nondestructive evaluation of pipelines," *Proceedings of 3rd Middle East Nondestructive Testing Conference & Exhibition*, Nov. 2005, Manama.
- [87] P. Y. Joubert, J. Pinassaud, "Linear magneto-optic imager for non-destructive evaluation," *Sensors Actuator A*, vol. 129, pp. 126-130, 2006.
- [88] Y. H. Cheng, Z. F. Zhou, G. Y. Tian, "Enhanced magneto-optic imaging system for nondestructive evaluation," *NDT&E International*, vol. 40, pp. 374-377, 2007.
- [89] Y. Deng, X. Liu, Y. Fan, Z. Zeng, L. Udpa, and W. Shih, "Characterization of magneto-optic imaging data for aircraft inspection", *IEEE Transactions on Magnetics*, vol. 42, pp. 3228-3230, Oct. 2006.
- [90] G. Rubinacci, A. Tamburrino, S. Ventre, P. Joubert and J. Pinassaud, "Numerical modeling of a continuous level Eddy Current Imager," *Electromagnetic Non-destructive Evaluation (X)*, pp. 33-40, 2007.
- [91] B. Wincheski and M. Namkung, "Electromagnetic detection of fatigue cracks under protruding head ferromagnetic fasteners," *Technical Report*, NASA Langley Research Center, USA, 1999.
- [92] B. Wincheski, J. Simpson, M. Namkung, D. Perey, Ed Scales and R. Louie, "Development of giant magnetoresistive inspection system for detection of deep fatigue cracks under airframe fasteners," *Review of Progress in QNDE*, vol. 21, pp. 1007-1014, 2002.
- [93] T. Dogaru, C. H. Smith, R. W. Schneider, and S. T. Smith, "Deep crack detection around fastener holes in airplane multi-layered structures using GMR-based eddy current probes," *Proceedings of AIP Conference*, vol. 700, pp. 398-405, 2004.
- [94] D. J. Harrison, "The detection of corrosion in layered structures using transient eddy currents," *Nondestructive Testing of Materials*, pp. 115-124, 1995.
- [95] T. W. Krause, C. Mandache, and J. H. V. Lefebvre, "Diffusion of pulsed eddy currents in thin conducting plates," *Proceedings of AIP Conference*, vol. 975, pp. 368-375, 2008.

- [96] S. Giguere, "Pulsed eddy current for corrosion detection", M. S. thesis, Royal Military College of Canada, 1999.
- [97] J. H. Vivier Lefebvre, "Simultaneous conductivity and thickness measurements using pulsed eddy current," M. S. thesis, Royal Military College of Canada, 2003.
- [98] A. Sophian, "Characterisation of surface and sub-surface discontinuities in metals using pulsed eddy current sensors," Ph.D. dissertation, Huddersfield University, 2003.
- [99] C. Murner and J. P. Hansen, "Buried corrosion detection in multi-layer airframe structures using pulsed eddy current," *Proceedings of 17th World Conference on Nondestructive Testing*, 2008.
- [100] D. L. Waidelich, J. A. DeShong and W. J. McGonnagle, "A pulsed eddy current technique for measuring clad thickness," *Argonne National Laboratory Report*, 1955.
- [101] S. Giguere, B. A. Lepine and J. M. S. Dubois, "Pulsed eddy-current characterization of material loss in multi-layer structures," *Canadian Aeronautics and Space Journal*, vol. 46, pp. 204-208, 2000.
- [102] D. J. Harrison, "Progress in the detection of cracks under installed fasteners using eddy currents," *Proceedings of AGARD Conference*, vol. 462, 1989.
- [103] D. J. Harrison, "Eddy current inspection using Hall sensor and transient excitation," *Defense Research Agency DRA/SMC/TR941008*, 1995.
- [104] J. S. R. Giguere, B. A. Lepine and J. M. S. Dubois, "Detection of cracks beneath rivet heads via pulsed eddy current technique," *Review of Progress of Quantitative Nondestructive Evaluation*, vol.21, pp. 1968-1975, 2002.
- [105] B. Lebrun, Y. Jayet and J. C. Babous, "Pulsed eddy current applications to the detection of deep cracks," *Materials Evaluation*, vol. 53, pp. 1296-1300, 1995.
- [106] B. Lebrun and J. C. Babous, "Pulsed eddy current signal analysis: application to the experimental detection and characterization of deep flaws in highly conductive materials," *NDT&E International*, vol.30, pp. 163-170, 1997.
- [107] C. C. Tai, J. H. Rose and J. C. Moulder, "Thickness and conductivity of metallic layers from pulsed eddy current measurements," *Review of Scientific Instruments*, vol.67, pp. 3965-3972, Nov. 1996.

- [108] J. C. Moulder, J. A. Bieber, W. W. Ward III and J. H. Rose, "Scanned pulsed-eddy-current instrument for non-destructive inspection of aging aircraft," *Nondestructive Evaluation of Aging Aircraft, Airports and Aerospace Hardware, Proceedings of SPIE*, vol. 2945, pp. 2-13, 1996.
- [109] J. A. Bieber, S. K. Shaligram and J. H. Rose, "Time-gating of pulsed eddy current signals for defect characterization and discrimination in aircraft lap-joints," *Review of Progress in QNDE*, vol. 16, pp. 1915-1922, 1997.
- [110] R. A. Smith and G. R. Hugo, "Deep corrosion and crack detection in aging aircraft using transient eddy current NDE," *Proceedings of 5th Joint NASA/FAA/DoD Conference on Aging Aircraft*, Orlando, 2001.
- [111] R. A. Smith, G. R. Hugo and D. J. Harrison, "Essential factors in improving the characterization of cracks and corrosion using transient eddy currents," *Proceedings of 6th Joint FAA/NASA/DoD Conference on Aging Aircraft*, San Francisco, Sep. 2002.
- [112] A. Sophian, G. Y. Tian, D. Taylor and J. Rudlin, "Design of a pulsed eddy current sensor for detection of defects in aircraft lap-joints," *Sensors & Actuators: A. Physical*, vol. 101, pp. 92-98, 2002.
- [113] M. J. Johoson, J. R. Bowler and F. Azzem, "Pulsed eddy-current at Iowa State University-recent progress and results," *Review of Quantitative Nondestructive Evaluation*, vol. 22, pp. 390-396, 2003.
- [114] T. Hocking, F. Spears and Y. Plotnikov, "Pulsed eddy current technology and aerospace application," *GE Research*, 2005.
- [115] G. Y. Tian, A. Sophian, "Defect classification using a new feature for pulsed eddy current sensors," *NDT&E International*, vol.38, no. pp.77-82, Jan. 2005.
- [116] B. F. Yang, F. L. Luo and D. Han, "Scanned pulsed eddy current technique used for nondestructive inspection of aging aircraft," *Insight*, pp.6129-6132, 2006.
- [117] Y. He, F. Luo, M. Pan, F. Weng, X. Hu, J. Gao and B. Liu, "Pulsed eddy current technique for defect detection in aircraft riveted structures," *NDT & E International*, vol. 43, pp. 176-181, 2010.
- [118] Y. He, F. Luo, M. Pan, X. Hu, B. Liu and J. Gao, "Defect edge identification with rectangular pulsed eddy current sensor based on transient response signals," *NDT & E International*, vol. 43, pp. 409-415, 2010.

- [119] B. A. Lepine, B. P. Wallace, D. S. Forsyth and A. Wyglinski, "Pulsed eddy current method developments for hidden corrosion detection in aircraft structures," *NDT.net*, vol.4, no. 1, Jan. 1999.
- [120] B. A. James, "Time-domain solutions of two and three-dimensional transient electromagnetic fields," Ph.D. dissertation, Carnegie-Mellon University, 1990.
- [121] C. C. Tai and S. S. Lee, "Time-domain and frequency-domain eddy current simulations by the finite element method," *Key Engineering Materials*, vols. 270-273, pp. 585-592, Aug. 2004.
- [122] E. E. Kriezis, T. D. Tsiboukis, S. M. Panas and J. A. Tegopoulos, "Eddy currents: theory and applications," *Proceedings of the IEEE*, vol. 80, no. 10, Oct. 1992.
- [123] J. Mackerle, "Finite-element modelling of non-destructive material evaluation, an addendum: a bibliography," *Modeling and Simulation in Materials Science and Engineering*, vol. 12, pp. 799-834, 2004.
- [124] David H. S. Cheng, "The reflected impedance of a circular coil in the proximity of a semi-infinite medium," *IEEE Transactions on Instrumentation and Measurement*, vol. 14, no. 3, pp. 107-116, Sep. 1965.
- [125] C.V. Dodd and W. E. Deeds, "Analytical solutions to eddy-current probe-coil problems," *Journal of Applied Physics*, vol. 39, no. 6, pp. 2829-2838, May. 1968.
- [126] R. Ludwig and X. W. Dai, "Numerical and analytical modeling of pulsed eddy-currents in a conducting half-space," *IEEE Transactions on Magnetics*, vol. 26, no. 1, pp. 299-307, Jan. 1990.
- [127] J. Bowler and M. Johnson, "Pulsed eddy-current response to a conducting half-space," *IEEE Transactions on Magnetics*, vol. 33, no. 3, pp. 2258-2264, May. 1997.
- [128] N. Ida, *Numerical Modeling for Electromagnetic Non-Destructive Evaluation*, Chapman & Hall, London, 1995.
- [129] J. R. Bowler, "Pulsed eddy current inversion for the determination of crack shape," *Electromagnetic Nondestructive Evaluation (III)*, pp. 263-269, 1997.
- [130] F. Fu, "Transient eddy current response due to a subsurface crack in a conductive plate," Ph.D. dissertation, Iowa State University, 2006.
- [131] T. Theodoulidis, "Developments, in calculating the transient eddy current response from a conductive plate," *IEEE Transactions on Magnetics*, vol. 28, no. 2, pp. 97-102, April, 1995.

- [132] T. J. Cadeau and T. W. Krause, "Pulsed eddy current probe design based on transient circuit analysis," *Review of Progress in Quantitative Nondestructive Evaluation*, vol. 28, pp. 327-334, 2009.
- [133] V. Babbar, P. Whalen and T. Krause, "Finite element modelling of transient eddy currents from defects in the presence of ferrous fasteners in multi-layered aluminum structures," *Conference of 3rd International CANDU In-Service-Inspection and NDT*, Canada, 2010.
- [134] F. Thollon, B. Lebrun, N. Burais and Y. Jayet, "Numerical and experimental study of eddy current probes in NDT of structures with deep flaws," *NDT & E International*, vol. 41, pp. 477-483, 2008.
- [135] Y. Li, G. Y. Tian and A. Simm, "Fast analytical modeling for pulsed eddy current evaluation," *NDT & E International*, vol. 41, pp. 477-483, 2008.
- [136] G. Preda, B. Cranganu-Cretu, F. I. Hantila, O. Mihalache, Z. Chen, and K. Miya, "Nonlinear FEM-BEM formulation and model-free inversion procedure for reconstruction of cracks using pulse eddy currents," *IEEE Transactions on Magnetics*, vol. 38, no. 2, pp. 1241-1244, Mar. 2002.
- [137] S. Xie, Z. Chen, T. Takagi, and T. Uchimoto, "Efficient numerical solver for simulation of pulsed eddy-current testing signals," *IEEE Transactions on Magnetics*, vol. 47, pp. 4582 - 4591, 2011.
- [138] C. H. Ahn, B. S. Jeong, and S. Y. Lee, "Efficient hybrid finite element-boundary element method for 3-dimensional open-boundary field problems," *IEEE Transactions on Magnetics*, vol. 27, no. 5, pp. 4069-4072, Sep. 1991.
- [139] J. R. Bowler and D. J. Harrison, "Measurement and calculation of transient eddy-currents in layered structures," *Review of Progress in Quantitative Nondestructive Evaluation*, vol.11, pp. 241-248, 1992.
- [140] I. A. Tsukerman, A. Konrad, G. Bedrosian and M. V. K. Chari, "A Survey of Numerical Methods for Transient Eddy Current Problems," *IEEE Transactions on Magnetics*, vol. 29, no. 2, pp. 1711-1716, 1993.
- [141] U. Patel and D. Rodger, "Finite element modeling of pulsed eddy currents for nondestructive testing," *IEEE Transactions on Magnetics*, vol. 32, pp. 1593-1596, 1996.
- [142] O. Biro, P. Bohm, K. Preis and G. Wachutka, "Edge finite element analysis of transient skin effect problem," *IEEE Transactions on Magnetics*, vol. 36, no. 4, pp. 835-839, Jul. 2000.

- [143] L. Xuan, Z. Zeng, B. Shanker and L. Udpa, "Meshless method for numerical modeling of pulsed eddy currents," *IEEE Transactions on Magnetism*, vol. 40, no. 6, pp. 3457-3462, Nov. 2004.
- [144] I. Elshafiey, 'Comparison of computational modeling techniques of pulsed eddy current inspection', *Review of Progress in Quantitative Nondestructive Evaluation*, vol. 28, pp. 319-326, 2009.
- [145] C. Lee, M. J. Johnson and N. Nakagawa, "Development of a pulsed eddy current system and its characterization," *Review of Progress in Quantitative Nondestructive Evaluation*, vol.26, pp. 354-361, 2007.
- [146] M. Dadic, "A system identification approach to the modeling of pulsed eddy-current system," *NDT&E international*, vol. 38, pp. 107-111, 2005.
- [147] M. Dadic, "Enhanced time-stepping FEM simulation using digital signal processing," *Simulation*, vol. 84, no. 4, pp. 169–178, April 2008.
- [148] Y. K. Shin, D. M. Choi, H. S. Jung and T. G. Um, "Performance evaluation of several types of pulsed eddy current probes for detecting wall thickness reduction," *Review of Progress in Quantitative Nondestructive Evaluation*, vol. 29, pp. 393-400, 2010.
- [149] R. D. Rempt and G. A. Perry, "Flexible hand held MR scanning array for cracks/flaws," *Unite States Patent*, May 2008.
- [150] N. Nair., V. Melapudi., J. Hector, X. Liu, Y. Deng, Z. Zeng, L. Udpa, J. M. Thomas and S. Udpa, "A GMR-based eddy current system for NDE of aircraft structures," *IEEE Transactions on Magnetism*, vol. 42, pp. 3312-3314, 2006.
- [151] S. Yamada, K. Chomsuwan and M. Iwahara, "Application of giant magnetoresistive sensor for nondestructive evaluation," *Proceedings of the IEEE Sensors*, pp. 927-930, Oct. 2006.
- [152] A. Tamburrino, S. Ventre, L. Ferrigno, and S. Udpa, "Characterization and implementation of a GMR based probe for eddy current testing," *International Journal of Applied Electromagnetics and Mechanics*, vol. 28, pp. 329-336, 2008.
- [153] O. Biro and K. Preis, "On the use of the magnetic vector potential in the finite-element analysis of three-dimensional eddy currents," *IEEE Transactions on Magnetism*, vol. 25, no. 4, pp. 3145-3159, Jul. 1989.

- [154] O. Biro and K. Preis, "Finite element analysis of 3-D eddy currents," *IEEE Transactions on Magnetics*, vol. 26, no. 2, pp. 418-423, Mar. 1990.
- [155] J. Jin, *The Finite Element Method in Electromagnetics*, IEEE press: Wiley, May. 2002.
- [156] Z. Zeng, X. Liu, Y. Deng, L. Udpa, L. Xuan, W. C. L. Shih and G. L. Fitzpatrick, "A parametric study of magneto-optic imaging using finite-element analysis applied to aircraft rivet site inspection," *IEEE Transactions on Magnetics*, vol. 42, pp. 3737-3744, 2006.
- [157] Z. Zeng, X. Liu, Y. Deng and L. Udpa, "Reduced magnetic vector potential and electric scalar potential formulation for eddy current modeling," *Przeglad Elektrotechniczny*, vol. 83, no. 6, pp. 35-37, Mar. 2007.
- [158] Z. Zeng, L. Udpa, S. S. Udpa, and M. S. C. Chan, "Reduced magnetic vector potential formulation in the finite element analysis of eddy current nondestructive testing," *IEEE Transactions on Magnetics*, vol. 45, no. 3, pp. 964-967, Mar. 2009.
- [159] L. Ljung, *System Identification: Theory for the user*, Englewood Cliffs: Prentice-Hall, 1999.
- [160] T. Clauzon, F. Thollon and A. Nicolas, "Flaws characterisation with pulsed eddy current NDT," *IEEE Transactions on Magnetics*, vol.35, no. 3, pp.1873-1876, 1999.
- [161] G. Yang Z. Zeng, Y. Deng, X. Liu, L. Udpa, A. Tamburrino, S. S. Udpa, "3D EC-GMR sensor system for detection of subsurface defects at steel fastener sites," *NDT and E International*, vol. 50, pp. 20-28, Sep. 2012.
- [162] H. S. Mohammad Saleh "Detection of hidden corrosion by pulsed eddy current using time frequency analysis," Ph.D. dissertation, University of Montreal, 2012.
- [163] G. Y. Tian, A. Sophian, D. Taylor and J. Rudlin, "Wavelet-based PCA defect classification and quantification for pulsed eddy current NDT," *IEE Proceedings: Science Measurement and Technology*, vol. 152, no.4, pp. 141-148, Jul. 2005.
- [164] T. L. Chen, G. Y. Tian, A. Sophian, P. W. Que, "Feature extraction and selection for defect classification of pulsed eddy current NDT," *NDT & E international*, vol.41, no.6, pp. 467-476, Apr. 2008.
- [165] M. S. Safizadeh, B. A. Lepine, D. S. Forsyth and A. Fahr, "Time-frequency analysis of pulsed eddy current signals," *Journal of Nondestructive Evaluation*, vol. 20, pp. 73-86, 2001.

- [166] M. S. Safizadeh, Z. Liu, D. S. Forsyth and A. Fahr, "Automatic classification and characterization of hidden corrosion using pulsed eddy current data," *Proceedings of 5th International Workshop, Advances in Signal Processing for Non Destructive Evaluation of Materials*, vol.27, pp. 25-30, 2006.
- [167] D. G Park and C. S. Angani, "Evaluation of pulsed eddy current response and detection of the thickness variation in the stainless steel," *IEEE Transactions on Magnetics*, vol. 45, pp. 3893-3896, 2009.
- [168] Z. Q. Lang, A. Agurto, G. Y. Tian and A. Sophian, "A system identification based approach for pulsed eddy current non-destructive evaluation," *Measurement Science and Technology*, vol. 18, pp. 2083-2091, 2007.
- [169] B. F. Yang, F. L. Luo and D. Han, "Research on edge identification of a defect using pulsed eddy current based on principal component analysis," *NDT & E International*, vol. 40, pp. 294-299, 2007.
- [170] G. Yang, G. Y. Tian, P. W. Que and T. L. Chen, "Independent Component Analysis-Based Feature Extraction Technique for Defect Classification Applied for Pulsed Eddy Current NDE," *Research in Nondestructive Evaluation*, vol. 20, no. 4, pp. 230-245, Oct. 2009.
- [171] P. Horan, P. R. Underhill and T. W. Krause, "Pulsed eddy current detection of cracks in F/A-18 inner wing spar without wing skin removal using modified principal component analysis," *NDT & E International*, vol. 55, pp. 21-27, 2013.
- [172] J. M. Lattin, J. D. Carroll and P. E. Green, *Analyzing Multivariate Data*, CA : Thomson Brooks/Cole, 2003.
- [173] H. Wolfgang, and S. Léopold, *Applied multivariate statistical analysis*, New York: Springer, 2007.
- [174] F. Lingvall, T. Stepinski, "Automatic detecting and classifying defects during eddy current inspection of riveted lap-joints," *NDT and E International*, vol.33, pp. 47-55, 2000.
- [175] Y. L. Diraison, P. Y. Joubert and D. Placko, "Characterization of subsurface defects in aeronautical riveted lap-joints using multi-frequency eddy current imaging," *NDT and E International*, vol. 42, no. 2, pp. 133-140, Mar. 2009.

- [176] P. Y. Joubert, E. Vourch, A. Tassin and Y. L. Diraison, "Source separation techniques applied to the detection of subsurface defects in the eddy current NDT of aeronautical lap-joints," *NDT and E International*, vol. 43, no. 7, pp. 606-614, Oct. 2010.
- [177] K. V. Mardia, "Measures of multivariate skewness and kurtosis with applications," *Biometrika*, vol. 57, no. 3, pp. 519-530, 1970.
- [178] J. P. Egan, *Signal detection theory and ROC analysis, series in cognition and perception*, New York: Academic Press, 1975.
- [179] Receiver operating characteristic:
http://en.wikipedia.org/wiki/Receiver_operating_characteristic
- [180] S. Mandayam, L. Udpa, S. S. Udpa and W. Lord, "Invariance transformation for magnetic flux leakage signals," *IEEE Transactions on Magnetics*, vol. 32, no. 3, pp. 1577-1580, 1996.
- [181] D. Kim, L. Udpa and S. S. Udpa, "Lift-off invariance transformations for eddy current nondestructive evaluation signals," *Review of Progress in QNDE*, vol. 21, pp. 615-622, 2002.
- [182] J. C. Aldrin and J. S. Knopp, "Method for crack characterization with noise invariance for eddy current inspection of fastener sites," *Review of Progress in QNDE*, vol. 25, pp. 315-322, 2006.
- [186] C. Pierre, "Independent component analysis: a new concept?" *Signal Processing*, vol. 36, no. 3, pp. 287-314, 1994.
- [187] A. Oja E. Hyvärinen, "Independent component analysis: algorithms and applications," *Neural Networks*, vol. 13, no. 4-5, pp. 411-430, 2000.
- [188] B. H. Shin, P. Ramuhalli, L. Udpa, and S. Udpa, "Independent component analysis for enhanced feature extraction from NDE," *Review of Progress in QNDE*, vol. 23, pp. 597-604, 2004.

PUBLICATIONS

* Journals

- [1] **G. Yang**, Z. Zeng, Y. Deng, et al, 'Sensor-tilt Invariance Analysis for Eddy Current Signals', *NDT & E International*, Vol. 52, 2012.
- [2] **G. Yang**, Z. Zeng, Y. Deng, et al, '3D EC-GMR Sensor System for Detection of Subsurface Defects at Steel Fastener Sites', *NDT & E International*, Vol. 50, 2012.
- [3] **G. Yang**, T. Khan, L. Zhang, L. Udpa, et al, 'Pre-processing Methods for Eddy Current Data Analysis using Hilbert-Huang Transform', *International Journal of Applied Electromagnetics and Mechanics*, Vol. 39, 2012.
- [4] **G. Yang**, A. Tamburrino, L. Udpa, et al, 'Pulsed Eddy Current based GMR System for the Inspection of Aircraft Structures', *IEEE Transactions on Magnetics*, Vol. 46(3), 2010.
- [5] Q. Zhang, T. Chen, **G. Yang**, et al, 'Time and Frequency Domain Feature Fusion for Defect Classification Based on Pulsed Eddy Current NDT', *Research in Nondestructive Evaluation*, Vol. 23(3), 2012.
- [6] J. Kim, **G. Yang**, L. Udpa, et al, 'Classification of Pulsed Eddy Current GMR Data on Aircraft Structures', *NDT & E International*, Vol. 43(2), 2010.
- [7] G. Dib, R. Lattral, L. Udpa, **G. Yang**, 'A wireless sensor node for structural health monitoring using guided wave inspection', *Material Evaluation*, Vol. 71, 2013.

* Conference Proceedings

- [8] **G. Yang**, Y. Huang, L. Udpa, S. Udpa, 'Enhanced EC-GMR Inspection of Buried Cracks at Ferromagnetic Fastener Sites', *Proceedings of 18th International Workshop on Electromagnetic NonDestructive Evaluation, Bratislava, Slovak Republic, 2013*, In Press.
- [9] **G. Yang**, A. Tamburrino, Z. Zeng, et al, 'Low frequency EC-GMR detection of cracks at ferromagnetic fastener sites in thick layered structure', *Review of Progress in QNDE*, Vol. 32, 2013.
- [10] **G. Yang**, G. Dib, J. Kim, et al, 'Nonlinear, Non-stationary Image Processing Technique for Eddy Current NDE', *Review of Progress in QNDE*, Vol. 31, 2012.
- [11] **G. Yang**, Z. Zeng, L. Udpa, et al, 'Modeling and Signal Processing Sensor Tilt in Eddy current-GMR Inspection', *Electromagnetic Nondestructive Evaluation (XIV)*, Vol. 35, 2011.

[12] **G. Yang**, Q. Zhang, Y. Yang, ‘Novel Statistical Technique of Defective Information Extraction in Pulsed Eddy Current NDE’, *Information and Automation, IEEE Conference Publications*, 2011.

[13] **G. Yang**, J. Kim, S. Udpa, et al, ‘Classification of Pulsed Eddy Current-GMR Data using Principle Component Analysis’, *Electromagnetic Nondestructive Evaluation (XIII)*, Vol. 33, 2010.

[14] **G. Yang**, Z. Zeng, Y. Deng, et al, ‘Pulsed Eddy Current-GMR Inspection and Image Analysis of Multilayer Airframe Structures’, *Proceedings of Global Chinese Forum on NDT Technologies*, 2011.

[15] Y. Deng, X. Liu, **G. Yang**, ‘Model Based POD Techniques for Enhancing Reliability of Steam Generator Tube Inspection’, *Prognostics & Health Management, IEEE Conference Publications*, 2011.

[16] M. Cacciola, G. Ripepi, **G. Yang**, et al, ‘ICA based Algorithms for Flaw Classification in Pulsed Eddy Current Data: A Study’, *Proceedings of the conference on Neural Nets WIRN*, 2011.

*** Peer-Reviewed Conference Papers and Presentations**

[17] **G. Yang**, A. Tamburrino, Z. Zeng, et al, ‘Sensitivity of EC-GMR Sensors to Orientation of Radial Cracks at Fastener Sites’, *39th Review of Progress in QNDE*, Denver, Colorado, July, 2012.

[18] **G. Yang**, Y. Deng, L. Udpa, et al, ‘Development of Novel EC-GMR Sensor Systems for Inspection of Multilayer Structures with Steel Fasteners’, *18th World Conference on NDT*, Durban, South Africa, April, 2012.

[19] **G. Yang**, Y. Deng, Z. Zeng, et al, ‘Invariant Analysis of Sensor-tilt Effect in Eddy Current NDE’, *30th Progress In Electromagnetics Research Symposium Conference*, Suzhou, China, September, 2011.

[20] **G. Yang**, Z. Zeng, Y. Deng, et al, ‘EC-GMR Detection of Subsurface Defects at Steel Fastener Sites in Multilayer Structures’, *38th Review of Progress in QNDE*, Burlington, Vermont, July, 2011.

[21] **G. Yang**, Z. Zeng, Y. Deng, et al, ‘Detection of Subsurface Defects in Multilayer Structures with Steel Fasteners’, *29th Progress In PIERS*, Marrakesh, Morocco, March , 2011.

[22] **G. Yang**, L. Udpa, S. Udpa, et al, ‘Modelling of Sensor Tilt in Eddy Current–GMR Inspection and its Use in POD Estimation’, *36th Review of Progress in QNDE*, Kingston, Rhode Island, July 2009.

[23] **G. Yang**, L. Udpa, S. Udpa, ‘A GMR Based System for Pulsed Eddy Current NDE of Aircraft Structures’, *IEEE International Magnetics Conference*, Madrid, Spain, May, 2008.